Supported Bilayer Lipid Membranes and their Applications to Neuroengineering

By

Carolin Madwar

A thesis submitted to McGill University in partial fulfillment of the requirements for the degree of Doctor of Philosophy

Department of Chemistry, McGill University

Montreal, Quebec, Canada

2015

Dedicated to my family, my teachers and my former and future students.

Because of you - I am smarter, I am stronger.

Abstract

Despite impressive progress in the field of biomimetic membrane models, some of the main limitations concerning their synergy with biological systems arise from: (*i*) the physical instability of non-supported lipid bilayers, and/or (*ii*) the geometrical unsuitability of planar supports for such applications. This Thesis presents the use of bilayer lipid membranes assembled on spherical as well as fiber supports as robust and versatile experimental platforms that expand the experimental interface between model membranes and biological systems. The fabrication of spherically supported bilayer membranes (SS-BLMs) is based on tethering lipid bilayers to micron-diameter silica beads which effectively increase their compositional versatility and mechanical stability. The heterogeneous lateral organization of biomembranes (*e.g.* lipid rafts) is mimicked in SS-BLMs' co-existing lipid domains and investigated using fluorescence microscopy methods. An experimental protocol that interfaces SS-BLMs to live cultured cells, while maintaining the lipid membrane structure under physiological conditions and throughout the various manipulations necessary for their examination, is developed. This approach allows one to address membrane structural and functional roles in a biologically-relevant environment. The interactions between model and native membranes are evaluated by fluorescence correlation of the organization of the cellular cytoskeleton in response to SS-BLMs from various lipid compositions. This investigation is further used as a validation for the applicability of SS-BLMs as stable yet dynamic cell interfaces. By applying the same experimental approach, the SS-BLMs are used as artificial interfaces suitable for inducing and probing functional communication with brain cells (*i.e.* neurons). SS-BLMs having a specific composition leading to lateral heterogeneity and lipid phase separation are found to induce synapse formation from the neurons they are interfaced to. In this context, SS-BLMs are used as an experimentally accessible platform for investigating how lipid domains or rafts regulate synapse formation at artificial contacts. The SS-BLM approach is further extended to geometries with 2-dimensional curvature (*i.e.* fibers). Glass fiber-coated bilayer lipid membranes (GF-BLMs) are found to also be suitable as neuronal interfaces as they promote the formation of stable functional synapses. Bilayer lipid membranes formed on silica beads or fibers are thus excellent model membrane systems for use as engineered substrates for promoting functional neuronal networks.

Resumé

En dépit d'impressionnants progrès dans le domaine des modèles membranaires biomimétiques, leur synergie avec des systèmes biologiques est encore limitée en raison de l'instabilité physique des bicouches de lipides non supportées ou de la géométrie inadéquate des supports planaires pour de telles applications. Cette thèse présente l'assemblage de bicouches de lipides sur des supports sphériques ou fibreux et leur utilisation comme plate-forme robuste et polyvalente pour l'étude des interactions entre modèles membranaires et systèmes biologiques. Les bicouches de lipides sur supports sphériques (SS-BLMs) sont fabriquées par attachement d'une bicouche à des billes micrométriques de silice, ce support permettant d'augmenter la polyvalence compositionnelle des lipides de la membrane et la stabilité mécanique globale. L'organisation latérale hétérogène des biomembranes (telle que le phénomène des radeaux lipidiques) est imitée dans les domaines lipidiques coexistants dans les SS-BLMs et étudiée par la microscopie de fluorescence. Un protocole expérimental est développé dans le but de faire interagir les SS-BLMs avec des cellules vivantes en culture, tout en maintenant l'intégrité de la structure membranaire sous des conditions physiologiques et sous les multiples manipulations nécessaires à leur étude. Cette approche permet d'examiner les capacités structurelles et fonctionnelles de la membrane dans un environnement pertinent biologiquement. Les interactions entre les membranes modélisées et celles natives sont étudiées en corrélant avec la fluorescence l'organisation du cytosquelette cellulaire en réponse à son exposition aux SS-BLMs de diverses compositions de lipides. Cette étude est utilisée subséquemment afin de valider la possibilité d'utiliser les SS-BLMs comme une interface cellulaire stable, mais aussi dynamique. En appliquant la même approche expérimentale, la pertinence de l'utilisation des SS-BLMs comme interface artificielle pouvant induire et sonder une communication fonctionnelle avec des cellules du cerveau (*i.e.* neurones) est explorée. Les SS-BLMs, ayant une composition spécifique démontrant une hétérogénéité latérale et une séparation des phases lipidiques, induisent la formation de synapse à partir des neurones avec lesquels ils interagissent. Dans ce contexte, les SS-BLMs sont utilisées comme une plate-forme simplifiée et adéquate pour investiguer comment les radeaux lipidiques régulent la formation de synapse aux contacts artificiels. L'approche par les SS-BLMs est étendue aux supports ayant une géométrie comprenant une courbure en deux dimensions (*i.e.* des fibres). Des fibres de verre recouvertes d'une bicouche de lipides (GF-BLMs) ont été déterminées adéquates comme interface neuronale favorisant la

formation de synapses stables et fonctionnelles. Cette découverte a un potentiel attrayant pour ce qui est de la conception de détecteurs neuronaux basés sur la fibre optique pouvant capturer le signal sortant des synapses artificielles et le transmettre par la suite à d'autres cellules. En somme, les bicouches de lipides formées sur des billes ou des fibres de silice sont des modèles membranaires attirants qui démontrent un potentiel comme substrat artificiel pour promouvoir des réseaux neuronaux fonctionnels.

Acknowledgments

This dissertation would not have been possible without the help of many of my colleagues and collaborators. I would especially like to thank my supervisor, Prof. R. Bruce Lennox, for his guidance, support and encouragement; Prof. Blum, Prof. Damha, and Prof. Wiseman for their service as committee members and for inspiring scientific discussions; Prof. Sleiman and Dr. Justin Conway for their helpful collaborations, and Prof. Cuccia for his continuous mentorship and rewarding friendship. I would also like to thank the staff at the Chemistry Department and Montreal Neurological Institute of McGill University for their support and assistance.

I would like to acknowledge Dr. Gopakumar Gopalakrishan for his continuous help in shaping my knowledge about lipid chemistry, Dr. Asmahan Abu-Arish for endless discussions about fluorescence techniques and data analyses, and Dr. Patricia Yam and Dr. Margaret Magdesian for teaching me everything I know about neuronal cell cultures. Special thanks to Amélie Tessier and Prof. Xavier Ottenwaelder for their help in translating the abstract of this Thesis.

I am grateful for the undergraduate students who have worked with me; Elodie Warren and Jorge Luis Flores Anato as well as the all members of the Lennox, Colman and Fournier research groups who assisted me over the years and to whose friendships I am indebted.

Finally, I am grateful to all my family and friends who, in their unique ways, taught me how to be free-minded, follow my passion, work very hard, be patient and never compromise on quality.

Thank you.

Table of Contents

List of Figures

List of Tables

List of Abbreviations

μL: microliter

μm: micrometer

μM: micromolar

1D: one dimensional

2D: two dimensional

3D: three dimensional

5'OH: 5' hydroxyl

A: adenine

ACN: acetonitrile

AFM: atomic force microscopy

BG: background signal

bp: base pair

Bodipy-PC: 4,4-difluoro-5,7-dimethyl-4-bora-3a,4a,diaza-*s*-indacene-3-pentanoic acid

BP: band pass

C: cytosine

CB: cerebroside

CHOL: cholesterol

CL: cardiolipin

CLSM: confocal laser scanning microscopy

CNS: central nervous systems

CPG: controlled pore glass

Cryo-EM: cryogenic electron microscopy

Cy3: Cyanine 3

Cy5: Cyanine 5

DIC: diffusion interference contrast

DiI-C_{20}: 1'-dieicosanyl-3,3,3,3' -tetramethylindocarbocyanine perchlorate

DIV: days *in vitro*

DMPG: 1,2-dimyristoyl-*sn*-glycero-3-phosphoglycerol

DMT: dimethoxy trityl

DPG: diphosphatidylglycerol

DMEM: modified Eagle medium

DNA: deoxyribonucleic acid

DOPC: 1,2-dioleoyl-*sn*-glycero-3-phosphocholine

DOPE: 1,2-dioleoyl-*sn*-glycero-3-phosphoethanolamine

DOPS: 1,2-dioleoyl-*sn*-glycero-3-phospho-L-serine, sodium salt

DOTAP: 1,2-dioleoyl-3-trimethylammonium-propane, chloride salt

DPPC: 1,2-dipalmitoyl-*sn*-glycero-3-phosphocholine

DPPE: 1,2-dipalmitoyl-*sn*-glycero-3-phosphoethanolamine

DPPS: 1,2-dipalmitoyl-sn-glycero-3-phospho-L-serine, sodium salt

DS: displacement strands

ds: double stranded

DSPE-PEG2000-biotin: 1,2-distearoyl-*sn*-glycero-3-phosphatidylethanolamine-N-biotinyl (polyethylene glycol 2000)], ammonium salt

DSPC: 1,2-distearoyl-*sn*-glycero-3-phosphocholine

E17: embryonic day 17

em: emission

EM: electron microscopy

ESR: electron spin resonance

ex: excitation

FCS: fluorescence correlation spectroscopy

FRAP: fluorescence recovery after photobleaching

FRET: fluorescent resonant energy transfer

FTIR: Fourier transform infrared

G: guanine

GF-BLM: glass fiber-coated bilayer lipid membranes

GP: generalized polarization

GUV: giant unilamellar vesicle

HBSS: Hank's balanced salt solution

HPLC: high-performance liquid chromatography

hr: hour

Hz: hertz

I: intensity

ITO: indium tin oxide

L_α: fluid phase

L_β: gel phase

L_c: subgel phase

L_d: liquid-disordered phase

L_o: liquid-ordered phase

LP: long pass

LPC: lysophosphatidylcholine

LUV: large unilamellar vesicle

M: molar

mg: milligram

mL: milliliter

MLVs: multilamellar vesicles

mM: millimolar

mW: milliwatts

MW: multiwalled

Nano-SIMS: nano-secondary ion mass spectrometry

NBD PE: 1,2-dipalmitoyl-*sn*-glycero-3-phosphoethanolamine-N-(7-nitro-2-1,3-benzoxadiazol-4-yl), ammonium salt

NDS: normal donkey serum

NH: amine

nm: nanometer

nM: nanomolar

NMR: nuclear magnetic resonance

N-Rh-DHPE: Lissamine™ Rhodamine B 1,2-dihexadecanoyl-*sn*-glycero-phosphoethanolamine, triethylammonium salt

n.s.: not significant

nt: nucleotide

P: phosphate

PA: phosphatidic acid

PAGE: polyacrylamide gel electrophoresis

P_{β}': ripple phase

PC: phosphatidylcholine

PCC: Pearson correlation coefficient

PDL: poly-D-lysine

PE: phosphatidylethanolamine

PEG: polyethylene glycol

PI: phosphatidylinositol

PLL: poly-L-lysine

PNS: peripheral nervous systems

QCM: quartz crystal microbalance

rpm: revolutions per minute

PS: phosphatidylserine

ROI: region of interest

RT: room temperature

s: second

ss: single stranded

S-BLM: supported bilayer lipid membrane

SD: standard deviation

SM: sphingomyelin

S_o: solid-ordered

SS-BLM: spherical supported lipid bilayer membrane

SPR: surface plasmon resonance

STED: stimulated emission depletion

SUV: small unilamellar vesicle

SV: Synaptic vesicle

T: thymine

TEM: transmission electron microscopy

TP: triangular prism

T_m: main phase transition temperature

T_{pre}: pre-transition temperature

TRITC-DHPE: *N*-(6-tetramethylrhodaminethiocarbamoyl)-1,2-dihexadecanoyl-*sn*-glycero-3-phosphoethanolamine, triethylammonium salt

UV: ultraviolet

V: volts

w/v: weight per volume

Contributions of Authors

This Thesis consists of 5 Chapters. Chapter 1 is a general introduction to membrane lipid chemistry and neuronal cell structures. Chapter 2 has been published, while Chapters 3 and 4 will be submitted to peer-reviewed journals. Other published work which closely relates to the main body of the research presented in this Thesis, and where the author of this Thesis was closely involved, is included as Appendices. Conclusions and future work are provided in Chapter 5.

Chapter 2: "Interfacing Living Cells and Spherically Supported Bilayer Lipid Membranes"
Co-authored by Gopakumar Gopalakrishnan and R. Bruce Lennox.
Langmuir, 2015, *31*, 4704-4712.

Chapter 3: "Spherical Supported Bilayer Lipid Membrane Microdomains and Synapse Formation"
Co-authored by Gopakumar Gopalakrishnan and R. Bruce Lennox.
To be submitted to *ACS Chemical Neuroscience*.

Chapter 4: "Micron-Scale Glass Fiber Supported Lipid Membranes as Functional Biomimetic Materials for Neuroengineering Applications"
Co-authored by R. Bruce Lennox.
To be submitted to *Advanced Functional Materials*.

Appendix I: "Label-free Visualization of Ultrastructural Features of Artificial Synapses *via* Cryo-EM."
Co-authored by Gopakumar Gopalakrishnan, Patricia T. Yam, Mihnea Bostina, Isabelle Rouiller, David R. Colman, and R. Bruce Lennox.
ACS Chem. Neurosci. 2011, *2*, 700-704.

Appendix II: "Dynamic Behavior of DNA Cages Anchored on Spherically Supported Lipid Bilayers"
Co-authored by Justin W. Conway, Thomas Edwardson, Christopher K. McLaughlin, Johans J. Fahkoury, R. Bruce Lennox, and Hanadi F. Sleiman.
JACS 2014, 136, 12987-12997.

The work presented in Chapters 2 and 3 was initiated by Dr. Gopakumar Gopalakrishnan. Carolin Madwar designed and performed the experiments as well as data analysis. Carolin Madwar wrote the manuscripts with the assistance of Dr. Gopakumar Gopalakrishnan and Prof. R. Bruce Lennox.

The work presented in Chapter 4 was initiated and performed by Carolin Madwar. Prof. R. Bruce Lennox provided guidance and contributed to writing the manuscript.

The study presented in Appendix I was designed by Dr. Gopakumar Gopalakrishnan, Prof. David R. Colman, and Prof. R. Bruce Lennox. Carolin Madwar, Dr. Gopakumar Gopalakrishnan, Dr. Patricia T. Yam, and Prof. Isabel Rouiller contributed to experiments and writing the manuscript. Dr. Mihnea Bostina provided technical support for the cryo-TEM experiments. All the authors contributed to the editing of the manuscript.

The study presented in Appendix II was initiated by Dr. Justin Conway and Carolin Madwar. Carolin Madwar contributed to many aspects of the experimental design, prepared SS-BLM/DNA samples, performed all the microscopy experiments and analysis and contributed to the interpretation of the results. Dr. Justin Conway with the assistance of Dr. Thomas Edwardson and Dr. Christopher McLaughlin designed, synthesized and characterized the DNA scaffolds. Dr. Johans Fahkoury assisted in figure design. Carolin Madwar, Dr. Justin Conway and Prof. Hanadi Sleiman wrote and edited the manuscript with the assistance of Prof. R. Bruce Lennox.

Chapter 1

Introduction

1.1 General Introduction

"The survival of all life rests on this veil of material; a subtle membrane just two molecules thick."[1]

From a biological perspective, the basic unit that contains the fundamental molecules of life is defined as a cell.[2] Indeed, it is the *cell membrane* that provides unity and guides the evolution of a cell. The cell membrane defines the spatial organization of genetic material and living machinery inside the cell, with respect to one another and their surroundings. In this way it allows the biochemical reactions essential for life to occur in a well-defined volume and enclosed environment. The membrane also acts as a selective barrier that allows for the controlled influx and efflux of molecules that are required for growth. The membrane is physically flexible, thus allowing shape and size changes to occur, and it is fluid to allow for the lateral diffusion of membrane constituents, which is necessary for their proper function. Indeed, the cell membrane not only turns the cell into an efficient and dynamic reaction vessel, but is also a specific compartment that accommodates many of the cell's vital functions. Examples include communicating with the environment, transporting nutrients and waste, and generating electric potential. [3, 4, 5, 6]

Ideas concerning the structure of the cell membrane are constantly evolving. The notion of some kind of barrier that encloses cells dates back to the early 1800s at which time the existence of the cell itself was introduced.[7] Scientists today continue to investigate how cell membranes are structured and how their organization contributes to cellular function. Lipids, in combination with proteins, are the major constituents of cell membranes. Ever since it was established that cells are surrounded by a bimolecular sheet of lipid molecules,[8] lipid bilayers have remained dominant in our understanding of biomembrane architectures. Moreover, they have become common laboratory models for studying the physicochemical properties of lipids and relating

how these may contribute to the functional roles of biological membranes.[9] Several membrane models involving the self-assembly of lipid molecules into lipid bilayers and other higher-order architectures have been developed to address questions related to lipid/cell biology.[10, 11] Figure 1.1 illustrates some examples of model membrane systems. These are constantly being developed in an effort to build general theories regarding the organization of cell membranes and how they function. Indeed, such experimental models not only help to forge connections between membrane theory and structure/function, but also help to develop methodologies, plan experiments, and interpret results.

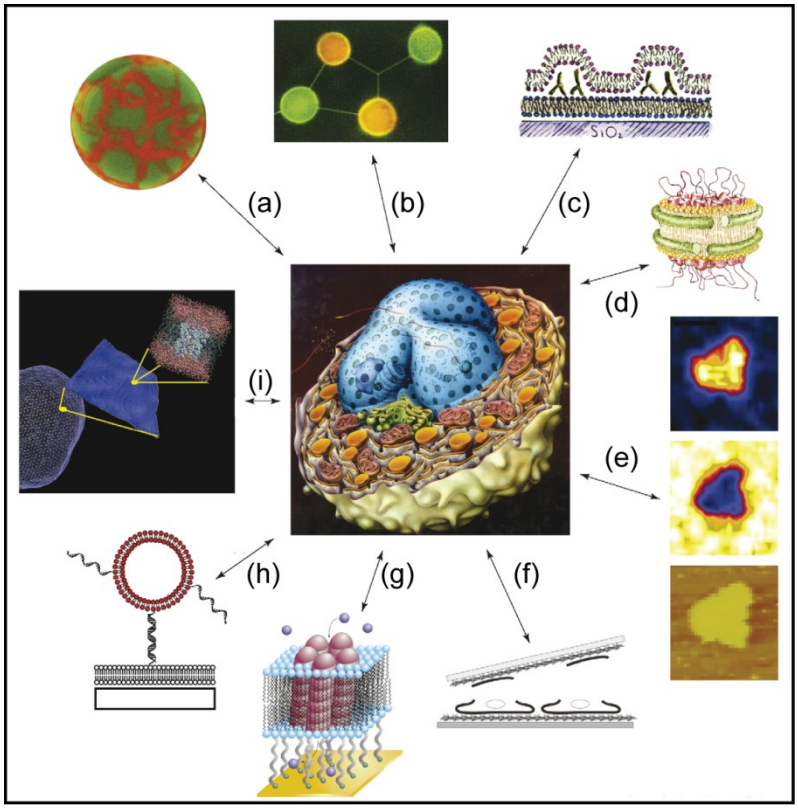

Figure 1.1 Model membrane systems. The sketch in the center illustrates the complex multi-component architectures of a eukaryotic cell, and the images surrounding it are examples of model membrane systems, which are applied to study the properties of the lipid bilayer as it is the structural basis of the cell membrane: (*a*) giant unilamellar vesicles (GUVs) from varying lipid mixtures; (*b*) networks of GUVs connected by membrane tubular extensions; (*c*) ruptured GUVs on solid supported bilayer lipid membranes (S-BLMs); (*d*) membrane nanodiscs incorporating transmembrane proteins; (e) S-BLMs analyzed by nano-secondary ion mass spectrometry (Nano-SIMS); (*f*) ruptured cell membranes on solid supports; (*g*) ion channels-containing bilayers tethered to a solid support; (*h*) DNA-tethered vesicles on a S-BLMs; and (*i*) visual representation of multi-scale simulations of cells and their lipid bilayer membranes.[12] Adapted with permission from reference 12 (Elsevier 2007).

The motivation for this Thesis stems from a realization that model lipid membranes can facilitate our understanding of biological phenomena and can also have potential applications beyond basic research. This Thesis discusses the possible synergy between *in vitro* membrane systems and their use in a biological context for developing artificial surfaces-neuronal interfaces. In order to establish useful outcomes of membrane models, it is necessary to understand the basic physicochemical features of lipids in the membrane model, as their role and influence on biological functions are dependent on their physical properties, organization and behavior. This introductory Chapter provides a brief overview of the structural features of lipids in cell membranes, the physical properties that impact their lateral organization into phase-separated domains, as well as the different model systems that address lipid features which ultimately influence cell membrane function. This Chapter also introduces the model systems of interest to this Thesis, namely supported bilayer membranes on spherical substrates. The motivation for developing supported membranes as model systems, the advantages of using them in biological research, and their potential in bioengineering applications are described.

The following reviews provide a comprehensive discussion of membrane lipids with an emphasis on structural or functional properties: Dowhan, W.; 1997,[13] van Meer, G.; 2008,[14] Eeman, M. & M. Deleu; 2010,[15] Koynova, R. & Tenchov, B.; 2013[16] and Lombard, J.; 2014.[17]

1.2 Fundamentals

1.2.1 Cell Membranes

Cell membranes contain a remarkable variety of lipid molecules. Given that generation of such a large collection of molecules requires multiple and complex metabolic pathways, lipid structural diversity must be advantageous to the cell and its membrane-bound compartments. In fact, this diversity leads to lipids having many functional roles in essential processes that are mediated by the cell membrane.[14] The fundamental role of lipids involves providing a matrix for the cell membrane and enabling the self-integrity of the cell. This has been recognized since the early experiments of Gorter and Grendell (1925), which indicated that cell membranes are made up of a double layer (*i.e.* bilayer) of lipids.[8] For many years, membrane lipids were assumed to be passive molecules that, in addition to providing the boundary that separates intra- and intercellular aqueous media, serve as an environment where membrane proteins can be

specifically and selectively assembled to achieve proper cell signaling. Although this conclusion is correct, the structural diversity of lipids and their complex organization, as observed with new analytical techniques, have extended the knowledge of the roles that lipids play in membrane function. It is now known that the physicochemical state of the cell membrane is influenced to a great extent by its lipid composition. Membrane properties, such as curvature, fluidity, charge distribution, thickness, and affinity to specific molecules are determined for the most part by the constituent lipid molecules. These vary across organelles and species depending on the specific functional requirements.[18, 19, 20]

The following sections highlight the chemical features of membrane lipids that encompass the fundamental principles behind the formation of the bilayer structure and its physicochemical properties.

1.2.1.1 Lipids in Cell Membranes

The eukaryotic cell dedicates about 5% of its genome to the synthesis and homeostasis of lipids, producing several thousand distinct lipid species.[13, 14] Lipids found in cell membranes are amphiphilic, containing a polar head group and non-polar tail(s) (Fig. 1.2). The major structural lipids that form cell membranes are the glycerophospholipids (Fig. 1.2a). Commonly referred to as phospholipids, these are composed of a glycerol molecule bonded to a phosphate group at the glycerol *sn*-3 position. The phosphate forming the polar headgroup can be further esterified with an alcohol (*e.g.* choline, ethanolamine, serine, inositol or glycerol), which yields a number of different phospholipids. The glycerol backbone can also be modified by ester, alkyl ether or alkenyl ether bonds, at the glycerol *sn*-1 and *sn*-2 positions, with fatty acid chains forming the non-polar tails. These tails can further vary in terms of length and degree of unsaturation.[23] Phosphatidylcholine (PC) lipids represent more than 50% of the phospholipid content in eukaryotic membranes. Most PC lipids have one *cis*-unsaturated fatty acyl chain (see example in Fig. 1.2a), which adds to the fluid nature of the cell membrane bilayer. Sphingolipids are another class of lipids found in membranes (Fig. 1.2b). These are structurally similar to the glycerophospholipids, but instead of glycerol, their backbone is based on sphingosine (an amide bonded to a fatty acid forming what is known as a ceramide). Depending on the functional groups attached to the hydrophobic ceramide backbone, different classes of sphingolipids result (*i.e.* sphingophospholipids and glycerosphingolipids). When the polar headgroup contains a

phosphate moiety, the sphingolipids are classified as phospholipids. For example, sphingomyelins (SM) which form the myelin sheath of nerve axons are functionalized with phosphatidylcholine (PC) or phosphatidylethanolamine (PE). Due to the presence of long saturated acyl chains in SMs, these lipids add rigidity to the cell membrane.[22] Cholesterol (Fig. 1.2c) is another essential component of cell membranes in many organisms.[21] It is distinguished by a four-fused carbon rings structure connected to a hydroxyl group (Fig. 1.2c), which gives it its amphiphilic character.

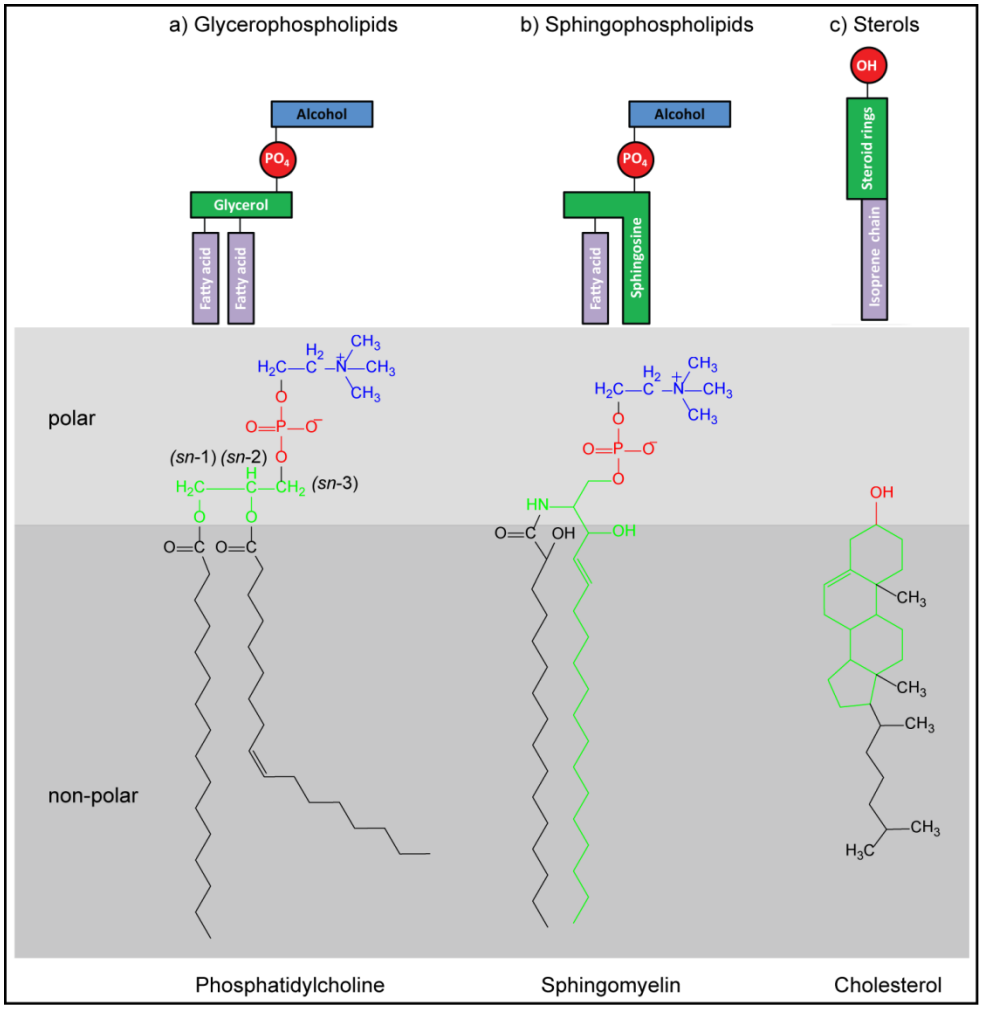

Figure 1.2 Cell membrane lipids. Schematic representation of a: (a) glycerophospholipid, (b) sphingophospholipid and (c) sterol, with chemical structures of common examples. The amphiphilic nature of these lipids is exemplified by their polar and non-polar constituents.

As mentioned above, the lipid composition of cell membranes is highly variable depending on the species and the subcellular compartments they form. Furthermore, even within the same

organelle, the lipid composition is quite different between the inner and the outer leaflets of the bilayer membrane. It is also constantly changing, depending on the developmental stage, environmental and physiological conditions as well as disease circumstances. Such lipid asymmetry and compositional variability is used to fine-tune the membrane properties and consequently modulate many of its functions, as will be explored in the following sections. Figure 1.3a illustrates the lipid composition in different membranes throughout the eukaryotic cell.[14, 22] Because the membrane contains a high percentage of glycerophospholipids (*e.g.* phosphatidylcholine (PC), phosphatidylethanolamine (PE), phosphatidylserine (PS), phosphatidylinositol (PI) and phosphatidic acid (PA)) in comparison to other lipid types, the cell membrane is usually referred to as the phospholipid membrane. It should also be noted that cholesterol is typically present in equimolar amounts relative to the total quantity of phospholipids in mammalian plasma membranes.[14] Moreover, the unique presence of certain lipid components in some cell types may indeed be connected to the specialized function of these cells.[14] For example, Figure 1.3b shows the variable lipid compositions found in plasma membranes of different neuronal cell types.

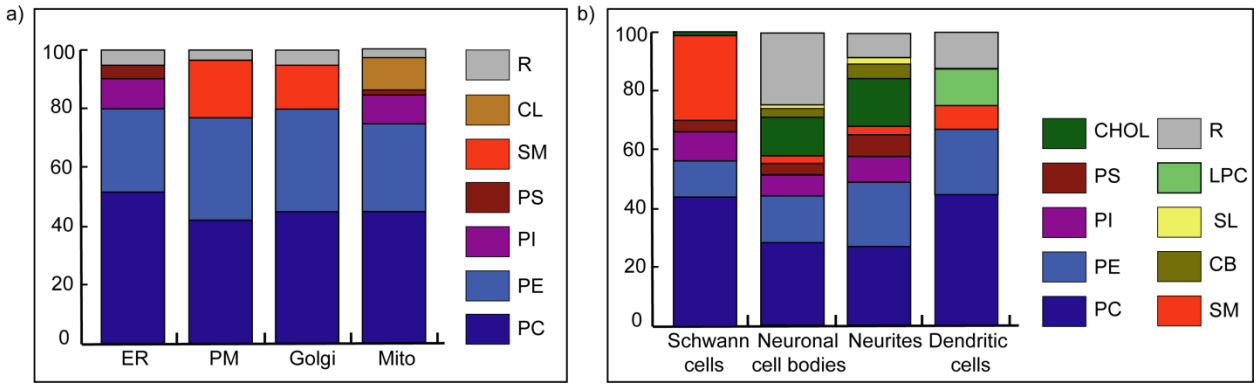

Figure 1.3 Lipid compositions of different membranes in eukaryotic cells. Graphical representation of the lipid compositional data (*a*) in different subcellular compartments (expressed as a percentage of the total phospholipids);[14] and (*b*) in different types of neuronal cells (values are given as percentages of the total weight %).[23, 24, 25] The following abbreviations are used: CB: cerebroside, CHOL: cholesterol, CL: cardiolipin or diphosphatidylglycerol (DPG), LPC: lysophosphatidylcholine, PC: phosphatidylcholine, PE: phosphatidylethanolamine, PI: phosphatidylinositol, PS: phosphatidylserine, SM: sphingomyelin, and R: remaining lipids. Adapted with permission from reference 14 (Nature Publishing Group 2008), reference 23 (John Wiley and Sons 1997), reference 24 (John Wiley and Sons 2002) and reference 25 (Elsevier Masson SAS 2006).

1.2.1.2 Lipid Bilayer Assemblies

The physical behavior of lipid molecules in solution and their ability to adopt a bilayer organization is a result of their amphiphilic nature, exemplified by the polar (hydrophilic) headgroups and the non-polar (hydrophobic) tails (Fig. 1.2). It is indeed this feature that causes lipid molecules, above a certain concentration, to self-assemble in aqueous solution into larger extended macromolecular structures (Fig. 1.4). Because the chemical details of these polar and non-polar regions can vary to a large extent, different assemblies can result. Their formation is rapid and spontaneous as they represent the lowest-energy molecular orientations, mainly driven by the hydrophobic effect at the hydrocarbon chains to minimize their unfavourable interactions with the polar environment. Once formed, these assemblies are further stabilized by van der Waals attractive forces favouring the close packing of the hydrophobic tails, as well as electrostatic interactions and hydrogen bonds between the headgroup moiety and the surrounding water molecules.[22, 26]

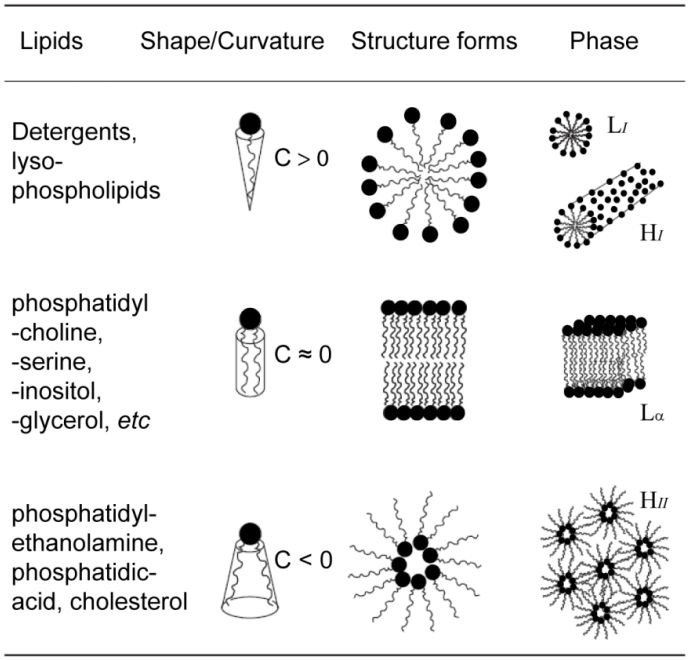

Figure 1.4 Self-assembly of lipid molecules in aqueous media. Different assemblies result depending on the structure and 3D geometry of the lipid molecules. Circles represent the hydrophilic headgroups and wavy lines represent the hydrophobic tails.[27] Adapted with permission from reference 27 (Elsevier Inc. 2011).

As shown in Fig. 1.4, in addition to the common lipid bilayer organization, lipid molecules can self-assemble into a variety of liquid-crystalline structures, depending on the effective shape of the constituent lipid.[28, 29, 30, 31] For example, when the cross-sectional area of the headgroup matches that of the acyl chains, the lipid molecule has an overall cylindrical shape and tends to adopt bilayer structures with lamellar morphologies (L_α), as is typically observed in cell membranes. Interestingly, the lipids found in biological bilayer membranes (Fig. 1.3) display the full spectrum of effective shapes: (*i*) the cylindrical shape (*e.g.* PC and PS), (*ii*) the conical shape (PE) and (*iii*) the inverted conical shape (*e.g.* lysophosphatidylcholine; LPC). Although some of these lipids do not support the planar bilayer arrangement of the membrane, when mixed with other lipid species with varying geometries, their different shapes may complement one another and allow for the formation of a stable bilayer structure. The variability of lipids within the bilayer, and also between its two leaflets, is of particular importance for various cellular events such as vesicle budding and membrane fusion.[32] It also contributes to the membrane potential,[33, 34, 35] and is critical for membrane-mediated processes including protein binding and transport.[36]

1.2.1.3 Lipid Diffusion in Bilayer Membranes

Within a bilayer membrane, lipid molecules can rotate about their own axes. They also move laterally (within their monolayer) or transversely (between the two monolayers). These dynamics (Fig. 1.5a) impart fluidity to cell membranes. In fact, studying the diffusion of lipids in bilayer membranes helps to understand the mechanism of membrane permeation and diffusion of membrane-bound molecules. Methods based on magnetic resonance as well as fluorescence imaging have been applied to the measurement of lipid diffusion in bilayer structures. Fluorescence quenching[37] and energy transfer,[38] as well as nuclear magnetic resonance (NMR)[39, 40] and electron spin resonance spectroscopy (ESR),[41] are useful in addressing short-range diffusion, based on the frequency of bimolecular collisions within the membrane. On the other hand, fluorescence recovery after photobleaching (FRAP)[42] and fluorescence correlation spectroscopy (FCS)[43] are useful in addressing long-range diffusion and are based on the time required to transverse a defined area of the membrane. Information regarding the pathway and range of motion for lipids in the plane of the membrane can also be obtained through fluorescence single particle tracking.[44] In these techniques, the fluidity of the bilayer is characterized by measuring a diffusion coefficient, which describes the timescale associated with

a specific mode of movement. For example, the lateral diffusion coefficient of phospholipids in a variety of bilayer membranes, based on FRAP and NMR techniques, is between 10^{-2} and 10 $\mu m^2/s$.[45] In comparison, lipids can also precess around their own axis, but within a timescale on the order of nanoseconds rather than microseconds. In contrast, when lipids undergo "flip-flop" transferring from one monolayer to the other, a much longer timescale (on the order of several hours and up to days) is required. This is because lipid flip-flop involves unfavourable exposure of the polar headgroup to the hydrophobic core of the bilayer, and is thus a high energy and infrequent state. In cell membranes, cholesterol with its smaller polar headgroup (a single hydroxyl group) can more easily undergo transbilayer movement.[46, 47] In addition to the translational diffusion described above, the chains of lipid molecules can also undergo internal rotation *via* conformational changes (*trans-gauche* isomerisation, Fig. 1.5b). For saturated lipids this type of rotation can occur over timescales of a few picoseconds. However the presence of double bonds hinders this type of motion.[15]

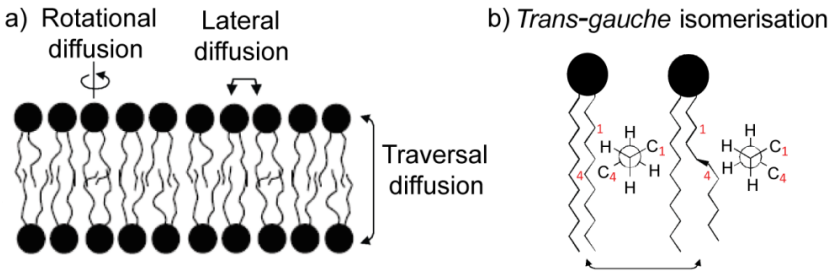

Figure 1.5 Lipid diffusion in bilayer membranes. Sketch illustrating (a) the different types of translational diffusion modes, and (b) the conformational changes that can occur within lipid bilayers.[15] Adapted from reference 15 (open access).

1.2.1.4 Lipid Phase Transitions in Bilayer Membranes

The lipid bilayer can assume a number of different physical states (Fig. 1.6). These are governed by the chemical structure of its lipid constituents (*e.g.* the type of hydrophilic moiety, the length of the acyl chains, their degree of unsaturation, *etc.*) as well as external environmental parameters (*e.g.* temperature, pressure, and aqueous phase composition). These parameters influence the lipid-lipid interactions and result in the formation of different lamellar phases, which have unique physical properties and biological significance. In fact, the phase behavior of bilayer lipids reflects their molecular order within the membrane and consequently defines their

translational diffusion and the resulting membrane fluidity. The characterization of the different physical states require the use of several techniques, including calorimetry, Fourier transform infrared (FTIR), NMR spectroscopy and freeze-fracture electron microscopy (EM). Each has proven to be very useful for studying the thermodynamic and structural properties of lipid bilayers.[16]

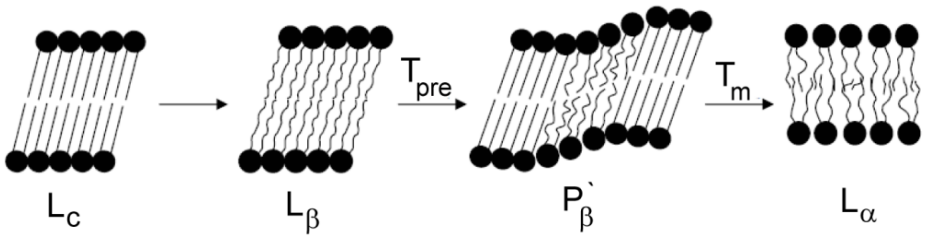

Figure 1.6 Bilayer lamellar phases. Schematic representation of the thermally-induced transitions between different lamellar phases of a single-component lipid bilayers: subgel phase (L_c), gel phase (L_β), ripple phase (P_β') and fluid liquid crystalline phase (L_α). T_m denotes the main phase transition temperature and T_{pre} denotes the pre-transition temperature.[48] Adapted with permission from reference 48 (The Royal Society of Chemistry 2009).

In addition to the fluid liquid crystalline phase (L_α), single-component lipid bilayers can organize in solid ordered or "gel" states. These include the subgel phase (L_c), where the acyl chains are highly ordered, the gel phase (L_β), where chains remain ordered but the lipid headgroups are more hydrated, or the ripple phase (P_β'), where the lipid monolayers splay inwards and the chains possibly interdigitate. These different bilayer lipid phases convert into one another driven by changes in temperature, pressure, composition and water content. Figure 1.6 shows a generalized phase sequence of the thermally-induced phase transition[49] of bilayer-forming lipids. For some lipids, the thermal lamellar transitions involve additional stages, such as the "pre-transition" which is detected a few degrees lower than the main transition temperature, resulting in the formation of what is known as the "ripple phase" (P_β'). This ripple phase is generally found in the case of lipids with large headgroups such as PCs, where the acyl chains can adapt a tilted orientation, with respect to the plane of the membrane, and interdigitate. This phase results in alternating regions of ordered and disordered acyl chains. The surface texture of membranes in this phase appears as periodic ripples when examined by freeze-fracture EM.[50, 51, 52]

In the L_β gel phase (also known as the solid-ordered; S_o phase) the lipid acyl chains are fully extended and assume a uniform all-*trans* orientation, thereby increasing the thickness of the

bilayer. The lipid chains are more rigid and their headgroups are tightly packed resulting in a very compact network and consequently decreasing the dynamics within the bilayer. On the other hand, the L_α fluid phase (also known as the liquid-disordered; L_d phase) is characterized by increased molecular motion, both laterally and rotationally, due to a much less extended orientation of the acyl chains, as they can assume *gauche* conformations thus becoming more disordered and loosely-packed. As a result, the lipid molecule assumes a larger area per molecule in the fluid phase in comparison to the gel phase[53] and the overall thickness of the bilayer is reduced.[54]

The (L_β–L_α) gel–liquid crystalline transition (also referred to as the order–disorder or solid–fluid transition) is the main transition occurring in lipid bilayers, and is the most relevant to cell membranes. It occurs when the temperature is increased above a specific temperature, defined as the lipid phase transition temperature ((*i.e.* melting; T_m). "Melting" the acyl chains as they convert from *all-trans* to *gauche* conformations (Fig. 1.5) results in increased headgroup hydration and increased intermolecular entropy.[53] These events require energy input as they involve expanding the acyl chain region against attractive van der Waals interactions, as well as exposing the hydrophobic core to the aqueous interface. This explains the large change in enthalpy associated with this transition (Fig. 1.7a).[22]

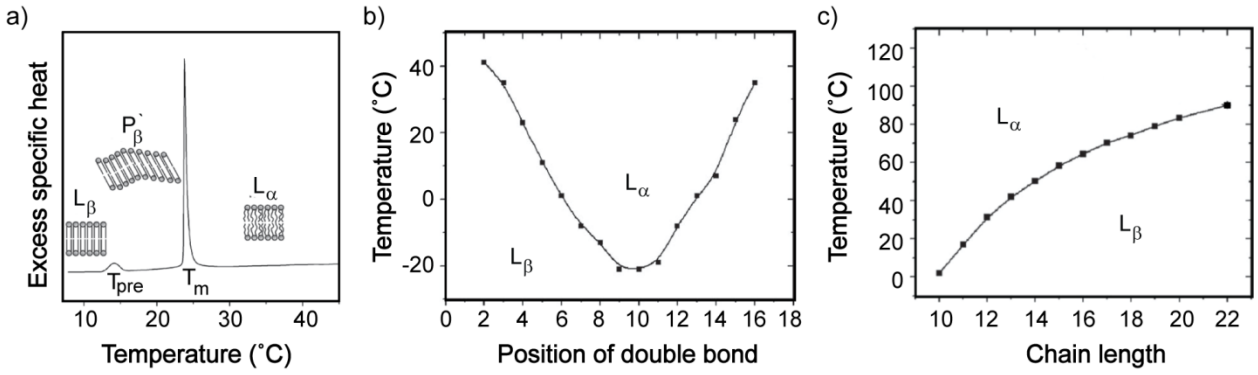

Figure 1.7 Phase transition temperatures and their dependence on lipid chemical structure. (a) Differential scanning calorimetry (DSC) trace of DMPG multilamellar vesicles with schematic representations of lamellar phases.[55] Dependence of transition temperature T_m on: (b) the double-bond position for DOPC bilayers[56] and (c) the hydrocarbon chain length in saturated PE lipids.[57] The following abbreviations are used: DOPC: 1,2-dioleoyl-*sn*-glycero-3-phosphocholine, DMPG: 1,2-dimyristoyl-*sn*-glycero-3-phosphoglycerol, T_m: main transition temperature, T_{pre}: pre-transition temperature. Adapted with permission from reference 55 (open access), reference 56 (American Chemical Society 1983) and reference 57 (Elsevier 1998).

The phase transition temperature is a characteristic value that depends on the lipid chemical structure, most importantly the acyl chains. The degree and position of unsaturation in the lipid acyl chain significantly alters the T_m (Fig. 1.7b). Double bonds cause kinks in the lipid structure leading to less compact packing and resulting in unsaturated lipids having lower T_m. Similarly, the longer and more saturated the acyl chains are, the higher the T_m value, due to the additional van der Waals attractive interactions that develop between them. Therefore higher thermal energy is required to "melt" their tightly-packed bilayers (Fig. 1.7c). In addition to the structural details of the acyl chains, those of the headgroup can also influence the nature of the lipid phase, since the size of the headgroup affects their hydration level as well as their hydrogen bonding to neighboring lipids.

In the case of cellular bilayers, saturated acyl chains are found in sphingomyelins, and therefore areas rich in these lipids exist in a gel-like phase. On the other hand, cholesterol, with its amphiphilic character and inverted conical shape, plays the role of a molecular spacer that intercalates between sphingolipids in cell membranes, and greatly influences the membrane lamellar nature. An intermediate bilayer physical state, referred to as the liquid-ordered phase (L_o) exists in the presence of cholesterol, and exhibits characteristics between those of the solid ordered (S_o or L_β) and the liquid disordered (L_d or L_α) phases. This L_o phase has indeed been the subject of many research studies because of its relevance to the functional phases of cell membranes.[58] The following sections provide details of current views on the organization of cell membranes and their implications on cellular events mediated by the membrane.

1.2.1.5 Lipid Phase Separation in Cell Membranes

Growing knowledge concerning the heterogeneous lateral and transmembrane organization of lipids in cellular membranes[59, 60, 61] stimulated evolution of the "fluid-mosaic model"[62] postulated in 1972 by Singer and Nicolson. The fluid-mosaic model describes membranes of eukaryotic cells as homogenous bilayers existing in the L_d fluid phase, where lipids are randomly distributed and in a constant lateral state of motion. An important refinement of this model is the widely-discussed and more recent "lipid raft model".[63, 64] The lipid raft model describes a specific case of lipid phase separation within cellular membranes whereby L_o domains co-exist with a surrounding L_d environment (Fig. 1.8). The raft model accounts for observations concerning membrane regions that confine the lateral diffusion of membrane components. This confinement

regulates molecular interactions and membrane functions.[58] The current view is that these domains or rafts result from lipid-lipid interactions, specifically of saturated glycerophospholipids, glycosphingolipids and sphingomyelin, with cholesterol. These assemblies are further stabilized through lipid-protein interactions (*i.e.* with the actin cytoskeletal scaffold)[65] and protein-protein interactions (*i.e.* cross-linking and binding of membrane proteins to cell surface receptors).[66, 67]

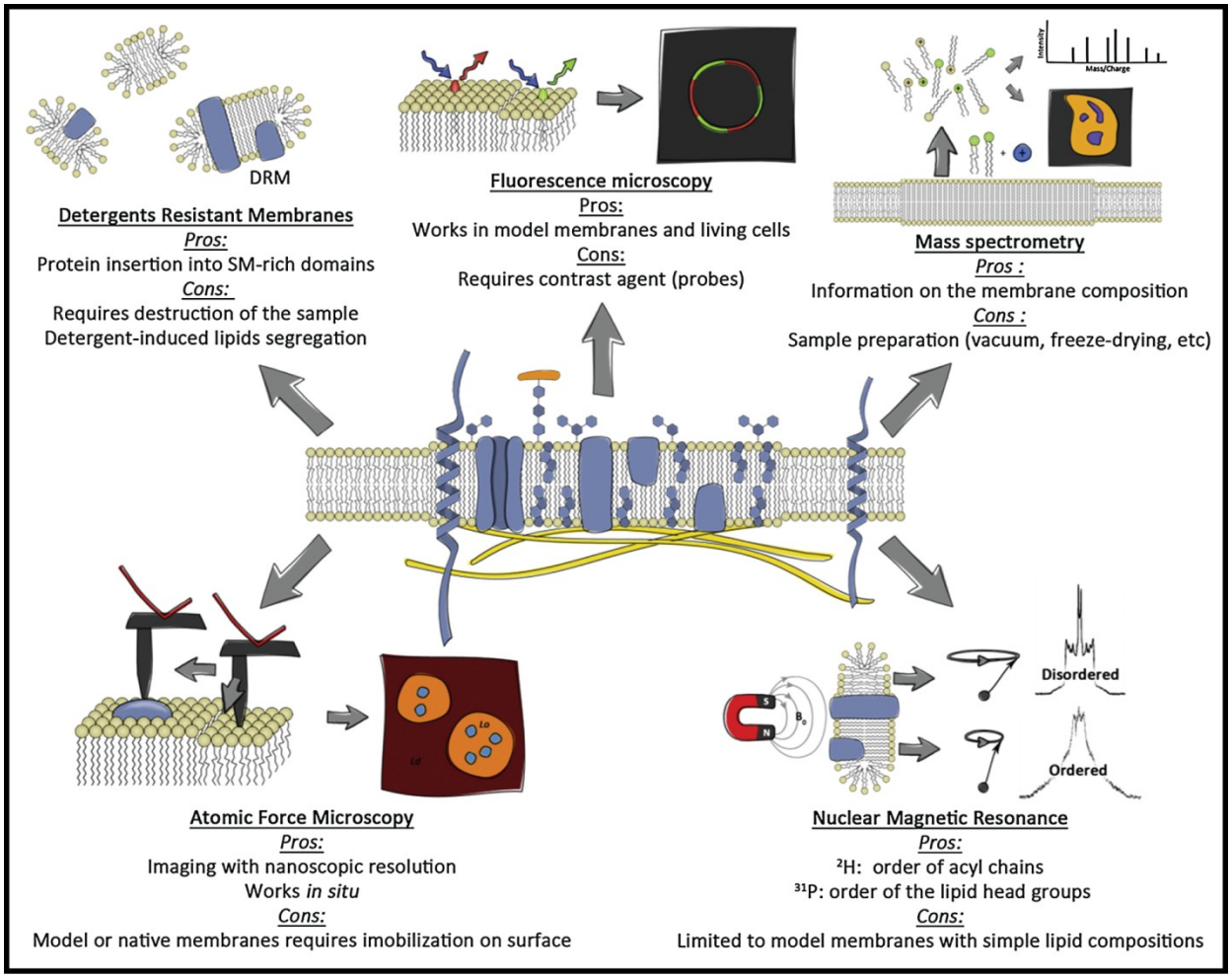

Figure 1.8 Common characterization methods for lipid rafts in model and native membranes. Since different phases display distinct physical properties (*e.g.* packing, lipid diffusion, bending modulus), co-existence of such domains exerts a change in many physical parameters of the membrane (*e.g.* permeability, mechanical properties), which can be measured using a variety of analytical techniques. The advantages and disadvantages of the different approaches are highlighted.[68] Adapted with permission from reference 68 (Elsevier Ltd. 2014).

Although the heterogeneous lateral organization of lipids in cell membranes is well-established, the exact composition, stability, and functionality of lipid rafts remain a matter of debate. A variety of sophisticated methods have been developed to characterize lipid rafts (Fig. 1.8).[68] However, the fact that they are highly dynamic structures results in their characterization being very challenging.[69] Their reported size is in the range of 10 – 200 nm,[69, 70] requiring detection methods with high spatial resolution (*e.g.* fluorescence correlation spectroscopy; FCS,[71] fluorescence resonance energy transfer; FRET[72] and stimulated emission depletion; STED microscopy).[73] However, lipid rafts can also self-associate to form larger domains that can be detected with conventional optical microscopies.[74, 75] Variability has also been reported in their lifetimes (from <1 ms to >1 s)[70] due to the existence of different types of lipid rafts or different formation mechanisms.[2, 76, 77] This variability can also be attributed to the use of detection methods with different time resolution. Indeed, the complexity and the dynamic nature of lipid rafts in cell biology require the development of model systems which represent the organization of cell membranes in a simplified frame. Lipid rafts contribute to a variety of cellular events by modulation of protein function *via* (*i*) inducing conformational changes by the rigidity of the raft regions and/or (*ii*) promoting/inhibiting specific protein-protein or lipid-protein interactions.[78] The development of simplified model membranes with minimal components will be valuable for determining the structural and functional roles of lipid rafts individual components.

1.2.2 Membrane Model Systems

Cell membranes are dynamic structures which display a high level of lipid association, functional phase transitions as well as complex transfer of molecular information.[22] In addition, the existence of multiple lipid-lipid, lipid-protein and protein-protein interactions define the complexity of addressing and realizing the functional roles of distinct membrane constituents.[12] Different model systems with controllable compositions and geometries have been developed to retain the essential membrane lipid bilayer structure it in order to: (*i*) study membrane properties, structures and processes, (*ii*) assess and visualize the roles of individual membrane components, their organization and dynamics and (*iii*) investigate the membrane activities in response to diverse natural and synthetic compounds, such as therapeutic agents.[9, 10, 12, 15, 79] The most studied model systems include bilayers from synthetic lipids and from cell membrane extracts.[80] These are studied in the form of vesicles (*i.e.* giant unilamellar vesicles, GUVs) which are either free-

standing[81] or tethered[82] to supports, and also in the form of planar[79] and spherical bilayers[83] supported either directly or tethered[84, 85] on solid substrates (Fig. 1.1). Many analytical characterization techniques have been applied to these model membranes, especially since the solid supported set-up allows for the application of surface-sensitive techniques[86] (*vide infra*).

The following sections summarize the advantages and disadvantages of model membrane systems (GUVs and S-BLMs) in applications related to reconstructing a simplified arrangement of biological membranes and exploring their physical properties, specifically the phase behavior of lipid bilayers and its related functional roles in membrane-mediated processes. A brief overview of the fabrication methods and characterization techniques is also provided. These topics are further reviewed in: Bagatolli, L. A.; 2010,[87] Brown, D. A.; 2001,[88] London, E.; 2002 and 2005.[89, 90]

1.2.2.1 Lipid Vesicles

Lipid vesicles (or liposomes) are formed from two lipid monolayers spontaneously closing into nano- or microspheres with the hydrophilic lipid headgroups exposed to the surrounding aqueous environment and to the enclosed internal volume. Typical lipids used for their formation include combinations of phospholipids (*e.g.* PC, PE, PG, PI and PS), sphingomyelin and cholesterol.[22] Their structures can be readily assembled into a variety of sizes and lamellarities by the hydration of dried lipid films (*i.e.* lipid film swelling) at a temperature above the relevant T_m (Fig. 1.9). This method is based on hydrophobic interactions driving the spontaneous formation of stratified lipid bilayers on solid hydrophilic surfaces such as glass substrates. Once hydrated, the bilayers swell and detach from the surface, closing into principally multilamellar vesicles with a uniform lipid composition.[91]

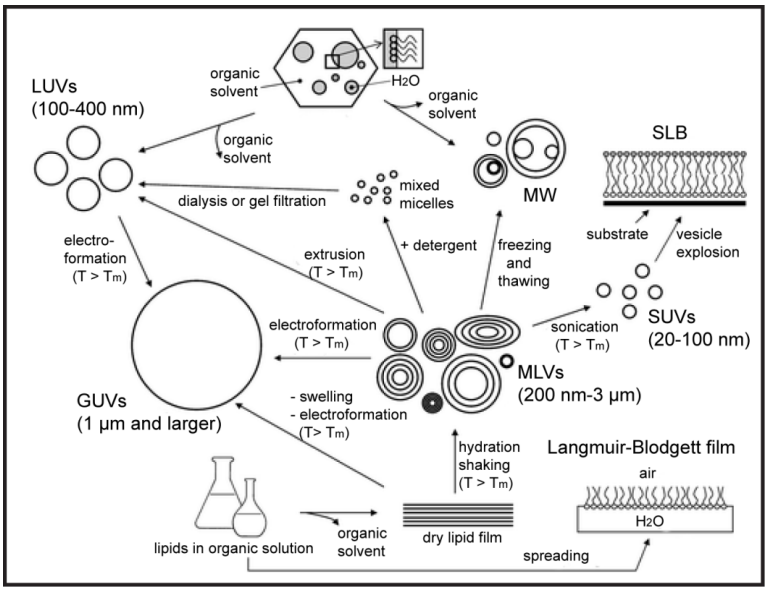

Figure 1.9 Examples of preparation protocols for different model membranes. The following abbreviations are used: T: temperature, T_m: main transition temperature, MLVs: multilamellar vesicles, SUVs: small unilamellar vesicles, LUVs: large unilamellar vesicles, GUVs: giant unilamellar vesicles and MW: multiwalled.[92] Adapted from reference 92 with permission (Royal Society of Chemistry 2009).

Single bilayer vesicles with diameters in the range of 1 – 100 µm (*i.e.* GUVs) are particularly relevant as biomimetic model systems.[15] Firstly, their size and fluidity are comparable to those of most living cells. Second, their size allows for examination and manipulation by optical microscopies (*e.g.* fluorescence and confocal microscopy). Their large size is advantageous for studying membrane phase behavior and also membrane fusion, molecular recognition and cell adhesion.[12] Optical microscopy of GUVs allows one to address the effect of lipid composition on the mechanical properties of their membrane surfaces[93] and also their interactions with different proteins.[94] In addition, GUVs have been used to study membrane interactions with other cellular components (*e.g.* non-membrane proteins[95] and nucleic acids).[96]

The versatility of GUVs extends to their preparation methods. The most common methods involve slow hydration (*i.e.* lipid film swelling for long periods of times) and electroformation (*i.e.* lipid film deposition on conductive glass substrates and hydration under an alternating electric field). The electroformation method is recommended for reproducibility under controlled conditions but is not applicable to systems with low salt concentration buffers.[91]

Although they are appealing for addressing several membrane properties, the use of GUVs as biomimetic membrane models for *in vitro* or *in vivo* applications have significant limitations,

mainly due to their mechanical instability.[97, 98] For example, their use is problematic for experimental procedures involving extensive mechanical manipulations (*e.g.* vigorous mixing, washings, *etc.*) or environmental changes (*i.e.* temperature, pH, salt concentrations, *etc.*). In order to overcome such limitations, the use of solid supports to increase the robustness of these bilayers is an attractive solution. The following section describes the formation of S-BLMs and highlights their applications in membrane-related studies.

1.2.2.2 Supported Bilayer Lipid Membranes (S-BLMs)

S-BLMs are bilayers assembled on solid substrates (planar or spherical), with the advantage of added mechanical stability. Examples of surfaces used as supports include mica, silica, alumina and titanium oxide.[83, 99, 100, 101, 102, 103, 104, 105, 106] In these systems, the polar head groups of one lipid monolayer faces the aqueous surroundings while the second monolayer faces the support with a thin layer of water separation (*ca.* 10 – 20 Å) intervening.[102] The presence of this "hydration cushion" effectively preserves the supported membrane fluidity.[107] However, its small thickness does not prevent potential denaturation or decreased lateral mobility of incorporated proteins. S-BLMs formed with the use of lipopolymer tethers and polymer cushions can overcome such limitations. Their use increases the water layer thickness and effectively reduces the bilayer interactions with planar[108, 109, 110, 111] or spherical[85, 112] substrates. The solid support does not significantly alter the structural, thermodynamic or molecular dynamic properties of S-BLMs, but rather adds to their robustness.[97, 113] S-BLMs are extensively used to study membrane biophysics and molecular organization using surface-sensitive techniques.[114] In addition, they are convenient for studying molecular interactions for biomedical applications and drug screening.[115] Furthermore, when assembled on functional surfaces (*e.g.* semiconductors and magnetic or electro-optical devices), S-BLMs become a conduit for smart devices. These would be particularly relevant as cell interfaces for bioengineering applications.[116]

Planar S-BLMs were initially fabricated by the Langmuir-Blodgett method (Fig. 1.9), which involves sequential transfer of two monolayers from an air-water interface onto a solid support.[113] This approach ideally allows one to control the lipid composition and bilayer asymmetry, which is typically not possible for liposomes. Another method for preparing S-BLMs is the fusion of unilamellar lipid vesicles onto a solid support (Fig. 1.9). This method can be applied to both planar and spherical S-BLMs.[97, 117] The fusion mechanism involves the

adsorption of vesicles onto the solid substrate and their subsequent deformation and rupture. Hydrophobic interactions at the bilayer edges drive the formation of continuous supported bilayers. Both preparation approaches described above are simple and can effectively yield lipid bilayers with higher stability, in comparison to non-supported vesicles. Furthermore, the confinement of lipid bilayers to a surface provides a controllable environment that is suitable for characterization by a variety of analytical techniques which are not always feasible for free-floating liposomes. When supported on planar substrates, lipid bilayers can be studied by atomic force microscopy (AFM), surface plasmon resonance (SPR), the quartz crystal microbalance (QCM) technique, optical ellipsometry, fluorescence microscopy, FTIR, as well as X-ray and neutron reflectivity.[117, 118, 119, 120, 121, 122, 123, 124, 125] Among some of the above mentioned techniques, flow cytometry, NMR, and DSC,[83, 126, 127, 128, 129, 130] are also applicable for characterizing the dynamic and structural properties of bilayers supported on spherical substrates.

Altogether, S-BLM systems are attractive as model membranes and the choice of using planar *versus* spherical supports ultimately depends on the desired application. In the context of this Thesis, spherical supported lipid bilayer membranes (SS-BLMs) are promising model systems for use as cell interfaces in bio- and neuroengineering applications. The following section provides an overview of SS-BLMs formed on silica beads.

1.2.2.3 Spherical Supported Bilayer Lipid Membranes (SS-BLMs) on Silica Beads

Model membrane systems consisting of lipid bilayers assembled on silica beads have multiple benefits and applications.[97] In fact, substrates made of silica are suitable candidates for biological applications due to their biocompatibility and low toxicity. In addition, their physical and chemical properties can be precisely modified, which allows for specific and unique applications that would otherwise not be possible. For example, their particle size, shape, and porosity can be specifically controlled. Furthermore, their surface can be easily functionalized by reaction with organosilanes or chemical conjugation to biomolecules. When their surface coatings are lipid bilayers, silica substrates become particularly attractive as biomimetic platforms. Specifically, the use of silica supports with a spherical shape (silica beads) allows the formation of SS-BLMs that combine the advantages of liposomes with the convenience of mechanical stability and controlled size distribution. In addition, the possibility to use silica beads with various diameters

(ranging from submicrons to several microns) allows the formation of lipid bilayers that mimic cell membranes in terms of composition *and* curvature. These improved liposome analogs are therefore quite attractive not only as model systems for membrane biophysical studies but also as biomimetic cell interfaces for bioengineering applications.[97, 116] The following sections describe some methods for their preparation, characterization, and applications as membrane models.

1.2.2.3.1 Preparation of SS-BLMs

Lipid bilayers can be deposited on silica beads by combining them with liposomes, typically in the form of SUVs. The spontaneous adsorption of liposomes on silica beads followed by their rupture and fusion allows for the formation of SS-BLMs.[129, 130, 131] Vesicles derived from plasma cell membranes can also be deposited on silica beads in the same manner.[132, 133] SS-BLMs can also be formed on porous silica beads,[128, 134, 135, 136] which are particularly advantageous as carries for chemical agents or biomolecules.[110] In addition to passive adsorption, other methods exist for assembling more stable and versatile SS-BLMs. For example, covalent,[137, 138] and non-covalent (*e.g.* bioconjugates) linkages onto functionalized silica beads.[85, 139]

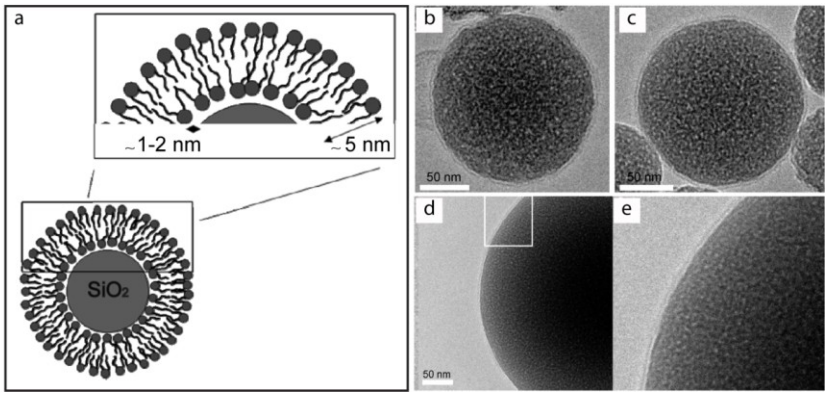

Figure 1.10 Lipid bilayers assembled on silica beads. (a) Sketch illustrating the formation of bilayer membranes (thickness *ca.* 5 nm) on silica beads.[97] (b-e) Cryo-transmission electron microscopy (TEM) images of a single lipid bilayer assembled on different size silica beads. The bilayer in image (c) is supported directly on the silica beads, whereas the bilayers in images (b) and (d) are tethered using biotin-avidin interactions and PEG polymers. The image shown in (e) is a magnified view of the selected area in image (d) showing the single bilayer membrane assembled on the bead surface.[85] Adapted with permission from references 97 (open access) and reference 85 (American Chemical Society 2009).

1.2.2.3.2 Characterization of SS-BLMs

The characteristics of lipid bilayers are maintained when supported or tethered on silica beads (Fig. 1.10), as examined by several analytical techniques.[110] As previously mentioned, SS-BLMs are typically separated from the silica beads by a thin (*ca.* 10 – 20 Å) hydration cushion, which allows them to maintain their fluid nature as demonstrated by DSC,[148] FRAP,[147] and NMR.[143] In addition, the use of polymers (*e.g.* PEG) for tethering lipid bilayers onto silica beads has minimal effect on the lateral diffusion of the bilayer lipids.[85, 140] The phase transition behavior in lipid bilayers that are either supported or tethered onto silica beads is also comparable to their vesicle counterparts, as studied by DSC and NMR.[85, 141] When directly supported on silica beads, the bilayer exhibits decreased stability with higher transition temperature lipids and is also restricted to lipid compositions with intrinsic curvature compatible with a spherical support. This however is not the case for tethered bilayers which can be made from a variety of lipid mixtures.[85]

1.2.2.3.3 Applications of SS-BLMs

SS-BLMs offer multiple advantages as model membrane systems, such as high mechanical stability, compositional versatility, controllable and homogenous size and ease of washing by centrifugation. An example of successfully using SS-BLMs as biomimetic membrane models includes incorporating biomolecules into the bilayer while preserving their function. These biomolecules include protein pumps (*e.g.* bacteriorhodopsin),[112, 128] neurotransmitter receptors (*e.g.* human type 3 serotonin),[128] adhesion molecules (*e.g.* ICAM-1[129] and P-selectin),[142] cell membrane glycolipids (*e.g.* ganglioside GM1),[143] calcium transporters (*e.g.* calcium-ATPase)[127] and electron transporters (*e.g.* cytochrome c oxidase).[131] SS-BLMs functionalized with biomolecules can be used for molecular detection purposes. This allows one to address protein-protein interactions and their cellular consequences. For example, the functionalization of SS-BLMs with the postsynaptic protein neuroligin and their subsequent addition to a live cell culture enabled for the investigation of cellular effects following neuroligin binding to its cellular partner neurexin.[144] The proper assembly of neuroligin into the SS-BLM, along with the mechanical stability provided by the beads, make this experimental protocol feasible. Protein-lipid interactions can also be addressed using SS-BLMs, and have been proven useful for biosensing applications. For example, fluorescence-based detection of antibodies binding specifically to cardiolipin lipids has been illustrated using SS-BLMs.[145, 146] The versatility of

analytical techniques applicable to SS-BLMs have been demonstrated in a similar protocol using NMR and DSC for the detection of the myelin basic protein on anionic SS-BLMs.[147]

The use of SS-BLMs in triggering neuronal responses has also been demonstrated and is a major focus of this Thesis. The interactions between live neurons and specifically designed SS-BLMs (Fig. 1.11) were found to induce functional neuronal networks.[148] In this context, the possibility to modulate the lipid composition in SS-BLMs, using conventional bioconjugations protocols, addresses the role of bilayer composition at membrane contacts. It is of considerable interest to further investigate the contribution of lipid membrane heterogeneity in triggering neuronal function. Understanding the influence of specific structural details on membrane interactions at neuronal contacts is critical for developing artificial networks and is a central aim of this Thesis.

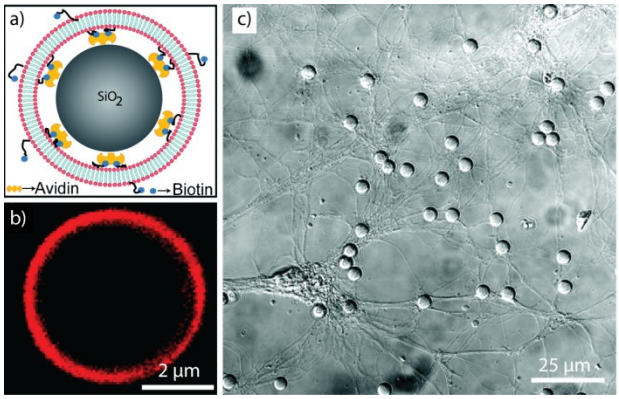

Figure 1.11 Spherically supported bilayer membranes (SS-BLMs). (A) Sketch illustrating the assembly of bilayer membranes onto silica beads using biotin–avidin interactions and polymer spacers. (B) Confocal fluorescence image of SS-BLMs from DOPC/DOTAP/DPPE (25:25:50) with 0.1 mol % for the fluorescent lipid (TRITC-DHPE). (C) Representative DIC image of hippocampal neurons (16 DIV) interacting with SS-BLMs.[148] Adapted with permission from reference 148 (American Chemical Society 2010). The following abbreviations are used, DOTAP: 1,2-dioleoyl-3-trimethylammonium-propane (chloride salt), TRITC-DHPE: *N*-(6-tetramethylrhodaminethiocarbamoyl)-1,2-dihexadecanoyl-sn-glycero-3-phosphoethanolamine, triethylammonium salt, DIC: diffusion interference contrast and DIV: days *in vitro*.

Despite the fact that SS-BLMs have found application in addressing biomolecular and membrane-membrane interactions, these studies have been conducted without a detailed understanding of the SS-BLM structure or the dynamics of its lipid constituents. For example, the nature and thickness of the water layer is little understood. Similarly, the extent to which thermal phase properties, lipid flip-flop, and lipid phase separation are similar to or different than their liposome analogues has not been systematically documented. SS-BLMs mimic the cell

membrane and can be used for addressing membrane biophysics in a simplified, stable and reproducible model membrane. However, an understanding of their structure and dynamics is critical for evaluating their potential use as membrane mimics and cell interfaces.

The following section describes the use of model systems (specifically GUVs) in studying lipid phase separation. This will be followed by a proposal of how SS-BLMs can add to the current knowledge regarding lipid phase separation and how this information can be further employed toward developing functional interfaces for bio- and neuroengineering applications.

1.2.3 Model Membrane Systems for Studying Bilayer Phase Separation

The *in vivo* existence of lipid rafts is still subject to debate despite the fact that co-existing lamellar phases in model lipid mixtures are well-established. In the context of phase behavior in lipid mixtures, the two most studied model systems are GUVs and planar S-BLMs. These models do not necessarily represent the complexity of the lipid environment in cell membranes or the multifaceted interactions between lipids and proteins. However, they do provide a simplified platform which can be used to assess the roles of individual membrane components as well as their organization and dynamics.[12]

1.2.3.1 GUVs for Studying Bilayer Phase Separation

GUVs have been used extensively for studying phase separation in lipid bilayers. As mentioned earlier, the average size of GUVs (mean diameter *ca*. 25 μm) is comparable to that of cells, and therefore they represent an attractive model for addressing lateral order and organization of cellular membranes.[92] Their size also enables using optical microscopies for observing specific membrane structural details at the level of single vesicles. This is not necessarily feasible using other characterization methods (*e.g.* DSC, fluorescence spectroscopy, X-ray diffraction, FTIR, or NMR) which collect bulk measurements from liposomal solutions (*e.g.* MLVs, LUVs or SUVs). In fact, fluorescence imaging (*e.g.* using epifluorescence, confocal or two-photon microscopy) of GUVs has been extensively used to study bilayer phase coexistence. These fluorescence techniques examine single GUVs in order to measure the intrinsic physical properties of fluorescent probes present in the lipid mixture. Examples of such measurements include determining diffusion coefficients,[149] dipolar relaxation,[74, 145, 146] and the preferential partitioning of fluorescent probes into co-existing lipid phases.[147, 148] GUVs are typically made from lipid

components that, at relevant compositions and temperatures, exist in distinct phases. GUV experiments initially concentrated on bilayers from single component synthetic lipids or mixtures with few (*i.e.* two or three) components, however it is now possible to form GUVs from natural lipid extracts[149, 150] and cellular membrane fragments.[80, 151] In addition, fluorescent probes available for phase separation studies are continuously improving to accommodate advanced fluorescence techniques as well as complex membrane compositions.[68] Generally, such probes can distinguish different lipid phases by either: (*i*) binding to specific membrane lipids (*e.g.* GM1 ganglioside[152] or cholesterol),[147] (*ii*) partitioning into specific phases depending on structural similarities,[144] or (*iii*) displaying different intrinsic properties in response to the surrounding environment[153] (Fig. 1.12). Based on these different strategies, fluorescence methods allow for direct visualization of micron-sized lipid domains, which can be addressed under controlled physical conditions. Quantitative data gathered from fluorescence images (such as domain size and shape) has been useful for constructing phase diagrams for lipid mixtures (Fig. 1.12, a3).[148, 154, 155] These diagrams can predict the phases existing in a membrane at equilibrium and at various temperatures and compositions.[156] In the context of cell membrane models, phase diagrams are developed for binary mixtures of phospholipids, which display coexistence of solid ordered (L_β) and liquid disordered (L_d) phases or mixtures of a sphingophospholipid and cholesterol (Fig. 1.12 B3), which represents the simplest approximation of liquid ordered phase (L_o) of mammalian membranes. The addition of cholesterol to binary systems (with one high T_m lipid and one low T_m lipid) has also been extensively studied to model cellular membranes. Figure 1.12 shows an example of a phase diagram for such a ternary lipid mixture (*i.e.* DOPC/DSPC/CHOL),[157] where the correlation between lipid fractional composition and the corresponding distribution of phase domains at various temperatures is summarized.

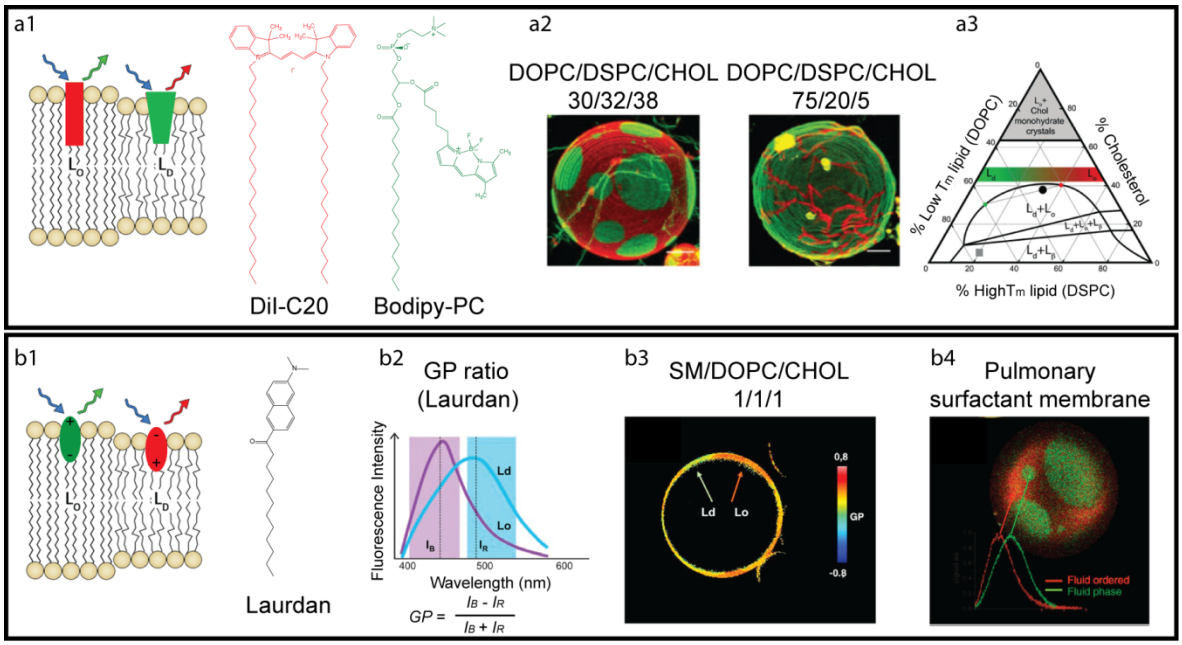

Figure 1.12 Examples of fluorescence characterization of lipid phase separation in GUVs. (a1) Principle of partitioning probes which preferentially segregate into a specific lipid phase based on structural similarities (left) and examples of their chemical structures (right).[157] (a2, a3) Confocal microscopy Z-scanning of GUVs from DOPC/DSPC/CHOL with partitioning probes. The red fluorphore (DiI-C_{20}) segregates into ordered phases (either L_o or L_β) while the green fluorophore (Bodipy-PC) segregates into disordered phases (L_d). (a4) Phase diagram of DOPC/DSPC/CHOL bilayers displaying different lipid fractional compositions and corresponding phases at different temperatures.[157] Adapted with permission from reference 157 (Elsevier 2007). (b1) Principle of solvatochromic probes which display different absorption/emission spectra according to changes in solvent polarity (left) and an example of their chemical structure (right). (b2) Fluorescence spectra of Laurdan in model membranes.[158] (b3, b4) Application of Laurdan for studying phase separation in GUVs from SM/DOPC/CHOL (b3) and from native pulmonary surfactant membrane (b4).[153] (b2) adapted with permission from reference 158 (Nature Publishing Group 20100) and (b3, b4) from reference 153 (Elsevier 2006). The following abbreviations are used: DOPC: 1,2-dioleoyl-*sn*-glycero-3-phosphocholine, DSPC: 1,2-distearoyl-*sn*-glycero-3-phosphocholine, CHOL: cholesterol, DiI-C20: ,1'-dieicosanyl-3,3,3',3'-tetramethylindocarbocyanine perchlorate, GP: generalized polarization, I: intensity, SM: sphingomyelin.

1.2.3.2 Developing a New Model System for Studying Bilayer Phase Separation

The existing data from GUVs indicate different physical properties of the co-existing lipid domains. However, they do not provide any direct correspondence to membrane behaviour in a physiological environment, where lipids encounter various and complex molecular triggers that can influence and enforce specific phase behaviors. It is of critical importance in any study of membrane models to validate the lipid phase coexistence under physiological conditions and

relate them to the cell membrane environment. Despite impressive progress in the field of membrane model systems, there are very few examples of their application to biological systems, where they are interfaced with native cellular components.[9] Although there are many advantages to the current model systems, thus far studies have focused on addressing membrane physical properties in a very controlled environment, which is not representative of biological conditions. There are many technical challenges in experimental approaches, where model systems are interfaced with biological membranes in a live cell culture. GUVs also require additional mechanical stability if they are to be used under physiological conditions. In this regard, SS-BLMs are attractive variants of GUVs. The use of SS-BLMs in biologically-representative environments will help overcome the limitations of physical instability (in the case of GUVs)[98, 159] and also the technical restrictions related to planar geometries (in the case of planar S-BLMs).[97]

1.3 The Nervous System: Facts, Function, and Diseases

The work presented in this thesis involves the use of SS-BLMs with phase separated domains as cell interfaces for neuroengineering applications. This section is dedicated to highlight some of the basic nervous system structures and processes that are involved in developing functional neuronal interactions.

The nervous system is composed of a complex network of nerves and specialized cells known as neurons, which form organized circuits to enable signal transmission and communication between different parts of the body. Structurally, the nervous system has two major divisions; the peripheral and the central nervous systems (PNS and CNS, respectively). The PNS consists of the nerves outside of the brain and spinal cord and is responsible for connecting the limbs and the organs to the CNS. The significance of the CNS is overwhelming, as it is responsible for coordinating the activities of all parts of the body. It consists of both the brain and spinal cord. The brain marks the very center of the nervous system and is the most complex biological organ. It controls the functions of the organism by deriving information from the sensory organs in order to refine actions. To perform this complicated task, the brain coordinates between a series of functional subsystems; the sensory neurons, the motor neurons and the interneurons. Sensory neurons allow the reception of information from the outside world through the senses. Sensory neurons are usually present in the sensory organs, and transmit information from the periphery

via the spinal cord to the brain. The motor neurons carry information in the opposite direction away from the brain *via* the spinal cord to the muscles and organs in the periphery. The interneurons, which form the majority of the brain, process this information in the form of a final action(s).[165, 166]

1.3.1 Neurons

Exchanging information between the different types of neurons is the basis of functional communication in a healthy nervous system. This process, termed synaptic signalling is unidirectional in nature. Information flows from a presynaptic to a postsynaptic neuron across a narrow gap (*ca.* 20 nm) known as the synapse.[167] Neurons have specialized structures that allow them to receive and send chemical or electrical potential signals rapidly and precisely. As shown in Fig. 1.13, dendrites, projecting extensions of the neuron cell body, are the main locale that capture the signals being sent to the neuron in the form of chemical messengers (neurotransmitters). The axon, or the nerve fiber, conveys the incoming signal as a series of electrical impulses and, in contrast to the dendrites, carries it away from the cell body. The presence of many electrically active transmembrane proteins creates short-lived electrical impulses (*i.e.* the action potential) along the axon by controlling the diffusion of ions across the cell membrane. Many axons are surrounded by a segmented insulating sheath of myelin, which effectively accelerates propagation of an electrical signal from one node to the next, along the axon. Once the action potential reaches the axon terminus, it stimulates the release of neurotransmitters from the neuron *via* exocytosis of neurotransmitter-filled vesicles (*i.e.* the synaptic vesicles). The neurotransmitters move across the synapse gap and then align to receptors on the membrane of the next dendrites (Fig. 1.13). In some rare cases, the membranes of the pre- and postsynaptic neurons become connected through intercellular channels (known as the gap junction pores), which allow for the diffusion of ions as well as other second messengers and metabolites between the two communicating neurons. This ionic flow changes the postsynaptic membrane potential thereby generating, or inhibiting, postsynaptic action potentials. This chemical and electrical cellular circuitry allows for communication within the nervous system.[167, 168]

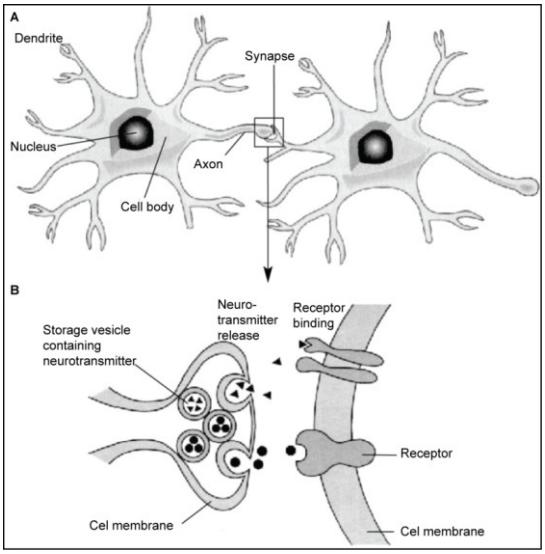

Figure 1.13 Neuronal communications across the synapse. Scheme illustrating (A) pre- and post-synaptic neurons and (B) chemical signal transmission across a synapse.[169] Adapted with permission from reference 169 (open access).

1.3.2 The Chemical Synapse and the Neurotransmitter System

In an ultrastructural sense, the synapse is comprised of three distinct compartments: the presynaptic bouton, the postsynaptic density, and a synaptic cleft which forms the gap (*ca.* 20 nm) between them. Within the presynaptic bouton, *i.e.* the end terminal of the presynaptic axon, neurotransmitter-filled vesicles are tightly clustered. Upon stimulation of a chemical synapse, synaptic vesicles fuse with the plasma membrane in order to release neurotransmitters into the synaptic cleft. The neurotransmitters (*e.g.* acetylcholine, norepinephrine, dopamine, serotonin and gama aminobutyric acid) diffuse across the synaptic cleft, where the pre- and postsynaptic membranes align, so that they can bind to and activate receptors on the postsynaptic site, in order to complete the process of synaptic transmission.[170] The postsynaptic density is visibly thicker compared to the presynaptic side and appears in transmission electron microscopy (TEM) image as an electron dense region of the plasma membrane.[171]

Synaptic vesicles (SVs) are fundamental organelles in the synaptic signalling as they contain the neurotransmitter molecules which allow for excitatory or inhibitory postsynaptic effects. The various processes associated with SVs uptake, storage, fusion, retrieval and release involve numerous biochemical reactions and are highly regulated by a variety of proteins.[172] For example, the cytoskeleton protein actin is a major component of the underlying presynaptic scaffold. Its filaments are thought to form the molecular tracks across which SVs travel.

Synapsins, which are integral SV membrane proteins, link the SVs to the F-actin filaments and also bind SV together into clusters, and in doing so, control their storage. Synaptophysin is another integral SV protein which participates in the exocytosis process. Other cytosolic proteins such as bassoon can modulate the functions of SVs by secondary interactions with SV membrane proteins. The above are just a few examples of the vast array of proteins that control the functions of SVs. Most importantly, because SVs and their associated proteins are basic components of synaptic signaling, their identification is a fundamental part of investigating functional communication between neurons. In this regard, immunochemistry and fluorescence microscopy are invaluable tools that enable the detection of SV protein expression by the use of fluorescently-labeled antibodies.[172, 173]

1.3.3 Brain Disorders and the Field of Neuroengineering

Synaptic transmission is essential for brain function. Neurological disorders, stroke, trauma and tumors can all contribute to brain damage by affecting the structure or function of neurons and therefore compromising the dynamic interplay between the various components of the nervous system.[174] In addition, the disruption of membrane rafts has been shown to affect several cellular processes essential for neuronal activity leading to a number of brain disorders.[175] Brain injury is extremely difficult to repair endogenously, and often leads to permanent damage of the affected sensory or motor organs.[174, 176] The field of neuroengineering seeks to develop alternative strategies to improve these outcomes. Although the brain is the most complex biological structure, it can also recognize simple molecular and physical cues and use them to adapt to changes due to disease and/or injury.[176] An example of a promising neuroengineering approach is explored in this Thesis, where artificial substrates that promote presynapse formation are developed.

1.4 Context and Scope of Thesis Research

The field of model membranes is both diverse and creative, as each generation of model systems has specific advantages in addressing questions concerning basic membrane science, or in establishing functional devices.[9, 10] The research presented in this Thesis is focused on developing an experimental platform that can be used for probing the structural and functional roles of model membranes in biologically-relevant environments. This approach both reinforces

basic knowledge regarding membrane organization, and also provides fundamental insight into the contribution of the lipid constituents to various membrane functions. The experimental platform introduced in this Thesis uses SS-BLMs on silica substrates as stable interfaces that can present well-characterized molecular and physical cues to an environment of living cells.

Chapter 2 presents the development and fabrication of the model membrane system (SS-BLMs) consisting of bilayers formed from various lipid mixtures tethered onto avidin-coated silica beads using biotinylated-PEG lipids. The characterization of SS-BLMs is carried out using fluorescence imaging, specifically confocal laser scanning microscopy (CLSM). Establishing reproducible co-existing lipid domains in SS-BLMs is fundamental to developing biomimetic interfaces that resemble cell membranes, not only in terms of composition but also lateral organization. In order to address lipid phase behavior in membranes, co-existing microdomains in SS-BLMs from a variety of mixtures containing low-melting and high-melting PC lipids as well as cholesterol are explored. Their fluorescence visualization is achieved using partitioning probes which further allow addressing membrane fluidity in SS-BLMs by the FRAP technique.

Chapter 2 also introduces the experimental approach developed for combining a simplified model system (*i.e.* SS-BLMs) with living cells. The suitability of SS-BLMs in such applications is examined by addressing their physical and mechanical stability in a cell culture environment, specifically with living neurons. This type of validation constitutes an experimental approach that, to our knowledge, has not been previously reported in other model systems, such as GUVs or planar S-BLMs. In this context, the behavior of SS-BLMs is assessed using 3D fluorescence images, which contain information (*i.e.* quantitative morphological data) regarding the model membrane in the presence of living cells. In order to explore how components of the model membrane interact with complex cellular components, the organization of cytoskeletal filaments (*i.e.* actin and microtubules) of live neurons is examined in response to the SS-BLMs they are interfaced to.

The use of SS-BLMs as functional cell interfaces for neuroengineering applications is demonstrated in Chapter 3. The development of artificial substrates for promoting neuronal regeneration in the nervous system is indeed a promising approach to improving the outcomes of brain damage following disease or trauma. The *in vitro* formation of presynapses on micron-diameter SS-BLMs displaying co-existing lipid phases was previously demonstrated.[148] In Chapter 3, we investigate the involvement of lipid phase separation in directing lipid membrane-

induced synapse formation. The SS-BLMs are used to examine how extracellular membrane heterogeneity presented on the model membrane influences the dynamics of cellular microenvironments, specifically at artificial synaptic junctions.

These studies have led us to extend the SS-BLM approach to glass supports with 2D curvature (*i.e.* fibers). This allows one to address the relative importance of substrate geometry and its role in contributing to the observed lipid membrane-induced synapse formation. Chapter 4 explores the possibility to establish functional neuronal contacts on fibers coated with bilayer membranes, which further advances the development of optical fiber-based sensors for detecting and transmitting the generated synaptic information.

This Thesis demonstrates how mixed lipid bilayer membranes supported on spherical as well as fiber substrates provide a versatile experimental platform. This experimental platform is promising for bio- and neuroengineering applications as it highlights meaningful connections between membrane structure and function.

1.5 Experimental Techniques

The studies presented in this Thesis involve the use of specialized experimental approaches that are often not common to chemistry research. The following section highlights these techniques and their advantages in the context of the performed experiments.

1.5.1 Fluorescence Microscopy

The majority of the work presented in this Thesis relies on the optical investigation of lipid bilayers and cell cultures. Lipid bilayers were doped with fluorescently-labeled lipids to allow their observation using fluorescence microscopy. As for the cell cultures, they were imaged using phase contrast microscopy during growth and with fluorescence microscopy after fixation and immunochemistry labeling. Confocal laser scanning microscopy (CLSM) was the fluorescence technique of choice as it yields high resolution images and uses a considerable number of commonly used excitation and emission laser sources.

1.5.1.1 Confocal Laser Scanning Microscopy (CLSM)

Confocal imaging is an advanced optical microscopy technique that provides many advantages for imaging biological specimens as well as synthetic materials. Confocal microscopy is an

optical sectioning technique that makes use of spatial filters (*i.e.* pinholes) to collect fluorescence resulting from a defined focal plane. This eliminates a significant amount of blur or "out-of-focus light", which is basically the fluorescence occurring at areas above and below the designated focal plane. This plane is defined by pinhole apertures positioned in front of the excitation source (laser system) and in front of the detector (photomultiplier tube). In this way, the confocal technique results in superior spatial resolution compared to conventional wide-field microscopy. Furthermore, confocal microscopy allows for the generation of in-focus 3D images based on collecting consecutive optical sections. This approach, known as Z-imaging, also allows for the localisation of multiple fluorescent probes in 3D space within a single sample.[177] The observation of lipid microdomains in SS-BLMs with high-quality morphologies is therefore possible with confocal Z-imaging. For imaging cell cultures, the confocal microscope conveniently allows for the use of a phase contrast mode in addition to the fluorescence scanning mode, without the need to manipulate the experimental set-up. In addition, being equipped with an inverted objective lens allows for imaging the bottom of culture dishes thus avoiding contamination of the culture medium.

1.5.1.2 Fluorescence Recovery after Photobleaching (FRAP)

The observation and quantification of fluorescence recovery after photobleaching (FRAP) allows for the investigation of molecular diffusion.[178] This technique has proven to be useful for studying the mobility of fluorescently-labeled lipids in supported bilayers or in cell membranes of living cells.[42, 179] In this technique, fluorescent molecules within a defined region are first photobleached by applying a high intensity laser or in some cases by using a higher magnification objective lens. This is followed by observing the recovery of fluorescence within this region, which results from the exchange between bleached and non-bleached fluorophores from the surroundings areas. Mathematical modeling of the FRAP data enables extraction of parameters which define the diffusion of the fluorophores. The extracted diffusion parameters include the relative distribution of mobile and immobile populations and the characteristic diffusion half-time. Based on the area dimension of the bleached region, an effective diffusion coefficient can be calculated. The above mentioned diffusion parameters are used as an evaluation of the dynamics of fluorescent molecules within the environment under

investigation.[178, 179] For example, in the work presented in this Thesis, FRAP is used to assess the effect of the solid support and tethering molecules on the dynamics of the bilayer.

1.5.2 Cell Culture

Cell culture refers to the process of removing cells from an organism and transferring them to an artificial environment that is suitable for their growth. The conditions of cell culture vary according to the cell type, but most commonly require a sterilized medium supplemented with essential nutrients, growth factors and gases (O_2 and CO_2) in addition to regulated physic-chemical parameters (pH, temperature, and osmotic pressure). Polylysine surface coatings are usually used to increase the adhesion of cells to the dishes where they are cultured.[180]

The majority of cell cultures used in this Thesis involve primary cultures of hippocampal neurons which are isolated from embryonic rat brains. Primary cultures are chosen for co-culture experiments with model membranes because (*i*) they do not proliferate and therefore do not crowd the culture dish and obstruct the observation of model membrane/native membrane interactions, and (*ii*) they are less active compared to cell lines and therefore are less likely to destroy soft substrates such as lipid bilayers.[181] Neurons isolated from the hippocampus region of the brain are commonly used for addressing the neuronal basis of memory and learning, which makes them attractive models for neuroengineering applications. Synaptic activities in these cultures are mostly examined after growing the neurons for *ca.* 14 days *in vitro* (DIV), at which time their maturation stage is appropriate for formation of pre- and postsynaptic assemblies. In the presented studies, the cells are examined after their fixation, a process that stabilizes their morphologies and strengthens them to withstand further manipulations necessary for with their subsequent staining. In this process, chemical fixatives, such as formaldehyde, are added to the cells in order to cross-link their proteins and disable their activities.[182]

1.5.3 Immunofluorescence Labeling

Immunofluorescence is a versatile technique for cell staining and, when combined with confocal microscopy, enables the investigation of several processes associated with cellular proteins. Immunofluorescence is commonly applied to detect the location a specific protein and measure its relative abundance. This technique relies on the specific binding between the target molecules (antigens) and their antibodies. In secondary immunofluorescence, an unlabeled primary

antibody which specifically binds to the target protein is used. A fluorescently-labeled secondary antibody which recognizes the primary antibody is also used in order to allow for their visualization using fluorescence microscopy. The fluorescence signal is effectively amplified since multiple secondary antibodies can bind a single primary antibody. Analysis of fluorescence images allows for approximating relative protein abundance levels and their localization within cell structures.[183]

In the work presented in this Thesis, primary antibodies specific for binding the synaptic proteins synaptophysin, bassoon, and synapsin-I are used. This enables one to evaluate whether or not the neurons are expressing these proteins, which is indicative of their synaptic activities (specifically in regards to SV accumulation). The antibodies are dissolved in buffer and added to the cell culture after fixation. Additionally, blocking solutions consisting of normal animal serum are added prior to this step in order to block nonspecific binding sites.

1.6 References

1. Sardet, C. (2007) *Voyage inside the Cell: Membrane* [Video file]. Retrieved from https://www.youtube.com/watch?v=GW0lqf4Fqpg (accessed on 08/08/2015)

2. Koshland, D. E., Jr. Special essay. The seven pillars of life. *Science* **2002,** *295*, 2215-2216.

3. Darnell, J.; Lodish, H.; Baltimore, D. *Molecular Cell Biology* W.H. Freeman: San Francisco, **1990**.

4. De Weer, P. A century of thinking about cell membranes. *Annu. Rev. Physio.* **2000,** *62*, 919-926.

5. Deamer, D. W. Role of amphiphilic compounds in the evolution of membrane structure on the early earth. *Origins Life* **1986,** *17*, 3-25.

6. Lipowsky, R.; Sackmann, E. *Structure and Dynamics of Membranes*; North-Holland: Amesterdam, **1995**.

7. Wilson, E. B. *The Cell in Development and Heredity*; 3rd ed.; The Macmillan Co: New york, **1925**; p 1-20

8. Gorter, E.; Grendel, F. On bimolecular layers of lipids on the chromocytes of the blood. *J. Exp. Med.* **1925,** *41*, 439-443.

9. Mouritsen, O. G. Model answers to lipid membrane questions. *Cold Spring Harbor Perspect. Biol.* **2011,** *3*, a004622.

10. Lagny, T. J.; Bassereau, P. Bioinspired membrane-based systems for a physical approach of cell organization and dynamics: usefulness and limitations. *Interface Focus* **2015,** *5*, 20150038.

11. Liu, A. P.; Fletcher, D. A. Biology under construction: in vitro reconstitution of cellular function. *Nat. Rev. Mol. Cell Biol.* **2009,** *10*, 644-650.

12. Chan, Y.-H. M.; Boxer, S. G. Model membrane systems and their applications. *Curr. Opin. Chem. Biol.* **2007,** *11*, 581-587.

13. Dowhan, W. Molecular basis for membrane phospholipid diversity: why are there so many lipids? *Ann. Rev. Biochem.* **1997,** *66*, 199-232.

14. van Meer, G.; Voelker, D. R.; Feigenson, G. w. Membrane lipids: where they are and how they behave. *Nat. Rev.* **2008,** *9*, 112-124.

15. Eeman, M.; Deleu, M. From biological membranes to biomimetic model membranes. *Biotechnol. Agron. Soc. Environ.* **2010,** *14*, 719-736.

16. Koynova, R.; Tenchov, B. Transitions between lamellar and nonlamellar phases in membrane lipids and their physiological roles. *OA Biochem.* **2013,** *1*, 1-9.

17. Lombard, J. Once upon a time the cell membranes: 175 years of cell boundary research. *Biol. Direct* **2014,** *9*, 32.

18. Johansson, A. C.; Lindahl, E. The role of lipid composition for insertion and stabilization of amino acids in membranes. *J. Chem. Phys.* **2009,** *130*, 185101.

19. Lee, A. G. How lipids affect the activities of integral membrane proteins. *Biochim. Biophys. Acta.* **2004,** *1666*, 62-87.

20. Lee, A. G. The effects of lipids on channel function. *J. Biol.* **2009,** *8*, 86.

21. Berg, J. M.; Tymoczko, J. L.; Stryer, L. *Biochemistry*; 5th ed.; W. H. Freeman: New York, **2002**; p 702-707.

22. Gennis, R. B. *Biomembranes: Molecular Structure and Function*; Springer: New York, **1989**.

23. Calderon, R. O.; Attema, B.; DeVries, G. H. Lipid composition of neuronal cell bodies and neurites from cultured dorsal root ganglia. *J. Neurochem.* **1995,** *64*, 424-429.

24. Calderon, R. O.; DeVries, G. H. Lipid composition and phospholipid asymmetry of membranes from a Schwann cell line. *J. Neurosci. Res.* **1997,** *49*, 372-380.

25. Subra, C.; Laulagnier, K.; Perret, B.; Record, M. Exosome lipidomics unravels lipid sorting at the level of multivesicular bodies. *Biochmie* **2007,** *89*, 205-212.

26. Alberts, B.; Johnson, A.; Lewis, J.; Raff, M.; Roberts, K.; Walter, P. *Molecular Biology of the cell*; Garland Science: New York, **2002**.

27. Israelachvili, J. N. Thermodynamic Principles of Self-Assembly In *Intermolecular and surface forces,* revised third ed.; Elsevier: **2011**; Chapter 19.

28. Cullis, P. R.; de Kruijff, B. Lipid polymorphism and the functional roles of lipids in biological membranes. *Biochim. Biophys. Acta.* **1979,** *559*, 399-420.

29. Damodaran, K. V.; Merz, K. M., Jr. A comparison of DMPC- and DLPE-based lipid bilayers. *Biophys. J.* **1994,** *66*, 1076-1087.

30. Israelachvili, J. N.; Marcelja, S.; Horn, R. G. Physical principles of membrane organization. *Q. Rev. Biophys.* **1980,** *13*, 121-200.

31. Seddon, J. M.; Templer, R. H. Polymosphism of lipid-water systems. In *Handbook of biological physics*, Lipowsky, R.; Sackmann, E., Eds.; North-Holland: Amesterdam, **1995**; pp 97-160.

32. Zimmerberg, J.; Chernomordik, L. V. Membrane fusion. *Adv. Drug Delivery Rev.***1999,** *38*, 197-205.

33. Gurtovenko, A. A.; Vattulainen, I. Lipid transmembrane asymmetry and intrinsic membrane potential: two sides of the same coin. *JACS* **2007,** *129*, 5358-5359.

34. Gurtovenko, A. A.; Vattulainen, I. Membrane potential and electrostatics of phospholipid bilayers with asymmetric transmembrane distribution of anionic lipids. *J. Phys. Chem. B* **2008,** *112*, 4629-4634.

35. Gurtovenko, A. A.; Vattulainen, I. Calculation of the electrostatic potential of lipid bilayers from molecular dynamics simulations: methodological issues. *J. Chem. Phys.* **2009,** *130*, 215107.

36. McLaughlin, S. The electrostatic properties of membranes. *Annu. Rev. Biophys.Biophys. Chem.* **1989,** *18*, 113-136.

37. Fato, R.; Battino, M.; Parenti Castelli, G.; Lenaz, G. Measurement of the lateral diffusion coefficients of ubiquinones in lipid vesicles by fluorescence quenching of 12-(9-anthroyl)stearate. *FEBS letters* **1985,** *179*, 238-42.

38. Berg, J. M.; Tymoczko, J. L.; Stryer, L. *Biochemistry*; 5th ed.; W. H. Freeman: New York, **2002**.

39. Stejskal, E. O.; Tanner, J. E. Spin diffusion measurements: spin echoes in the presence of a time dependent field gradient. *J. Chem. Phys* **1965,** *42*, 288-292.

40. Tanner, J. E. Use of the stimulated echo in NMR diffusion studies. *J. Chem. Phys.* **1970,** *52*, 2523-2526.

41. Borbat, P. P.; Costa-Filho, A. J.; Earle, K. A.; Moscicki, J. K.; Freed, J. H. Electron spin resonance in studies of membranes and proteins. *Science* **2001,** *291*, 266-269.

42. Axelrod, D.; Koppel, D. E.; Schlessinger, J.; Elson, E.; Webb, W. W. Mobility measurement by analysis of fluorescence photobleaching recovery kinetics. *Biophys. J.* **1976,** *16*, 1055-1069.

43. Magde, D.; Webb, W. W.; Elson, E. Thermodynamic Fluctuations in a Reacting System - Measurement by Fluorescence Correlation Spectroscopy. *Phys. Rev. Lett.* **1972,** *29*, 705.

44. Guo, L.; Har, J. Y.; Sankaran, J.; Hong, Y.; Kannan, B.; Wohland, T. Molecular diffusion measurement in lipid bilayers over wide concentration ranges: a comparative study. *Chemphyschem.* **2008,** *9*, 721-728.

45. Berg, J. M.; Tymoczko, J. L.; Stryer, L. *Biochemistry*; 4th ed.; W. H. Freeman: New York, **1995**.

46. Muller, P.; Herrmann, A. Rapid transbilayer movement of spin-labeled steroids in human erythrocytes and in liposomes. *Biophys. J.* **2002,** *82*, 1418-1428.

47. Steck, T. L.; Ye, J.; Lange, Y. Probing red cell membrane cholesterol movement with cyclodextrin. *Biophys. J.* **2002,** *83*, 2118-2125.

48. Winter, R.; Jeworrek, C. Effect of pressure on membranes. *Soft matter* **2009,** *5*, 3157-3173.

49. Tenchov, B. On the reversibility of the phase transitions in lipid-water systems. *Chem. Phys. Lipids* **1991,** *57*, 165-77.

50. Hicks, A.; Dinda, M.; Singer, M. A. The ripple phase of phosphatidylcholines: effect of chain length and cholesterol. *Biochim. Biophys. Acta* **1987,** *903*, 177-85.

51. Krbecek, R.; Gebhardt, C.; Gruler, H.; Sackmann, E. Three dimensional microscopic surface profiles of membranes reconstructed from freeze etching electrol micrographs. *Biochim. Biophys. Acta* **1979,** *554*, 1-22.

52. Meyer, H. W. Pretransition-ripples in bilayers of dipalmitoylphosphatidylcholine: undulation or periodic segments? A freeze-fracture study. *Biochim. Biophys. Acta* **1996,** *1302*, 138-144.

53. Nagle, J. F. Theory of lipid monolayer and bilayer phase transitions: effect of headgroup interactions. *J. Memb. Biol.* **1976,** *27*, 233-250.

54. John, K.; Schreiber, S.; Kubelt, J.; Herrmann, A.; Muller, P. Transbilayer movement of phospholipids at the main phase transition of lipid membranes: implications for rapid flip-flop in biological membranes. *Biophys. J.* **2002,** *83*, 3315-3323.

55. Caillon, L.; Killian, J. A.; Lequin, O.; Khemtemourian, L. Biophysical investigation of the membrane-disrupting mechanism of the antimicrobial and amyloid-like peptide dermaseptin S9. *PloS one* **2013,** *8*, e75528.

56. Seddon, J. M.; Cevc, G.; Marsh, D. Calorimetric studies of the gel-fluid (L_β-L_α) and lamellar-inverted hexagonal (L_α-H_{II}) phase transitions in dialkyl- and diacylphosphatidylethanolamines. *Biochem.* **1983,** *22*, 1280-1289.

57. Koynova, R.; Caffrey, M. Phases and phase transitions of the phosphatidylcholines. *Biochim. Biophys. Acta* **1998,** *1376*, 91-145.

58. Simons, K.; Ikonen, E. Functional rafts in cell membranes. *Nature* **1997,** *387*, 569-572.

59. Bloom, M.; Evans, E.; Mouritsen, O. G. Physical properties of the fluid lipid-bilayer component of cell membranes: a perspective. *Q. Rev. Biophys.* **1991,** *24*, 293-397.

60. Mouritsen, O. G.; Jorgensen, K. Micro-, nano- and meso-scale heterogeneity of lipid bilayers and its influence on macroscopic membrane properties. *Mol. Memb. Biol.* **1995,** *12*, 15-20.

61. Tenchov, B. G.; Koynova, R. D. The effect of nonideal lateral mixing on the transmembrane lipid asymmetry. *Biochim. Biophys. Acta* **1985,** *815*, 380-91.

62. Singer, S. J.; Nicolson, G. L. The fluid mosaic model of the structure of cell membranes. *Science* **1972,** *175*, 720-731.

63. Simons, K.; Sampaio, J. L. Membrane organization and lipid rafts. P*erspec. Biol.* **2011,** *3*, a004697.

64. Simons, K.; van Meer, G. Lipid sorting in epithelial cells. *Biochem.* **1988,** *27*, 6197-6202.

65. Viola, A.; Gupta, N. Tether and trap: regulation of membrane-raft dynamics by actin-binding proteins. *Nat. Rev. Immunol.* **2007,** *7*, 889-896.

66. Friedrichson, T.; Kurzchalia, T. V. Microdomains of GPI-anchored proteins in living cells revealed by crosslinking. *Nature* **1998,** *394*, 802-805.

67. Harder, T.; Scheiffele, P.; Verkade, P.; Simons, K. Lipid domain structure of the plasma membrane revealed by patching of membrane components. *J. Cell Biol.* **1998,** *141*, 929-942.

68. Klymchenko, A. S.; Kreder, R. Fluorescent probes for lipid rafts: from model membranes to living cells. *Chem. Biol.* **2014,** *21*, 97-113.

69. Klammt, C.; Lillemeier, B. F. How membrane structures control T cell signaling. *Front. Immunol.* **2012,** *3*, 291.

70. Jacobson, K.; Mouritsen, O. G.; Anderson, R. G. Lipid rafts: at a crossroad between cell biology and physics. *Nat. Cell Biol.* **2007,** *9*, 7-14.

71. Lenne, P. F.; Wawrezinieck, L.; Conchonaud, F.; Wurtz, O.; Boned, A.; Guo, X. J.; Rigneault, H.; He, H. T.; Marguet, D. Dynamic molecular confinement in the plasma membrane by microdomains and the cytoskeleton meshwork. *EMBO J.* **2006,** *25*, 3245-3256.

72. Goswami, D.; Gowrishankar, K.; Bilgrami, S.; Ghosh, S.; Raghupathy, R.; Chadda, R.; Vishwakarma, R.; Rao, M.; Mayor, S. Nanoclusters of GPI-anchored proteins are formed by cortical actin-driven activity. *Cell* **2008,** *135*, 1085-1097.

73. Eggeling, C.; Ringemann, C.; Medda, R.; Schwarzmann, G.; Sandhoff, K.; Polyakova, S.; Belov, V. N.; Hein, B.; von Middendorff, C.; Schonle, A.; Hell, S. W. Direct observation of the nanoscale dynamics of membrane lipids in a living cell. *Nature* **2009,** *457*, 1159-1162.

74. Bagatolli, L. A.; Gratton, E. Two-photon fluorescence microscopy observation of shape changes at the phase transition in phospholipid giant unilamellar vesicles. *Biophys. J.* **1999,** *77*, 2090-20101.

75. Jacobson, K.; Dietrich, C. Looking at lipid rafts? *Trend. cell biol.* **1999,** *9*, 87-91.

76. Zacharias, D. A.; Violin, J. D.; Newton, A. C.; Tsien, R. Y. Partitioning of lipid-modified monomeric GFPs into membrane microdomains of live cells. *Science* **2002,** *296*, 913-6.

77. Wilson, B. S.; Steinberg, S. L.; Liederman, K.; Pfeiffer, J. R.; Surviladze, Z.; Zhang, J.; Samelson, L. E.; Yang, L. H.; Kotula, P. G.; Oliver, J. M. Markers for detergent-resistant lipid rafts occupy distinct and dynamic domains in native membranes. *Mol. Biol. Cell* **2004,** *15*, 2580-2592.

78. Sonnino, S.; Prinetti, A. Membrane domains and the "lipid raft" concept. *Curr. Med. Chem.* **2013,** *20*, 4-21.

79. Sackmann, E. Supported membranes: scientific and practical applications. *Science* **1996,** *271*, 43-48.

80. Baumgart, T.; Hammond, A. T.; Sengupta, P.; Hess, S. T.; Holowka, D. A.; Baird, B. A.; Webb, W. W. Large-scale fluid/fluid phase separation of proteins and lipids in giant plasma membrane vesicles. *Proc. Nat. Acad. Sci. U. S. A.* **2007,** *104*, 3165-3170.

81. Angelova, M. I.; Dimitrov, D. S. Liposome electroformation. *Faraday Discuss. Chem. Soc.* **1986,** *81*, 303-311.

82. Atanasov, V.; Atanasova, P. P.; Vockenroth, I. K.; Knorr, N.; Koper, I. A molecular toolkit for highly insulating tethered bilayer lipid membranes on various substrates. *Bioconj. Chem.* **2006,** *17*, 631-637.

83. Troutier, A. L.; Ladaviere, C. An overview of lipid membrane supported by colloidal particles. *Adv. Colloid Intererface Sci.* **2007,** *133*, 1-21.

84. Giess, F.; Friedrich, M. G.; Heberle, J.; Naumann, R. L.; Knoll, W. The protein-tethered lipid bilayer: a novel mimic of the biological membrane. *Biophys. J.* **2004,** *87*, 3213-3220.

85. Gopalakrishnan, G.; Rouiller, I.; Colman, D. R.; Lennox, R. B. Supported bilayers formed from different phospholipids on spherical silica substrates. *Langmuir* **2009,** *25*, 5455-5458.

86. Gozen, I.; Jesorka, A. Instrumental methods to characterize molecular phospholipid films on solid supports. *Analyt. Chem.* **2012,** *84*, 822-838.

87. Bagatolli, L. A.; Ipsen, J. H.; Simonsen, A. C.; Mouritsen, O. G. An outlook on organization of lipids in membranes: searching for a realistic connection with the organization of biological membranes. *Prog. Lipid Res.* **2010,** *49*, 378-389.

88. Brown, D. A. Seeing is believing: visualization of rafts in model membranes. *Proc. Nat. Acad. Sci. U. S. A.* **2001,** *98*, 10517-10518.

89. London, E. How principles of domain formation in model membranes may explain ambiguities concerning lipid raft formation in cells. *Biochim. Biophys. Acta* **2005,** *1746*, 203-220.

90. London, E. Insights into lipid raft structure and formation from experiments in model membranes. *Curr. Opin. Struct. Biol.* **2002,** *12*, 480-486.

91. Gregoriadis, G. Overview of liposomes. *J. Antimicrob. Chemother.* **1991,** *28*, 39-48.

92. Bagatolli, L.; Kumar, P. B. S. Phase behavior of multicomponent membranes: Experimental and computational techniques. *Soft Matter* **2009,** *5*, 3234-3248.

93. Evans, E.; Kwok, R. Mechanical calorimetry of large dimyristoylphosphatidylcholine vesicles in the phase transition region. *Biochem.* **1982,** *21*, 4874-4879.

94. Liu, A. P.; Fletcher, D. A. Actin polymerization serves as a membrane domain switch in model lipid bilayers. *Biophys. J.* **2006,** *91*, 4064-4070.

95. Fischer, A.; Oberholzer, T.; Luisi, P. L. Giant vesicles as models to study the interactions between membranes and proteins. *Biochim. Biophys. Acta* **2000,** *1467*, 177-188.

96. Angelova, M. I.; Tsoneva, I. Interactions of DNA with giant liposomes. *Chem. Phys. Lipids* **1999,** *101*, 123-37.

97. Chemburu, S.; Fenton, K.; Lopez, G. P.; Zeineldin, R. Biomimetic silica microspheres in biosensing. *Molecules* **2010,** *15*, 1932-1957.

98. Schwille, P.; Diez, S. Synthetic biology of minimal systems. *Crit. Rev. Biochem. Mol. Biol.* **2009,** *44*, 223-242.

99. Schmitt, E. K.; Vrouenraets, M.; Steinem, C. Channel activity of OmpF monitored in nano-BLMs. *Biophys. J.* **2006,** *91*, 2163-2171.

100. Rossetti, F. F.; Textor, M.; Reviakine, I. Asymmetric distribution of phosphatidyl serine in supported phospholipid bilayers on titanium dioxide. *Langmuir* **2006,** *22*, 3467-3473.

101. Richter, R. P.; Brisson, A. QCM-D on mica for parallel QCM-D-AFM studies. *Langmuir* **2004,** *20*, 4609-4613.

102. Richter, R. P.; Berat, R.; Brisson, A. R. Formation of solid-supported lipid bilayers: an integrated view. *Langmuir* **2006,** *22*, 3497-3505.

103. Keller, C. A.; Glasmastar, K.; Zhdanov, V. P.; Kasemo, B. Formation of supported membranes from vesicles. *Phys. Rev. Lett.* **2000,** *84*, 5443-5446.

104. Boxer, S. G. Molecular transport and organization in supported lipid membranes. *Curr. Opin. Chem. Biol.* **2000,** *4*, 704-709.

105. Saleem, Q.; Zhang, Z.; Petretic, A.; Gradinaru, C. C.; Macdonald, P. M. Single lipid bilayer deposition on polymer surfaces using bicelles. *Biomacromol.* **2015,** *16*, 1032-1039.

106. Saleem, Q.; Zhang, Z.; Gradinaru, C. C.; Macdonald, P. M. Liposome-coated hydrogel spheres: delivery vehicles with tandem release from distinct compartments. *Langmuir* **2013,** *29*, 14603-14612.

107. Raedler, J.; Strey, H.; Sackmann, E. Phenomenology and kinetics of lipid bilayer spreading on hydrophilic surfaces. *Langmuir* **1995,** *11*, 4539-4548.

108. Merzlyakov, M.; Li, E.; Gitsov, I.; Hristova, K. Surface-supported bilayers with transmembrane proteins: role of the polymer cushion revisited. *Langmuir* **2006,** *22*, 10145-10151.

109. Koper, I. Insulating tethered bilayer lipid membranes to study membrane proteins. *Mol. Biosys.* **2007,** *3*, 651-657.

110. Kiessling, V.; Tamm, L. K. Measuring distances in supported bilayers by fluorescence interference-contrast microscopy: polymer supports and SNARE proteins. *Biophys. J.* **2003,** *84*, 408-418.

111. Garg, S.; Ruhe, J.; Ludtke, K.; Jordan, R.; Naumann, C. A. Domain registration in raft-mimicking lipid mixtures studied using polymer-tethered lipid bilayers. *Biophys. J.* **2007,** *92*, 1263-1270.

112. Sharma, M. K.; Jattani, H.; Gilchrist, M. L., Jr. Bacteriorhodopsin conjugates as anchors for supported membranes. *Bioconj. chem.* **2004,** *15*, 942-647.

113. Tamm, L. K.; McConnell, H. M. Supported phospholipid bilayers. *Biophys. J.* **1985,** *47*, 105-113.

114. Alessandrini, A.; Facci, P. Phase transitions in supported lipid bilayers studied by AFM. *Soft matter* **2014,** *10*, 7145-7164.

115. Peetla, C.; Stine, A.; Labhasetwar, V. Biophysical interactions with model lipid membranes: applications in drug discovery and drug delivery. *Mol. Pharmaceutics* **2009,** *6*, 1264-1276.

116. Hatsopoulos, N. G.; Donoghue, J. P. The science of neural interface systems. *Ann. Rev. Neurosci.* **2009,** *32*, 249-266.

117. Mingeot-Leclercq, M. P.; Deleu, M.; Brasseur, R.; Dufrene, Y. F. Atomic force microscopy of supported lipid bilayers. *Nat. Prot.* **2008,** *3*, 1654-1659.

118. Wacklin, H. P.; Thomas, R. K. Spontaneous formation of asymmetric lipid bilayers by adsorption of vesicles. *Langmuir* **2007,** *23*, 7644-7651.

119. Puu, G.; Gustafson, I. Planar lipid bilayers on solid supports from liposomes - factors of importance for kinetics and stability. *Biochim. Biophys. Acta* **1997,** *1327*, 149-161.

120. Miller, C. E.; J., M.; Kuhl, T. L. Characterization of single biological membranes at the solid-liquid interface by X-ray reflectivity. *Colloid Surf. A* **2006,** *284-285*, 434-439.

121. Lin, W. C.; Blanchette, C. D.; Ratto, T. V.; Longo, M. L. Lipid domains in supported lipid bilayer for atomic force microscopy. *Methods Mol. Biol.* **2007,** *400*, 503-513.

122. Keller, C. A.; Kasemo, B. Surface specific kinetics of lipid vesicle adsorption measured with a quartz crystal microbalance. *Biophys. J.* **1998,** *75*, 1397-1402.

123. Goksu, E. I.; Vanegas, J. M.; Blanchette, C. D.; Lin, W. C.; Longo, M. L. AFM for structure and dynamics of biomembranes. *Biochim. Biophysica Acta* 2009, *1788*, 254-266.

124. Crane, J. M.; Tamm, L. K. Fluorescence microscopy to study domains in supported lipid bilayers. *Methods Mol. Biol.* **2007,** *400*, 481-488.

125. Chan, Y. H.; Boxer, S. G. Model membrane systems and their applications. *Curr. Opin. Chem. Biol.* **2007,** *11*, 581-587.

126. Naumann, C.; Brumm, T.; Bayerl, T. M. Phase transition behavior of single phosphatidylcholine bilayers on a solid spherical support studied by DSC, NMR and FTIR. *Biophys. J.* **1992,** *63*, 1314-139.

127. Loidl-Stahlhofen, A.; Schmitt, J.; Nöller, J.; Hartmann, T.; Brodowsky, H.; Schmitt, W.; Keldenich, J. Solid-supported Biomolecules on modified silica surfaces - a tool for fast physicochemical characterization and high-throughput screening. *Adv. Mat.* **2011,** *13*, 1829-1834.

128. Davis, R. W.; Flores, A.; Barrick, T. A.; Cox, J. M.; Brozik, S. M.; Lopez, G. P.; Brozik, J. A. Nanoporous microbead supported bilayers: stability, physical characterization, and incorporation of functional transmembrane proteins. *Langmuir* **2007,** *23*, 3864-3872.

129. Buranda, T.; Huang, J.; Ramarao, G. V.; Ista, L. K.; Larson, R. S.; Ward, T. L.; Sklar, L. A.; Lopez, G. P. Biomimetic molecular assemblies on glass and mesoporous silica microbeads for biotechnology. . *Langmuir* **2003,** *19*, 1654-1663.

130. Bayerl, T. M.; Bloom, M. Physical properties of single phospholipid bilayers adsorbed to micro glass beads. A new vesicular model system studied by 2H-nuclear magnetic resonance. *Biophys. J.* **1990,** *58*, 357-362.

131. Nordlund, G.; Lonneborg, R.; Brzezinski, P. Formation of supported lipid bilayers on silica particles studied using flow cytometry. *Langmuir* **2009,** *25*, 4601-4606.

132. Roizard, S.; Danelon, C.; Hassaine, G.; Piguett, J.; Schulze, K.; Hovius, R.; Tampe, R.; Vogel, H. Activation of G-protein-coupled receptors in cell-derived plasma membranes supported on porous beads. *JACS* **2011,** *133*, 16868-16874.

133. Tutus, M.; Kaufmann, S.; Weiss, I. M.; Tanaka, M. Functional coating of porous silica microparticles with native biomembranes towards portable flow-through biochemical microreactors. *Adv. Funct. Mater.* **2012,** *22*, 4873-4878.

134. Buranda, T.; Huang, J.; Ramarao, G. V.; Ista, L. K.; Larson, R. S.; Ward, T. L.; Sklar, L. A.; Lopez, G. P. Biomimetic molecular assemblies on glass and mesoporous silica microbeads for biotechnology. *Langmuir* **2003,** *19*, 1654-1663.

135. Loidl-Stahlhofen, A.; Eckert, A.; Hartmann, T.; Schottner, M. Solid-supported lipid membranes as a tool for determination of membrane affinity: high-throughput screening of a physicochemical parameter. *J. Pharma. Sci.* **2001,** *90*, 599-606.

136. Piyasena, M. E.; Zeineldin, R.; Fenton, K.; Buranda, T.; Lopez, G. P. Biosensors based on release of compounds upon disruption of lipid bilayers supported on porous microspheres. *Biointerphases* **2008,** *3*, 38-49.

137. Ma, A. H.; Rosenzweig, Z. Synthesis and analytical properties of micrometric biosensing lipobeads. *Analyt. Bioanalyt. Chem.* **2005,** *382*, 28-36.

138. Katagiri, K.; Caruso, F. Functionalization of colloids with robust inorganic-based lipid coatings. *Macromol.* **2004,** *37*, 9947-9953.

139. Sharma, M. K.; Gilchrist, M. L. Templated assembly of biomembranes on silica microspheres using bacteriorhodopsin conjugates as structural anchors. *Langmuir* **2007,** *23*, 7101-7112.

140. Madwar, C.; Gopalakrishnan, G.; Lennox, R. B. Interfacing living cells and spherically supported bilayer lipid membranes. *Langmuir* **2015,** *31*, 4704-4712.

141. Naumann, C.; Brumm, T.; Bayerl, T. M. Phase-transition behavior of single Phosphatidylcholine bilayers on a solid spherical support studied by DSC, NMR and FTIR. *Biophys. J.* **1992,** *63*, 1314-1319.

142. Gilbert, G. E.; Drinkwater, D.; Barter, S.; Clouse, S. B. Specificity of phosphatidylserine-containing membrane binding sites for factor VIII. Studies with model membranes supported by glass microspheres (lipospheres). *J. Biol. Chem.***1992,** *267*, 15861-15868.

143. Moura, S. P.; Carmona-Ribeiro, A. M. Biomimetic particles for isolation and reconstitution of receptor function. *Cell biochem. Biophys.* **2006,** *44*, 446-452.

144. Dean, C.; Scholl, F. G.; Choih, J.; DeMaria, S.; Berger, J.; Isacoff, E.; Scheiffele, P. Neurexin mediates the assembly of presynaptic terminals. *Nature Neurosci.* **2003,** *6*, 708-716.

145. Eschwege, V.; Laude, I.; Toti, F.; Pasquali, J. L.; Freyssinet, J. M. Detection of bilayer phospholipid-binding antibodies using flow cytometry. *Clin. Exper. Immunol.* **1996,** *103*, 171-175.

146. Obringer, A. R.; Rote, N. S.; Walter, A. Antiphospholipid antibody binding to bilayer-coated glass microspheres. *J. Immunol. Meth.* **1995,** *185*, 81-93.

147. Reinl, H. M.; Bayerl, T. M. Interaction of myelin basic protein with single bilayers on a solid support: an NMR, DSC and polarized infrared ATR study. *Biochim. Biophys. Acta* **1993,** *1151*, 127-136.

148. Gopalakrishnan, G.; Thostrup, P.; Rouiller, I.; Lucido, A. L.; Belkaid, W.; Colman, D. R.; Lennox, R. B. Lipid bilayer membrane-triggered presynaptic vesicle assembly. *ACS Chem. Neurosci.* **2010,** *1*, 86-94.

149. Korlach, J.; Schwille, P.; Webb, W. W.; Feigenson, G. W. Characterization of lipid bilayer phases by confocal microscopy and fluorescence correlation spectroscopy. *Proc. Nat. Acad. Sci. USA* **1999,** *96* , 8461-6.

150. Bagatolli, L. A.; Gratton, E. A correlation between lipid domain shape and binary phospholipid mixture composition in free standing bilayers: a two-photon fluorescence microscopy study. *Biophys. J.* **2000,** *79*, 434-447.

151. Bagatolli, L. A.; Gratton, E. Two photon fluorescence microscopy of co-existing lipid domains in giant unilamellar vesicles of binary phospholipid mixtures. *Biophys. J.* **2000,** *78*, 290-305.

152 . Baumgart, T.; Hunt, G.; Farkas, E. R.; Webb, W. W.; Feigenson, G. W. Fluorescence probe partitioning between L_o/L_d phases in lipid membranes. *Biochim. Biophys. Acta* **2007,** *1768*, 2182-2194.

153. Veatch, S. L.; Keller, S. L. Seeing spots: complex phase behavior in simple membranes. *Biochim. Biophys. Acta* **2005,** *1746*, 172-185.

154. Bagatolli, L.; Gratton, E.; Khan, T. K.; Chong, P. L. Two-photon fluorescence microscopy studies of bipolar tetraether giant liposomes from thermoacidophilic archaebacteria sulfolobus acidocaldarius. *Biophys. Journal* **2000,** *79*, 416-25.

155. Nag, K.; Pao, J. S.; Harbottle, R. R.; Possmayer, F.; Petersen, N. O.; Bagatolli, L. A. Segregation of saturated chain lipids in pulmonary surfactant films and bilayers. *Biophys. J.* **2002,** *82*, 2041-2051.

156. Montes, L. R.; Alonso, A.; Goni, F. M.; Bagatolli, L. A. Giant unilamellar vesicles electroformed from native membranes and organic lipid mixtures under physiological conditions. *Biophys. J.* **2007,** *93*, 3548-3554.

157. Merritt, E. A.; Sarfaty, S.; van den Akker, F.; L'Hoir, C.; Martial, J. A.; Hol, W. G. Crystal structure of cholera toxin B-pentamer bound to receptor GM1 pentasaccharide. *Prot. Sci.* **1994,** *3*, 166-175.

158. Bagatolli, L. A. To see or not to see: lateral organization of biological membranes and fluorescence microscopy. *Biochim. Biophys. Acta* **2006,** *1758*, 1541-1556.

159. Kahya, N.; Scherfeld, D.; Bacia, K.; Poolman, B.; Schwille, P. Probing lipid mobility of raft-exhibiting model membranes by fluorescence correlation spectroscopy. *J. Biol. Chem.* **2003,** *278*, 28109-28115.

160. Veatch, S. L.; Keller, S. L. Separation of liquid phases in giant vesicles of ternary mixtures of phospholipids and cholesterol. *Biophys. J.* **2003,** *85*, 3074-3083.

161. Feigenson, G. W. Phase diagrams and lipid domains in multicomponent lipid bilayer mixtures. *Biochim. Biophysica Acta* **2009,** *1788*, 47-52.

162. Zhao, J.; Wu, J.; Heberle, F. A.; Mills, T. T.; Klawitter, P.; Huang, G.; Costanza, G.; Feigenson, G. W. Phase studies of model biomembranes: complex behavior of DSPC/DOPC/cholesterol. *Biochim. Biophys. Acta* **2007,** *1768*, 2764-2776.

163. Owen, D. M.; Rentero, C.; Magenau, A.; Abu-Siniyeh, A.; Gaus, K. Quantitative imaging of membrane lipid order in cells and organisms. *Nat. Prot.* **2012,** *7*, 24-35.

164. Prashar, J.; Sharp, P.; Scarffe, M.; Cornell, B. Making lipid membranes even tougher. *J Mater. Res.* **2007,** *22*, 2189-2194.

165. Finger, S. The brain in antiquity. In *Origins of neuroscience: a history of explorations into brain function*; Oxford University Press: New York, **2001**.

166. Nowakowski, R. S. Stable neuron numbers from cradle to grave. *Proc. Nat. Aca. Sci. USA* **2006,** *103*, 12219-20.

167. Hu, W.; An, C.; Chen, W. J. Molecular mechanoneurobiology: an emerging angle to explore neural synaptic functions. *BioMed. Res. Intl.* **2015,** *2015*, 486827.

168. Goda, Y.; Davis, G. W. Mechanisms of synapse assembly and disassembly. *Neuron* **2003,** *40*, 243-264

169. Cruz, M. T.; Bajo, M.; Schweitzer, P.; Roberto, M. Shared mechanisms of alcohol and other drugs. *J Natl. Inst. Alcohol Abuse Alcohol.* **2008,** *31*, 137-47.

170. Guillery, R. W. Observations of synaptic structures: origins of the neuron doctrine and its current status. *Philos. Trans. R. Soc., B* **2005,** *360*, 1281-307.

171. Palade, G. E.; Palay, S. L. Electron microscope observations of interneuronal and neuromuscular synapses. *Anat. Rec.* **1954**, *118*, 335-336.

172. Sudhof, T. C. The synaptic vesicle cycle. *Ann. Rev. Neurosci.* **2004,** *27*, 509-547.

173. Ikeda, K.; Bekkers, J. M. Counting the number of releasable synaptic vesicles in a presynaptic terminal. *Proc. Nat. Acad. Sci. USA* **2009,** *106*, 2945-2950.

174. Fornito, A.; Zalesky, A.; Breakspear, M. The connectomics of brain disorders. *Nature Rev. Neurosci.* **2015,** *16*, 159-172.

175. Hering, H.; Lin, C. C.; Sheng, M. Lipid rafts in the maintenance of synapses, dendritic spines, and surface AMPA receptor stability. *J. Neuro. Sci.* **2003,** *23*, 3262-3271.

176. Rothschild, R. M. Neuroengineering tools/applications for bidirectional interfaces, brain-computer interfaces, and neuroprosthetic implants - a review of recent progress. *Front. Neuroeng.* **2010,** *3*, 112.

177. Wright, S. J.; Centonze, V. E.; Stricker, S. A.; DeVries, P. J.; Paddock, S. W.; Schatten, G. Introduction to confocal microscopy and three-dimensional reconstruction. *Meth. Cell Biol.* **1993,** *38*, 1-45.

178. Ishikawa-Ankerhold, H. C.; Ankerhold, R.; Drummen, G. P. Advanced fluorescence microscopy techniques - FRAP, FLIP, FLAP, FRET and FLIM. *Molecules* **2012,** *17* (4), 4047-132.

179. Mullineaux, C. W.; Kirchhoff, H. Using fluorescence recovery after photobleaching to measure lipid diffusion in membranes. In *Methods in membrane lipids*, Dopico, A. M., Ed.; Humana Press Inc.: Totowa, NJ, **2007**.

180. Arora, M. Cell Culture Media: A Review. *Mater. Methods* **2013,** *3*, 175.

181. Pan, C.; Kumar, C.; Bohl, S.; Klingmueller, U.; Mann, M. Comparative proteomic phenotyping of cell lines and primary cells to assess preservation of cell type-specific functions. *MCP* **2009,** *8*, 443-450.

182. Thavarajah, R.; Mudimbaimannar, V. K.; Elizabeth, J.; Rao, U. K.; Ranganathan, K. Chemical and physical basics of routine formaldehyde fixation. *JOMFP* **2012,** *16*, 400-405.

183. Odell, I. D.; Cook, D. Immunofluorescence techniques. *J. Invest. Dermatol.* **2013,** *133*, e4.

Chapter 2

Interfacing Living Cells and Spherically Supported Bilayer Lipid Membranes

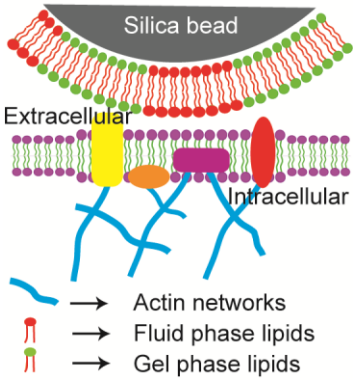

This chapter is reprinted with permission from "Interfacing Living Cells and Spherically Supported Bilayer Lipid Membranes", C. Madwar, G. Gopalakrishnan, and R. B. Lennox, Langmuir, 2015, 31 (16), 4704-4712. Copyright (2015) American Chemical Society. The text below is a verbatim copy of the published paper.

2.1 Abstract

Spherically supported bilayer lipid membranes (SS-BLMs) exhibiting co-existing membrane microdomains were created on spherical silica substrates. These 5 μm SiO_2-core SS-BLMs are shown to interact dynamically when interfaced with living cells in culture, while keeping the membrane structure and lipid domains on the SS-BLM surface intact. Interactions between the SS-BLMs and cellular components could potentially be examined *via* correlating fluorescently labeled co-existing microdomains on the SS-BLMs, their chemical composition and biophysical properties with the consequent organization of cell membrane lipids, proteins and other cellular components. This experimental approach is demonstrated in a proof-of-concept experiment involving the dynamic organization of cellular cytoskeleton, monitored as a function of the lipid domains of the SS-BLMs. The compositional versatility of SS-BLMs provides a means to address the relationship between the phenomenon of lipid phase separation and the other contributors to cell membrane lateral heterogeneity such as interactions with the cytoskeleton of living cells.

2.2 Introduction

Membrane heterogeneity is fundamental to many cellular events including signaling, protein/receptor trafficking, and membrane fusion.[1, 2, 3, 4] Although the driving force(s) behind these inhomogeneities are not fully understood, it is becoming increasingly evident that cell membranes possess lateral domains or rafts that are constituted of lipids, proteins and other membrane-associated entities.[5, 6] There is considerable evidence that the lateral distribution of membrane components and their respective lipid-lipid and lipid-protein interactions are important in membrane heterogeneity. The regulation of the formation and maintenance of membrane heterogeneity at physiological conditions involves factors such as protein aggregation on the membrane leaflet,[7, 8] lipid domains with distinct physical and mechanical properties,[3, 9, 10] and cytoskeleton-induced asymmetric lipid distributions and protein domain stabilization.[11, 12] Particularly interesting in the context of the present study is the existence of thermodynamically stable lipid microdomains that have been convincingly illustrated using model membrane systems.[13, 14, 15, 16, 17, 18] The two most studied model systems used in lipid phase separation studies are giant unilamellar vesicles (GUVs)[14, 16, 19] and planar supported bilayer membranes (S-BLMs).[20, 21, 22, 23] However, studies involving these membrane models have focused on the

physical/mechanical/dynamical properties of lipid domains rather than experiments involving living cells in culture. This limitation is due in part to the physical instability (in the case of GUVs)[24, 25] or the technical difficulties and restrictions in relation to planar geometries (in the case of S-BLMs).[26] The approach we introduce here circumvents these limitations and allows one to explore how co-existing lipid microdomains of a well-characterized model system interact with complex cellular components.

We report here an experimental platform where co-existing lipid microdomains are formed on a micron-scale solid, spherical substrate. The resulting lipid microdomains parallel both the chemical and dynamical properties of those in cell membranes. The tailor-made character of these synthetic membranes, in terms of both size and composition, along with the physical stability they demonstrate under physiological conditions, allow for their use as an active system capable of interacting and inducing a measurable response from living cells in culture. To assess the versatility of this system, spherical supported bilayer membranes (SS-BLMs) are used as a platform to examine the correlation between the lipid phase separation phenomenon and the organization of cellular components such as the cytoskeletal networks. This is achieved *via* co-culturing SS-BLMs which display lipid phase separation (*i.e.* co-existing lipid microdomains) with living cells under physiological conditions.[28] The SS-BLM system combines the versatility of GUVs and the robustness of S-BLMs.[26, 27, 29] The presence of the SiO_2-core with a well-defined diameter allows for facile observation of these rigid membrane structures using time-resolved microscopy and spectroscopy techniques and also serves to differentiate them from other native vesicle membranes present in the cell culture milieu. Furthermore, unlike planar S-BLM, the SS-BLM system enables introduction of model lipid membranes to living cells *in vitro* at any time of the cell culture. As established here, this experimental versatility allows use of this system in experiments involving cell culture, long term live cell imaging, immunofluorescence as well as other experimental procedures involving the use of detergents, change of pH or osmotic pressure - all without compromising the structural integrity of the membrane domains within the model membranes.

2.3 Co-existence of Lipid Microdomains on SS-BLMs

Lipid phase separation on the spherical solid support is established by varying the composition of the lipid mixture and tuning the procedure for preparing the SS-BLMs. Figure 2.1 shows the co-

existence of these lipid microdomains on SS-BLMs. Visualization of lipid phase separation, using confocal microscopy, is achieved using fluorescent lipid markers which preferentially partition into different microdomains.[32] Different combinations of synthetic lipids as well as lipid dyes confirm phase separation in the SS-BLM. As seen in Figures 1a and 1c, the images are representative of the sample population. In these experiments, a binary lipid mixture was used with the appropriate combination of fluorescent lipids. Bodipy-PC (Fig. 2.1, green) and DiI-C_{20} (Fig. 2.1, red) are used to identify co-existing microdomains in a DOPC/DSPC lipid mixture.[33, 34]

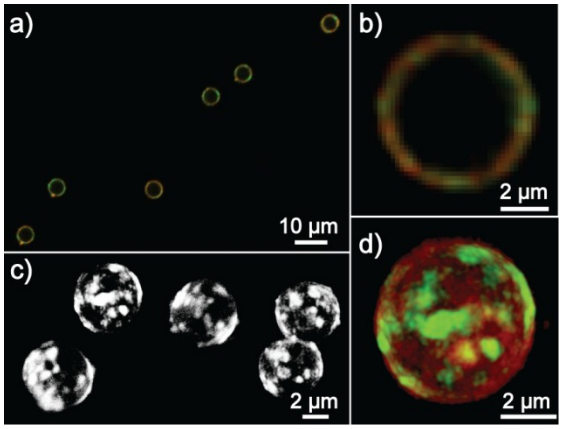

Figure 2.1 Visualization of phase separated lipid microdomains on SS-BLMs using confocal fluorescence microscopy. Representative confocal cross-sectional images (a & b) of the binary lipid mixture DOPC/DSPC (70:30), where the ordered domains (DSPC-rich) are labeled using 0.1 mol% DiI-C_{20} (red) and the fluid domains (DOPC-rich) are labeled using 0.1 mol% Bodipy-PC (green). Representative confocal 3D-reconstruction images (c & d) of the same lipid mixture. In panel (c) only the fluid domains (DOPC-rich) are shown in white. In all preparations, 5 µm silica beads, coated with avidin, were used as the solid spherical support and 0.1 mol% DSPE-PEG2000-biotin was used in the lipid mixture for tethering purposes. It is important to note that although the extent to which each dye occupies a distinct phase is not definitively known,[13] the observed contrast is consistent with preferential partitioning. This figure thus establishes that lipid domains are present in the SS-BLMs studied.

2.4 Domain Shape and Organization

Cholesterol is an important component of membrane rafts and studies using cholesterol-containing lipid model systems have shown that net changes in cholesterol content considerably influence lipid organization and diffusion within the membrane.[35] The effect of cholesterol on the stability and organization of the co-existing lipid microdomains in SS-BLMs is illustrated in

Fig. 2.2 a-b. Inclusion of 30 mol% cholesterol into a phase-separated binary lipid mixture causes a noticeable change in the ordering of fluid phase (DOPC-rich) domains within the gel phase (DSPC-rich) domains. Comparison of Figs 2.2a and 2.2b reveals that the fluid domains (DOPC-rich, labeled) are more connected and branched within the ordered domains (DSPC-rich, unlabeled) when cholesterol is present in the mixture, resulting in a decrease in the net area of the ordered phase. The effect of cholesterol starts to appear at concentrations of 10 and 20 mol% cholesterol (images not shown), becoming more prominent at 30 mol%.[16] By modulating the lipid composition and lipid/cholesterol ratio, the SS-BLM can serve as a stable bilayer model system which mimics native cellular membranes and incorporates lipid domains and raft components.

It has also been suggested that temperature of the lipid film formation and the temperature at which the film is hydrated should be kept above the characteristic lipid phase transitions (T_m) of the constituent lipids.[36] In order to test if these conditions contribute to the quality of the resulting membrane domains, the SS-BLMs are subjected to multiple temperature cycles through the T_m after assembling the lipid bilayer on the spherical support as previously reported.[27] The application of heat/cool/heat cycles at a relatively slow rate (0.1 ˚C/second) promotes the segregation of lipid phases into well-defined co-existing two-phase milieu (Fig. 2.2e-f), similar to that reported in repetitive freeze-thaw cycling of small unilamellar vesicles (SUVs).[37] These samples were examined using confocal microscopy through a time series study of 24 hrs after preparation, which was found to be a period of time sufficient for the lipid microdomains to achieve a steady state structure on the micron scale (Fig. 2.2g).

Similar to the effects of cholesterol, temperature and time, the size of the starting lipid vesicles (used in the preparation of the SS-BLMs) influences the organization of lipids and resulting shape of co-existing domains. For example, in a 70:30 DOPC/DSPC lipid mixture, relatively smaller, disconnected fluid domains (Fig. 2.2a) are reproducibly formed when SUVs of diameter < 200 nm were used to prepare the SS-BLMs. On the other hand, when 1-3 μm GUVs are used to prepare the SS-BLMs (Fig. 2.2c), a more connected network of fluid domains (Fig. 2.2d) results. Using GUVs of sizes ≥ 10 μm (data not shown) led to a wide variation in the domain shape and size. These observations are likely related to vesicle fusion and rupture processes taking place during the formation of SS-BLMs.[38] This might also contribute to a rearrangement of lipid components that takes place as vesicles fuse onto the solid substrate[39] and these factors

altogether influence the individual shape, size and distribution of c-existing lipid domains on SS-BLMs. When using larger GUVs in the preparation of SS-BLMs, only a small number fuse to the spherical solid support, resulting in a noticeable variation between different sample preparations. This however is not the case when using SUVs.

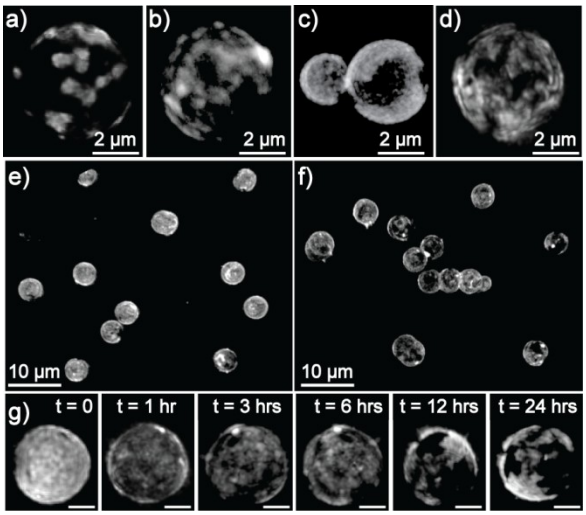

Figure 2.2 Visualization of the shape and organization of phase separated lipid microdomains on SS-BLMs and GUVs using confocal fluorescence microscopy as a function of multiple factors: confocal 3D-reconstruction images of the binary lipid mixture DOPC/DSPC (70:30) with no cholesterol (a) and with 30% cholesterol (b). Representative GUVs (c) and corresponding SS-BLMs (d) formed from the same lipid mixture. SS-BLMs of the ternary lipid mixture DOPC/DPPE/DOTAP (25:50:25) with ordered domains (DPPE-rich) prior to (e) and after (f) the application of two heat/cool/heat cycles starting at 4 ˚C, passing through the T_m of DPPE at 63 ˚C and ending at 80 ˚C. Panel g displays a time series collected following the temperature cycles (scale bars are 1 µm). (a-d) The fluid domains (DOPC-rich) are labeled using 0.1 mol% Bodipy-PC and (e-g) the ordered domains (DPPE-rich) are labeled using 0.1 mol% N-Rh-DHPE.[40] In all preparations, 5 µm silica beads, coated with avidin, were used as the solid spherical support and 0.1 mol% DSPE-PEG2000-biotin was used in the lipid mixture for tethering purposes.

2.5 SS-BLM Fluidity and Lipid Diffusion Characteristics

The dynamics of the lipids within the SS-BLMs were studied in order to evaluate their ability to self organize within their respective microdomains as well as to further re-organize when interfaced with cellular membranes. Despite the use of biotin-avidin tethering for their preparation, the SS-BLMs retain their fluidity[27] as confirmed using comparative fluorescence recovery after photobleaching (FRAP).[41] This involves evaluating the diffusion of fluorescent lipids included in the SS-BLM lipid mixture. Figure 2.3 summarizes a FRAP study for SS-BLMs

from DOPC lipids labeled using 0.1 mol% of the fluorescent lipid Bodipy-PC. The apparent diffusion coefficients (D), half-life of fluorescence recovery (τ), and the ratio of mobile to immobile lipid molecules are measured and compared to those of non-supported bilayers, *i.e.* GUVs of equivalent size (Table 2.1).

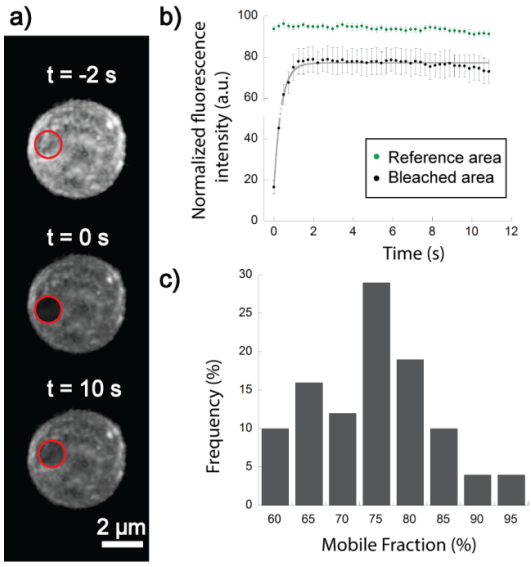

Figure 2.3 Diffusion properties of DOPC SS-BLMs labeled using 0.1 mol% Bodipy-PC and tethered on 5 µm avidin coated silica beads using 0.1 mol % DSPE-PEG2000-biotin: (a) time series displaying fluorescence recovery after photobleaching of a circular ROI (1 µm, shown in red). Fluorescence intensity data were collected from an additional non-bleached reference circular ROI of the same diameter (1 µm, not shown) and used in subsequent data analysis to correct for any bleaching occurring during imaging. (b) Averaged fluorescence data and corresponding standard error for bleached (shown in black) and reference (shown in green) regions. The data correspond to 50 bleaching experiments on different SS-BLMs and collected in a single experimental set up. After normalization to pre-bleaching fluorescence levels, the averaged FRAP data is fit (curve shown in grey) to a one diffusing component model (R value of 0.989). (c) Histogram displaying the frequency of different % mobile fractions measured for the 50 SS-BLMs from the same sample preparation.

Recovery of fluorescence in the SS-BLM confirms the presence of a continuous and fluid lipid bilayer membrane coating the solid support, as opposed to a layer of adhered vesicles. The diffusivity of Bodipy-PC fluorescent lipids in homogenous DOPC membranes that were either supported (SS-BLMs) or free standing (GUVs) are very similar (τ *ca.* 0.3 s), suggesting that the tethering caused by the biotinylated lipid (DSPE-PEG2000-biotin at 0.1 mol%) binding to

avidin-coated silica bead does not significantly hinder the diffusion of supported lipids. The estimated diffusion constant is in agreement with previous reports for DOPC lipid bilayers supported on planar glass substrates (values *ca.* 1 – 2.5 $\mu m^2/s$).[42, 43, 44, 45, 46] However, the measured fractions of mobile fluorescent lipid molecules in SS-BLMs vary significantly (Fig. 2.3c). This variability may be related to the actual quantity of lipopolymers (*i.e.*, DSPE-PEG2000-biotin) incorporated in the SS-BLMs and possibly their uneven distribution between the inner and outer membrane leaflets.

Table 2.1. Summary of SS-BLMs diffusion parameters.

Lipid System	Diffusion Half-time τ (s)	Diffusion constant D ($\mu m^2/s$)[b]	Mobile fraction (%)
GUVs[a]	0.315	1.02	91.9
SS-BLMs[a]	0.358	0.901	75.1

[a] lipid mixture composed of DOPC labeled using 0.1 mol% Bodipy-PC and tethered using 0.1 mol% DSPE-PEG2000-biotin

[b] Due to the spherical nature of the lipid bilayers, the equations which have been derived for planar systems become unsuitable to analyze the FRAP data. Therefore an apparent diffusion coefficient was estimated from the fluorescence recovery half time measured on these curves using the equation $D \geq 0.224.w^2/\tau$ (see Section 2.6) and used for comparative purposes rather than to report an absolute value.

2.6 Domain-Specific Cytoskeletal Organization

Scheme 2.1 depicts the steps involved in a typical experiment involving SS-BLMs and their interactions with living cells: (*i*) SS-BLMs with co-existing microdomains are prepared on 5 μm silica beads, (*ii*) SS-BLMs are added to cells in culture (in this case rat embryonic hippocampal neural culture) and are allowed to interact with the living cells for up to 24 hrs,[28] and (*iii*) immunofluorescence and confocal microscopy are used to examine the organization of the cellular proteins (in this case the cytoskeletal network) in relation to the lipid microdomains in the SS-BLMs. As depicted in part (*iii*) of Scheme 2.1, actin filaments and microtubules preferentially extend and assemble around the fluid lipid domains rather than the gel or solid-like lipid domains. Actin and microtubules are major cytoskeletal components known to be involved in important cellular processes including the maintenance of cell shape, providing mechanical

support, signal transduction, axon path-finding, and synaptic vesicle trafficking.[47, 48] The actin cytoskeleton has also been shown to be critical in establishing raft formation in cell membranes.[11, 12, 49] To our knowledge, this is the first report of the relationship between lipid microdomains on a model membrane and a raft-influenced component in living cells, such as the cytoskeleton organization.[11, 12, 49] The SS-BLM thus provides a platform for mechanistic studies involving different contributors to membrane heterogeneity.

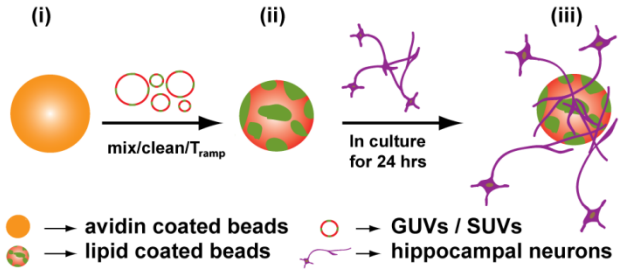

Scheme 2.1 Scheme (not to scale) illustrating the preparation of SS-BLMs displaying co-existing lipid microdomains and their subsequent interaction with living cells.

Cytoskeleton-induced domain formation[11] is known to be one of the factors which influence membrane heterogeneity in biological membranes. Studies have shown that the cytoskeletal networks are important in establishing and maintaining membrane organization.[11, 12, 49] For example, Liu *et. al.* have shown that actin networks can control the spatial and temporal organization of lipid domains.[50] This was demonstrated by allowing dendritic actin monomers to polymerize on model membranes (GUVs) which exhibit lipid domains.[50] The importance of obtaining new insights into the coupling of the model membrane bilayer and native membrane skeleton was stressed.[51]

The SS-BLM platform described here provides for facile access to BLMs with robust yet fluid lipid microdomains. Two different lipid phase domain situations were used to explore the spatial correlation between lipid microdomains and the cytoskeleton of living cells. One involves co-existing "liquid disordered (L_d)–liquid ordered (L_o)" phases (Fig. 2.4) and the other involves co-existing "fluid–gel" phases (Fig. 2.5). Figure 2.4 shows a representative primary neuron/SS-BLM co-culture, where SS-BLMs consisting of DOPC/DPPC/CHOL (50:30:20) were incubated with living cells in culture up to 24 hrs. The addition of 0.1 mol% DiI-C_{20} was used to label (red)

the L_o phase (DPPC-rich). In this study, cellular microtubules, an important dynamic cytoskeletal element that is responsible for intracellular transport are labeled (Figs. 2.4a and 2.4c; green) using β-tubulin primary antibodies *via* immunochemistry and filamentous actin, another important cytoskeletal element that is involved in cell motility and in cell signaling are labeled (Figs. 2.4b and 2.4e; green) using Alexa-488−phalloidin. The magnified views in Fig. 2.4c and 2.4e show the close association between the cytoskeleton filaments and the lipid domains of the SS-BLMs, in this case the unlabeled region (L_d phase; DOPC-rich). Figs. 2.4d and 2.4f provide additional views of the domain organization on the SS-BLM. It is important to note that the fluorescence visualized in the SS-BLMs derives solely from the proximal surface, because the excitation light does not pass through the silica core of the SS-BLM.

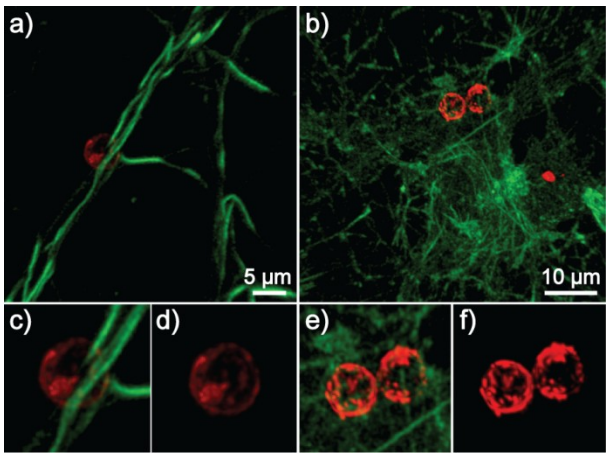

Figure 2.4 Representative confocal 3D-reconstruction images showing the co-localization of cytoskeletal networks with lipid microdomains on SS-BLMs presenting an L_d–L_o phase separation. Assembly of (a) microtubules (β-tubulin, green), and (b) actin (phalloidin, green) around the fluid phase on DOPC/DPPC/CHOL (50:30:20) SS-BLMs. Panels c & e are magnified views of images a & b respectively, showing the specific organization of the cytoskeletal networks around the unlabeled regions on the SS-BLMs, representing the fluid phase (DOPC-rich). Panels d & f are single channel images of c & e, showing the exact location of ordered (DPPC-rich) domains on SS-BLMs that are labeled using 0.1 mol% DiI-C_{20} (red). The SS-BLMs are co-cultured with hippocampal neurons (DIV 9) for 24 hrs and immunostained for either microtubules or actin filaments.

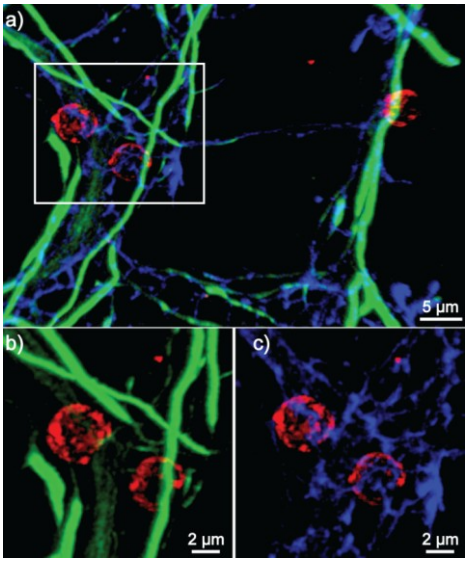

Figure 2.5 A representative 3-channel confocal 3D-recontruction image showing the co-localization of cytoskeletal networks with lipid microdomains on SS-BLMs presenting a fluid – gel phase separation: (a) assembly of microtubules (β-tubulin, green) and actin (phalloidin, blue) around the fluid phase on DOPC/DPPE/DOTAP (25:50:25) SS-BLMs. The ordered domains (DPPE-rich) are labeled using 0.1 mol% N-Rh-DHPE (red). Magnified views of image "a" show microtubule (b) and actin (c) co-localization with the lipid microdomains.

The association between the cellular cytoskeleton and the lipid microdomains derived from a ternary lipid mixture composed of DOPC/DPPE/DOTAP (25:50:25) was also studied. This lipid mixture exhibits fluid – gel phase domain co-existence at 37 ˚C and has also been shown to induce interesting cellular responses when model membranes containing these lipids interact with biological membranes.[28, 52] We recently reported the ability of such model membranes to induce artificial synapse formation when interfaced with hippocampal neurons.[28] Similar to the DOPC/DPPC/CHOL mixture discussed in Fig. 2.4, the association of cytoskeletal networks with the SS-BLM lipid domains is observed. Fig. 2.5 is a representative 3D confocal image showing co-staining of F-actin (blue) and microtubules (green) when primary neurons were co-cultured with SS-BLMs consisting of DOPC/DPPE/DOTAP. In this case, 0.1 mol% N-Rh-DHPE was used to label (red) the gel phase (DPPE-rich).[40] Fig. 2.5b and 2.5c are magnified views of individual channels of the selected area (white box) in Fig. 2.5a. Both channels show that the cytoskeletal labeling is preferentially co-localized with the disordered fluid phase (unlabeled dark region) of the SS-BLMs.

This study, as well as that of Liu *et. al.*,[50] uses DOPC as the fluid phase lipid. The question arises as to whether a domain-specific interaction correlates with cytoskeletal organization, or if molecular specificity is also a determinant. The adaptability of the SS-BLM system to such experimental questions is exemplified in the ability to modulate the lipid compositions and functionalities in order to assess each of these possibilities. For example, SS-BLMs consisting of a DOPE-rich fluid phase and a DPPC-rich gel phase were examined (see Experimental Section Fig. 2.8). Thus, unlike the lipid composition used in Figs. 2.4 and 2.5, in this experiment the fluid phase involves phosphatidylethanolamine (PE) headgroups and the gel phase involves phosphatidylcholine (PC) headgroups. The observed cytoskeletal organization (favouring the fluid phase) however remains unchanged with this change in molecular specification. In addition, the inclusion of a cationic lipid (such as DOTAP) acts to promote the adhesion of the cells to SS-BLMs.[28] This is concluded by the closer assembly of the cellular membranes around them. However, DOTAP does not influence the phase-specific cytoskeleton co-localization in the lipid mixtures examined (DOPC/DPPC/CHOL or DOPC/DPPE). Moreover, it appears that the cytoskeletal filaments direct the cells away from associating with the surface of those SS-BLMs which do not display phase-separated co-existing lipid microdomains. Control studies conducted using SS-BLMs with uniform compositions that do not exhibit lipid phase separation (for example 100% DOPC or 100% DPPE) revealed non-specific cellular organization and no significant interactions between the living cells with the co-cultured SS-BLMS (see Experimental Section Fig. 2.9).

2.7 Comparison to GUVs

The stability of model membranes is a critical factor when considering their applications. It is important to note that we observed that the fragility of GUVs precludes their use when the experimental protocol involves either or both *in vitro* cell culture and immunostaining methods (see Experimental Section Table 2.2). This is consistent with reported limitations of GUVs[25, 26] and is due to a combination of factors such as: (*i*) shrinkage and rupture when exposed to detergents[53, 54, 55, 56, 57] during immunostaining procedure, (*ii*) structural fluctuations and deformation due to osmotic stress resulting from using multiple solutions of different salt concentrations[58, 59] (*iii*) general sensitivity to solution conditions and environmental changes (*i.e.* pH, temperature, extensive washings and so on)[60] and (*iv*) unexpected topological

transformations, vesicle budding or fusion occurring during long incubation periods especially in the presence of non-liposomal components in cell culture medium.

2.8 Quantification of Domain-Specific Cytoskeletal Organization

The co-localization of the fluorescently-labeled microtubules and actin filaments with either one of co-existing SS-BLM domains was quantified. As described in the Experimental Section 2.10.7, this was measured by the presence or absence of a spatial overlap of their respective fluorescence signals (Fig. 2.6).

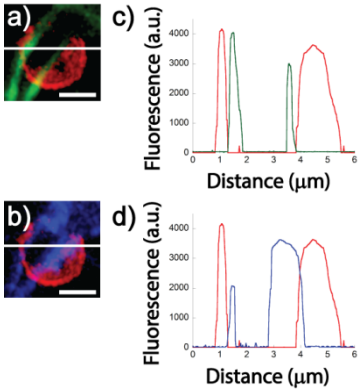

Figure 2.6 Quantification of co-localization between cytoskeletal filaments and SS-BLM co-existing domains from the lipid mixture DOPC/DPPE/DOTAP (25:50:25), where the ordered phase (DPPE-rich) is labeled using 0.1 mol% N-Rh-DHPE (red). Panels (c, d) displaying the fluorescence intensity profiles across an area of the SS-BLM (indicated by white lines in images a and b), using the same color codes for the fluorescence channels where microtubules are labeled in green (a) and actin is labeled in blue (b). (Scale bars = 2 μm).

The % preferential co-localization with the more fluid phases from different lipid systems is summarized in Fig. 2.7. In the case of microtubules and F-actin filaments, it was found that more than 50% fluorescence co-localization occurs with the more fluid phases for SS-BLM populations from different lipid mixtures. It is important to note that experiments involving no phase separation (*e.g.* only fluid phase or solid phase present) did not show comparatively high promotion of cytoskeletal network assembly. Phase separated lipid state clearly promotes cytoskeleton preferential assembly.

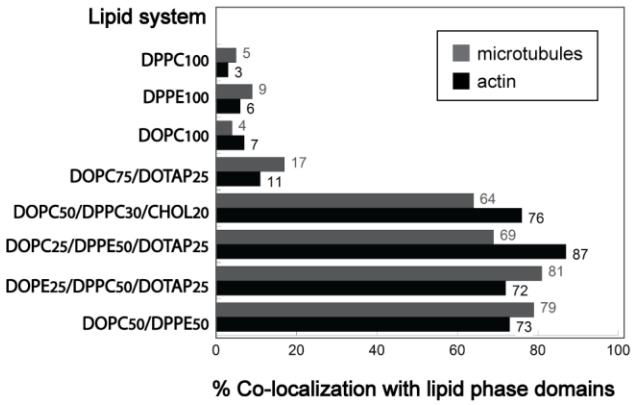

Figure 2.7 Preferential co-localization of cytoskeletal filaments with lipid phase domains in SS-BLMs. % co-localization is calculated with respect to the single lipid phase present or with the disordered phase when co-existing lipid phases are present. For quantification details see Experimental Section 2.10.7 and Fig. 2.6.

These observations are consistent with suggestions that components of the cellular cytoskeleton regulate and/or favour membrane heterogeneity in lipid membranes and, in particular, in biological membranes.[11] Although the mechanism through which this correlated action is regulated still not understood, the system and experimental approach presented here offers a novel platform for investigating the collective role of multiple raft components in regulating membrane heterogeneity.

It is important to note that although primary neuronal cultures were used in the experiments described here, the generality of this approach was demonstrated by also performing the cell interaction experiments using COS-7 cell lines. As shown in Experimental Section Fig. 2.10, the cytoskeletal networks follow the same trend observed in primary neuronal cultures.

2.9 Conclusions

The results presented here establish that the lipid microdomains in SS-BLMs interact with living cells in culture. Because they are both robust and dynamic, SS-BLM domains can withstand cell culture conditions and the experimental manipulations necessary to investigate their interactions with cellular components of living cells. As a demonstration of their versatility, experiments presented here follow the organization of cytoskeleton networks as a function of the specific lipid domain present. The interactions with living cells explored here are in very good agreement

with those performed on GUVs in combination with purified and/or synthetic actin monomers.[50] Since both lipid domains and the cellular cytoskeleton clearly contribute to cell membrane heterogeneity, the SS-BLM system provides a means to further address the fundamental relationship between membrane heterogeneity and membrane-mediated functions. Future experiments will help establish if certain types of lipids, adhesion molecules and/or actin-binding proteins associated with the cell membranes also take part in the observed lipid domain preferential organization of cellular components. Finally, because of its simplicity, robustness and experimental versatility, the SS-BLM platform is an attractive complement to GUVs and planar S-BLMs in membrane biophysical studies, especially in experiments involving live cell cultures as well as in guiding the development of new materials for bioengineering applications.

2.10 Experimental Section

2.10.1 Lipids

Cholesterol, 1,2-dioleoyl-*sn*-glycero-3-phosphocholine (DOPC), 1,2-dioleoyl-3-trimethylammonium propane chloride salt (DOTAP), 1,2-dipalmitoyl-*sn*-glycero-3-phosphocholine (DPPC), 1,2-dipalmitoyl-*sn*-glycero-3-phosphoethanolamine (DPPE), 1,2-distearoyl-*sn*-glycero-3-phosphocholine (DSPC), 1,2-distearoyl-sn-glycero-3-phosphatidylethanolamine-N-biotinyl-(polyethylene glycol 2000)] ammonium salt (DSPE-PEG2000-biotin), and 1,2-dipalmitoyl-*sn*-glycero-3-phosphoethanolamine-N-(7-nitro-2-1,3-benzoxadiazol-4-yl) (ammonium salt) (NBD PE) were purchased from Avanti Polar Lipids (purity >99%). 4,4-difluoro-5,7-dimethyl-4-bora-3a,4a,diaza-*s*-indacene-3-pentanoic acid (Bodipy-PC) was purchased from Molecular Probes, Invitrogen (NY, USA). 1,1'-dieicosanyl-3,3,3',3'-tetramethylindocarbocyanine perchlorate (DiI-C_{20}) was purchased from Molecular Targeting Technologies (Pennsylvania, USA). Lissamine™ Rhodamine B 1,2-dihexadecanoyl-*sn*-glycero-3-phosphoethanolamine, triethylammonium salt (N-Rh-DHPE), secondary antibodies and Alexa-488/Alexa-647−phalloidin were purchased from Molecular Probes, Invitrogen (NY, USA). Poly-L-lysine hydrobromide was purchased from Sigma (NY, USA). GelTol (aqueous mounting media) was purchased from Shandon Lipshaw Co., Lerner Labs (PA, USA). All other culture media were purchased from Gibco, Invitrogen (NY, USA).

2.10.2 Preparation of Lipid Bilayer-Coated Silica Beads (SS-BLMs)

All reported SS-BLMs are tethered lipid bilayers supported on spherical silica substrates. SS-BLMs were prepared as reported previously[27], starting with a solution of 5 μm silica beads from Bangs Laboratories (IN, USA) at a concentration of 9×10^6 particles/mL in phosphate buffer saline (PBS), pH = 7.4. A volume of 100 μL of this solution was mixed with 0.1 mg/mL avidin for 20 minutes and incubated overnight at 4 ˚C. The avidin-coated beads were then washed by centrifugation (3× at 10^4 rpm for 10 minutes), and then re-suspended in the same buffer prior to incubation with the lipids. For the formation of small unilamellar vesicles (SUVs), chloroform solutions of respective lipids (1 mg/mL, 95 μL), and DSPE-PEG2000-biotin (0.1 mg/mL, 5 μL) were mixed and dried overnight under vacuum. The film was then hydrated using PBS (warmed to temperatures higher than the phase transition temperature (T_m) of lipids) through vortex mixing, followed by sonication in a bath sonicator for 2 – 5 minutes. Giant unilamellar vesicles (GUVs) were prepared *via* electroformation on the automated Vesicle Prep Pro (Nanion Technologies; Munich, Germany) chamber. In this method, 10 μL of a lipid-chloroform solution was dried overnight under vacuum on a glass slide coated with indium tin oxide (ITO). The lipid film was then hydrated by incubating with approximately 150 μL of PBS (at temperatures higher than the T_m of the constituent lipids). The formation chamber was assembled using two of the ITO electrodes facing one another, spaced and sealed by a rubber O-ring. An electric field of 10 Hz and 1.4 V was applied for 30 minutes to obtain vesicles with a diameter of 1 – 3 μm. A volume of 100 μL of the vesicle solution (SUVs or GUVs) was mixed with 100 μL of the avidin-coated silica beads dispersed in PBS, shaken gently, and incubated for 20 minutes. The bead-vesicle solution was then sonicated for 1 minute, washed by centrifugation (3× at 7×10^3 rpm for 10 minutes) and the resulting pellet was re-suspended in PBS. The resulting bilayer-coated beads (SS-BLMs) were then subjected to two successive heat/cool cycles at a controlled rate of 0.1 ˚C/second starting at 4 ˚C and ending at 80 ˚C using a TProfessional Thermocycler (Biometra; Göttingen, Germany). SS-BLMs were then incubated at 4 ˚C for 24 hrs prior to examination.

2.10.3 Primary Cultures of Rat Hippocampal Neurons

Cultures of dissociated rat hippocampal neurons were prepared using a modified protocol described by Banker.[30] Hippocampi were dissected from E17 embryos, treated with 0.25% (w/v) trypsin at 37 ˚C followed by Dulbecco's modified Eagle medium (DMEM) supplemented with

10% horse serum, and mechanically dissociated with a plastic Pasteur pipette. The dissociated neurons were plated at a density of (1.75 – 2.0) × 10^4 cm^{-1} on poly-L-lysine coated glass coverslips (Ted Pella Inc., CA, USA) in serum-free Neurobasal medium supplemented with *l*-glutamine, penicillin, streptomycin and B-27. The culture was kept in a humidified 5% CO_2 atmosphere at 37 ˚C and one-third of the medium was replaced every 2 − 3 days. All animal work was performed in accordance with the Canadian Council of Animal Care Guidelines.

2.10.4 Co-cultures with SS-BLMs and Immunochemistry

Primary cells were cultured to at least 9 days *in vitro* (DIV) before the addition of beads. SS-BLMs suspended in sterile PBS, pH = 7.4, were added to the cells drop wise at a concentration of (1.0 − 1.5) × 10^5 beads/coverslip. The bead/cell co-culture was incubated for 24 hrs in a humidified 5% CO_2 atmosphere at 37 ˚C. Cells were fixed with 4% (w/v) paraformaldehyde in phosphate buffer, pH 7.4, for 15 minutes and washed 3× in PBS. The cells were then incubated in blocking solution (PBS, pH = 7.4, containing 4% normal donkey serum (NDS) and 0.1% (w/v) saponin) for 30 min, and then in primary antibody solution (rabbit anti-β-tubulin 1:100 in PBS containing 0.1% (w/v) saponin and 0.5% (w/v) NDS), overnight at 4 ˚C. Cells were washed 3× in PBS, incubated in Alexa-488/Alexa-647 (as appropriately) coupled secondary antibodies (rabbit-specific, highly cross-adsorbed IgG, 1:200 in PBS-0.5% (w/v) NDS) for 30 minutes, washed 3× in PBS. For actin labeling, Alexa-488/Alexa-647−phalloidin (as appropriately) were used (1:50 dilution) in the secondary antibody buffer. The stained samples (on glass coverslips) were mounted on microscopic slides using GelTol and sealed prior to imaging.

2.10.5 Confocal Microscopy

All fluorescence images were obtained using a Zeiss LSM-710 confocal microscope (Carl Zeiss AG, Germany) with a 63x/1.4 oil-immersion objective lens, using either one or a combination of the following optical settings (*i*) λ_{ex} 488 nm/ λ_{em} LP > 505 nm (single channel imaging) or λ_{em} BP 505 − 550 nm (multi-channel imaging), (*ii*) λ_{ex} 543 nm/ λ_{em} LP > 565 nm, and (*iii*) λ_{ex} 633 nm/ λ_{em} LP > 685 nm. The acquired intensity images were checked to avoid detector saturation and loss of offsets by adjusting the laser power, the detector gain and the detector offset. The 3D image stacks were acquired at a sampling rate that satisfies the Nyquist frequency. The obtained confocal raw fluorescence image stacks were deconvolved by AutoQuant X3 software using

blind deconvolution algorithm. All raw confocal images were processed using Imaris 7.4.0 software.

2.10.6 Fluorescence Recovery after Photobleaching (FRAP)

Measurements were performed using a Zeiss LSM-710 confocal laser-scanning microscope with a 63x/1.4 oil-immersion objective lens and a 488 nm argon ion laser (25 mW power). The samples used for FRAP experiments were either GUVs or SS-BLMs (prepared starting with SUVs) from DOPC lipids labeled with 0.1 mol% Bodipy-PC. For tethering, 0.1 mol % DSPE-PEG2000-biotin was used in the lipid mixture to allow formation of SS-BLMs on 5 μm avidin coated silica beads or stabilization of GUVs on avidin coated glass coverslips. The FRAP experiment started by choosing a single SS-BLM or GUV in the image field of view, followed by defining three 1.2 μm radius circular regions of interest (ROI) for subsequent imaging; a bleach ROI, a reference ROI outside the bleach area and a third background ROI outside the field of view of the SS-BLM. Five images were captured prior to bleaching in order to measure the initial pre-bleach fluorescence intensity, followed by 10 consecutive bleach iterations using 100% laser intensity. The laser power was reduced to 5% for collecting the following 50 post-bleaching images. The total scan time was minimized by imaging only the three circular regions of interest rather than the whole SS-BLM in the field of view. This allowed a reduction of the total experiment time to *ca.* 14 s. For each experiment, the background signal (BG) was subtracted from the bleached ROI and then normalized to their initial pre-bleaching fluorescence intensity. In order to correct for any photobleaching during the measurement, the normalized bleached ROI intensity was divided by the normalized intensity of the reference region:

$$\frac{\dfrac{F_{ROI} - BG}{F_{ROI}(prebleached) - BG}}{\dfrac{F_{REF} - BG}{F_{REF}(prebleached) - BG}} \qquad \textbf{Equation 2.1}$$

The corrected fluorescence curves f (from 50 separate experiments) were used to construct an average FRAP curve which was then fitted to a one component fit model describing one diffusive species according to Equation 2.2.

$$f(t) = A(1 - e^{\pi}) \qquad \textbf{Equation 2.2}$$

where A is the ratio of mobile to immobile populations and τ is the half-time of fluorescence recovery (*i.e.* the diffusion time required to recover 50% of initial fluorescence intensity).
Taking into account that the reported half-time of recovery corresponds to the fastest recovery time that can be measured with the confocal set up and experimental parameters described above, a lower limit of the diffusion constant D was calculated according to Equation 2.2.[31]

$$D \geq 0.224.w^2 / \tau \qquad \textbf{Equation 2.3}$$

where w is the radius of the circular ROI.
All data processing and fitting were performed using Kaleidagraph (Synergy software).

2.10.7 Description of Co-culture Experiments and Quantification of % Co-localization of Cytoskeletal Network with SS-BLM Co-existing Lipid Domains

For each co-culture experiment, both cytoskeletal filaments (actin and microtubules) are fluorescently co-labeled *via* immunochemistry, and the SS-BLMs are fluorescently labeled using a fluorescent lipid dye that differentiates the more ordered lipid phases (*i.e.* the gel phase or liquid ordered (L_o) are labeled using N-Rh-DHPE or DiI-C_{20}, respectively). Confocal z-stacks were collected using a three-channel confocal fluorescence microscope and represented as 3D reconstruction images. If the cells were fluorescently labeled for only one cellular component (either actin or microtubules) then both co-existing lipid domains could have been fluorescently-labeled. However, the goal of the reported co-culture experiments was to co-label both cytoskeletal filaments in the same experiment rather than individually. The preferential co-localization between the cytoskeletal filament (either actin or microtubules) and either one of the co-existing lipid phases was assessed by the presence or absence of a spatial overlap of their respective fluorescence intensity signals across the surface of the SS-BLM, for at least 50 samples. The presence of an overlap describes a co-localization with the labeled domains (*i.e.* the ordered domains in this experimental set up), whereas an absence of overlap describes a co-localization with the non-labeled domains (*i.e.* the disordered domains, in this experimental set up).

2.10.8 Interaction of DOPE fluid phase SS-BLMs with the cellular cytoskeleton

The interactions of SS-BLMs consisting of a DOPE-rich fluid phase and a DPPC-rich gel phase were examined. The fluid (not labeled) phase in SS-BLMs shown in Fig. 2.8 involves phosphatidylethanolamine (PE) headgroups and the gel phase (labeled, red) involves phosphatidylcholine (PC) headgroups. The cytoskeletal organization remains favouring the fluid phase.

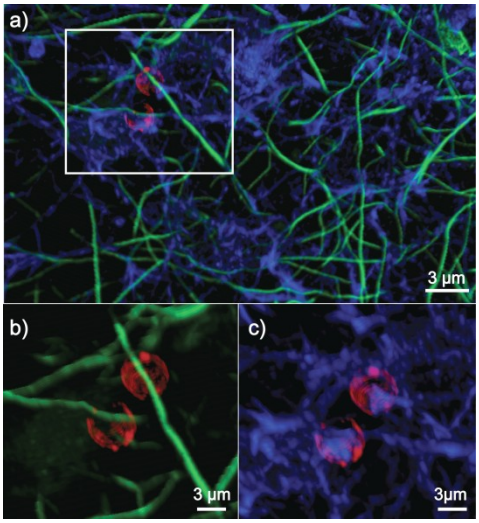

Figure 2.8 A representative 3-channel confocal 3D-reconstruction image showing the co-localization of cytoskeletal networks with SS-BLMs displaying DOPE-rich fluid phase: (a) assembly of microtubules (β-tubulin, green) and actin (phalloidin, blue) around the fluid phase on DOPE/DPPC/DOTAP (25:50:25) SS-BLMs. The ordered domains (DPPC-rich) are labeled using 0.1 mol% DiI-C_{20} (red). Close-up views of image "a" show either microtubule (b) or actin (c) co-localization with the fluid domains (DOPE-rich) (dark areas). The SS-BLMs are co-cultured with hippocampal neurons (DIV 8) for 24 hrs and immunostained for both microtubules and actin.

2.10.9 Co-localization of cytoskeletal filaments with fluid phases of SS-BLMs that do not exhibit lipid phase separation

Control studies conducted using SS-BLMs with uniform compositions that do not exhibit lipid phase separation (for example 100% DOPC or 100% DPPE) show non-specific cellular organization and no significant interactions between the living cells with the co-cultured SS-BLMS (Fig. 3.10 b, 3.10c and 3.10d). The addition of cationic lipid DOTAP (Fig. 3.10 a) appears to favour the adhesion to SS-BLMs. A comparison to SS-BLMs exhibiting co-existing

microdomains is also shown (Fig. 3.10e and 3.10d) to highlight the closer interactions of cytoskeletal filaments when interfaced with an environment display lipid phase separation.

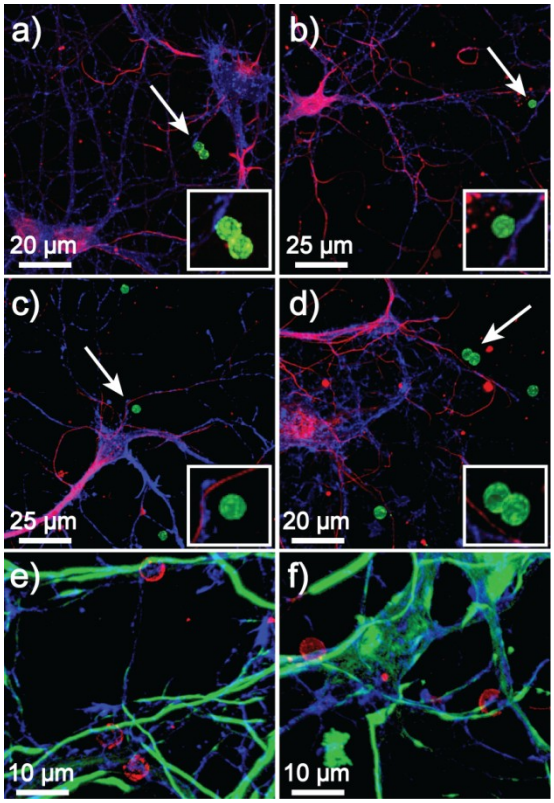

Figure 2.9 Representative 3-channel confocal 3D-recontruction images showing a comparison of the assembly of cytoskeletal networks on regular *versus* phase-separated SS-BLMs: DOPC/ DOTAP (75:25) (a), DOPC only (b), DPPC only (c) and DPPE only (d) labeled using 0.1 mol% NBD PE (green). The SS-BLMs are co-cultured with hippocampal neurons (DIV 8) for 24 hrs and then immunostained for both microtubules (β-tubulin, red) and actin (phalloidin, blue). Close-up views of SS-BLMs from areas indicated by the white arrows are shown as insets. For comparison, assembly of actin (phalloidin, blue) and microtubules (β-tubulin, green) around SS-BLMs from lipid mixtures displaying lipid phase separation of liquid ordered – liquid disordered (DOPC/DPPC/CHOL, 50:30:20) are shown in (e) with the ordered domains (DPPC-rich) labeled using 0.1 mol% DiI-C_{20} (red) and those displaying fluid–gel phase separation (DOPC/DPPE/DOTAP, 25:50:25) are shown in (f) with the gel domains (DPPE-rich) labeled using 0.1 mol% N-Rh-DHPE (red). For images (e) and (f) microtubules are shown in green and actin is shown in blue.

2.10.10 Application of co-culture experiments and immunochemistry procedures to GUVs

The following procedures were performed in order to test the applicability of using GUVs in various experimental steps carried out using the SS-BLM system (*i.e.* co-culture with neurons

followed by immunochemistry). Two lipid mixtures were used in this study; DOPC/DPPC/DOTAP/CHOL (30:30:20:20) labeled with 0.1 mol% DiI-C_{20} and DOPC/DPPE/DOTAP (25:50:25) labeled with 0.1 mol% N-Rh-DHPE. The experimental procedure included (*i*) incubation of GUVs in cell culture media for 24 hours, (*ii*) addition of a fixative, (*iii*) washing with buffer, and (*iv*) addition of a detergent. The experimental procedure and results are summarized in Table 2.2. The experiments were carried out both in series as well as in parallel. The results indicate that it is not possible to use GUVs for such experimental procedure.

Table 2.2 Application of co-culture and immunochemistry procedure to GUVs.

Treatment	incubation with cell culture media[a]	addition of fixative solution[b]	washing with buffer[c]	addition of detergent[d]
DOPC/DPPC/ DOTAP/CHOL (30:30:20:20) mixture	✔ ✔ ✔	✔ ✔	×	×
DOPC/DPPE/DOTAP (25:50:25) mixture	×	✔ ✔	×	✔

[a] the cell culture media is serum-free Neurobasal medium supplemented with *l*-glutamine, penicillin, streptomycin and B-27. The GUVs were incubated in this media in a humidified 5% CO_2 atmosphere at 37 °C for 24 hours. [b] The fixative solution is 4% paraformaldehyde in phosphate buffer, pH 7.4. [c] The buffer is phosphate buffer saline, pH 7.4. [d] The detergent is 0.1% Saponin.

2.10.11 Co-culture of SS-BLMs with COS-7 cell lines

Monkey kidney cells (COS-7) were cultured in DMEM supplemented with 10% fetal calf serum, in a humidified 5% CO_2 atmosphere at 37 ˚C. Cells were split at regular intervals. For co-culture experiments, COS-7 cells were seeded into 12-well plates (Nalge Nunc International, NY, USA) containing 18-mm-diameter glass coverslips (TED PELLA Inc., CA, USA), in culture medium (2 mL) containing 10% fetal calf serum. The cells were grown for 24 hrs at 37 ˚C, before adding SS-BLMs.

The preferential organization of the cytoskeletal networks of COS-7 cells with fluid phases of SS-BLMs was observed (Fig. 2.10). However, the interactions with the bead-supported

membrane were found to be relatively easier to visualize with the primary neural cultures due to the thin neurite outgrowths extending onto the SS-BLMs. The red arrows in Fig. 2.10 indentify the regions where co-localization of the cytoskeletal networks around the SS-BLM becomes unclear due to the thickness/density of cell lines.

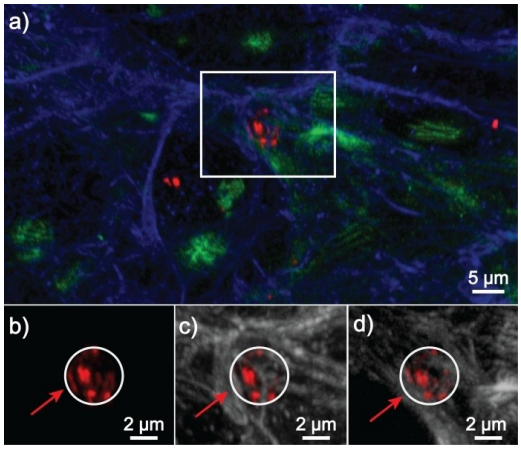

Figure 2.10 A representative 3-channel confocal 3D-reconstruction image showing the co-localization of cytoskeletal networks of COS-7 cells with SS-BLMs: (a) assembly of actin (phalloidin, blue) and microtubules (β-tubulin, green) around DOPC/DPPC/CHOL (50:30:20) SS-BLMs. Single channel magnified view of image "a" showing the location of ordered (DPPC-rich) domains on SS-BLMs (b) that are labeled using 0.1 mol% DiI-C_{20} (red). The actin (c) and microtubules (d) organize around the unlabeled regions of the bilayer, representing the fluid phase (DOPC-rich). The SS-BLMs are co-cultured with COS-7 cells for 24 hrs and then immunostained for both microtubules and actin. White circles (b-d) identify the beads in culture.

2.10.12 Differential Scanning Calorimetry (DSC) Measurements of SS-BLMs Phase Transition

The effect of additives (*i.e.* fluorescent probes and spacer polymers) on SS-BLM phase transition was examined using DSC. DSC thermograms were recorded using a DSC Q2000 (TA Instruments). SS-BLMs were prepared on 5 µm silica beads as described in Experimental Section 2.10.2. A volume of 25 µL of SS-BLM aqueous solution (4.5×10^9 beads/mL in PBS buffer) was added to aluminum hermetic pans and tightly closed with an aluminum lid. An empty pan was used as reference during the measurements. Both the reference and sample pans were weighed before starting the measurements. The samples were heated at a rate of 1 ˚C/minute from –30˚C to –5˚C over three cycles (heat/cool/heat). The DSC thermograms show that the T_m is the same in the SS-BLMs samples from DOPC lipids in the absence or presence of

0.1 mol% fluorescent probes or spacer polymers. This indicates that these different additives do not affect the phase transition of SS-BLM lipids.

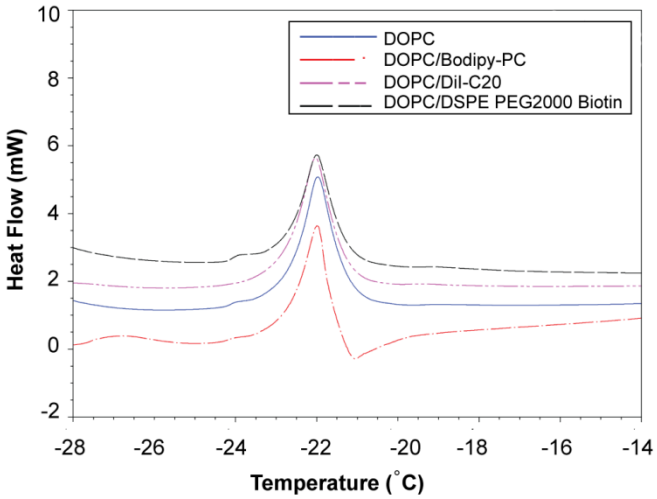

Figure 2.11 DSC thermograms of SS-BLMs on silica beads. The curves show that the T_m of the SS-BLMs from DOPC lipids (measured to be -22 ˚C) is not affected by the presence of 0.1 mol% of fluorescent probes (*i.e.* Bodipy-PC or DiI-C_{20}) and polymer spacers (*i.e.* DSPE-PEG2000-Biotin lipids) in the lipid mixture. In all preparations, 5 µm silica beads, coated with avidin, were used as the solid spherical support and 0.1 mol% of the different additive was included in the lipid mixture.

2.11 References

1. Brown, D. A.; London, E. Functions of lipid rafts in biological membranes. *Annu. Rev. Cell. Dev. Bi.* **1998,** *14*, 111-136.

2. Mueller, N.S.; Wedlich-Soldner, R.; Spira, F. From mosaic to patchwork: Matching lipids and proteins in membrane organization. *Mol. Membr. Biol.* **2012,** *29*, 186-196.

3. Rietveld, A.; Simons, K. The differential miscibility of lipids as the basis for the formation of functional membrane rafts. *Biochim. Biophys. Acta. Rev. Biomembr.* **1998,** *1376*, 467-479.

4. Simons, K.; Ikonen, E. Functional rafts in cell membranes. *Nature* **1997,** *387*, 569-572.

5. Lingwood, D.; Simons, K. Lipid rafts as a membrane-organizing principle. *Science* **2010**, *327*, 46-50.

6. Coskun, U.; Simons, K. Cell membranes: the lipid perspective. *Structure* **2011,** 19, 1543-1548.

7. Brown, D. A.; London, E. Structure and origin of ordered lipid domains in biological membranes. *J. Membrane. Biol.* **1998,** *164*, 103-114.

8. Thomas, J. L.; Holowka, D.; Baird, B.; Webb, W. W. Large-scale coaggregation of fluorescent lipid probes with cell-surface proteins. *J. Cell. Biol.* **1994,** *125*, 795-802.

9. van Meer, G.; Voelker, D. R.; Feigenson, G. W. Membrane lipids: where they are and how they behave. *Nat. Rev. Mol. Cell Biol.* **2008,** *9*, 112-124.

10. Johnston, I.; Johnston, L. J. Ceramide promotes restructuring of model raft membranes. *Langmuir* **2006,** *22*, 11284-11289.

11. Chichili, G. R.; Rodgers, W. Cytoskeleton-membrane interactions in membrane raft structure. *Cell. Mol. Life Sci.* **2009,** *66*, 2319-2328.

12. Holowka, D.; Sheets, E. D.; Baird, B. Interactions between Fc epsilon RI and lipid raft components are regulated by the actin cytoskeleton. *J. Cell. Sci.* **2000,** *113*, 1009-1019.

13. Bagatolli, L. A. To see or not to see: Lateral organization of biological membranes and fluorescence microscopy. *Biochim. Biophys. Acta Biomembr.* **2006,** *1758*, 1541-1556.

14. Hac, A. E.; Seeger, H. M.; Fidorra, M.; Heimburg, T. Diffusion in two-component lipid membranes - a fluorescence correlation spectroscopy and Monte Carlo simulation study. *Biophys. J.* **2005,** *88*, 317-333.

15. Honerkamp-Smith, A. R.; Veatch, S. L.; Keller, S. L. An introduction to critical points for biophysicists; observations of compositional heterogeneity in lipid membranes. *Biochim. Biophys. Acta Biomembr.* **2009,** *1788* , 53-63.

16. Korlach, J.; Schwille, P.; Webb, W. W.; Feigenson, G. W. Characterization of lipid bilayer phases by confocal microscopy and fluorescence correlation spectroscopy. *Proc. Natl. Acad. Sci. USA.* **1999,** *96*, 8461-8466.

17. McConnell, H. M.; Vrljic, M. Liquid-liquid immiscibility in membranes. *Annu. Rev. Biophs. Biom.* **2003,** *32*, 469-492.

18. Mohwald, H. Phospholipid and phospholipid-protein monolayers at the air/water interface. *Annu. Rev. Phys. Chem.* **1990,** *41*, 441-476.

19. Bagatolli, L. A.; Gratton, E. Two-photon fluorescence microscopy observation of shape changes at the phase transition in phospholipid giant unilamellar vesicles. *Biophys. J.* **1999,** *77*, 2090-2101.

20. Groves J. T.; Ulman, N.; Cremer, P. S.; Boxer, S. G. Substrate-membrane interactions: mechanisms for imposing patterns on a fluid bilayer membrane. *Langmuir* **1998,** *12*, 3347-3350.

21. Tamm, L. K.; McConnell, H. M. Supported phospholipid-bilayers. *Biophys. J.* **1985,** *47*, 105-113.

22. Merkel, R.; Sackmann, E.; Evans, E. Molecular friction and epitactic coupling between monolayers in supported bilayers. *J. Phys. (Paris)* **1989,** *50* , 1535-1555.

23. Anderson, T. H.; Min, Y. J.; Weirich, K. L.; Zeng, H. B.; Fygenson, D.; Israelachvili, J. N. formation of supported bilayers on silica substrates. *Langmuir* **2009,** *25*, 6997-7005.

24. Prashar, J.; Sharp, P.; Scarffe, M.; Cornell, B. Making lipid membranes even tougher. *J. Mater. Res.* **2007,** *22*, 2189-2194.

25. Schwille, P.; Diez, S. Synthetic biology of minimal systems. *Crit. Rev. Biochem. Mol.* **2009,** *44*, 223-242.

26. Chemburu, S.; Fenton, K.; Lopez, G. P.; Zeineldin, R. Biomimetic silica microspheres in biosensing. *Molecules* **2010,** *15*, 1932-1957.

27. Gopalakrishnan, G.; Rouiller, I.; Colman, D. R.; Lennox, R. B. Supported bilayers Formed from different phospholipids on spherical silica substrates. *Langmuir* **2009,** *25*, 5455-5458.

28. Gopalakrishnan, G.; Thostrup, P.; Rouiller, I.; Lucido, A. L.; Belkaid, W.; Colman, D. R.; Lennox, R. B. Lipid bilayer membrane-triggered presynaptic vesicle assembly. *ACS Chem. Neurosci.* **2010,** *1*, 86-94.

29. Bayerl, T.M.; Bloom, M. Physical properties of single phospholipid bilayers adsorbed to micro glass beads. A new vesicular model system studied by 2H-nuclear magnetic resonance. *Biophys. J.* **1990,** *58*, 357-362.

30. Goslin, K.; Asmussen, H.; Banker, G. In *Culturing Nerve Cells*. Banker G., Goslin K, Eds.; 2nd ed.; MIT Press: Cambridge, Massachusetts, **1998**; p 666.

31. Soumpasis, D. M. Theoretical analysis of fluorescence photobleaching recovery experiments. *Biophys. J.* **1983,** *41*, 95-97.

32. Davenport, L. Fluorescence probes for studying membrane heterogeneity. *Method. Enzymol.* **1997,** *278*, 487-512.

33. Huang, N. N.; Florinecasteel, K.; Feigenson, G. W.; Spink, C. Effect of fluorophore linkage position of normal-(9-anthroyloxy) fatty-acids on probe distribution between co-existing gel and fluid phospholipid phases. *Biochim. Biophys. Acta* **1988,** *939*, 124-130.

34. Spink, C. H.; Yeager, M. D.; Feigenson, G. W. Partitioning behavior of indocarbocyanine probes between co-existing gel and fluid phases in model membranes. *Biochim. Biophys. Acta* **1990,** *1023*, 25-33.

35. Silvius, J. R. Role of cholesterol in lipid raft formation: lessons from lipid model systems. *Biochim. Biophys. Acta Biomembr.* **2003,** *1610*, 174-183.

36. Gennis, R. B. The structures and properties of membrane lipids. In *Biomembranes: molecular structure and function*; Cantor, C. R., Ed.; Springer: New York, 1989;. pp. 64-83

37. MacDonald, R. C.; MacDonald, R. I. *Applications of freezing and thawing in liposome technology*. 3rd ed.; CRC Press: Boca Raton, **1984**; Vol. 1, p 209-228.

38. Richter, R. P.; Berat, R.; Brisson, A. R. Formation of solid-supported lipid bilayers: An integrated view. *Langmuir* **2006,** *22*, 3497-3505.

39. Giocondi, M. C.; Vie, V.; Lesniewska, E.; Milhiet, P. E.; Zinke-Allmang, M.; Le Grimellec, C. Phase topology and growth of single domains in lipid bilayers. *Langmuir* **2001,** *17*, 1653-1659.

40. Bagatolli, L. A.; Gratton, E. Two photon fluorescence microscopy of co-existing lipid domains in giant unilamellar vesicles of binary phospholipid mixtures. *Biophys. J.* **2000,** *78*, 290-305.

41. Vaz, W. L. C.; Stumpel, J.; Hallmann, D.; Gambacorta, A.; Derosa, M. Bounding fluid viscosity and translational diffusion in a fluid lipid bilayer. *Eur. Biophys. J. Biophy.* **1987,** *15*, 111-115.

42. Berquand, A.; Mazeran, P. E.; Pantigny, J.; Proux-Delrouyre, V.; Laval, J. M.; Bourdillon, C. Two-step formation of streptavidin-supported lipid bilayers by PEG-triggered vesicle fusion. Fluorescence and atomic force microscopy characterization. *Langmuir* **2003,** *19*, 1700-1707.

43. Cambrea, L. R.; Hovis, J. S. Formation of three-dimensional structures in supported lipid bilayers. *Biophys J* **2007,** *92*, 3587-3594.

44. Guo, L.; Har, J. Y.; Sankaran, J.; Hong, Y. M.; Kannan, B.; Wohland, T. Molecular diffusion measurement in lipid Bilayers over wide concentration ranges: A comparative study. *Chemphyschem.* **2008,** *9*, 721-728.

45. Seu, K. J.; Cambrea, L. R.; Everly, R. M.; Hovis, J. S. Influence of lipid chemistry on membrane fluidity: Tail and headgroup interactions. *Biophys. J.* **2006,** *91*, 3727-3735.

46. Shenoy, S.; Moldovan, R.; Fitzpatrick, J.; Vanderah, D. J.; Deserno, M.; Losche, M. In-plane homogeneity and lipid dynamics in tethered bilayer lipid membranes (tBLMs). *Soft Matter* **2010,** *6*, 1263-1274.

47. Doherty, G. J.; McMahon, H. T. Mediation, modulation, and consequences of membrane-cytoskeleton interactions. *Annu. Rev. Biophys.* **2008,** *37*, 65-95.

48. Pollard, T. D.; Cooper, J. A. Actin, a central player in cell shape and movement. *Science* **2009,** *326*, 1208-1212.

49. Lenne, P. F.; Wawrezinieck, L.; Conchonaud, F.; Wurtz, O.; Boned, A.; Guo, X. J.; Rigneault, H.; He, H. T.; Marguet, D. Dynamic molecular confinement in the plasma membrane by microdomains and the cytoskeleton meshwork. *Embo. J.* **2006,** *25*, 3245-3256.

50. Liu, A. P.; Fletcher, D. A. Actin polymerization serves as a membrane domain switch in model lipid bilayers. *Biophys. J.* **2006,** *91*, 4064-4070.

51. Edidin, M. Switching sides: The actin/membrane lipid connection. *Biophys. J.* **2006,** *91*, 3963-3963.

52. Gopalakrishnan, G.; Danelon, C.; Izewska, P.; Prummer, M.; Bolinger, P. Y.; Geissbuhler, I.; Demurtas, D.; Dubochet, J.; Vogel, H. Multifunctional lipid/quantum dot hybrid nanocontainers for controlled targeting of live cells. *Angew. Chem. Int. Edit.* **2006,** *45*, 5478-5483.

53. Ahyayauch, H.; Bennouna, M.; Alonso, A.; Goni, F. M. Detergent effects on membranes at subsolubilizing concentrations: transmembrane lipid motion, bilayer permeabilization, and vesicle lysis/reassembly are independent phenomena. *Langmuir* **2010,** *26*, 7307-7313.

54. Delamaza, A.; Parra, J. L. Vesicle-micelle structural transition of phosphatidylcholine bilayers and triton X-100. *Biochem. J.* **1994,** *303*, 907-914.

55. Goni, F. M.; Alonso, A. Spectroscopic techniques in the study of membrane solubilization, reconstitution and permeabilization by detergents. *Biochim. Biophys. Acta Biomembr.* **2000,** *1508*, 51-68.

56. Heerklotz, H.; Seelig, J. Titration calorimetry of surfactant-membrane partitioning and membrane solubilization. *Biochim. Biophys. Acta Biomembr.***2000,** *1508*, 69-85.

57. Sudbrack, T. P.; Archilha, N. L.; Itri, R.; Riske, K. A. Observing the solubilization of lipid bilayers by detergents with optical microscopy of GUVs. *J. Phys. Chem. B* **2011,** *115*, 269-277.

58. Oglecka, K.; Sanborn, J.; Parikh, A.; Kraut, R. Osmotic gradients induce bio-reminiscent morphological transformations in giant unilamellar vesicles. *Front. Physiol.* **2012,** *3*, 120.

59. Mathivet, L.; Cribier, S.; Devaux, P. F. Shape change and physical properties of giant phospholipid vesicles prepared in the presence of an AC electric field. *Biophys. J.* **1996,** *70*, 1112-1121.

60. Wesolowska, O.; Michalak, K.; Maniewska, J.; Hendrich, A. B. Giant unilamellar vesicles - a perfect tool to visualize phase separation and lipid rafts in model systems. *Acta. Biochim. Pol.* **2009,** *56*, 33-39.

Linking Statement to Chapter 3

Chapter 2 examined the suitability of SS-BLMs as an experimental platform that allows for interfacing biomimetic model membranes with living neurons. Using fluorescence techniques, it was demonstrated that co-existing lipid phase domains in these model membranes are stable under cell culture conditions. In Chapter 3, similar approaches are applied to explore the contribution of lipid phase separation in SS-BLMs in generating an environment that triggers neuronal synaptic responses. This allows for investigation of the relationships between lipid phase separation and their associated domains (*i.e.* lipid rafts) and neuronal communication under controlled conditions. Such knowledge will aid in designing SS-BLMs suitable for use as neuronal interfaces. To this end a statistical analysis is conducted to compare and contrast SS-BLMs formed from various lipid mixtures in terms of their relative ability to interact with neurons and induce synapses. The SS-BLMs used in this study display different molecular features (*i.e.* different charges and different chemical functional groups) and different structural features (*i.e.* different thermodynamic phases). This allows for exploration of the factors that influence artificial synapse formation in the presence of synthetic lipid bilayer membranes.

Chapter 3

Spherical Supported Bilayer Lipid Membrane Microdomains in Synapse Formation

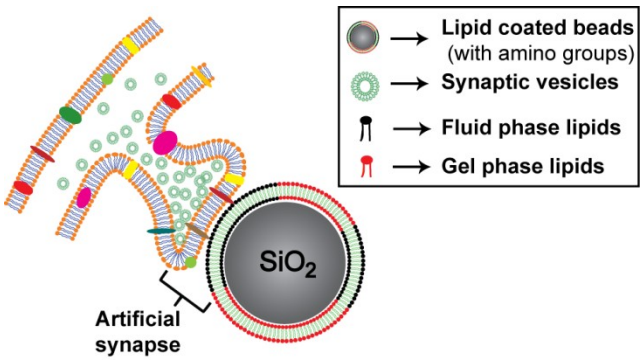

The text of this Chapter will be submitted to the *ACS Journal of Chemical Neuroscience* as "Spherical Supported Bilayer Lipid Membrane Microdomains in Synapse Formation", C. Madwar, G. Gopalakrishnan, and R. B. Lennox. The text below is a verbatim copy of the manuscript.

3.1 Abstract

Membrane lipid rafts (*i.e.* cholesterol/sphingolipids domains) exhibit functional roles in both healthy and pathological states of the nervous system.[1] However, due to their highly dynamic nature, it remains a challenge to characterize the fundamental aspects of lipid rafts that are important for specific neural processes. An experimental approach is presented here that allows for interfacing living neurons with an experimentally accessible model membrane where lipid order in cellular rafts is reproducibly mimicked. It is demonstrated that rafts in model membranes, formed from co-existing lipid microdomains, can regulate axonal guidance and establish stable presynaptic contacts when interfaced with neurons *in vitro*. This suggests that raft proteins or postsynaptic components are not necessary to establish such active synaptic sites. Experimental evidence is provided wherein specific functional groups and lateral organizations are favoured by the neurons for establishing synaptic connections. The model membrane platform presented in this work provides a simple and direct means to investigate how lipid rafts regulate synapse formation. This experimental platform can similarly be extended to explore a variety of other cellular events where lipid lateral organization is believed to be important.

3.2 Introduction

Lipid rafts are specialized membrane domains that have been shown to exist in cell plasma membranes.[2] They are responsible for a number of cellular processes including regulation of signaling molecules, neuronal outgrowth, axonal guidance and synaptic transmission.[3, 4, 5, 6, 7] Such microdomains consist of both protein and lipid components with an enrichment of sphingolipids and cholesterol resulting in a more ordered lipid bilayer state that exists within the rest of the fluid plasma membrane.[8, 9, 10] The dynamic nature of the molecular ordering and packing in these lipid rafts provides modulation of signaling molecules within the membrane and is therefore linked to the excitatory and inhibitory effects of signaling events.[11] Several reports provide evidence for the involvement of lipid rafts in different neuronal processes, establishing their functional roles in both healthy and pathological states of the nervous system.[12, 13, 14, 15, 16, 17, 18] It has also been shown that disruption of membrane rafts can lead to an eventual retraction of neurite outgrowths.[19] A variety of cellular processes essential for neuronal activity and membrane turnover in the brain are thus regulated at lipid rafts and are highly dependent on their organization and dynamics.[18, 20] However, the fundamental aspects of lipid rafts that are

important in axonal outgrowth and more importantly, in the initial signaling to establish neuronal activity are still not known. It is therefore of interest to explore the relationship between neuronal activity and lipid rafts using an experimentally accessible and reproducible model system. We demonstrate here the application of a synthetic platform that contains only lipids which display co-existing microdomains. These are shown to regulate axonal guidance and can establish synaptic contacts without any participation of other raft components or post-synaptic elements. Experimental evidence is presented where one particular co-existing lipid phase is favoured by the neurons in establishing synaptic contacts.

We have previously demonstrated the *in vitro* formation of presynapses on micrometer-sized spherical substrates coated with either a synthetic polypeptide (*i.e.* poly-D-lysine; PDL)[21, 22] or lipid bilayer membranes.[23, 24] The spherical geometry of these substrates was shown to be required in inducing a functional synaptic response. In addition, preliminary evidence suggested that co-existing membrane domains direct lipid membrane-induced synapse formation.[25] However, experimentally establishing the role of lipid rafts at the initial stages of synapse formation remains a technical challenge. This prompted us to generate co-existing lipid microdomains on spherically supported bilayer membranes (SS-BLMs) and use these as an accessible form of lipid rafts. In this proof-of-concept study, we demonstrate how extracellular membrane heterogeneity presented on SS-BLMs influence the dynamics of cellular microenvironments.[25] This physicochemical model is (*i*) robust and can withstand cell culture conditions and characterization/imaging procedures, (*ii*) interactive with cells at any point in time during the period of cell culture, (*iii*) compositionally versatile and can display structural properties of membranes with minimal components and (*iv*) of great potential for incorporating functional molecules, such as purified membrane raft components, into the bilayer structure of SS-BLMs.

3.3 Validation of the Minimal Raft Model in Primary Neuronal Co-cultures

To demonstrate the suitability of our approach in investigating lipid raft-dependent neuronal outgrowth, SS-BLMs exhibiting co-existing lipid domains were co-cultured with primary hippocampal neurons. The interactions between neurons and SS-BLMs can be visualized and examined *via* fluorescence imaging (Fig. 3.1) using fluorescently-tagged lipids. These probes are chosen on the basis of their ability to partition into different phases by structural similarities.[25]

Artificial synapse formation was explored *via* immunofluorescence methods for visualizing several synaptic proteins in hippocampal neurons. These cells were grown for at least 14 days *in vitro* (DIV) and then co-cultured with SS-BLMs from various lipid mixtures for 24 hrs. Quantification of the fluorescence intensity serves as an indicator of the accumulation level of synaptic proteins in the vicinity of SS-BLMs. This allows for exploration of the various chemical and physical parameters of lipid bilayers that trigger a functional synaptic response from the neurons. Moreover, imaging *via* successive optical sections of the neuron/SS-BLM co-cultures (using confocal Z-stack imaging), enables the study of co-localization of synaptic proteins and cytoskeletal networks with different lipid domains. In Fig. 3.1, the imaged neuron was labeled with Cell Tracker^{TM} dye and the SS-BLMs were labeled with N-Rh-DHPE. This fluorescent lipid preferentially partitions into the ordered lipid domains. Confocal laser scanning microscopy (CLSM) and Z-stack imaging were used to examine the assembly of neurons around the different domains of SS-BLMs in 3D.

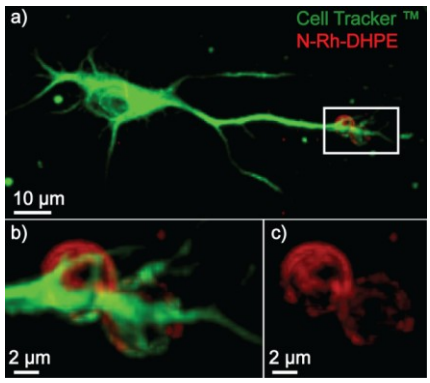

Figure 3.1 Representative confocal 3D-reconstruction images showing the interaction of neurons with lipid microdomains on SS-BLMs displaying a fluid–gel (L_d–S_o) co-existence. (a) Assembly of rat hippocampal neurons (DIV 9) around SS-BLMs from DOPC/DPPE/DOTAP (25:50:25). The cells are co-cultured with SS-BLMs for 24 hrs and then labeled with Cell Tracker ™ dye (green). Panels (b) & (c) are magnified views of image (a), showing the close interactions of the neuron with the lipid phases of SS-BLMs. Panel (c) is a single channel image of (b), showing the ordered (DPPE-rich) SS-BLM domains labeled using 0.1 mol% N-Rh-DHPE (red areas) and the fluid domains (DOPC-rich) that are unlabeled (dark areas). In this preparation, 5 µm silica beads, coated with avidin, were used as the solid spherical support and 0.1 mol% DSPE-PEG2000-biotin was used in the lipid mixture for tethering.

3.4 Lipid Compositions *versus* Synaptic Assembly

In our previous studies, SS-BLMs from a particular lipid mixture, DOPC/DPPE/DOTAP (25:50:25) were shown to induce the formation of presynapses at neuronal contacts. This ternary lipid mixture bears a net positive charge and exhibits co-existing lipid microdomains at 37 °C (see Experimental Section Fig. 3.6). In order to study which factors favour synapse formation (*i.e.* headgroup, charge, lipid phase), various mixtures of synthetic phospholipids (Figs. 3.2, 3.3, 3.10 and 3.11) that have different molecular (*i.e.* different charges and different chemical functional groups) and structural (*i.e.* different thermodynamic phases) features were used. A statistical analysis comparing the effect of SS-BLMs formed from the above lipid mixture to that of uncoated silica beads (see Experimental Section Fig. 3.8) was first conducted. In particular, the ability of these SS-BLMs to interact with neurons and induce the formation of presynapses is concluded from the enhanced immunofluorescence of the synaptic vesicle protein synaptophysin, the scaffolding active zone protein bassoon and the cytoskeletal protein actin in the vicinity of the neuron-bead contact points. The fluorescence quantification analysis compares the fluorescence intensity of these synaptic proteins at the bead surface to that of adjacent areas (see Experimental Section 3.7.2 and Fig. 3.7 for details on the quantification analysis). In this case, a fluorescence intensity ratio much greater than unity corresponds to a significant accumulation of the presynaptic vesicles and active zone markers around the SS-BLMs (ratios: synaptophysin 15.26±2.34 (SS-BLMs) *vs* 2.24±0.13 (uncoated beads), bassoon 11.65±1.76 (SS-BLMs) *vs* 1.26±0.22 (uncoated beads) and actin 20.37±2.74 (SS-BLMs) *vs* 1.76±0.19 (uncoated beads); see Experimental Section Fig. 3.8 and Table 3.1).

In the DOPC/DPPE/DOTAP mixture, the unsaturated DOPC lipids are organized in a loosely packed fluid phase whereas the saturated DPPE lipids are organized in a tightly packed gel phase.[25] Fluorescence intensity analysis shows a significantly low accumulation of the synaptic proteins around homogenous SS-BLMs in comparison to the above mentioned DPPE heterogeneous lipid mixtures (Figs. 3.2 and 3.3). For example, those derived from a lipid mixture containing DOPC/DOPE/DOTAP (25:50:25) where both DOPC and DOPE are intermixed in a homogenous fluid phase, or those derived from DPPC/DPPE/DOTAP (25:50:25) where both DPPC and DPPE are intermixed in a homogenous gel phase, show no significant synaptic accumulation at the bead-neuron contacts. As summarized in the Experimental Section Table 3.1, the DOPC/DOPE/DOTAP mixture yields synaptophysin 1.06±0.65, bassoon 1.19±0.36 and

actin 1.46±0.52 and DPPC/DPPE/DOTAP mixture yields fluorescence ratios of: synaptophysin 1.15±0.31, bassoon 1.51±0.23 and actin 1.65±0.62. However, it is striking that when co-existing lipid microdomains formed from a mixture of phosphatidylcholine (PC) lipids (without inclusion of any phosphatidylethanolamine (PE) lipids) were presented to neurons in culture, no presynatic accumulation was observed. The fluorescence ratios associated with the DOPC/DPPC/DOTAP mixture (Fig. 3.2E) are: synaptophysin 1.83±0.21, bassoon 1.26±0.18 and actin 1.43±0.78.

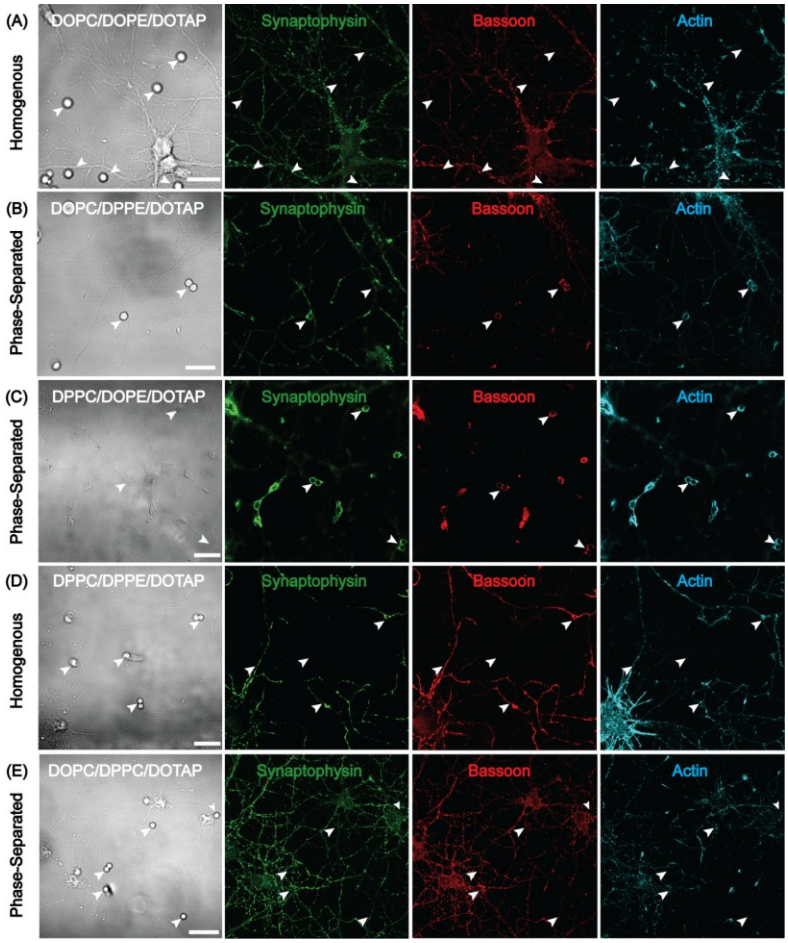

Figure 3.2 Representative confocal cross section images showing accumulation of presynaptic proteins around SS-BLMs from various lipid mixtures with PC and PE headgroups. In these experiments, SS-BLMs are not labeled. The fluorescence observed around SS-BLMs is due to the immunolabeled presynaptic proteins (*i.e.* synaptophysin, bassoon or actin). Rat hippocampal neurons (DIV 22) are incubated for 24 hrs with SS-BLMs (lipid mixtures are noted on the DIC images; left panel). Neurons are labeled with antibodies specific for synaptophysin (green), bassoon (red) and actin (blue). For each fluorescence image, the corresponding DIC channel is used to locate the beads (white arrows). In this preparation, 5 µm silica beads were coated with avidin and 0.1 mol% DSPE-PEG2000-biotin was used in the lipid mixture for tethering. Scale bars, 20 µm.

In order to determine if factors other than membrane heterogeneity and PE headgroups are in play, the effect of other membrane lipids (such as phosphatidylserine (PS) and cholesterol) in inducing synapse formation was examined. The fluorescence intensity analysis described earlier was performed on lipid mixtures containing PC and PS lipids. Similarly, the role of cholesterol was studied (representative images are shown in Experimental Section Fig. 3.10 and Fig. 3.11 and fluorescence intensity ratios are summarized in Table 3.1). Neither case showed an influence on presynapse formation at the lipid-neuron contact points. The quantification of synaptic and cytoskeletal protein levels around the SS-BLMs from the different lipid mixtures (*i.e.* PC, PE, PS and cholesterol), presented either in homogenous or heterogeneous lipid phases are summarized in Fig. 3.3 (see Experimental Section Table 3.1 for lipid composition and fluorescence ratio values). It is interesting to note that in the case of DOPC/DPPS and DPPC/DOPS, both exhibiting phase separation, there is an elevated actin assembly at the neuron/SS-BLM contact points but with no presynaptic protein accumulation. We therefore conclude from the data presented in Fig. 3.3 that lipid phase separation (more specifically, a fluid-gel phase separation) acts as an initial cue for neurons at the axon path-finding stage during artificial synapse formation. However, a combination of lipid phase separation together with headgroup specificity (*e.g.* PE) in SS-BLMs is the determining factor for transforming these contact sites into functional synaptic points. The question as to why PE headgroups are important in inducing presynaptic assembly requires more thorough investigation but it might be related to their local charge (cationic) or to the form of the membrane curvature that they induce.

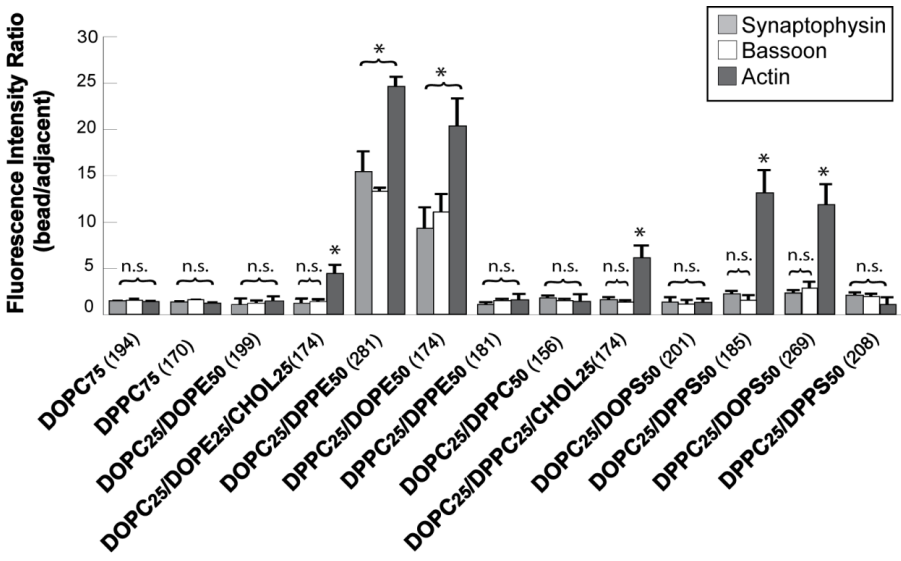

Figure 3.3 Histograms of fluorescence intensity ratio measurements comparing the accumulation of synaptic proteins (synaptophysin and bassoon) and cytoskeleton proteins (actin) in response to SS-BLMs prepared from various lipid mixtures. Each group was compared to uncoated beads, n.s. is not significant and * $p < 0.05$ by two-tailed Student's *t*-test after correction for non-equal variance. Values in the histograms are expressed as mean ± standard deviation. The total number of beads analyzed from three independent experiments is given in brackets. In all preparations, hippocampal neurons (DIV 22) were incubated with SS-BLMs for 24 hrs and then labeled with synaptophysin-, bassoon- and actin-specific antibodies. For SS-BLMs, 5 μm silica beads coated with avidin, were used as the solid spherical support, 25 mol% of the positively-charged lipid DOTAP was added to all mixtures and 0.1 mol% DSPE-PEG2000-biotin was used for tethering. Representative confocal images are presented in Figs. 3.2, 3.10 and 3.11.

3.5 Co-localization Analysis Demonstrates that Presynaptic Elements Favour Fluid Lipid Phases

The assembly of synaptic and cytoskeletal proteins around each of the co-existing lipid phases in the SS-BLM was assessed. A fluorescence co-localization analysis was carried out on dual-color images collected from neuron/SS-BLM co-cultures where the cells were immunolabeled for synaptophysin (green) and the SS-BLMs were derived from the synapse inducing lipid mixture DOPC/DPPE/DOTAP (25:50:25) where the ordered lipid domains (DPPE-rich) were labeled in red.

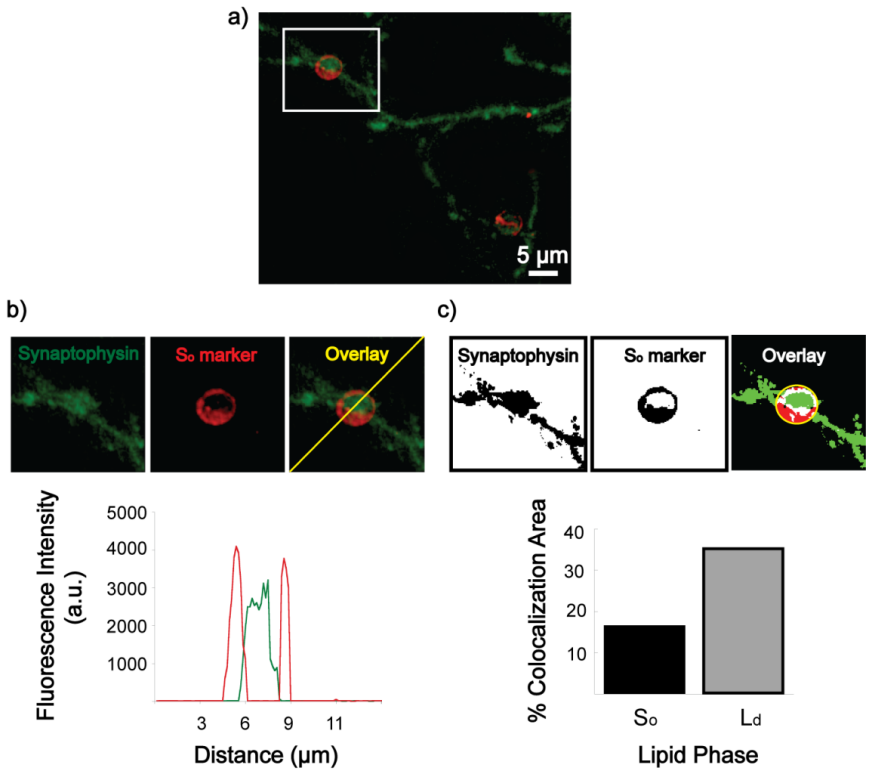

Figure 3.4 Representative images of a neuron/SS-BLM co-culture showing the steps involved in fluorescence co-localization analysis. (a) Confocal 3D-reconstruction image of rat hippocampal neurons (DIV 14) incubated for 24 hrs with SS-BLMs from the ternary mixture DOPC/DPPE/DOTAP (25:50:25) labeled using 0.1 mol% N-Rh-DHPE (red). A close-up on the area highlighted by the white box, which represents the area of the image used for subsequent analysis is shown in (b) as single channel images of the synaptic protein (synaptophysin, green) and ordered lipid phase (S_o, red). Binary images of the corresponding greyscale single channel images are shown in (c). Calculations of fluorescence co-localization from the overlay images by: (b) measuring the presence or absence of an overlap of fluorescence intensity profiles across the surface of the SS-BLM (along a defined line, shown in yellow) or (c) measuring the overlap area of fluorescent and non-fluorescent pixels (fluorescent protein pixels with fluorescent (S_o) or non-fluorescent (L_d) lipid pixels, shown in white or green, respectively).

Figure 3.4, panel (a) shows the merged fluorescence image for the synaptic protein (synaptophysin) and the gel phase domain. In order to evaluate their co-localization, the presence of an overlap in their respective fluorescence intensity profiles is examined. Panel (b) shows single fluorescence channels and corresponding fluorescence intensity profiles measured along a line that crosses the bead surface. As seen in the intensity profile (panel b), the absence of overlap between the green and red channels indicates the absence of co-localization between the synaptic protein synaptophysin (green) and the gel lipid domain (red), suggesting that the synaptic terminals are localized at the (non-labeled) fluid lipid domain. As outlined in panel (c),

the binary images (value of 1 for fluorescent pixels and value of 0 for non-fluorescent pixels) are used in this analysis. In this case, co-localization of the cellular proteins with the lipid phase is indicated by the presence of signal intensity (binary value of 1) from the two fluorescent labels in the same pixel. Within the field of view of the SS-BLM (roughly one-half of the sphere), different areas of pixel overlap (represented by different colors in the overlay image in panel (c)) are defined as: (*i*) white areas, which represent the labeled lipid domains (red) overlapping with the labeled synaptic protein (green), (*ii*) red areas, which represent the labeled lipid domains (red) not overlapping with the labeled synaptic protein (green), and (*iii*) green areas, which represent the non-labeled lipid domains overlapping with the labeled synaptic protein (green). Co-localization areas can be calculated as a fraction of the total bead area, according to the following equations:

$$\%\ \text{co-localization with } L_d = \frac{\text{area of overlap (defined by green area)}}{\text{total area of bead (defined by yellow circle)}} \times 100 \qquad \textbf{Equation 3.1}$$

$$\%\ \text{co-localization with } S_o = \frac{\text{area of overlap (defined by white area)}}{\text{total area of bead (defined by yellow circle)}} \times 100 \qquad \textbf{Equation 3.2}$$

This method was applied to analyze the co-localization between the different presynaptic proteins and lipid domains from mixtures containing PE lipids. Co-localization is expressed according to the following equation:

$$\text{Co-localization Ratio } \left({}^{L_d}/_{S_o}\right) = \frac{\%\ \text{Co-localization with } L_d}{\%\ \text{Co-localization with } S_o} \qquad \textbf{Equation 3.3}$$

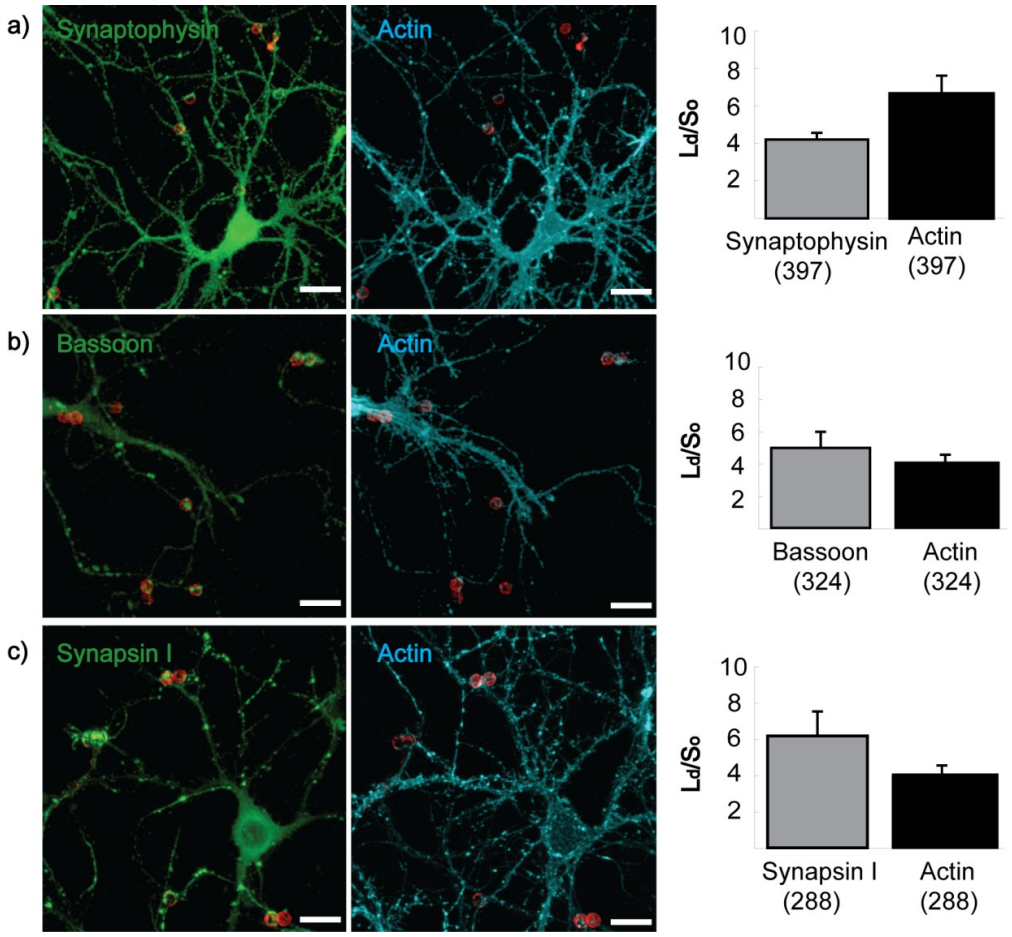

Figure 3.5 Co-localization of synaptic and cytoskeletal proteins with the lipid phases of SS-BLMs. (a) Representative confocal 3D-reconstruction images of rat hippocampal neurons (DIV 14) incubated for 24 hrs with SS-BLMs of the ternary mixture DOPC/DPPE/DOTAP (25/50/25) displaying fluid–gel (L_d–S_o) phase separation, with the ordered phases (DPPE-rich) labeled using 0.1 mol% N-Rh-DHPE (red). The neurons are labeled for synaptic proteins (green) using antibodies specific for (a) synaptophysin, (b) bassoon, and (c) synapsin I. The F-actin (blue) is labeled using phalloidin. Scale bars, 20 µm. Histograms of the L_d/S_o ratio are shown in the right panels and display the preferential co-localization of the synaptic proteins with the disordered lipid domains (L_d). Percent co-localization data, with either phase, are summarized in the Experimental Section Fig. 3.12 and calculated as described in Fig. 3.4. Histograms values are expressed as mean ± standard deviation. The total number of beads analyzed from three independent and identical experiments is given in brackets.

The quantitative analysis of co-localization (Fig 3.5) establishes that there is a significant preference for the accumulation of presynaptic components around fluid phase lipids. This is further confirmed by application of the Pearson Correlation Coefficient (PCC) methodology,[27] which measures the degree of co-localization between two fluorophores. PCC values generally range between +1 (a perfect co-localization) and -1 (an anti-correlation). The PCC value

calculated for the co-localization between the fluorescent proteins and the fluorescent lipid phase (*i.e.* gel phase) is < 0, indicating the absence of protein co-localization with the gel phase (see Experimental Section Fig. 3.13 for a summary of PCC results).

SS-BLMs are versatile model system for lipid rafts, and when interfaced to neurons in culture, yield new information regarding the initial steps of artificial synapse formation. In particular, new insight is developed regarding the chemical and physical properties of lipids that influence the neuronal response to artificial bilayer membranes when co-cultured with neurons under physiological conditions. The clustering of presynaptic proteins in the vicinity of SS-BLMs is evident from the presence of a synaptic vesicle protein (synaptophysin), a scaffolding active zone (bassoon), and the cytoskeletal protein (actin). The presence of these three proteins is considered as a positive neuronal response. Immunofluorescence quantification analysis shows that the interaction of neurons with SS-BLMs results in a significant enrichment of synaptophysin and bassoon at their contact sites. This is observed only when the lipids in SS-BLMs contain phosphatidylethanolamine (PE) headgroups and are in a lipid phase separated state. The presence of amino groups in SS-BLMs from other phospholipids such as phosphatidylserine (PS) did not yield the same results. This highlights the importance of both: (*i*) the structural details of the lipids (*i.e.* their functional groups, overall charge, intrinsic shape, curvature-inducing, *etc*.) and (*ii*) the cooperative and aggregative properties of the membrane (*i.e.* its physical organization and the presence of lateral heterogeneity) in lipid-induced artificial synapse formation.

Several studies have shown that a number of signaling molecules responsible for regulating neuronal processes are localized in membrane lipid rafts.[11] It has also been demonstrated that nerve growth cones respond to specific substrate surface features when allowed to grow on substrates with varying rheology. The rheological differences of membranes are due to the presence of lipid rafts that contain fluid phase and gel phase lipids.[26] Substrates with tunable surface properties have thus been shown to influence neuronal growth and synaptic processes. This study, on the other hand, addresses the question of how membrane phase influences neuronal differentiation and outgrowth. The data presented here establish that in forming functional synapses, neurons prefer the fluid phase within a lipid raft. Since the initial step in artificial synapse formation begins with axonal path-finding, *via* the actin cytoskeletal networks,[21, 28, 29] the cytoskeletal networks perhaps perform the "ground work" for the neurons to establish the first attachment points. However, these results clearly demonstrate that an

environment of lipid phase separation is not the only requirement, as some of these contact points do not necessarily develop into functional synapses. In order to achieve artificial synapses, additional parameters such as the headgroup specificity, overall charge and membrane curvature have to be taken into account.

3.6 Conclusions

In summary, fluid lipid phases within a raft model platform are found to mediate stable neuronal contact points on membrane substrates. This attachment step being the driving force, additional lipid properties are used to develop these contact points into functional synapses. Raft proteins or postsynaptic components are *not* necessary to establish these active synaptic sites. Given the importance of lipid rafts in cellular processes and cell signaling, the use of SS-BLM-based raft models is a step forward in the experimental study of raft-mediated biological events. Future experiments will involve SS-BLMs of increasing complexity by incorporating proteins and lipid/proteins complexes into the bilayer membrane, or by assembling the supported bilayer from native membrane vesicles. The robustness and ease of characterization which SS-BLMs offer will enable the study of the function of key lipids and proteins participating in artificial synapses or other cellular events that involve membrane-membrane interactions.

3.7 Experimental Information

3.7.1 Materials

1,2-dioleoyl-*sn*-glycero-3-phosphocholine (DOPC), 1,2-dioleoyl-*sn*-glycero-3-phosphoethanolamine (DOPE), 1,2-dioleoyl-*sn*-glycero-3-phospho-L-serine (sodium salt) (DOPS), 1,2-dioleoyl-3-trimethylammonium propane chloride salt (DOTAP), 1,2-dipalmitoyl-*sn*-glycero-3-phosphocholine (DPPC), 1,2-dipalmitoyl-*sn*-glycero-3-phosphoethanolamine (DPPE), 1,2-dipalmitoyl-sn-glycero-3-phospho-L-serine (sodium salt) (DPPS), and 1,2-distearoyl-sn-glycero-3-phosphatidylethanolamine-N-biotinyl-(polyethylene glycol 2000)] ammonium salt (DSPE-PEG2000-biotin) were purchased from Avanti Polar Lipids (purity >99%). Lissamine™ Rhodamine B 1,2-dihexadecanoyl-*sn*-glycero-3-phosphoethanolamine, triethylammonium salt (N-Rh-DHPE), secondary antibodies and Alexa-488/Alexa-647−phalloidin were purchased from Molecular Probes, Invitrogen (NY, USA). Poly-L-lysine

hydrobromide was purchased from Sigma (NY, USA). GelTol (aqueous mounting media) was purchased from Shandon Lipshaw Co., Lerner Labs (PA, USA). All other cell culture media were purchased from Gibco, Invitrogen (NY, USA).

3.7.2 Formation of SS-BLMs

SS-BLMs were prepared starting with lipid vesicles in the form of small unilamellar vesicles (SUVs). These were formed by mixing chloroform solutions of the lipids (1 mg/mL), and DSPE PEG2000-biotin (0.1 mol% of final mixture). The mixture was dried with a stream of nitrogen then under vacuum for several hours. The resulting lipid film was hydrated using phosphate buffer saline (PBS) at pH 7.4, which was warmed to a temperature higher than the phase transition temperatures (T_m) of the lipids. After vortex mixing (*ca.* 10 minutes) and sonication in a bath sonicator (*ca.* 5 minutes), the vesicles solution was used for the formation of SS-BLMs or stored at 4 ˚C. SS-BLMs were prepared as previously reported,[25] starting with a solution of 5 μm silica beads from Bangs Laboratories (IN, USA), which were washed by centrifugation (10^4 rpm for 10 minutes) and re-suspended at a concentration of 9×10^6 particles/mL in PBS. This solution was coated with avidin (0.1 mg/mL) and washed by centrifugation (3× at 10^4 rpm for 10 minutes) and re-suspension in PBS at the starting volume. The avidin-coated beads were then mixed with an equal volume of SUVs, and vortex mixed for at least 20 minutes. The resulting lipid-coated beads (*i.e.* SS-BLMs) were washed by centrifugation (3× at 7×10^3 rpm for 10 minutes) and re-suspension in PBS at the starting volume. Lipid phase separation in SS-BLMs was subsequently induced by the application of two successive heat/cool cycles starting at 4 ˚C and ending at 80 ˚C (at a controlled rate of 0.1 ˚C/second), using a TProfessional Thermocycler (Biometra; Göttingen, Germany).

3.7.3 Cell Culture

Low-density dissociated cell cultures from rat hippocampal neurons were prepared according to a modified protocol described by Banker.[30] Hippocampi were dissected from E17 embryos, treated with 0.25% (w/v) trypsin at 37 ˚C followed by Dulbecco's modified Eagle medium (DMEM) supplemented with 10% fetal bovine serum. They were then washed twice Hank's balanced salt solution (HBSS) followed by serum-free Neurobasal medium where they were mechanically dissociated with a glass Pasteur pipette. The dissociated neurons were plated at low

density (*ca.* 1.75×10^4 cm^{-1}) in serum-free Neurobasal medium supplemented with *l*-glutamine, penicillin, streptomycin and B-27 on glass coverslips from Ted Pella Inc. (CA, USA) previously coated with poly-L-lysine. The cell culture was kept in a humidified 5% CO_2 atmosphere at 37 ˚C and one-third of the medium was replaced every 3 days. All animal work was performed at the Montreal Neurological Institute in accordance with the Canadian Council of Animal Care Guidelines.

3.7.3 Neurons/SS-BLMs Co-cultures

SS-BLMs in sterile PBS solution at pH 7.4 were added dropwise to hippocampal neurons (cultured for at least 14 days *in vitro* (DIV)) at a concentration of *ca.* 1.0×10^5 beads/coverslip. After incubation for 24 hrs in a humidified 5% CO_2 atmosphere at 37 ˚C, the cells/SS-BLMs co-cultures were fixed using 4% (w/v) paraformaldehyde in phosphate buffer at pH 7.4, for 15 minutes and washed (3× with PBS). Immunofluorescence labeling was achieved by incubating the cells in blocking solution (PBS at pH = 7.4, containing 4% normal donkey serum (NDS) and 0.1% (w/v) saponin) for 30 min, followed by primary antibody solution (1:100 (v/v) rabbit anti-synaptophysin, 1:500 (v/v) mouse anti-bassoon and/or 1:500 (v/v) rabbit anti-synapsin I in PBS at pH 7.4 containing 0.1% (w/v) saponin and 0.5% (w/v) NDS) overnight at 4 ˚C. After washing (3× in PBS) the cells were incubated in secondary antibody solution (1:500 (v/v) antibodies coupled to Alexa-488, Alexa-543 or Alexa-647 (as appropriate) in PBS at pH 7.4 containing 0.5% (w/v) NDS) for 30 minutes, then washed (3× in PBS). For F-actin labeling, Alexa-488 or Alexa-647−phalloidin (as appropriate) were used (1:50 (v/v) in the secondary antibody solution). The immunolabeled samples were mounted on microscopic slides using GelTol and sealed prior to imaging.

3.7.4 Confocal Microscopy

Fixed samples were imaged using a LSM-710 confocal microscope (Carl Zeiss AG, Germany) with a 63x/1.4 oil-immersion objective lens. Image fields were first selected using the brightfield (*i.e.* differential interference contrast, DIC) channel. One (or a combination) of the following optical settings were then applied to acquire the fluorescence images: (*i*) λ_{ex} 488 nm/ λ_{em} LP > 505 nm (single channel imaging) or λ_{em} BP 505 − 550 nm (multi-channel imaging), (*ii*) λ_{ex} 543 nm/ λ_{em} LP > 565 nm, and (*iii*) λ_{ex} 633 nm/ λ_{em} LP > 685 nm. For multi-channel imaging,

sequential scanning was used. Laser power and detector gain were adjusted to avoid intensity saturation in all acquired images. Z-series image stacks were acquired at a sampling rate which satisfies the Nyquist frequency condition. The acquired image stacks were deconvolved using the blind deconvolution algorithm in AutoQuant X3 software. All images were subject to background subtraction and contrast enhancement (for presentation purposes only) using Imaris 7.4.0 software.

3.7.5 Fluorescence Intensity and Co-localization Quantification

Immunofluorescence and co-localization quantification were calculated using ImageJ software for at least 50 beads per experiment and averaged across 3 separate experiments per condition. Results are presented in histograms which are prepared in KaleidaGraph software and display the data mean and standard deviation. The significant difference between experiments is assessed using the two-tailed Student's *t*-test after correction for non-equal variance (see the Experimental Information Section 3.7.8 for details and equations of statistical analyses). For intensity quantification, the fluorescence ratio is calculated (using Image J software) from the average pixel overlap area values within an ROI at the SS-BLM location divided by that of another ROI of exactly the same size and located directly adjacent to the SS-BLM along the neuron (see the Experimental Section Fig. 3.7). For analyzing co-localization between synaptic and cytoskeletal proteins with lipid domains, the overlap of their respective fluorescence intensity signals across the surface of the SS-BLM was examined. Co-localization was analyzed quantitatively by calculating the area of overlap between the different fluorescence channels from their respective binary images. Additionally, pixel intensity correlation was performed using the co-localization plugin (Coloc 2) in ImageJ software which expressed the Pearson correlation coefficient (PCC) for the co-localization between the fluorescently labeled lipid domains (*i.e.* S_o domains) and fluorescently labeled proteins.

3.7.6 Fluorescence Visualization of Phase Separated Domains on PE-lipid SS-BLMs

As previously described, lipid phase separation in SS-BLMs can be visualized using confocal microscopy by using partitioning markers.[25] The lipid mixture DOPC/DPPE/DOTAP (25:50:25) displays fluid–gel lipid phase separation which can be visualized using the fluorescent lipid N-Rh-DHPE as it partitions into the ordered lipid domains (*i.e.* DPPE rich) as seen in Fig. 3.6.

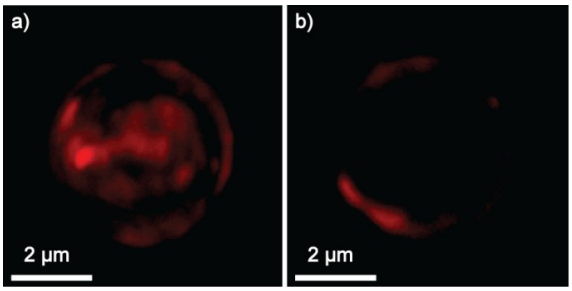

Figure 3.6 Lipid phase separation in PE-lipid SS-BLMs. (a) Representative confocal 3D reconstruction images and (b) corresponding cross-section of the ternary lipid mixture DOPC/DPPE/DOTAP (25:50:25), where the ordered domains (DPPE-rich) are labeled using 0.1 mol% N-Rh-DHPE (red). The fluid domains (DOPC-rich) are not labeled and therefore appear as dark areas in this image. In this preparation, 5 µm silica bead, coated with avidin, was used as the solid support and 0.1 mol% DSPE-PEG2000-biotin was added to the lipid mixture for tethering.

3.7.7 Fluorescence Ratio Analysis

In order that immunofluorescence quantification in a neuron/bead image field can be determined, the DIC channel is first used to locate the bead sites. Only beads interacting with neuron axons (and not cell bodies) are used for analyses. Using the ImageJ software, a circular region of interest (ROI) sized *ca.* 20% larger than the diameter of the bead is created. As a control, a second ROI of exactly the same size is created along the length of the neuron and placed immediately adjacent to the bead site (Fig. 3.7a). The fluorescence intensity ratio can then be calculated from the fluorescence overlap values calculated at the bead ROI and divided by that of the adjacent ROI. Fluorescence intensity values are measured directly from the grayscale image and range in value from 0 to 255 grey scale units. Such fluorescence intensity comparisons are only valid for ROIs that are part of the same sample, *e.g.* when comparing the fluorescence images collected from the same sample but at different time points. However, when comparing the fluorescence of two different samples, the pixel overlap area values rather than the intensity overlap values are used. These are derived from the binary image (Fig. 3.7b). The grayscale image is first subjected to the threshold function in ImageJ software, which converts all the fluorescence intensity values in the image into binary values (*i.e.* either 1 for fluorescent or 0 for not fluorescent pixels). From the resulting binary image the overlap area values within the ROI represent the fraction of overlapping pixels, in the corresponding greyscale image, irrespective of their relative intensity values (*i.e.* 1 − 255).

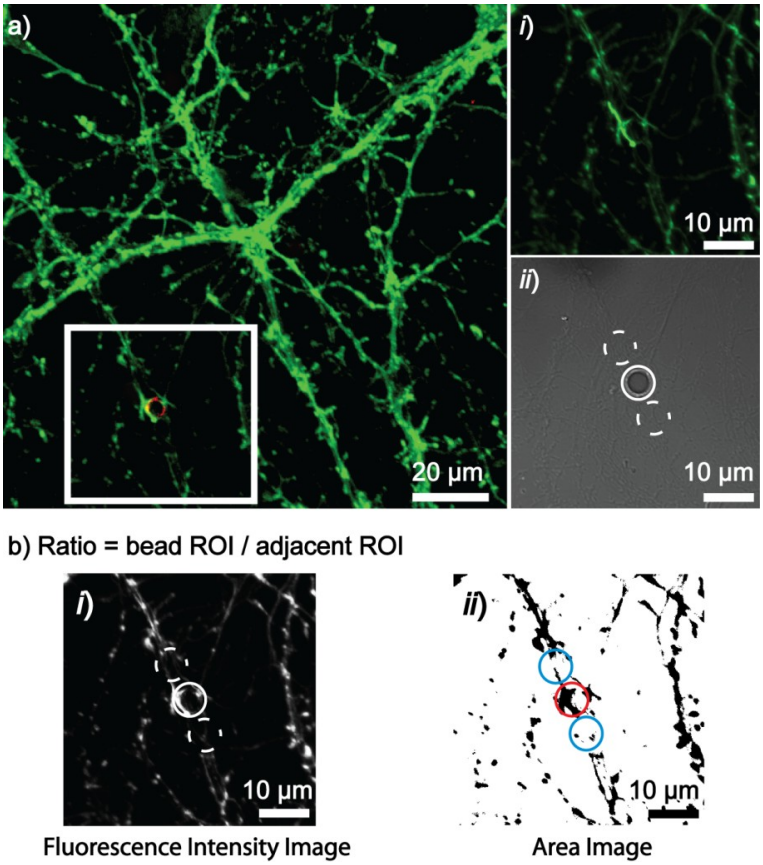

Figure 3.7 Representative image panels for a neuron/SS-BLM co-culture showing the steps involved in fluorescence analysis. (a) Image of rat hippocampal neurons (DIV 21) incubated for 24 hrs with SS-BLMs from the ternary mixture DOPC/DPPE/DOTAP (25:50:25) labeled using 0.1 mol% N-Rh-DHPE (red). A close-up on the area highlighted by the white box, which represents the field of the image used for subsequent analysis is shown in (*i*) as single channel image of the F-actin labeling (phalloidin; green) and in (*ii*) as DIC image with white circles at bead (solid) or adjacent (dashed) sites to be analyzed. (b) Subsequent determination of fluorescence ratios at the bead site compared to an adjacent site are calculated from either (*i*) fluorescence intensity values (greyscale of single-channel fluorescence image) or (*ii*) fraction of labeled pixels (threshold area image), within the solid circle (bead ROI) divided by dashed ones (adjacent ROI).

3.7.8 Accumulation of Synaptic and Cytoskeletal Proteins around Lipid-Coated Beads

The accumulation of proteins (*i.e.* synaptophysin, bassoon and actin) around lipid coated beads was examined using immunofluorescence. The intensity of labeled proteins in the vicinity of lipid-coated beads was analyzed quantitatively (as described in the Experimental Section 3.7.7). A statistical comparison to fluorescence intensity of the same proteins accumulated around uncoated beads was performed. The results indicate a significantly high expression of both

synaptic and cytoskeletal proteins around lipid-coated beads of the specified lipid composition (Fig. 3.8).

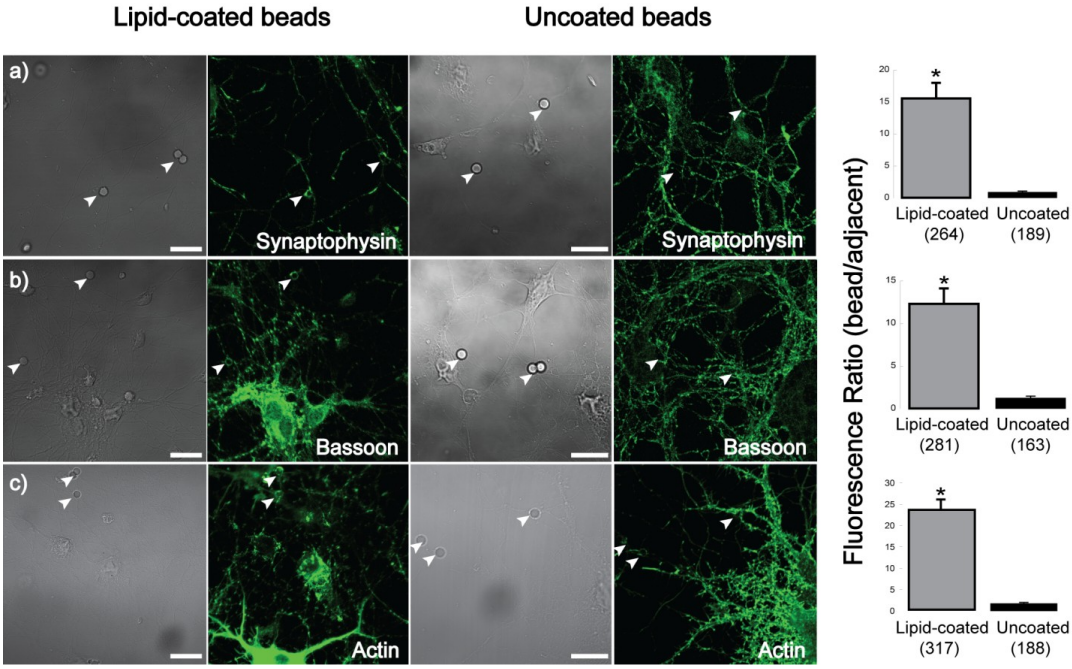

Figure 3.8 Expression of synaptic and cytoskeletal proteins around lipid-coated beads. Representative confocal cross section images of rat hippocampal neurons (DIV 21) incubated for 24 hrs with lipid-coated beads (left image panels) or uncoated beads (right image panels). The neurons are labeled (green) with antibodies for (a) synaptophysin, (b) bassoon, and (c) actin. For each fluorescence image, the corresponding DIC channel is shown on the left, to locate the beads (white arrows). In this preparation, SS-BLMs are from the lipid ternary mixture DOPC/DPPE/DOTAP (25/50/25), 5 µm silica beads, coated with avidin, were used as the solid spherical supports, and 0.1 mol% DSPE-PEG2000-biotin was added to the lipid mixture for tethering. Scale bars are 20 µm. Histograms of fluorescence ratio measurements are shown on the right where the expression of (a) synaptophysin, (b) bassoon, and (c) actin around lipid-coated beads is compared to that around uncoated beads (* $p < 0.05$ by the two-tailed Student's *t*-test after correction for non-equal variance). Values in the histograms are expressed as the mean ± standard deviation. Values in brackets are the total number of beads analyzed from three independent experiments.

3.7.9 Expression of Synaptic Protein around SS-BLMs as a Function of Lipid Phase Separation

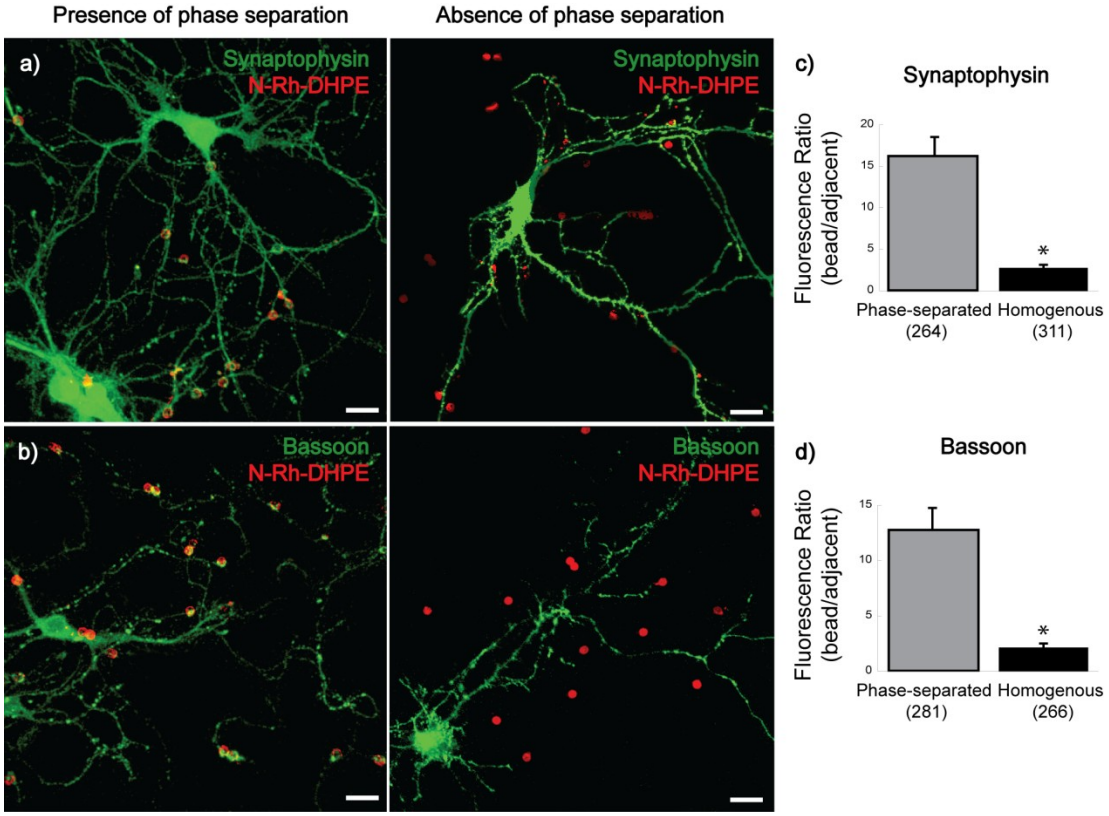

Figure 3.9 Expression of synaptic proteins around lipid-coated beads (*i.e.* SS-BLMs) as a function of the lipid phase separation phenomenon. Representative confocal 3D-reconstruction images of rat hippocampal neurons (DIV 21) incubated for 24 hrs with SS-BLMs displaying heterogeneous phases (DOPC/DPPE/DOTAP; 25/50/25) or homogenous phases (DOPC/DOPE/DOTAP; 25/50/25), where the lipid domains are labeled using 0.1 mol% N-Rh-DHPE (red). The neurons are labeled in green with antibodies for (a) synaptophysin and (b) bassoon. Scale bars are 20 µm. Histograms of the fluorescence ratio measurements comparing the expression of synaptic proteins in response to phase separation *versus* homogenous SS-BLMs are shown in (c) synaptophysin and (d) bassoon (* $p < 0.05$ by the two-tailed Student's *t*-test after correction for non-equal variance). Values in the histograms are expressed as the mean ± standard deviation. Values in brackets are the total number of beads analyzed from three independent experiments.

3.7.10 Accumulation of Synaptic and Cytoskeletal Proteins around SS-BLMs from Various Lipid Compositions (Containing PC and PS Lipids)

The following series of confocal fluorescence cross section images shows the accumulation of synaptic (*i.e.* synaptophysin and bassoon) and cytoskeletal (*i.e.* actin) proteins in the vicinity of SS-BLMs formed from lipid compositions that include phosphatidylserine (PS) headgroups. Immunofluorescence is analyzed quantitatively, as described in the Experimental Section 3.7.2. Histograms showing the quantification statistical analysis are given in Fig. 3.3.

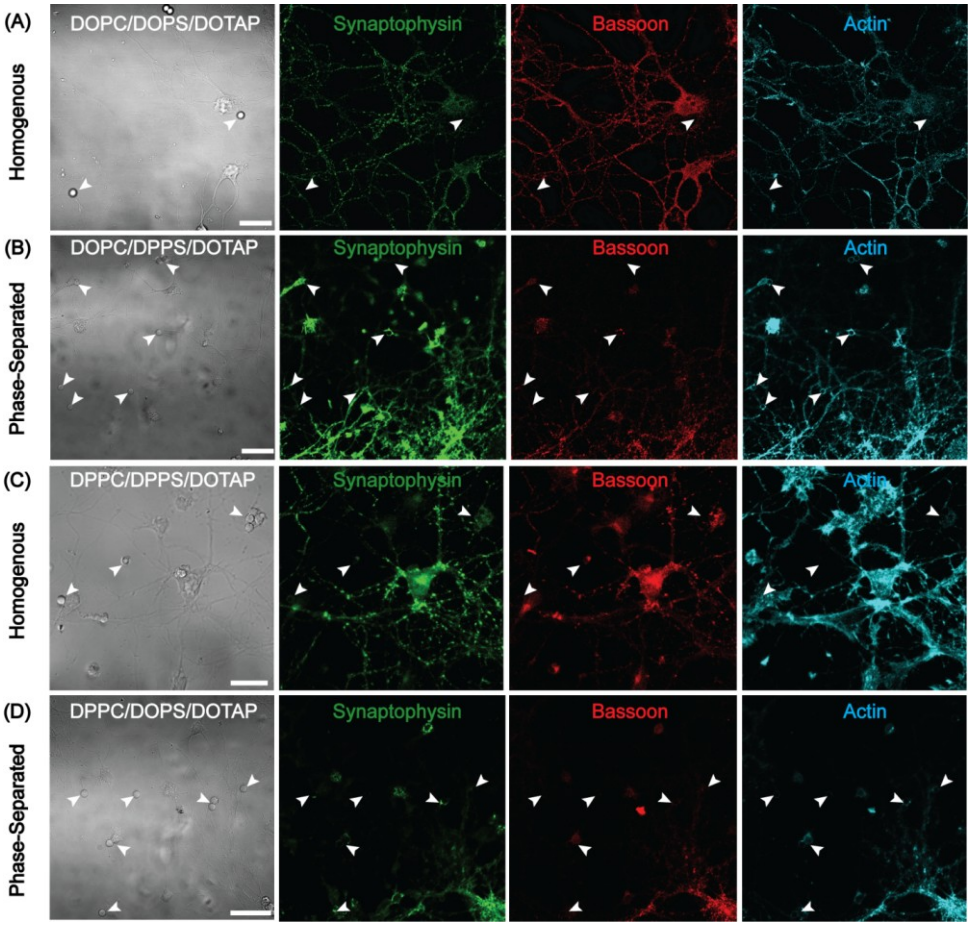

Figure 3.10 Representative confocal cross section images showing the accumulation of presynaptic proteins around SS-BLMs derived from various lipid mixtures with PC and PS headgroups. Rat hippocampal neurons (DIV 22) incubated for 24 hrs with SS-BLMs from different lipid mixtures, as noted in the left panel images (DIC). The neurons are labeled with antibodies specific for synaptophysin (green), bassoon (red), and actin (blue). For each fluorescence image, the corresponding DIC channel is used to locate the beads (white arrowheads). In this preparation, 5 μm silica beads, coated with avidin, were used as the solid support and 0.1 mol% DSPE-PEG2000-biotin was added to the lipid mixture for tethering. Scale bars are 20 μm.

3.7.11 Accumulation of Synaptic and Cytoskeletal Proteins around SS-BLMs from Various Cholesterol-Containing Lipid Compositions

The following series of confocal fluorescence cross section images shows the accumulation of synaptic (*i.e.* synaptophysin and bassoon) and cytoskeletal (*i.e.* actin) proteins in the vicinity of SS-BLMs formed from lipid compositions containing cholesterol. Immunofluorescence is analyzed quantitatively, as described in the Experimental Section 3.7.7. Histograms showing the quantification statistical analysis are given in Fig. 3.3.

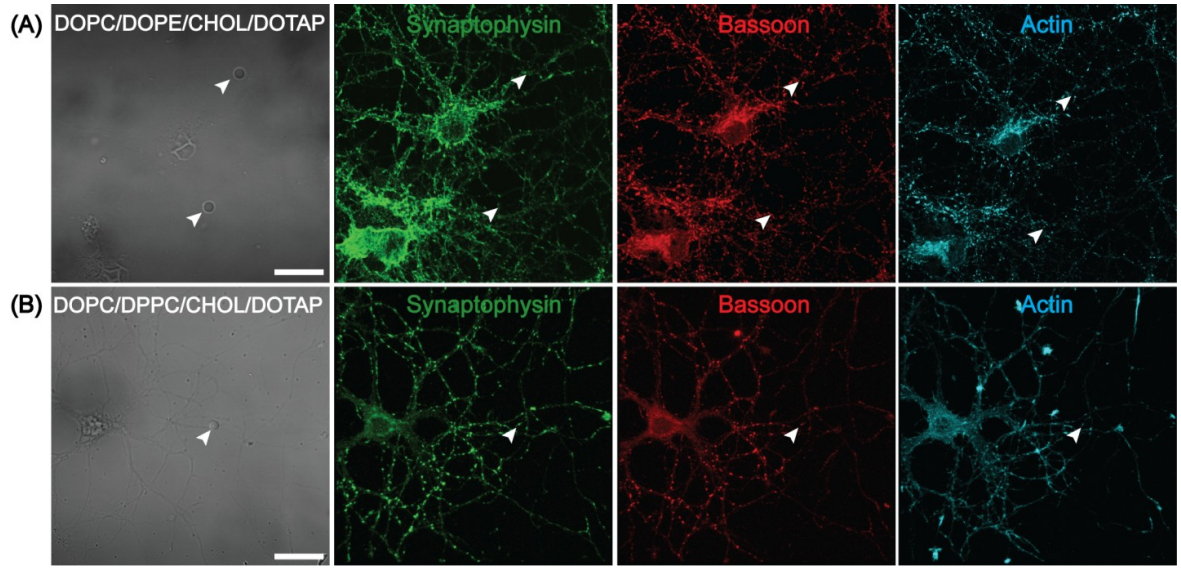

Figure 3.11 Representative confocal cross section images showing accumulation of presynaptic proteins around SS-BLMs derived from various lipid mixtures containing cholesterol. Rat hippocampal neurons (DIV 22) incubated for 24 hrs with SS-BLMs from different lipid mixtures, as noted in the DIC panel images on the left. The neurons are labeled with antibodies specific for synaptophysin (green), bassoon (red) and actin (blue). For each fluorescence image, the corresponding DIC channel is used to note the location of the beads (white arrowheads). In this preparation, 5 μm silica beads, coated with avidin, were used as the solid support and 0.1 mol% DSPE-PEG2000-biotin was added to the lipid mixture for tethering. Scale bars are 20 μm.

3.7.12 Summary of Fluorescence Intensity Ratio Data for Synaptic Proteins Accumulation in the Vicinity of SS-BLMs from Different Lipid Mixtures

Table 3.1 Fluorescence intensity ratio measurements of SS-BLM/neuron contacts. Summary of SS-BLM lipid compositions used for co-culture experiments and the corresponding fluorescence intensity ratio measured for the accumulation of synaptic proteins in their vicinity.

SS-BLM lipid composition	Fluorescence intensity ratio[a]		
	Synaptophysin	Bassoon	Actin
DOPC/DOTAP (75:25)	1.29±0.09	1.45±0.19	1.32±0.08
DPPC/DOTAP (75:25)	1.23±0.08	1.41±0.14	1.12±0.06
DOPC/DPPC/DOTAP (25:50:25)	1.83±0.21	1.26±0.18	1.43±0.78
DOPC/DPPC/CHOL/DOTAP (25:25:25:25)	1.06±0.65	1.36±0.26	6.15±1.26
DOPC/DOPE/DOTAP (25:50:25)	1.25±0.45	1.19±0.36	1.46±0.52
DOPC/DOPE/CHOL/DOTAP (25:25:25:25)	1.65±0.26	1.43±0.26	4.42±0.98
DOPC/DPPE/DOTAP (25:50:25)	15.26±2.3	11.65±1.8	24.35±1.30
DPPC/DOPE/DOTAP (25:50:25)	9.30±2.30	11.14±1.9	20.37±3.00
DPPC/DPPE/DOTAP (25:50:25)	1.15±0.31	1.51±0.23	1.65±0.62
DOPC/DOPS/DOTAP (25:50:25)	1.34±0.51	1.13±0.48	1.31±0.44
DOPC/DPPS/DOTAP (25:50:25)	2.26±0.37	1.56±0.56	12.99±2.60
DPPC/DOPS/DOTAP (25:50:25)	2.53±0.33	2.89±0.66	11.74±2.30
DPPC/DPPS/DOTAP (25:50:25)	2.13±0.26	1.96±0.25	1.13±0.81

[*a*] Errors cited are 1 SD about the mean, involving measurements for at least 150 beads from a total of 3 separate experiments. The exact number of beads analyzed is given in Fig. 3.4.

3.7.13 Summary of % Co-localization Area Data for Synaptic Proteins Preferential Accumulation around Specific Lipid Phases in SS-BLMs

The preferential expression of synaptic proteins (*i.e.* synaptophysin, bassoon and synapsin I) around one of the co-existing domains in SS-BLMs displaying lipid phase separation can be quantitatively evaluated by analyzing their fluorescence co-localization. Figure 3.12 summarizes the % co-localization area between each of the above mentioned proteins and lipid microdomains of SS-BLMs derived from the lipid mixture DOPC/DPPE/DOTAP (25:50:25). A statistical comparison of the co-localization with the gel *versus* the fluid lipid phases indicates a significantly higher preference of synaptic protein expression around the more fluid lipid phases (*i.e.* DOPC rich).

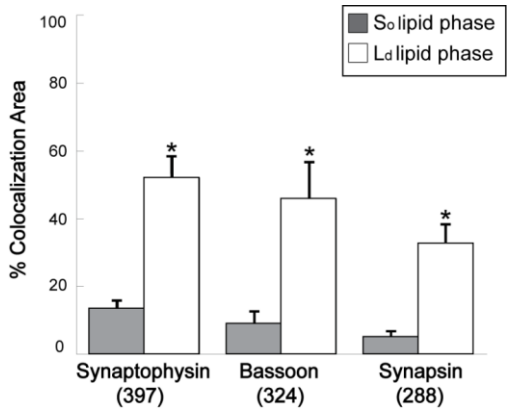

Figure 3.12 Histograms showing the % co-localization area between different synaptic markers and the co-existing L_o and L_d phases of SS-BLMs from the ternary mixture DOPC/DPPE/DOTAP (25:50:25) (* $p < 0.05$ by the two-tailed Student's *t*-test after correction for non-equal variance). Values in the histograms are expressed as mean ± standard deviation associated with the data. Brackets, total number of beads analyzed from at least three independent experiments. Analysis performed as described in Fig. 3.4. For these preparations, the neurons (DIV 14) are co-cultured with SS-BLMs for 24 hrs and then immunolabeled. SS-BLMs are labeled using 0.1 mol% N-Rh-DHPE, 5 μm silica beads coated with avidin were used as the solid support, and 0.1 mol% DSPE-PEG2000-biotin was added to the lipid mixture for tethering.

3.7.14 Summary of Pearson Correlation Coefficient (PCC) Values for the Co-localization of Synaptic Proteins with So Lipid Phases of SS-BLMs

Another method of co-localization analysis was applied to determine the preferential expression of synaptic proteins around the co-existing domains of SS-BLMs displaying lipid phase

separation. Using the plugin (Coloc 2) in ImageJ software, pixel intensity spatial correlation analysis was performed. From all the different co-localization parameters measured by this analysis, the PCC was chosen to express the fraction of co-localizing pixels between the fluorescent channels of the dual-color image in a neuron/SS-BLM co-culture experiment. In the experimental setup presented in this study, PCC is an estimate of the co-localization between the S_o lipid domains and the synaptic proteins, as these are the two fluorescently labeled components of the images. The coefficient is calculated as the ratio between the co-variance of the fluorescent channels and the product of their standard deviation, which is a significance test (r) for two channels (R; red and G; green) and is described by the following equation:

$$r = \frac{\sum_i (R_i - R_{avg}).(G_i - G_{avg})}{\sqrt{\sum_i (R_i - R_{avg})^2 . (G_i - G_{avg})^2}} \qquad \textbf{Equation 3.4}$$

where R_{avg} and G_{avg} are the averages of all the intensity values of both channels (R_i and G_i values), respectively.

This measure enables evaluation of the significance of true co-localization by calculating the probability that the measured value of (r) from the two fluorescent components is significantly greater than one calculated from a random overlap. In general, PCC > 0 indicates an evident overlay of structures, PCC ≈ 0 indicates randomly distributed objects, and PCC < 0 indicates segregated features (*i.e.*, anti-correlations). The PCC for the co-localization of different synaptic markers with the S_o lipid phase of SS-BLMs derived from the ternary mixture DOPC/DPPE/DOTAP (25:50:25) describes anti-correlation.

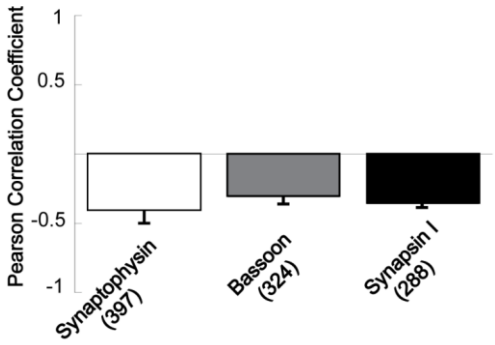

Figure 3.13 Pearson correlation coefficient values for the co-localization of different synaptic markers with the S_o lipid phase of SS-BLMs from the ternary mixture DOPC/DPPE/DOTAP (25:50:25). Values are expressed as the mean ± standard deviation associated with the data. Values in brackets are total number of beads analyzed from at least three independent experiments. For these preparations, the neurons (DIV 14) are co-cultured with SS-BLMs for 24 hrs and then immunolabeled, SS-BLMs are labeled using 0.1 mol% N-Rh-DHPE, 5 µm avidin-coated silica beads are used as the solid support and 0.1 mol% DSPE-PEG2000-biotin is added to the lipid mixture for tethering.

3.7.15 Statistical Analysis

Quantification analyses were performed using ImageJ software for at least 50 beads per experiment and averaged across 3 separate experiments per condition. Results were tabulated and presented in histograms using KaleidaGraph software. Histogram values represent the mean and standard deviation associated with the data. The significance difference between experiments was assessed using the two-tailed Student's *t*-test after correction for non-equal variance. The t-value is calculated according to Equations 3.5 and 3.6 and compared to the corresponding t-table value at the 95% confidence level.

$$t_{cal} = |M_1 - M_2| / \sqrt{s_1^2/n_1 + s_2^2/n_2} \qquad \textbf{Equation 3.5}$$

$$\text{Degrees of Freedom} = \frac{\left(s_1^2/n_1 + s_2^2/n_2\right)^2}{\left(s_1^2/n_1\right)^2/(n_1-1) + \left(s_2^2/n_2\right)^2/(n_2-1)} \qquad \textbf{Equation 3.6}$$

In the previous equations M is the mean value, n is the number of data points used to obtain the mean and s is the standard deviation of the data. When $t_{cal} > t_{table}$ then the difference is significant at the given confidence level. This is reported as the probability *p*-value being less than the significance level of 5% (*i.e.* $p < 0.05$).

3.8 References

1. Sebastiao, A. M.; Colino-Oliveira, M.; Assaife-Lopes, N.; Dias, R. B.; Ribeiro, J. A. Lipid rafts, synaptic transmission and plasticity: impact in age-related neurodegenerative diseases. *Neuropharmacology* **2013,** *64*, 97-107.

2. Lingwood, D.; Simons, K. Lipid rafts as a membrane-organizing principle. *Science* **2010,** *327*, 46-50.

3. Golub, T.; Wacha, S.; Caroni, P. Spatial and temporal control of signaling through lipid rafts. *Curr. Opin. Neurobiol.* **2004,** *14*, 542-550.

4. Kamiguchi, H. The region-specific activities of lipid rafts during axon growth and guidance. *J. Neurochem.* **2006,** *98*, 330-335.

5. Michel, V.; Bakovic, M. Lipid rafts in health and disease. *Biol. Cell.* **2007,** *99*, 129-140.

6. Paratcha, G.; Ibanez, C. F. Lipid rafts and the control of neurotrophic factor signaling in the nervous system: variations on a theme. *Curr. Opin. Neurobiol.* **2002,** *12*, 542-549.

7. Suzuki, T.; Yao, W.-D. Molecular and structural bases for postsynaptic signal processing: interaction between postsynaptic density and postsynaptic membrane rafts. *J. Neurorestoratol.* **2014,** *2014*, 1-14.

8. Lindner, R.; Naim, H. Y. Domains in biological membranes. *Exp. Cell. Res.* **2009,** *315*, 2871-2878.

9. Sonnino, S.; Prinetti, A. Membrane domains and the "lipid raft" concept. *Curr. Med. Chem.* **2013,** *20*, 4-21.

10. Simons, K.; Ikonen, E. Functional rafts in cell membranes. *Nature* **1997,** *387*, 569-572.

11. Simons, K.; Toomre, D. Lipid rafts and signal transduction. *Nat. Rev. Mol. Cell. Bio.* **2000,** *1*, 31-39.

12. Tillman, T. S.; Cascio, M. Effects of membrane lipids on ion channel structure and function. *Cell. Biochem. Biophys.* **2003,** *38*, 161-190.

13. Stetzkowski-Marden, F.; Recouvreur, M.; Camus, G.; Cartaud, A.; Marchand, S.; Cartaud, J. Rafts are required for acetylcholine receptor clustering. *J. Mol. Neurosci.* **2006,** *30*, 37-38.

14. Willmann, R.; Pun, S.; Stallmach, L.; Sadasivam, G.; Santos, A. F.; Caroni, P.; Fuhrer, C. Cholesterol and lipid microdomains stabilize the postsynapse at the neuromuscular junction. *Embo. J.* **2006,** *25*, 4050-4060.

15. Besshoh, S.; Chen, S.; Brown, I. R.; Gurd, J. W. Developmental changes in the association of NMDA receptors with lipid rafts. *J. Neurosci. Res.* **2007,** *85*, 1876-1883.

16. Huang, P.; Xu, W.; Yoon, S. I.; Chen, C. G.; Chong, P. L. G.; Liu-Chen, L. Y. Cholesterol reduction by methyl-beta-cyclodextrin attenuates the delta opioid receptor-mediated signaling in neuronal cells but enhances it in non-neuronal cells. *Biochem. Pharmacol.* **2007,** *73*, 534-549.

17. Korade, Z.; Kenworthy, A. K. Lipid rafts, cholesterol, and the brain. *Neuropharmacol.* **2008,** *55*, 1265-1273.

18. Sonnino, S.; Aureli, M.; Mauri, L.; Ciampa, M. G.; Prinetti, A. Membrane lipid domains in the nervous system. *Front. Biosci.* **2015,** *20*, 280-302.

19. Whitehead, S. N.; Gangaraju, S.; Aylsworth, A.; Hou, S. T. Membrane raft disruption results in neuritic retraction prior to neuronal death in cortical neurons. *Biosci. Trends.* **2012,** *6*, 183-191.

20. Sebastiao, A. M.; Colino-Oliveira, M.; Assaife-Lopes, N.; Dias, R. B.; Ribeiro, J. A. Lipid rafts, synaptic transmission and plasticity: impact in age-related neurodegenerative diseases. *Neuropharmacol.* **2013,** 97-107.

21. Lucido, A. L.; Gopalakrishnan, G.; Yam, P. T.; Colman, D. R.; Lennox, R. B. Isolation of functional presynaptic complexes from CNS neurons: a cell-free preparation for the study of presynaptic compartments *in vitro*. *ACS Chem. Neurosci.* **2010,** *1*, 535-541.

22. Lucido, A. L.; Sanchez, F. S.; Thostrup, P.; Kwiatkowski, A. V.; Leal-Ortiz, S.; Gopalakrishnan, G.; Liazoghli, D.; Belkaid, W.; Lennox, R. B.; Grutter, P.; Garner, C. C.; Colman, D. R. Rapid assembly of functional presynaptic boutons triggered by adhesive contacts. *J. Neurosci.* **2009,** *29*, 12449-12466.

23. Gopalakrishnan, G.; Thostrup, P.; Rouiller, I.; Lucido, A. L.; Belkaid, W.; Colman, D. R.; Lennox, R. B. Lipid bilayer membrane-triggered presynaptic vesicle assembly. *ACS Chem. Neurosci.* **2010,** *1*, 86-94.

24. Gopalakrishnan, G.; Yam, P. T.; Madwar, C.; Bostina, M.; Rouiller, I.; Colman, D. R.; Lennox, R. B. Label-free visualization of ultrastructural features of artificial synapses *via* cryo-EM. *ACS Chem. Neurosci.* **2011,** *2*, 700-704.

25. Madwar, C.; Gopalakrishnan, G.; Lennox, R. B. Interfacing living cells and spherically supported bilayer lipid membranes. *Langmuir* **2015,** *31*, 4704-4712.

26. Gupta, M.; Sarangi, B. R.; Deschamps, J.; Nematbakhsh, Y.; Callan-Jones, A.; Margadant, F.; Mege, R. M.; Lim, C. T.; Voituriez, R.; Ladoux, B. Adaptive rheology and ordering of cell cytoskeleton govern matrix rigidity sensing. *Nat. Commun.* **2015,** *6*, 7525.

27. Bewick, V.; Cheek, L.; Ball, J. Statistics review 7: correlation and regression. *Crit Care* **2003,** *7*, 451-459.

28. Doherty, G. J.; McMahon, H. T. Mediation, modulation, and consequences of membrane-cytoskeleton interactions. *Annu. Rev. Biophys.* **2008,** *37*, 65-95.

29. Janmey, P. A. The cytoskeleton and cell signaling: component localization and mechanical coupling. *Physiol. rev.* **1998,** *78*, 763-81.

Linking Statement to Chapter 4

Chapter 3 demonstrated the use of bilayer membranes formed on spherical supports (*i.e.* SS-BLMs) in the promotion of functional synaptic connections at artificial substrates. Chapter 4 presents research that extends the SS-BLM platform to 2-dimensional curvature geometry (*i.e.* fibers). Our particular interest in the fiber geometry relates to the potential development of optical fiber synaptic sensors that detect the formation of synapses and optically transmit this information from one neuron to another spatially distant neuron. The design of materials that are capable of transmitting neuronal electrical and/or chemical signals is a crucial functionality of artificial neuronal interfaces.

Cellular (and specifically neuronal) responses to artificial interfaces is mediated by chemical cues (surface composition) and physical cues (elasticity, topography and curvature). The research presented in the following Chapter uses glass fibers with a range of dimensions (lengths, diameter and curl), in order to address the relative importance of substrate shape and curvature in promoting *in vitro* synaptic responses. The coating of glass fibers with lipid bilayer membranes is described and examined using fluoresence techniques. The suitability of glass fiber-coated bilayer lipid membranes (GF-BLMs) in co-culture experiments with neurons is examined over extended periods of time. Developing functional neuronal interfaces based on GF-BLMs positions them as axonal-surface mimics in that they induce artificial synaptic responses.

Chapter 4

Micron-Scale Glass Fiber Supported Lipid Membranes as Functional Biomimetic Materials for Neuroengineering Applications

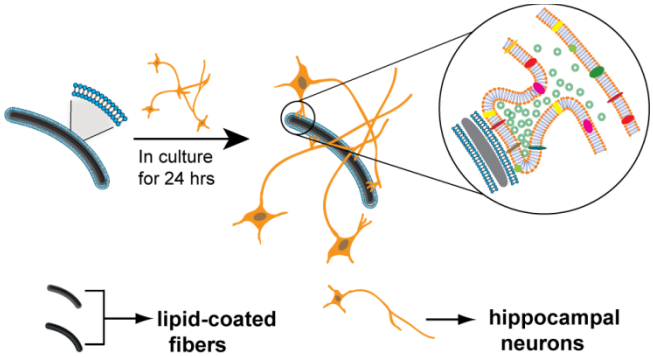

The text of this Chapter will be submitted to *Advanced Functional Materials* as "Micron-Scale Glass Fiber Supported Lipid Membranes as Functional Biomimetic Materials for Neuroengineering Applications", C. Madwar and R. B. Lennox. The text below is a verbatim copy of the manuscript.

4.1 Abstract

Damage to the central nervous system (CNS) is a significant cause of permanent disability in mammals.[1] Unfortunately, endogenous nerve repair is observed to be a slow and problematic process.[2] This deficit, coupled with there being few successful neuroregenerative strategies reported to date,[2, 3] has inspired new approaches that could improve these outcomes. An example of such an approach includes engineered materials that promote neuronal regeneration. It has been shown that the shape and surface chemistry of these materials are important features of a practical design. We recently reported the use of spherically supported bilayer lipid membranes (SS-BLMs) to demonstrate their suitability in promoting functional synapse formation.[4, 5] These serve as robust artificial membrane mimics of the chemical and physical environment provided by the cell membrane. Extensive evidence established that they induce the formation of artificial synapses *in vitro*. In the present study, we extend this approach to fabricate glass fibers coated with bilayer lipid membranes (GF-BLMs). The development of artificial neuronal interfaces based on the fiber geometry enables development of optical fiber neuronal sensors. In this regard, optical fibers can serve as materials that are capable of communicating neuronal electrical and/or chemical signals, which is crucial for improving the functionality of artificial neuronal interfaces. In order to determine if materials exhibiting 2D curvature (*i.e.* fibers) are suitable as functional neuronal interfaces, we have studied glass fibers of varying dimensions (lengths, diameter and curl). The relative importance of substrate geometry, shape and curvature in promoting artificial synapse formation is thus determined. The fabricated GF-BLMs are characterized using fluorescence recovery after photobleaching (FRAP). The diffusion properties of the component lipids are found to be comparable to those of comparable lipid bilayer model systems. Conventional immunostaining and confocal fluorescence imaging are used to observe neurite outgrowth and synapse formation at the neuron/GF-BLMs contacts. GF-BLMs were observed to induce the accumulation of presynaptic vesicles when they have been co-cultured with rat hippocampal neurons. These artificial connections are stable for up to 7 days *in vitro*. The results of this work suggest that bilayer membranes assembled on glass fibers can be used as neuron-mimicking bridging substrates that enhance outgrowth and regeneration, and potentially include optical links that will allow for the detection and transmission of artificial neuronal signals.

4.2 Introduction

The central nervous system (CNS) has a limited capability to spontaneously repair following traumatic injury or disease. Novel methodologies are thus required to treat CNS injury, facilitate its regeneration, and promote its functional recovery.[1, 2] Interfacing engineered functional materials with living neuronal tissue is at the forefront of neuroengineering. In particular, attempts to bridge damaged areas of the brain and induce synaptogenesis onto these artificial structures are sought.[3] Diverse chemical and physical cues related to the surface chemistry, shape and size of such materials can influence neuronal communication and synapse formation onto them by regulating axonal guidance[6, 7, 8, 9, 10, 11] and neurite outgrowth,[12, 13] their contact and attachment, and the survival of these artificial connections into functional synapses releasing information-containing synaptic vesicles.[14, 15] An understanding of the relative importance of physical design parameters is thus required. These parameters include geometry, curvature and length. We have previously demonstrated the application of micrometer-sized spherical substrates (silica beads) coated either with synthetic polypeptides[16, 17, 18] or lipid bilayer membranes[4, 5, 19] as artificial substrates that both promote neuronal adhesion and induce the formation of functional presynapses *in vitro*. These studies established that artificial synapse formation is dependent on certain signaling events that occur only in the presence of specific chemical and physical molecular elements present on the artificial substrate.[4, 5] In addition, the spherical 3D curvature of the substrate was demonstrated to be more effective at promoting neuronal networks in comparison to planar 2D surfaces. Our interest in exploring *in vitro* synapse formation on substrates with 2D curvature (*i.e.* fibers) have led us to examine the potential of bilayer membranes supported directly or tethered onto glass fibers as artificial interfaces that promote functional neuronal networks. Extension of the 3D curvature (beads) approach to 2D (fibers) enables an understanding of the role played by both the surface chemical and physical composition and also the nature of the substrate's surface curvature. More importantly, the ability to use functional neuronal interfaces based on fiber geometry sets the groundwork for designing neuronal optical fiber sensors. Specifically, a (silica) optical fiber can in principle be modified so that the measured property (*i.e.* chemical and/or electrical neuronal signals) modulates the light propagation through the fiber in terms of intensity, phase, polarization, wavelength or transit time. Light propagation through the optical fiber can therefore

yield an optical read-out of formed synapses as well as transmit information optically from presynaptic neurons to remote postsynaptic neurons interrupted by damage.

In this work, the neuronal responses to glass fibers coated with either poly-D-lysine (PDL) or lipid bilayer membranes within an *in vitro* dynamic co-culture environment are compared. The stability of the artificial connections under physiological conditions and for prolonged time periods was assessed in order to determine the suitability of these substrates in neuroengineering applications.

4.3 The Formation of Glass Fiber-Coated Bilayer Lipid Membranes (GF-BLMs)

The preparation of fiber-coated lipid bilayer membranes (GF-BLMs) used in the experiments described here is schematically represented in Fig. 4.1A. A previously described procedure[20] for the formation of fibers involving 'shattering' glass fiber filters was used. As seen in Fig. 4.1D the resulting fibers range from 0.5 to 2.0 μm in diameter with an average length of approximately 35 μm. In this preparation, the fiber diameter is controlled by the grade of the starting filters. The length distribution is varied by adjusting the vortexing and sonication time that is used to shatter the filter. Figures 4.1B and 4.1C are representative confocal images showing bilayer membranes coated on fibers obtained from different preparations (see the Experimental Section Fig. 4.5 for additional representative confocal images). DOPC and DPPE were used to demonstrate the coating of glass fibers with either fluid phase (DOPC) or gel phase (DPPE) lipid bilayers. In addition, the use of the previously-reported biotin-avidin tethering method[21] allowed coating the glass fibers with bilayers from mixed lipids which organize in different phases or have different geometries (see the Experimental Section 4.7.3 for a detailed description of the tethering protocol).Figures 4.1B and 4.1C show the fluorescence results from doping the bilayer membrane with 0.1 mol% of Bodipy-PC and N-Rh-DHPE, respectively. This enables observing the formation of the bilayer membrane, which appears to be uniform across different preparations.

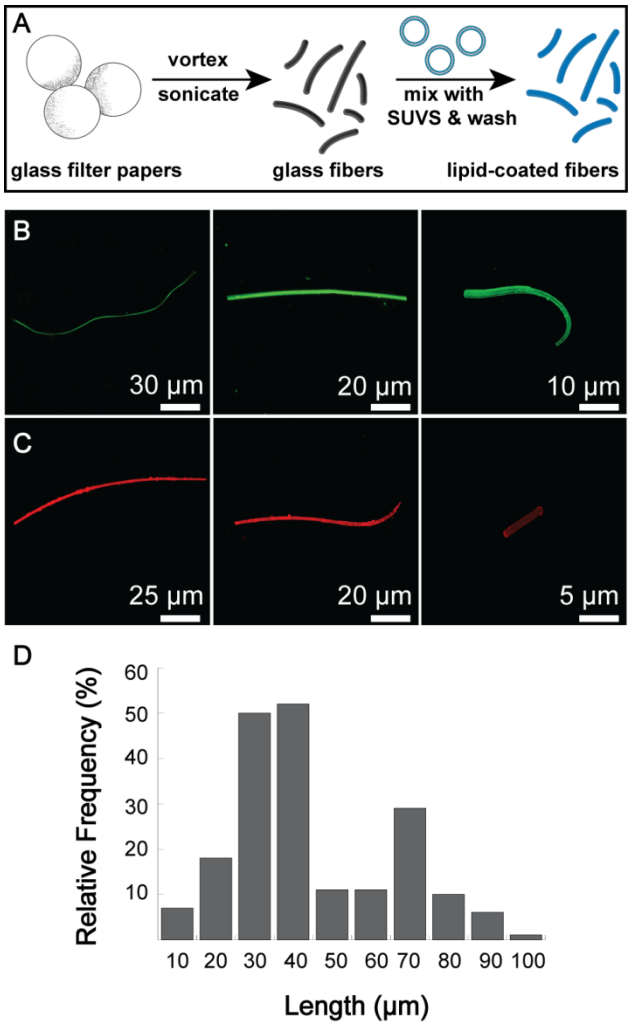

Figure 4.1 The fabrication of glass fiber-coated bilayer lipid membranes (GF-BLM). (A) Scheme illustrating the experimental steps leading to GF-BLMs starting from Whatman GF/A glass microfiber filters. (B) & (C) Confocal fluorescence images of GF-BLMs from DOPC labeled with 0.1 mol% Bodipy-PC and DPPE labeled with 0.1 mol% N-Rh-DHPE, respectively. (D) Histogram displaying the length distribution of fibers formed from shattered glass fiber filters.

4.4 Assessing the Fluidity of GF-BLMs

The use of fluorescent lipids further allowed examination of the diffusion properties of supported as well as tethered bilayer membranes and assessment of the effect of the fiber support on their fluidity. By using the fluorescence recovery after photobleaching (FRAP) technique, the lateral diffusion of the lipid molecules in both supported and tethered bilayers was characterized. Typically, the experiment proceeds by applying a short pulse of intense laser light, which irreversibly quenches the fluorescence (by photobleaching) within a defined area. Recovery of

the fluorescence within the photobleached area can occur as a result of diffusional exchange with fluorescent molecules from the surrounding non-bleached areas. In the experimental set-up used here, fluorescent images of the photobleached area were recorded after photobleaching using low intensity laser illumination every 247 ms (representative data shown in Fig. 4.2; see the Experimental Section 4.7.3 for detailed procedure). The fractions of mobile and immobile lipid molecules were calculated from the fluorescence recovery data by comparing the average fluorescence intensity, collected from the entire bleached area at the beginning, to that at the end of the recovery period. As summarized in Table 4.1, the diffusion properties indicate that the lipid bilayers, whether supported or tethered on the glass fibers, remain fluid and maintain their integrity.

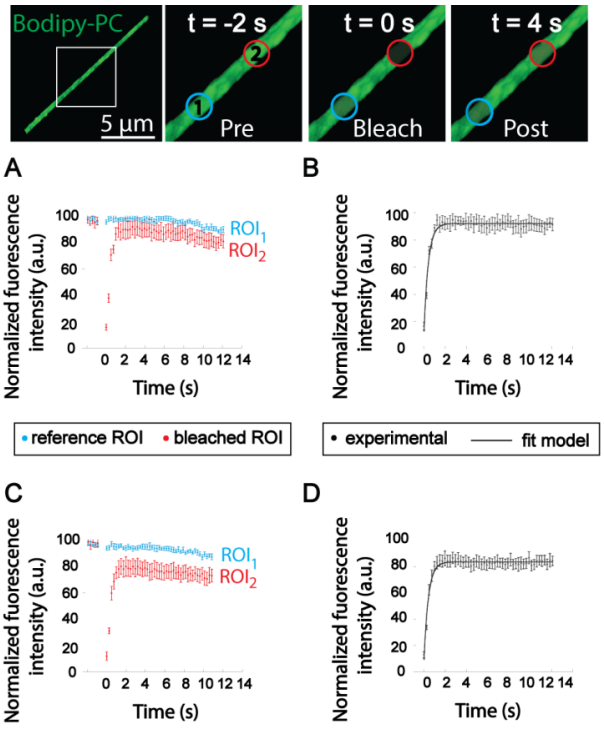

Figure 4.2 Summary of FRAP results. A series of confocal fluorescence images (top panel) as a function of pre- and post-bleaching time of Bodipy-PC labeled DOPC bilayers on glass fibers. The corresponding normalized fluorescence intensity plots for the bleached region of interest (ROI) is shown in red and the reference ROI in blue, display data as an average of 30 separate experiments where the bilayers are either directly supported (A) or tethered (C) using 0.1 mol% DSPE-PEG2000-biotin. Using the reference fluorescence data, the recovery was further corrected for bleaching occurring during imaging. This corrected data was then fit to a model involving a single diffusing component as shown in (B) for supported and (D) for tethered bilayers. In all plots, error bars reflect the standard deviation of 30 measurements. The extracted diffusion properties are summarized in Table 4.1.

Table 4.1 summarizes the FRAP data highlighting the diffusivity of the lipids in the fiber-supported and tethered bilayers. The recovery half-time and diffusion coefficient were determined by fitting the recovery experimental data to a theoretical model describing a single diffusing species.[22] The diffusion coefficient measured for the fiber-supported lipid bilayer system (0.784 $\mu m^2/s$) is virtually identical to the one measured for the tethered system (0.778 $\mu m^2/s$) indicating that the avidin-biotin tethering does not affect the lateral mobility of the lipids, and by inference, the fluidity of the membrane. However, a decrease of *ca.* 9% in the mobile lipid population was calculated in the case of the tethered system. This can be attributed to the presence of the biotinylated tethering polymer (*i.e.* DSPE-PEG2000-biotin), as it is expected to strongly bind to the avidin-coated fibers and therefore might limit the diffusivity of the lipid molecules. Nevertheless, the data measured in either system is in close agreement to previous reports of related systems (values of 1 – 2.5 $\mu m^2/s$,[23, 24, 25, 26, 27, 28] were reported for planar glass supported bilayers with similar lipid compositions and 0.4 – 1.0 $\mu m^2/s$ for silica-coated nanofiber supported bilayers).[29] These agreements further confirm the quality of the prepared membranes.

Table 4.1 Diffusion properties of fiber-supported and tethered lipid bilayers.

Lipid system	Recovery half-time τ (s)[b]	Diffusion constant D ($\mu m^2/s$)[c]	Mobile fraction (%)
Supported bilayers[a]	0.411	0.784	91.9
Tethered bilayers[a]	0.415	0.778	83.3

[a] lipid mixture composed of DOPC labeled using 0.1 mol% Bodipy-PC and [b] tethered using 0.1 mol% DSPE-PEG2000-biotin

[b] The measured values are based on examining multiple fibers from the same sample and during the same experimental set-up. This contributes to additional precision in the resulting data.

[c] The curvature of the fiber surface supporting the lipid bilayers was not accounted for in the calculations and only an apparent diffusion coefficient (for comparative purposes) was estimated from the experimental fluorescence recovery half-time using the equation, $D \geq 0.224.w^2/\tau$ (as previously explained in Section 2.5).

4.5 Co-cultures of GF-BLMs with Hippocampal Neurons

The use of GF-BLMs as artificial substrates for promoting *in vitro* synaptic responses upon contact with live neurons was addressed. In a typical protocol, bilayer membranes were tethered on glass fibers (as described earlier and under sterile conditions) and then co-cultured with hippocampal neurons from rat embryonic brains grown to at least 14 days *in vitro* (DIV). The co-cultures were fixed after a period of 24 hrs, 3 days, or 7 days and fluorescently labeled for confocal microscopy imaging. Neuronal interactions with the artificial bilayer membrane are visualized by labeling the actin cytoskeleton of the cells. Additionally, the formation of synapses at the neuron/fiber contact is examined by labeling of the synaptic vesicle protein synaptophysin. Fiber-coated lipid bilayers composed of the ternary lipid mixture DOPC/DPPE/DOTAP (25:50:25) were used in the present study for the co-culture experiments. Our previous studies have shown that the cationic lipid DOTAP promotes adhesion of neuronal cells to synthetic lipid membranes supported on spherical substrates[4] by electrostatic interactions, and that the use of PC and PE in an environment exhibiting lipid phase separation enhances the accumulation of synaptic proteins in their vicinity.[4, 5] Similar effects were reported for cationic polypeptides adsorbed onto spherical supports,[17, 30] particularly poly-D-lysine (PDL), the common coating agent for tissue culture dishes primarily used to promote cell adhesion.[17] PDL-coatings were also assessed in the fiber system (see the Experimental Section 4.7.2 for a description of the coating procedure and Fig. 4.7 for microscopy images). In order to assess the response of neurons to the coated fibers, examination using confocal imaging was carried out on neuron/fiber co-cultures that were immunofluorescently labeled for the synaptic vesicle protein synaptophysin. A co-stain for the cytoskeletal protein actin was also used, as actin influences relevant synaptic processes, such as axonal path-finding and synaptic vesicle trafficking.[31, 32, 33] Figure 4.3 clearly shows that the actin filaments (panels b, d and h) approach and contact the lipid-coated fiber with enhancement of the synaptophysin fluorescence (panels c, f and i) at the fiber/neuron contact points. A distribution of the lengths and widths of fibers, ranging from a few hundred nanometers and in some cases reaching several microns, is observed (Fig. 4.3). This does not appear to affect the adhesion of the neurons or their synaptic response and outgrowth. Similar results were observed for PDL-coated fibers (see Experimental Section Fig. 4.8). These observations are in good agreement with our earlier studies showing that spherical supports coated either with PDL or with synthetic lipid bilayers can induce the accumulation of

presynaptic vesicles when co-cultured with hippocampal neurons.[4, 5, 17] Fibers are therefore promising candidates for further studies in our search for artificial synapse-compliant materials.

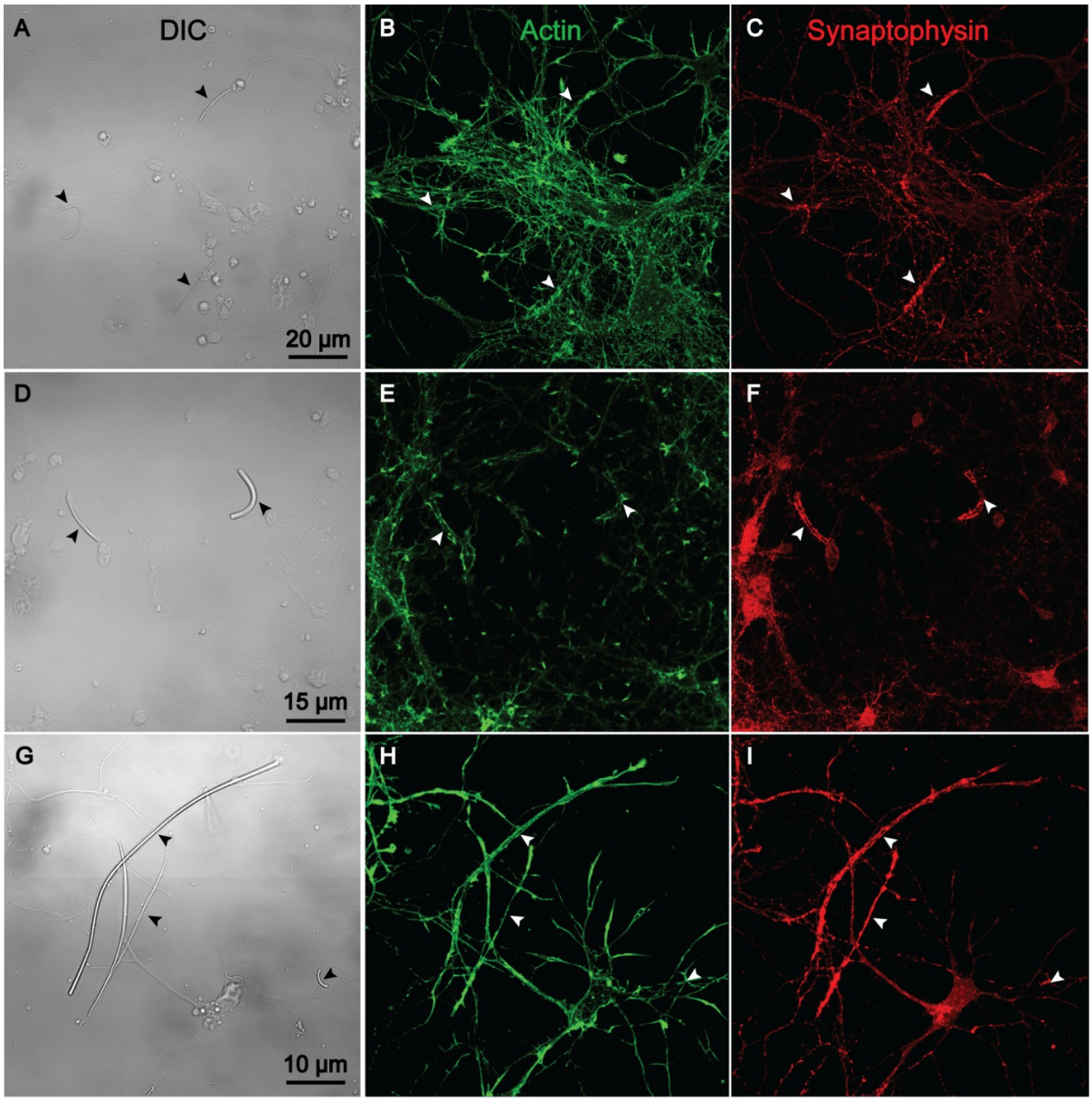

Figure 4.3 Interactions between hippocampal neurons and GF-BLMs. Representative diffusion interference contrast (DIC) (a, d & g) and corresponding confocal fluorescence images of rat hippocampal neurons (DIV 14) incubated for 24 hrs with GF-BLMs formed from tethered DOPC/DPPE/DOTAP (25:50:25) membranes. The neurons are immunolabeled with antibodies for actin (b, e & h; green) and synaptophysin (c, f & i; red). The DIC images are used to locate the fibers as indicated by the arrows. In this preparation, the glass fibers are first coated with avidin and then mixed with lipid vesicles containing 0.1 mol% DSPE-PEG2000-biotin for tethering.

A quantitative analysis enables further evaluation of the use of lipid coated-fibers as materials for neuronal interfaces. Specifically, the intensity of fluorescent synaptic proteins accumulated in the vicinity of fibers was measured over prolonged time periods in culture (see the Experimental Section 4.7.7 and Fig. 4.5 for details). As mentioned earlier, the coated fibers were co-cultured with hippocampal neurons for up to 7 DIV and were then fixed and immunofluorescently labeled (see Experimental Section Figs. 4.8 and 4.9 for representative confocal fluorescence images of co-cultures fixed at 3 and 7 DIV). The fluorescence images were then subjected to a quantitative analysis. A time-course evaluation where the fluorescence intensity of synaptophysin was measured in the vicinity of coated fibers in comparison to adjacent regions along the neurons. This analysis allows the quality and stability of the surface coating as well as the resulting artificial presynapses formed at the fiber/neuron contacts to be assessed with co-culture time under physiological conditions. The results for PDL- as well as lipid-coated fibers are summarized in Fig. 4.4 as histograms displaying the fluorescence intensity ratios at various co-culture times. Clear enhanced synaptophysin fluorescence is measured at the fiber/neuron contact points, indicating the accumulation of synaptic vesicles in these areas (Fig. 4.4c). However, this effect is significantly decreased as the time of co-culture increases, but only in the PDL case. On the other hand, those coated with lipid bilayers display continuously enhanced synaptophysin fluorescence in their vicinity. This indicates that substrate-supported lipid bilayers are more stable surface coatings compared to PDL under physiological conditions, and are therefore more advantageous for long-term neuronal interfacial co-culture studies.

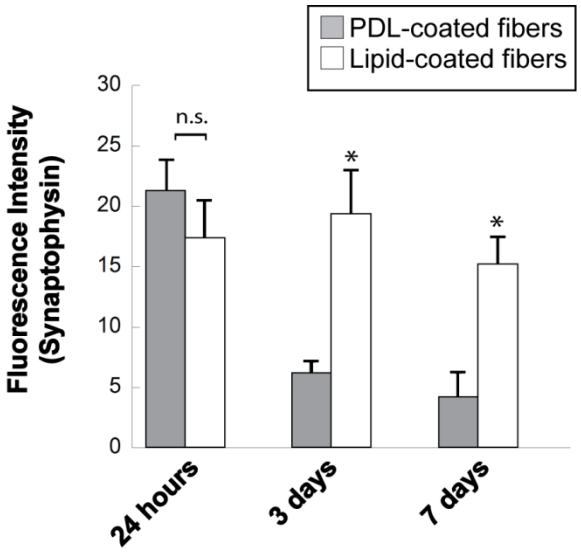

Figure 4.4 Histograms of fluorescence intensity ratio measurements comparing the accumulation of synaptophysin in response to glass fibers that are either coated with PDL or lipid bilayers. The extent of statistical significance between the two groups (n.s. is not significant and * is $p < 0.05$) is assessed by the two-tailed Student's *t*-test after correction for non-equal variance. Values in the histograms are expressed as mean ± standard deviation associated with data extracted from at least 50 coated fibers analyzed from three independent co-culture experiments. In these preparations, hippocampal neurons (DIV 14) were incubated with coated fibers for 24 hrs, 3 days or 7 days and then labeled with antibodies for synaptophysin. The bilayer-coated fibers are formed from DOPC/DPPE/DOTAP (25:50:25) and tethered onto avidin coated fibers using 0.1 mol% DSPE-PEG2000-biotin. Representative confocal images for these co-cultures are shown in Figs. 4.3, 4.8 and 4.9.

4.6 Conclusions

The results presented herein add to a growing body of knowledge that demonstrates how substrate-supported lipid bilayers provide a unique system for developing biomimetic platforms that are especially attractive as cellular interfaces.[19, 35] This is mainly because lipid bilayers are membrane-mimetic surfaces that are also stable under physiological conditions when supported on solid substrates.[36, 21, 37, 38] The fiber substrate geometry used in this study is a further step in creating artificial matrices suitable for neuronal growth applications as they mimic axon surfaces, not only in terms of physical shape but also surface chemistry, given the compositional tunability of the lipid bilayer membrane. In addition, demonstrating the applicability of fiber geometry as a synapse-inducing neural interface is promising for designing neural sensors based on optical fibers.

In this study, we have demonstrated the advantages of using lipid bilayers supported or tethered on glass fibers to promote adhesion and outgrowth of neurons in long term cell culture. The methods presented herein allow addressing the dimension and shape of fiber substrates that affect cellular response. Altogether, fiber-supported bilayer lipid membranes provide attractive features for developing artificial substrates that can encode molecular as well as physical cues to potentially be used *in vitro* and *in vivo* to induce, investigate as well as read-out synaptic functions.

4.7 Experimental Section

4.7.1 Material

1,2-dioleoyl-*sn*-glycero-3-phosphocholine (DOPC), 1,2-dioleoyl-3-trimethylammonium propane chloride salt (DOTAP), 1,2-dipalmitoyl-*sn*-glycero-3-phosphocholine (DPPC), 1,2-dipalmitoyl-*sn*-glycero-3-phosphoethanolamine (DPPE) and 1,2-distearoyl-sn-glycero-3-phosphatidylethanolamine-N-biotinyl-(polyethylene glycol 2000)] ammonium salt (DSPE-PEG2000-biotin) were purchased from Avanti Polar Lipids (purity >99%). 4,4-difluoro-5,7-dimethyl-4-bora-3a,4a,diaza-*s*-indacene-3-pentanoic acid (Bodipy-PC) was purchased from Molecular Probes, Invitrogen (NY, USA). 1,1'-dieicosanyl-3,3,3',3'-tetramethylindocarbocyanine perchlorate (DiI-C_{20}) was purchased from Molecular Targeting Technologies (Pennsylvania, USA). Lissamine™ Rhodamine B 1,2-dihexadecanoyl-*sn*-glycero-3-phosphoethanolamine, triethylammonium salt (N-Rh-DHPE), Alexa-488/Alexa-647−phalloidin as well as primary and secondary antibodies were all purchased from Molecular Probes, Invitrogen (NY, USA). Avidin from egg white, fluoromount™ aqueous mounting media, poly-L-lysine hydrobromide, poly-D-lysine hydrobromide, poly-L-lysine-FITC-labeled hydrobromide (molecular weight; 150 kD – 300kD) and Whatman GF/A glass microfiber filters (2.4 cm diameter; 1.6 μm pore size) were all purchased from Sigma (NY, USA). All other cell culture related supplies were purchased from Gibco, Invitrogen (NY, USA).

4.7.2 Formation of Glass Fibers

Single glass fibers were isolated from Whatman GF/A glass microfiber filters (2.4 cm diameter; 1.6 μm pore size), as previously described.[19] Briefly, filters were cut into small pieces (1 cm × 1

cm) and suspended in phosphate buffer saline (PBS, pH 7.4) by exhaustive vortexing. The fibers were separated from remaining non-suspended filters by centrifugation at 10^4 rpm for 10 minutes. Fibers were then coated either with poly-D-lysine (50 μg/mL), avidin (100 μg/mL) or lipid membranes (1 mg/mL) by incubation with these solutions for at least 20 minutes, as described below.

4.7.3 Formation of GF-BLMs

Lipids in the form of small unilamellar vesicles (SUVs) were first prepared by mixing their chloroform solutions (1 mg/mL) to achieve the desired molar ratio. In all cases the fluorescent lipid dye molar ratio was kept at 0.1 mol %. The solvent was evaporated under a stream of nitrogen and then maintained under vacuum for several hours. The lipid film was hydrated by adding PBS (pH 7.4, equal volume to the starting chloroform solution) at a temperature higher than the phase transition temperature (T_m) of the lipids. The lipids were dispersed in solution by vigorous vortex mixing followed by sonication in a bath sonicator (*ca.* 10 minutes) resulting in the formation of SUVs. These were then mixed with an equal volume of glass fiber suspension and left on a shaker for at least 20 minutes. During mixing, the sample was immersed in a water bath to keep the temperature above the T_m of the lipids. For tethered bilayers, the fibers were first coated with avidin and then mixed with SUVs containing 0.1 mol% DSPE-PEG2000-biotin. After mixing, excess SUVs, which did not participate in the formation of the bilayer were removed by centrifugation (3× at 7 × 10^3 rpm for 10 minutes) and the pelleted fibers were resuspended in PBS (pH 7.4). The fiber suspension was either used immediately or kept for several days at 4 ˚C.

4.7.4 Co-cultures with Rat Hippocampal Neurons

All animal work was performed at the Montreal Neurological Institute in accordance with the Canadian Council of Animal Care Guidelines. Hippocampal neuronal cell cultures from E17 rat embryos were prepared as described by Banker.[40] Dissected hippocampi were treated with 0.25% (w/v) trypsin at 37 ˚C for 15 minutes and then washed with Dulbecco's modified Eagle medium (DMEM) supplemented with 10% fetal bovine serum, followed by Hank's balanced salt solution (HBSS) and finally serum-free Neurobasal medium, where they were mechanically dissociated using a glass Pasteur pipette. The dissociated neurons were plated on poly-L-lysine glass

coverslips at low density (*ca.* 1.75×10^4 cm^{-1}) in serum-free Neurobasal media supplemented with *l*-glutamine, penicillin, streptomycin and B-27. The cell cultures were kept in a humidified 5% CO_2 atmosphere at 37 ˚C and one-third of the medium was replaced every 3-4 days. After at least 14 days *in vitro* (DIV)), glass fibers in sterile PBS solution at pH 7.4 were added dropwise to hippocampal neurons and returned to the incubator. The neuron/fiber co-cultures were fixed for imaging using 4% (w/v) paraformaldehyde in phosphate buffer at pH 7.4 for 15 minutes followed by washing (3× with PBS). Immunolabeling against synaptic proteins was achieved by incubating the cells in blocking solution (PBS at pH 7.4 containing 4% normal donkey serum (NDS) and 0.1% (w/v) saponin) for 30 min, followed by primary antibody solution (1:100 (v/v) rabbit anti-synaptophysin and/or 1:500 (v/v) mouse anti-bassoon and/or 1:500 (v/v) in PBS at pH 7.4 containing 0.1% (w/v) saponin and 0.5% (w/v) NDS) overnight at 4 ˚C. After washing (3× with PBS) the cells were incubated in secondary antibody solution (1:500 (v/v) antibodies coupled to Alexa-488, Alexa-543 or Alexa-647 (as appropriately) in PBS at pH 7.4 containing 0.5% (w/v) NDS) for 30 minutes followed by washing (3× with PBS). For F-actin labeling, Alexa-488 or Alexa-647−phalloidin (as appropriately) were used (1:50 (v/v) in the secondary antibody solution). The immunolabeled coverslips were mounted on glass microscopic slides using Fluoromount™, kept at 4 ˚C and sealed prior to imaging.

4.7.5 Confocal Microscopy Imaging

LSM 710 confocal microscope (Carl Zeiss AG, Germany) was used with a 63×/1.4 oil-immersion objective lens. Image fields were first selected using the bright field (*i.e.* differential interference contrast, DIC) channel. One (or a combination) of the following optical settings were then applied to acquire the fluorescence images: (*i*) λ_{ex} 488 nm/ λ_{em} LP > 505 nm (single channel imaging) or λ_{em} BP 505 − 550 nm (multi-channel imaging, sequential scanning), (*ii*) λ_{ex} 543 nm/ λ_{em} LP > 565 nm, and (*iii*) λ_{ex} 633 nm/ λ_{em} LP > 685 nm. Laser power and detector gain were adjusted to avoid intensity saturation in all acquired images. Z-series image stacks were acquired at a sampling rate which satisfies the Nyquist frequency, as suggested by the Zeiss software. Blind deconvolution was applied to the acquired image stacks using AutoQuant X3 software. All images were subject to background subtraction using Imaris 7.4.0 software.

4.7.6 Fluorescence Recovery after Photobleaching (FRAP)

A Zeiss LSM-710 confocal laser-scanning microscope with a 63×/1.4 oil-immersion objective lens and a 488 nm argon ion laser (25 mW power) was used for FRAP measurements. Glass fibers coated with DOPC bilayers were labeled with 0.1 mol% Bodipy-PC. The bilayers were assembled on the fibers either directly or using the avidin-biotin tethering protocol described above, with 0.1 mol % DSPE-PEG2000-biotin added in the SUVs lipid mixture. Using the DIC channel, a single fiber was centered in the image field of view. Three circular regions of interest (ROI) of 1.2 μm radius were then defined: (*i*) a bleached ROI where the FRAP measurements were carried out, (*ii*) a reference ROI outside the bleached area to correct for bleaching which occurred during imaging and (*iii*) a reference ROI outside the location of the fiber to account for any background fluorescence. Five images were acquired prior to bleaching in order to measure the initial pre-bleach fluorescence intensity, followed by 10 consecutive bleach iterations using 100% laser intensity. At least 50 post-bleaching images were subsequently acquired at 5% laser intensity to avoid further bleaching. The total scan time (*ca.* 12 s) was minimized by imaging only the ROIs rather than the full field of view. The fluorescence intensity signals measured for bleached ROI was corrected for the background signal (BG) and then normalized to their initial pre-bleaching fluorescence intensity, as well as to the normalized intensity of the reference region according to Equation 4.1:

$$\left(\frac{F_{ROI} - BG}{F_{ROI}(prebleached) - BG} \Big/ \frac{F_{REF} - BG}{F_{REF}(prebleached) - BG} \right) \times 100\% \qquad \textbf{Equation 4.1}$$

The corrected fluorescence curves (from 30 separate FRAP measurements, under the same experimental conditions) were used to construct an average FRAP curve which was then fitted to a single diffusing component model as described by Equation 4.2:

$$f(t) = A(1 - e^{\pi}) \qquad \textbf{Equation 4.2}$$

where, A is the ratio of mobile to immobile species and τ is the half-time of fluorescence recovery (*i.e.* the diffusion time required to recover 50% of the initial fluorescence intensity).

Taking into account that the reported half-time of fluorescence corresponds to the fastest recovery time that can be measured with the confocal set up and experimental parameters described above, a lower limit of the diffusion constant, D, was calculated according to Equation 4.3:[20]

$$D \geq 0.224.w^2 / \tau \qquad \textbf{Equation 4.3}$$

where, w is the radius of the bleach ROI.

All FRAP data processing and curve fitting were performed using Kaleidagraph 4.1 software.

4.7.7 Fluorescence Intensity Quantification

Measuring the fluorescence intensity at the fiber location in the neuron/fiber co-culture images is used to quantify synaptic protein accumulation. ImageJ software (Fiji version) was used for quantification analysis, where the fluorescence ratio was calculated for the intensity within a ROI at the fiber location divided by that of another control ROI. As seen in Figure S3, the DIC channel is first used to locate the fiber sites (only fibers interacting with neurons are used for analysis). Using ImageJ, a region of interest (ROI) sized *ca.* 20% larger than the size of the fiber is created and a second ROI of exactly the same size is created along the length of the neuron and placed immediately adjacent to the fiber as a control. The fluorescence intensity ratio can then be calculated from the fluorescence data of the fiber ROI divided by that of the adjacent ROI. Fluorescence intensity values can be measured directly from the grayscale image (values range from 0 to 255 grey scale units) or from the pixel area values from the binary image (values are either 1 for fluorescent or 0 for non-fluorescent pixels). Binary images are derived from the grayscale image by using the threshold function in ImageJ which converts all the fluorescence intensity values into fluorescent or non-fluorescent pixels irrespective of their relative intensity values (*i.e.* 1-255). This allowed comparing the area values of different ROIs from different samples and experiments. Histograms displaying the resulting data mean and standard deviation were prepared in KaleidaGraph 4.1 software. Significant differences between experiments were evaluated using a two-tailed Student's *t*-test after correction for non-equal variance.

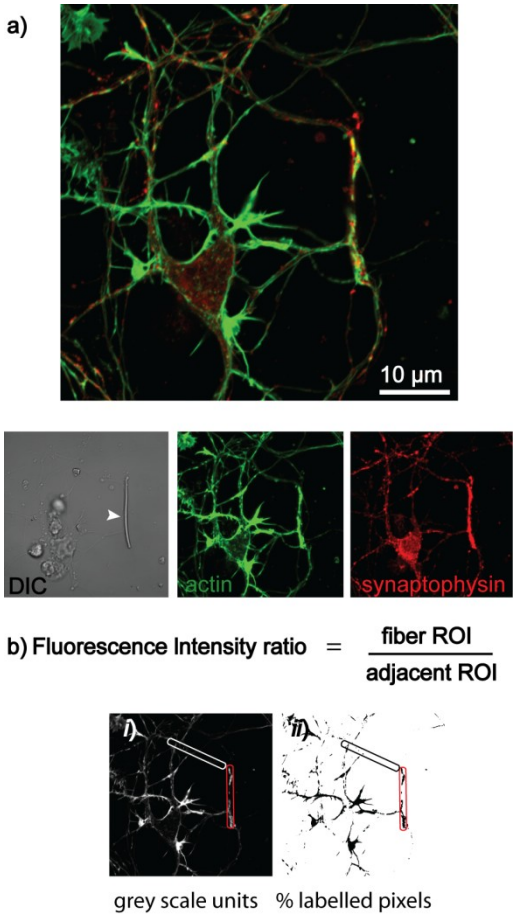

Figure 4.5 Representative image panels for a neuron/fiber co-culture showing the steps involved in fluorescence analysis. (a) Image of rat hippocampal neurons (DIV 14) incubated for 24 hrs with lipid-coated fibers from DOPC/DPPE/DOTAP (25:50:25). The corresponding DIC channel is used to determine the location of the fiber (as indicated by the arrowhead). The single fluorescence channel images for the actin (green) and synaptophysin (red) are also shown and are used for fluorescence intensity measurements. (b) Subsequent determination of fluorescence ratios at the fiber location compared to a defined adjacent area are calculated from either (*i*) fluorescence intensity values from the greyscale single channel image or (*ii*) area values from the threshold image, within the fiber ROI (shown in red) divided by that of the adjacent ROI (shown in white or black). The ROIs are the same size (*ca.* 20% > fiber size) and located along the neuron axon.

4.7.8 The Different Shapes of Glass Fibers

When prepared according to the described methods, glass fibers result in a variety of shapes and lengths. Figure 4.5 shows examples of straight- and curved-ending fibers formed during a single fiber preparation.

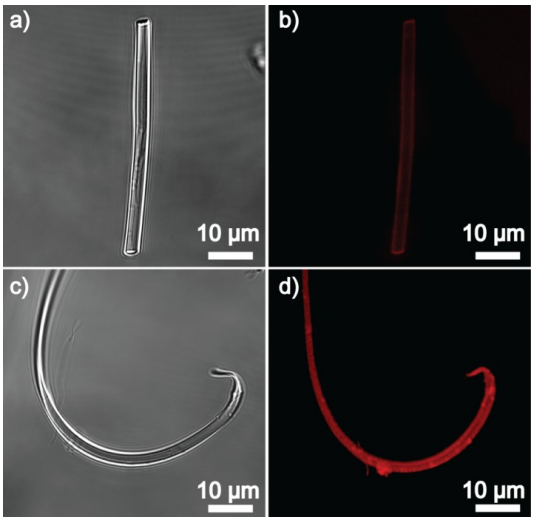

Figure 4.6 Diffusion interference contrast (DIC; a, c) and corresponding confocal fluorescence images (b, d) of glass fibers coated with DPPC lipid bilayers labeled with 0.1 mol% DiI-C_{20}.

4.7.9 Characterization of Polylysine-Coated Glass Fibers

Glass fibers are coated with polylysine (for imaging purposes, FITC-labeled poly-L-lysine (FITC-PLL); 50 µg/mL) by mixing equal volumes of their PBS solutions on a shaker for at least 20 minutes. After mixing, excess poly-lysine is removed by centrifugation (3× at 10 × 10^3 rpm for 10 minutes) and the pelleted fibers were resuspended in PBS (pH 7.4). The fiber solution can be kept at 4 ˚C for several days. In Fig. 4.6, coated-fibers from this preparation are shown.

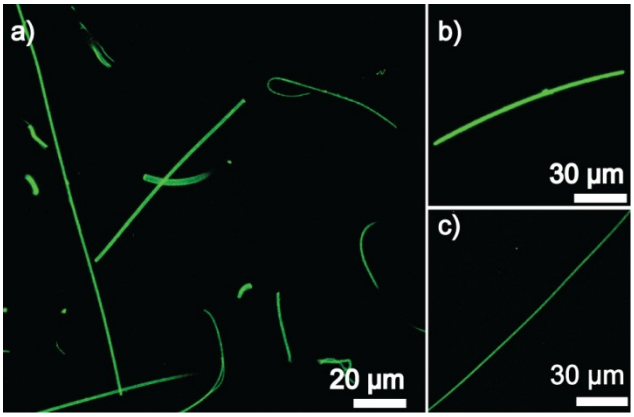

Figure 4.7 Representative confocal fluorescence images of polylysine-coated glass fibers showing (a) the different length distribution within one preparation as well as a close-up view of one of the shorter (a) and longer (b) fibers.

4.7.10 Co-culture of PDL-Coated Fibers with Neurons

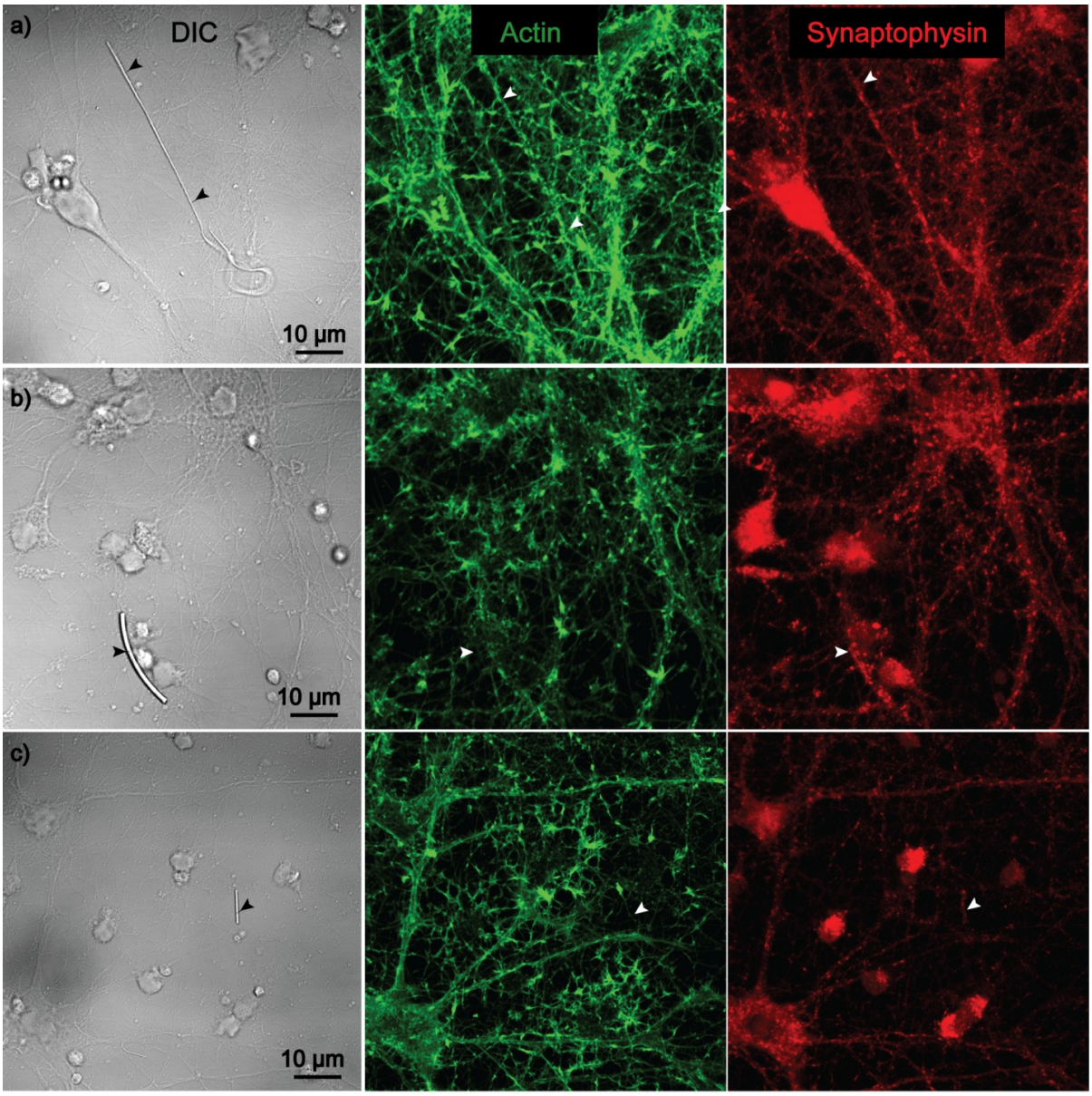

Figure 4.8 Interactions of hippocampal neurons with PDL-coated glass fibers. Representative DIC and the corresponding confocal fluorescence images of rat hippocampal neurons (DIV 14) incubated for (a) 24 hrs, (b) 3 days and (c) 7 days with PDL-coated fibers. The neurons are immunolabeled with antibodies for actin (green) and synaptophysin (red). The DIC images (left panel) are used to locate the fibers, as indicated by the arrows.

4.7.11 Interactions of Hippocampal Neurons with Lipid-Coated Fibers

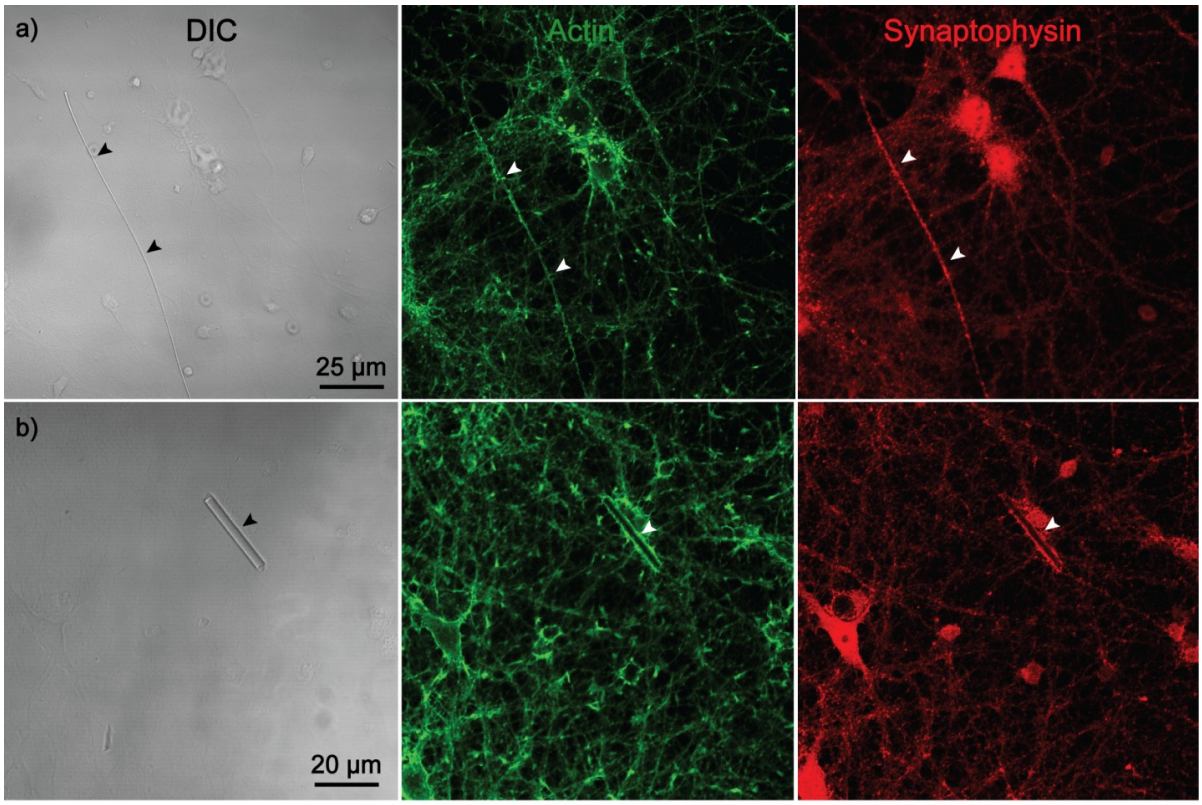

Figure 4.9 Interactions of hippocampal neurons with lipid-coated fibers. Representative diffusion interference contrast (DIC) and corresponding confocal fluorescence images of rat hippocampal neurons (DIV 14) incubated for (a) 3 days and (b) 7 days with glass fiber tethered lipid bilayer membranes formed from DOPC/DPPE/DOTAP (25:50:25). The neurons are immunolabeled with antibodies for actin (green) and synaptophysin (red). The DIC images (left panel) are used to locate the fibers as indicated by the arrowheads. In this preparation, the glass fibers are first coated with avidin and then mixed with lipid vesicles containing 0.1 mol% DSPE-PEG2000-biotin for tethering purposes.

4.8 References

1. Tam, R. Y.; Fuehrmann, T.; Mitrousis, N.; Shoichet, M. S. Regenerative therapies for central nervous system diseases: a biomaterials approach. *Neuropsychopharm.* **2014,** *39*, 169-188.

2. Zhong, Y.; Bellamkonda, R. V. Biomaterials for the central nervous system. *J. R. Soc. Interface* **2008,** *5*, 957-975.

3. Deumens, R.; Bozkurt, A.; Meek, M. F.; Marcus, M. A.; Joosten, E. A.; Weis, J.; Brook, G. A. Repairing injured peripheral nerves: Bridging the gap. *Prog. Neurobiol.* **2010,** *92*, 245-476.

4. Gopalakrishnan, G.; Thostrup, P.; Rouiller, I.; Lucido, A. L.; Belkaid, W.; Colman, D. R.; Lennox, R. B. Lipid bilayer membrane-triggered presynaptic vesicle assembly. *ACS Chem. Neurosci.* **2010,** *1*, 86-94.

5. Madwar, C.; Gopalakrishan, G.; Lennox, R. B. Specific lipid microdomains in membrane rafts play initial roles in synapse formation. **2015,** to be submitted.

6. Dowell-Mesfin, N. M.; Abdul-Karim, M. A.; Turner, A. M.; Schanz, S.; Craighead, H. G.; Roysam, B.; Turner, J. N.; Shain, W. Topographically modified surfaces affect orientation and growth of hippocampal neurons. *J. Neuro Eng.* **2004,** *1*, 78-90.

7. Ferrari, A.; Cecchini, M.; Dhawan, A.; Micera, S.; Tonazzini, I.; Stabile, R.; Pisignano, D.; Beltram, F. Nanotopographic control of neuronal polarity. *Nano lett.* **2011,** *11*, 505-511.

8. Fozdar, D. Y.; Lee, J. Y.; Schmidt, C. E.; Chen, S. Hippocampal neurons respond uniquely to topographies of various sizes and shapes. *Biofab.* **2010,** *2*, 035005.

9. Johansson, F.; Carlberg, P.; Danielsen, N.; Montelius, L.; Kanje, M. Axonal outgrowth on nano-imprinted patterns. *Biomat.* **2006,** *27*, 1251-1258.

10. Rajnicek, A.; Britland, S.; McCaig, C. Contact guidance of CNS neurites on grooved quartz: influence of groove dimensions, neuronal age and cell type. *J. Cell Sci.* **1997,** *110*, 2905-2913.

11. Yao, L.; Wang, S.; Cui, W.; Sherlock, R.; O'Connell, C.; Damodaran, G.; Gorman, A.; Windebank, A.; Pandit, A. Effect of functionalized micropatterned PLGA on guided neurite growth. *Acta biomat.* **2009,** *5*, 580-588.

12. Gomez, N.; Lu, Y.; Chen, S.; Schmidt, C. E. Immobilized nerve growth factor and microtopography have distinct effects on polarization versus axon elongation in hippocampal cells in culture. *Biomat.* **2007,** *28*, 271-284.

13. Kang, K.; Lee, S.; Kim, R.; Choi, I. S.; Nam, Y. Electrochemically driven, electrode-addressable formation of functionalized polydopamine films for neural interfaces. *Angew. Chem. Int. Ed.***2012,** *51*, 13101-13104.

14. Bruder, J. M.; Lee, A. P.; Hoffman-Kim, D. Biomimetic materials replicating Schwann cell topography enhance neuronal adhesion and neurite alignment in vitro. *J. Biomat. Sci., Polym. Ed.* **2007,** *18*, 967-982.

15. Brunetti, V.; Maiorano, G.; Rizzello, L.; Sorce, B.; Sabella, S.; Cingolani, R.; Pompa, P. P. Neurons sense nanoscale roughness with nanometer sensitivity. *Proc. Nat. Acad. Sci. USA* **2010,** *107*, 6264-6269.

16. Lucido, A. L.; Gopalakrishnan, G.; Yam, P. T.; Colman, D. R.; Lennox, R. B. Isolation of functional presynaptic complexes from CNS neurons: a cell-free preparation for the study of presynaptic compartments In vitro. *ACS Chem. Neurosci.* **2010,** *1*, 535-541.

17. Lucido, A. L.; Suarez Sanchez, F.; Thostrup, P.; Kwiatkowski, A. V.; Leal-Ortiz, S.; Gopalakrishnan, G.; Liazoghli, D.; Belkaid, W.; Lennox, R. B.; Grutter, P.; Garner, C. C.; Colman, D. R. Rapid assembly of functional presynaptic boutons triggered by adhesive contacts. *J. Neurosci.***2009,** *29*, 12449-12466.

18. Gopalakrishnan, G.; Yam, P. T.; Madwar, C.; Bostina, M.; Rouiller, I.; Colman, D. R.; Lennox, R. B. Label-free visualization of ultrastructural features of artificial synapses *via* cryo-EM. *ACS Chem. Neurosci.* **2011,** *2*, 700-704.

19. Madwar, C.; Gopalakrishnan, G.; Lennox, R. B. Interfacing living cells and spherically supported bilayer lipid membranes. *Langmuir* **2015,** *31*, 4704-4712.

20. Fishman, R. B.; Hatten, M. E. Multiple receptor systems promote CNS neural migration. *J. Neurosci.* **1993,** *13*, 3485-3495.

21. Gopalakrishnan, G.; Rouiller, I.; Colman, D. R.; Lennox, R. B. Supported bilayers formed from different phospholipids on spherical silica substrates. *Langmuir* **2009,** *25*, 5455-5458.

22. Soumpasis, D. M. Theoretical analysis of fluorescence photobleaching recovery experiments. *Biophys. J.* **1983,** *41*, 95-97.

23. Berquand, A.; Mazeran, P. E.; Pantigny, J.; Proux-Delrouyre, V.; Laval, J. M.; Bourdillon, C. Two-step formation of streptavidin-supported lipid bilayers by PEG-triggered vesicle fusion. Fluorescence and atomic force microscopy characterization. *Langmuir* **2003,** *19*, 1700-1707.

24. Brozell, A. M.; Muha, M. A.; Sanii, B.; Parikh, A. N. A class of supported membranes: formation of fluid phospholipid bilayers on photonic band gap colloidal crystals. *JACS* **2006,** *128*, 62-63.

25. Cambrea, L. R.; Hovis, J. S. Formation of three-dimensional structures in supported lipid bilayers. *Biophys. J.* **2007,** *92*, 3587-3594.

26. Guo, L.; Har, J. Y.; Sankaran, J.; Hong, Y.; Kannan, B.; Wohland, T. Molecular diffusion measurement in lipid bilayers over wide concentration ranges: a comparative study. *Chemphyschem.* **2008,** *9* , 721-728.

27. Seu, K. J.; Cambrea, L. R.; Everly, R. M.; Hovis, J. S. Influence of lipid chemistry on membrane fluidity: tail and headgroup interactions. *Biophys. J.***2006,** *9*, 3727-3735.

28. Shenoy, S.; Moldovan, R.; Fitzpatrick, J.; Vanderah, D. J.; Deserno, M.; Losche, M. In-plane homogeneity and lipid dynamics in tethered bilayer lipid membranes (tBLMs). *Soft Matter* **2010,** *6*, 1263-1274.

29. Yi, F.; Xu, J.; Smith, A. M.; Parikhc, A. N.; LaVan, D. A. Nanofiber-supported phospholipid bilayers. *Soft Matter* **2009,** *5*, 5037–5041.

30. Burry, R. W. Formation of apparent presynaptic elements in response to poly-basic compounds. *Brain Res.* **1980,** *184*, 85-98.

31. Doherty, G. J.; McMahon, H. T. Mediation, modulation, and consequences of membrane-cytoskeleton interactions. *Annu. Rev. Biophys.***2008,** *37*, 65-95.

32. Janmey, P. A. The cytoskeleton and cell signaling: component localization and mechanical coupling. *Physiol. Rev.* **1998,** *78*, 763-781.

33. Pollard, T. D.; Cooper, J. A. Actin, a central player in cell shape and movement. *Science* **2009,** *326*, 1208-1212.

34. Hoffman-Kim, D.; Mitchel, J. A.; Bellamkonda, R. V. Topography, cell response, and nerve regeneration. *Annu. Rev. Biomed. Eng.* **2010,** *12*, 203-231.

35. Eeman, M.; Deleu, M. From biological membranes to biomimetic model membranes. *Biotechnol. Agron. Soc. Environ.* **2010,** *14*, 719-736.

36. Chemburu, S.; Fenton, K.; Lopez, G. P.; Zeineldin, R. Biomimetic silica microspheres in biosensing. *Molecules* **2010,** *15*, 1932-1957.

37. Schwille, P.; Diez, S. Synthetic biology of minimal systems. *Crit. Rev. Biochem. Mol. Biol.* **2009,** *44*, 223-242.

38. Tamm, L. K.; McConnell, H. M. Supported phospholipid bilayers. *Biophys J.* **1985,** *4*, 105-113.

39. Groves, J. T.; Dustin, M. L. Supported planar bilayers in studies on immune cell adhesion and communication. *J. Immunol. Meth.* **2003,** *278*, 19-32.

40. Goslin, K.; Asmussen, H.; Banker, G. *Culturing Nerve Cells*. 2nd ed.; MIT-Press, Cambridge, MA: **1998**; p 666.

Chapter 5

Conclusions and Ideas for Future Work

5.1 Conclusions

Previously-established model membrane systems have been shown to maintain the fundamental lipid bilayer structure and have been used to address the function of individual membrane components and probe their organization and dynamics. GUVs and S-BLMs are typically examined under conditions which simplify their manipulation. They do not however provide any direct correlation with membrane behavior under physiological conditions. The underlying theme of this Thesis is the development of an improved experimental platform that can be interfaced to biological systems, more specifically, robust model systems based on bilayer membranes assembled on spherical and fiber solid substrates. We have demonstrated the use of this experimental platform in engineering artificial neuronal networks. The findings of this work are summarized below followed by a discussion of future directions in this field.

In Chapter 2, it was shown that a robust yet dynamic model membrane system can be created by tethering lipid bilayers to micron-diameter silica beads (*i.e.* the spherically supported bilayer lipid membrane; SS-BLM) using biotin-avidin conjugation and polymeric spacers. Experimental evidence was provided using fluorescence recovery after photobleaching (FRAP) to confirm the formation of single lipid bilayers on the silica beads and the maintenance of their fluidity despite the tethering protocol. It was also shown that the formation of co-existing lipid phases in SS-BLMs can be visualized using fluorescence microscopy techniques.

The studies presented in Chapter 2 also demonstrated that SS-BLMs which exhibit lipid phase separation are stable under physiological conditions in a cell culture environment. The membrane was found to maintain its structure and the organization of its lipid constituents despite various experimental manipulations used to probe the SS-BLM/cell interactions. These manipulations include immunofluorescence labeling, the use of detergents and multiple washing steps.

The co-culture experiments performed in this study also demonstrated the utility of SS-BLMs in examining the dynamics of cellular cytoskeletal filaments in response to the extracellular laterally-heterogeneous environment they are interfaced to. Both aspects, *i.e.* co-existing lipid phases in the plane of the membrane and the influence of the underlying cytoskeleton, contribute to the existence of cellular lipid rafts. The approach demonstrated in this work using the SS-BLM system thus provides an experimental platform for addressing the fundamental relationship between individual raft components and specific membrane-mediated events in a biological system.

Assessment of the roles of specific lipid raft components in neuronal events at artificial interfaces was elaborated in Chapter 3, where the contribution of phase separated lipid domains in initiating and stabilizing artificial synaptic junctions was indentified. One of the major findings of this work was that neurons can form synaptic networks with membranes containing only phase-separated lipids.

A particularly interesting aspect of neuronal synapse formation at synthetic interfaces was presented in Chapter 4 where it was demonstrated that substrates with 2D curvature, specifically glass fibers, were demonstrated to be suitable for promoting stable neuronal connections when coated with bilayer membranes (GF-BLMs). In comparison to another synaptogenic surface coating, glass-fiber bilayer lipid membranes (GF-BLMs) were found to be more stable under cell culture conditions.

These experimental studies advance our ability to prepare biomimetic platforms that can be manipulated and addressed in cell culture. As functional interfaces, they are valuable for addressing membrane biophysical questions in a biologically relevant environment and also for inducing specific cellular functions. In this context, bilayer membranes assembled on silica beads or fibers have great potential as tunable biomimetic materials that can be interfaced with brain cells.

5.2 Future Work

(*i*) The SS-BLM system is an interesting platform for the design of multifunctional biosensors and diagnostic tools, where various reporter biomolecules can be incorporated in a biomimetic environment. Appendix II demonstrates an example of such applications, where 3D DNA cages were incorporated within the SS-BLMs.[1] The robustness and ease of characterization, which SS-

BLMs offer enable the investigation of the structure and function of molecular assemblies (*i.e.* DNA scaffolds, proteins, *etc.*) in a simplified membrane environment. In addition, these investigations can benefit from the ability of the SS-BLM platform to serve as an interface to cells.

(*ii*) The SS-BLM system is a promising platform for investigating the physical properties of S-BLMs. Despite numerous publications concerning planar S-BLMs, the very low surface density of lipids in these systems (*ca.* 0.55 lipids per nm^2)[2] makes investigations using key characterization methods (such as NMR and DSC) not possible. The SS-BLM system, on the other hand, offers a high surface area analog to base such studies on. Chapter 2 describes a comparative DSC study which addressed the effect of various additives on the bilayer phase transition temperature. In a similar set-up, phase separation in lipid mixtures can be examined for SS-BLMs in terms of various compositions.

(*iii*) The SS-BLM-based lipid rafts provide an experimental tool for screening lipid phase separation promoters and inhibitors *via* fluorescence microscopy. This would be valuable in investigating the connection of lipid-raft alterations to certain pathologies.

(*iv*) Interfacing synthetic functional materials and living neuronal cultures is at the forefront of neuroengineering. These emerging strategies will greatly benefit from the experimental platforms presented herein.

- Lipid bilayer membranes coated on beads or fibers are examples of biocompatible active surfaces that can interact and induce measurable responses from living neurons. Additionally, lipid bilayers are stable under prolonged cell culture conditions and therefore their use as neuronal interfaces is attractive for long-term *in vivo* studies in a living rat brain. This will allow investigation of the "local foreign body reaction" of the CNS (specifically its glial cells) in response to the implanted substrates.

- In the context of synthetic synapse formation, incorporating neurologically-relevant membrane proteins or cell surface receptors into the SS-BLM platform would be a step toward forming completely functional synapses.

- The GF-BLM is an especially promising configuration because the fiber could in principle be an optical fiber, stripped of its cladding. In this context, lipid-coated optical fibers can be designed to induce synthetic synapses and subsequently transmit the electrical and/or chemical synaptic outputs by light propagation through the fiber to either detectors or other cells a distance away. To function as neuronal sensors, optical fibers can be designed to incorporate chemical- or voltage-sensitive probes that detect changes associated with synapse formation.

5.3 References

1. Conway, J. W.; Madwar, C.; Edwardson, T. G.; McLaughlin, C. K.; Fahkoury, J.; Lennox, R. B.; Sleiman, H. F. Dynamic behavior of DNA cages anchored on spherically supported lipid bilayers. *JACS* **2014,** *136*, 12987-12997.

2. Jing, B. X.; Hutin, M.; Connor, E.; Cronin, L.; Zhu, Y. X. Polyoxometalate macroion induced phase and morphology instability of lipid membrane. *Chem Sci* **2013,** *4*, 3818-3826.

Linking Statement to Appendix I

Appendix I aims to characterize the ultrastructural details of artificial synapses developed between hippocampal neurons and artificial substrates. Specifically cryo-electron microscopy (cryo-EM) is applied to visualize synaptic structures expressed in response to submicron silica beads coated with poly-D-lysine or lipid bilayers. This study confirms and establishes the structural details of chemically induced artificial synapse.

Appendix I

Label-Free Visualization of Ultrastructural Features of Artificial Synapses *via* Cryo-EM

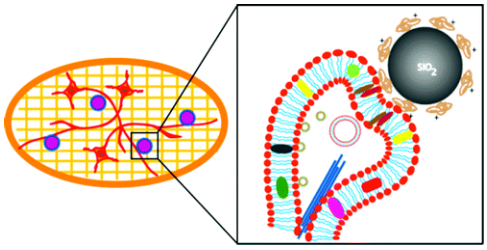

The following Appendix is reprinted with permission from "Label-Free Visualization of Ultrastructural Features of Artificial Synapses *via* Cryo-EM", G. Gopalakrishnan, P. T. Yam, C. Madwar, M. Bostina, I. Rouiller, D. R. Colman and R. B. Lennox, ACS Chem. Neurosci., 2011, 2 (12), 700-704. The text below is a verbatim copy of the manuscript.

AI.1 Abstract

The ultrastructural details of presynapses formed between artificial substrates of submicrometer silica beads and hippocampal neurons are visualized *via* cryo-electron microscopy (cryo-EM). The silica beads are derivatized by poly-D-lysine or lipid bilayers. Molecular features known to exist at presynapses are clearly present at these artificial synapses, as visualized by cryo-EM. Key synaptic features such as the membrane contact area at synaptic junctions, the presynaptic bouton containing presynaptic vesicles, as well as microtubular structures can be identified. This is the first report of the direct, label-free observation of ultrastructural details of artificial synapses.

AI.2 Introduction

Synapses are specialized cell-cell junctions formed between neuronal cells or between neurons and muscle cells through which they communicate with one another.[1, 2, 3] Neuronal synapses are generally formed between axons (presynaptic side) and dendrites (postsynaptic side). In chemical synapses, the presynaptic side releases low molecular weight neurotransmitters upon depolarization of a neuron. These released neurotransmitters are then received at the postsynaptic side *via* specific postsynaptic receptors. In healthy neurons, the synaptic cleft (the region between the pre- and postsynaptic membranes) is *ca.* 20−25 nm wide.[4, 5, 6] The synaptic cleft allows for efficient diffusion of released neurotransmitters from the presynaptic side to the postsynaptic side of a synapse. Although optical microscopy techniques have been much-used to observe synapse formation and related studies *in vitro*,[7, 8, 9] the high resolution capabilities of electron microscopy are required for observing the molecular details of such structures.[11, 12, 13] It has been shown that cryo-electron tomography can be used for morphological characterization of native synapses formed in culture when primary neurons were grown directly on electron microscopy grids.[14, 15] Artificial neural network formation has been explored using a number of substrates.[16, 17, 18, 19, 20] One approach to generate alternative methods to repair damaged nerve terminals is to create some form of functional artificial synapses. We have shown recently that functional presynapses can in fact be formed on surfaces interfaced with either poly-D-lysine (PDL) or cationic bilayer lipid-membranes (SS-BLMs) deposited on micrometer-sized spherical substrates.[19, 20] While studies to date have focused on the structural and functional properties of artificial synapses, their ultrastructural features are presently not known. Given that molecular

level details are clearly interrelated with structural and functional characteristics, such a lack of ultrastructural details diminishes the range of experimental paths to follow.

AI.3 Results and Discussion

We demonstrate here that *in vitro* presynapses, when formed on submicrometer sized spherical substrates, can be visualized at nanometer length scales using cryo-electron microscopy (cryo-EM). Cryo-EM is a transmission electron microscopy (TEM) based technique that allows biological samples to be observed in a fully hydrated physiological environment without fixing or staining.[21] Although the approach presented here requires some alternative methods in cell culture, the observation is direct and does not require further sample processing steps that can be both tedious and experimentally biasing. This is especially true in the case of artificial synapses formed on silica beads, where thin sectioning of samples using an ultramicrotome would be difficult to achieve.

Scheme AI.1 shows the overall experimental steps involved. In a typical procedure, hippocampal neurons are dissected from embryonic day 17−18 rat embryos and dissociated to a single cell suspension as described previously.[22] Neurons were cultured on sterile, poly-L-lysine (PLL)-coated Au/Quantifoil EM grids in Neurobasal medium supplemented with *l*-glutamine and B27.

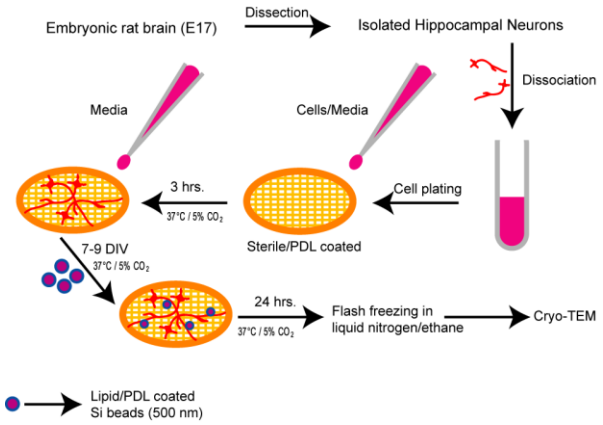

Scheme AI.1. Scheme (not to scale) illustrating the experimental steps. Isolated hippocampal neurons are plated onto sterile, PLL coated Au/Quantifoil EM grids. These cells are cultured for 7 days or more prior to cryo-EM imaging.

We initially observed that the small number of neurons grown on the EM grids were less healthy when grown alone in the absence of other neurons. Therefore, neurons were grown on separate

coverslips in the same dish, along with the EM grids, in order to provide trophic support to the neurons on the grids. The hippocampal neurons were resuspended in Neurobasal culture medium (250 000 cells/mL), and a small drop of this cell suspension was added to the EM grids and coverslips (6 and 80 μL, respectively). Confining the neurons to a small drop of media on the EM grids during the initial plating allows the neurons to specifically attach to the grid surface. After 3 − 4 h at 37 ˚C/5% CO_2, when the neurons have attached to the substrates, 3 − 4 mL of Neurobasal culture medium was added to the entire dish and left for 7 or more days *in vitro* (DIV). The cells are then vitrified by rapidly plunging the grid in ethane slush and kept under liquid nitrogen temperature (−180 ˚C) until they are ready to image.

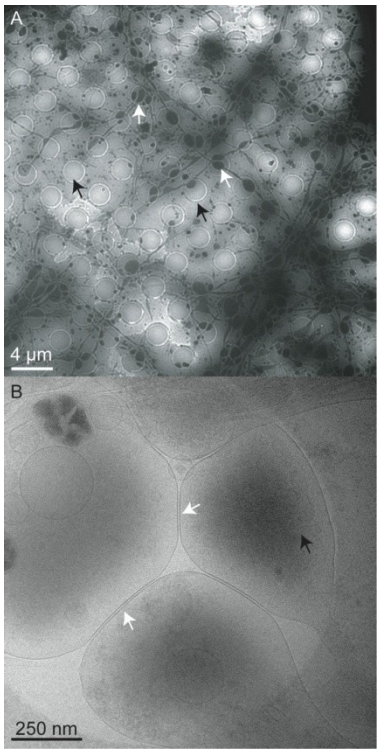

Figure AI.1 Representative cryo-EM images showing hippocampal neurons (DIV 8) grown on a sterile, PLL-coated Au/Quantifoil grid. (A) Neuronal differentiations are visible along the grids, which when on the holes (black arrows) grow a little wider (white arrows) than on the support portion of the grid. (B) Magnified view of one of the holes where synapses (white arrows) from closely associated neural processes are visible. High electron density is observed at the areas where synaptic vesicles have accumulated (black arrows).

Figure AI.1A shows a representative low magnification cryo-EM image of a Au/Quantifoil grid containing hippocampal neurons grown for 8 DIV. The circles (black arrows) are 2 μm diameter

holes in the EM grid that allow for the cells and the surrounding media to be vitrified. These vitreous films thus provide cells with an environment close to physiological conditions during EM sample preparation. The axons are observed across the grids, growing at very large length scales. The cell morphology appears to look slightly different from that observed on glass coverslips at physiological conditions.[19, 20] It is important to note that the axons are larger when they grow across a hole (white arrows). We believe that the axons in culture on the Au/Quantifoil support are growing wider mostly on the holes because (*i*) there is more space available for growth, or (*ii*) the axons find a more favorable substrate (plastic) underneath the grid while passing through the holes. A slight widening of axons is infrequently observed on the support as well, but this effect is more prominent in the holes as seen in Fig. AI.1A. Figure AI.1B is a magnified image of one of the holes in the EM grid. Several neuronal processes can be visualized in this area, and the higher electron density represents the areas where synaptic vesicles (black arrows) are present. The inset in Fig. AI.1B shows accumulated synaptic vesicles at a synaptic bouton. It is important to note that the ultrastructural details of the cellular entities are clearly visible in the absence of stain due to the difference in electron scattering of lipids, proteins, and water. Cell bodies or thicker bundles of neuronal processes are too thick to be transparent to the electrons and were not distinguishable from areas of the grids where the ice is too thick (data not shown). Additional images of neurons and neuronal synapses on grids are shown in the Experimental Information (Figs. AI.4 and AI.5).

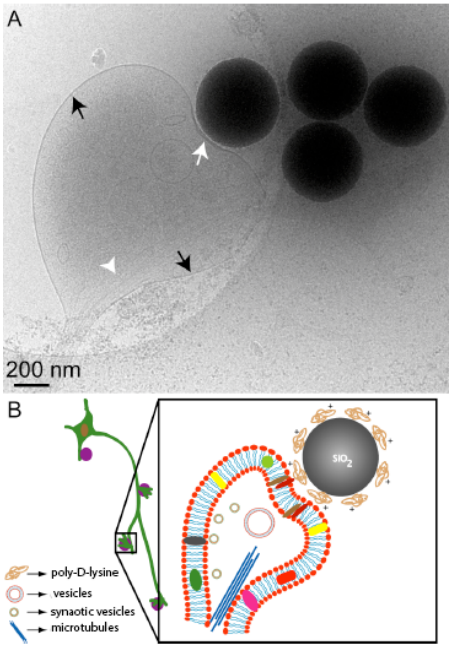

Figure AI.2 Representative cryo-EM image (A) showing an artificial synapse formed between hippocampal neurons (DIV 8) grown on a sterile, PLL coated Au/Quantifoil grid and poly-D-lysine coated 500 nm silica beads. Microtubular networks (white arrow heads) are also visible. Similarly coated beads that are not in contact with neurons also visible in the image. Few synaptic vesicles (black arrowheads) are also visible. White arrow indicates the contact area at the synaptic junction, which in this case is between an axon and a bead. (B) Sketch depicting the structural components of the artificial synapse seen in (A).

To observe the artificial synapses using cryo-EM, hippocampal neurons were grown on Au/Quantifoil EM grids as described above. Between 7 to 9 DIV, PDL coated or lipid coated beads (500 nm) were added to the culture. We have tried both 1 μm and 500 nm beads in our cryo-EM experiments and have observed that 500 nm beads were optimal. In the case of 1 μm beads, the vitreous films formed were too thick, which resulted in poor quality images. After 24 h of incubation of beads with the cells (Scheme AI.1), the grids were flash frozen in ethane slush and kept under liquid nitrogen until ready to image. Figure AI.2A shows a representative cryo-EM image of a presynapse formed between hippocampal neurons and PDL coated beads. The presynaptic bouton seen in this image is formed when a growing axon extends onto a bead and forms a synapse, which resembles known structures of native synapses.[11, 12, 13] In this case, the PDL coated bead serves as the postsynaptic side of a native synapse. The membrane contact area (white arrow) looks slightly thicker compared to the rest of the membrane around the presynaptic bouton (black arrows). This is consistent with the increased presence of adhesion molecules and

specific protein accumulation on membranes at the synaptic junctions. This corresponds to features observed in native synapses when imaged using conventional TEM.[11, 12, 13]

Microtubules (white arrowheads) following the direction of axonal growth are clearly seen in this image. The image in Fig. AI.2A, however, shows only a few presynaptic vesicles visible (black arrowheads). This could be attributed to the specific conditions used in cryo-EM imaging and/or the thickness of the sample. Small membrane structures such as synaptic vesicles are usually better visualized using different imaging parameters, as opposed to large membrane structures such as a synaptic bouton. This attributes to the difficulty in visualizing such entities simultaneously in a single image. The beads that are not in contact with any neuronal cells and thus did not take part in synapse formation are also seen in the same image. In general, we have observed an average of five to seven beads per square mesh (200 μm) on an EM grid that form synapses upon contact with axonal processes. One to two beads per 200 μm square mesh do not however form stable synapses. It is important to note that the concentration of beads that could be added to the culture is limiting, as higher concentrations of beads were found to be toxic to the cells. Figure AI.2B is a sketch depicting the cellular organization of different synaptic elements at the presynaptic bouton observed in Fig. AI.2A.

The presynaptic vesicle pool is clearly visible in Fig. AI.3A (white arrow heads) compared to the synaptic bouton shown in Fig. AI.2A. The majority of these vesicles are in the range of 30 nm, which is in good agreement with the size of synaptic vesicles. However, some larger vesicles ($\sim$100 nm) are also seen (black arrowheads) that could be attributed to transport vesicles. The presence of a thicker membrane at the synaptic junction as well as microtubular networks is also evident in this image. Black arrows show the axon shaft of the neuronal process from which the synaptic bouton is extended onto the bead in culture. As seen in this image, microtubules seem to follow the path of the axonal shaft. Fig. AI.3B is the corresponding sketch depicting the cellular level organization of the synaptic elements visible in Figure AI.3A. It is interesting to note that mitochondria are also clearly visible at the synaptic boutons as well as along the axons (Experimental Section Fig. AI.6). Cryo-EM based studies might thus be very useful for research involving such intracellular organelles, for example, following morphological changes in mitochondria in dysfunctional mitochondrial related diseases.[23, 24]

We and others have previously demonstrated the formation of artificial synapses on different substrates. Both planar and spherical substrates have been employed in these studies.[16, 17, 18, 19, 20, 25, 26, 27]

Spherical substrates are a powerful tool for interrogating and interfacing with cells. The formation of synapses on artificial substrates such as planar lipid bilayers requires that the cells either grow directly on these substrates or are grown separately in culture and added to the substrates at the appropriate time.

This is extremely difficult to achieve with many adherent cells, in particular, neurons, which must be grown in culture for at least 1 week before they are capable of forming synapses. Also, once mature, neurons cannot be detached from their original growth substrate and placed onto another substrate. Thus, spherical substrates, which can be modified as desired and then added to the cells at a specific point in time, allow cells to interface with artificial substrates at any time, without disturbing the growth environment of the cells.[19, 20] Spherical substrates provide enhanced imaging possibilities as well as the opportunity for applying other characterization techniques.

This is especially true when functionality studies were performed on artificial presynaptic boutons in culture and in isolated forms.[19, 28] Importantly, spherical substrates also provide the advantage of accessing different radii of curvature simply by using different size beads.[29]

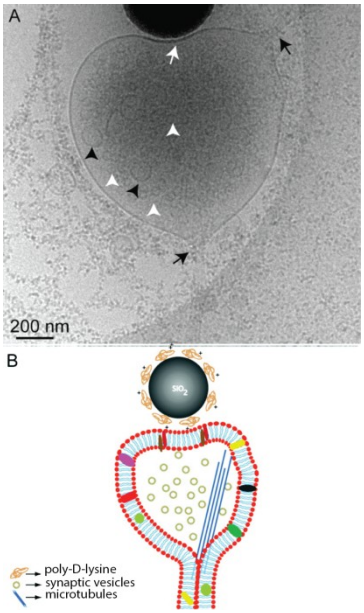

Figure AI.3 Representative cryo-EM image (A) showing an artificial synapse formed between hippocampal neurons (DIV 8) grown on a sterile, PLL coated Au/Quantifoil grid and poly-D-lysine coated 500 nm silica bead. Only part of the bead is seen in this image. The white arrow indicates the contact area at the synaptic junction. Synaptic vesicles are more clearly visualized (white arrowheads) in this image as compared to Fig. AI.1. The larger vesicles (black arrowheads) could be the transport vesicles. Black arrows show the direction of the axonal shaft growth. (B) Sketch depicting the structural components of the artificial synapse seen in A.

AI.4 Conclusions

The design of substrates for artificial synapse formation is of great interest both in applied and in fundamental aspects of *in vitro* studies involving synaptogenesis. However, studies to date have focused mainly on functional similarities between native and artificial synapses and thus often have not pursued the direct visualization of the structural details. Maintaining the surface chemistry constant on smaller size silica beads allows one to perform label-free visualization of artificial synapses using cryo-EM. The membrane contact area, synaptic vesicle pool, as well as microtubular networks that are essential components at a functional presynapse are clearly visible, showing the validity of our interpretation.

In summary, a cryo-EM approach has been utilized here for direct visualization of artificial synapses formed on different substrates. This is the first report to date that establishes the ultrastructural details of a chemically induced artificial synapse. Given the considerable interest in identifying structural and functional requirements for neuroregenerative approaches, this work confirms the structural details of artificial synapses.

AI.5 Experimental Section

AI.5.1 Primary Cultures of Rat Hippocampal Neurons on EM grids

Hippocampal neurons were dissected from rat embryos (embryonic day 17-18) and dissociated to a single cell suspension using a modification of a protocol described previously by Kaech and Banker.10 Neurons were cultured on sterile, PLL-coated Au/Quantifoil EM grids (Electron Microscopy Sciences, Hatfield, PA) together with sterile, PLL-coated coverslips in Neurobasal medium, as described below. Prior to use, the EM grids were immersed in ethanol for 15 min and washed several times using Milli-Q water. They were then cleaned with air plasma in a plasma cleaner (Harrick Plasma, Ithaca, NY) in order to remove any remaining contaminants and to make them more hydrophilic. The dissociated hippocampal neurons were resuspended in Neurobasal culture medium supplemented with *l*-glutamine and B27 at a density of 250 000 cells/mL, and a small drop of this cell suspension was added in a Petri dish containing EM grids and coverslips (6 and 80 μL, respectively). After 3-4 h in the incubator at 37 °C/5% CO_2, 3-4 mL of Neurobasal culture medium was added to the entire dish and the dish was returned to the incubator and kept for 7 or more days *in vitro* (DIV) prior to imaging, while replacing one-third of the medium every 3-4 days. All culture media were purchased from Gibco (Invitrogen). All animal work was performed in accordance with the Canadian Council on Animal Care Guidelines.

AI.5.2 Preparation of Poly-D-lysine Coated Beads

Silica beads of 500 nm (Bangs Laboratories) were diluted to a concentration of 3×10^6 particles/mL in PBS, washed twice in PBS by centrifugation, resuspended, and then incubated in 1 mL of PBS containing 0.05 mg/mL poly-D-lysine overnight at 4 ˚C. The poly-D-lysine treated beads were then washed several times in PBS by centrifugation.

AI.5.3 Co-culture with Silica Beads

A total of 5 μL of the poly-D-lysine coated silica bead solution (sterile PBS, pH 7.4) was added to the neural culture dish directly on top of the TEM grids. The bead/cell coculture was returned to the incubator and left at 37 ˚C/5% CO_2 for 24 h prior to freezing of the sample.

AI.5.4 Cryo-EM

The grids were taken directly from the incubator and were frozen immediately. A total of 5 μL solution of neural culture media was added to the EM grid held by tweezers, blotted, and then frozen hydrated by plunging into a bath of liquid ethane slush.[21] The Frozen TEM grids were stored at −180 °C until ready to image. A 626 Single Tilt Cryotransfer System (Gatan Inc.) was used to transfer the EM-grids, which were observed with a FEI G2 F20 cryo-STEM microscope operated at 200 kV (FEI, Inc.). Images were recorded under low dose conditions on a Gatan Ultrascan 4k × 4k digital (CCD) camera system camera.

AI.5.5 Cryo-EM Images

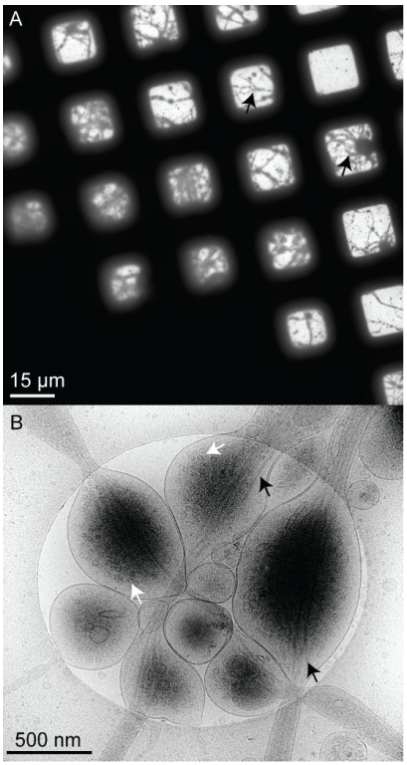

Figure AI.4 Representative cryo-EM images showing hippocampal neurons grown on Quantifoil/Au EM-grids. A low magnification image (A) showing overall neuronal growth on the grid that span over several squares (black arrows). A high magnification image (B) of neurons passing through one of the holes in these squares. Microtubules (black arrows) and synaptic vesicles (white arrows) are visible in this image.

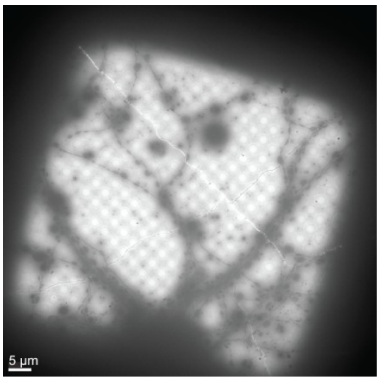

Figure AI.5 A representative cryo-EM image showing hippocampal neurons grown on Quantifoil/Au EM-grids. This low magnification image shows overall neuronal growth on the grid that span over several holes in a single square. As seen in this image, neuronal processes are extending over large length scales.

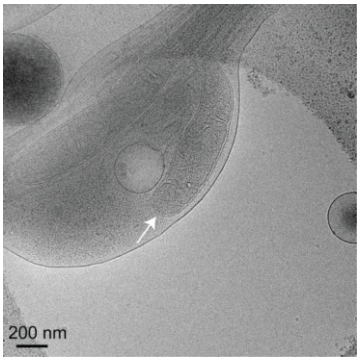

Figure AI.6 Representative cryo-EM image of a hippocampal neuron grown on Quantifoil/Au EM-grids. In this image mitochondria is clearly visible (white arrow).

AI.6 References

1. Cowan, W. M.; Südhof, T. C.; Stevens, C. F., Eds. *Synapses*, Johns Hopkins University Press: Baltimore, **2001**.

2. Dustin, M. L.; Colman, D. R. Neural and immunological synaptic relations. *Science* **2002,** *298*, 785-789.

3. Bury, L. A. D.; Sabo, S. L. Coordinated trafficking of synaptic vesicle and active zone proteins prior to synapse formation. *Mol. Interventions* **2010,** *10*, 282-292.

4. Agnati, L. F.; Zoli, M.; Stromberg, I.; Fuxe, K. Intercellular communication in the brain: wiring *versus* volume transmission. *Neuroscience* **1995,** *69*, 711-726.

5. Clemens, J. D. Transmitter timecourse in the synaptic cleft: its role in central synaptic function. *Trends Neurosci.* **1996,** *19*, 163-171.

6. Savtchenko, L. P.; Rusakov, D. A. The optimal height of the synaptic cleft. *Proc. Natl. Acad. Sci. USA* **2007,** *104*, 1823-1828.

7. Fletcher, T. L.; Decamilli, P.; Banker, G. J. Synaptogenesis in hippocampal cultures: evidence indicating that axons and dendrites become competent to form synapses at different stages of neuronal development. *Neurosci.* **1994,** *14*, 6695-6706.

8. Jontes, J. D.; Buchanan, J.; Smith, S. J. Growth cone and dendrite dynamics in zebrafish embryos: early events in synaptogenesis imaged *in vivo*. *Nat. Neurosci.* **2000,** *3*, 231-237.

9. Fuger, P.; Behrends, L. B.; Mertel, S.; Sigrist, S. J.; Rasse, T. M. Live imaging of synapse development and measuring protein dynamics using two-color fluorescence recovery after photo-bleaching at Drosophila synapses. *Nat. Protoc.* **2007,** *2*, 3285-3298.

10. Di Biase, V.; Obermair, G. J.; Flucher, B. Resolving sub-synaptic compartments with double immunofluorescence labeling in hippocampal neurons. *J. Neurosci. Methods* **2009,** *176*, 78-84.

11. Rostaing, P.; Real, E.; Siksou, L.; Lechaire, J. P.; Boudier, T.; Boeckers, T. M.; Gertler, F.; Gundelfinger, E. D.; Triller, A.; Marty, S. Analysis of synaptic ultrastructure without fixative using high-pressure freezing and tomography. *Eur. J. Neurosci.* **2006,** *24*, 3463-3474.

12. Leitch, B. Ultrastructure of electrical synapses. *Electron Microsc. Rev.* **1992,** *5*, 311-339.

13. Staehelin, L. Structure and function of intercellular junctions. *Int. Rev. Cytol.* **1974,** *39*, 191-283.

14. Fernandez-Busnadiego, R.; Zuber, B.; Maurer, U. E.; Cyrklaff, M.; Baumeister, W.; Lucic, V. Quantitative analysis of the native presynaptic cytomatrix by cryoelectron tomography. *J. Cell Biol.* **2010,** *188*, 145-156.

15. Lucic, V.; Yang, T.; Schweikert, G.; Forster, F.; Baumeister, W. Morphological characterization of molecular complexes present in the synaptic cleft. *Structure* **2005,** *13*, 423-434.

16. Burry, R. W. Presynaptic elements on artificial surfaces. A model for the study of development and regeneration of synapses. *Neurochem. Pathol.* **1986,** *5*, 345-360.

17. Blau, A.; Weini, C.; Mack, J.; Kienle, S.; Jung, G.; Ziegler, C. Promotion of neural cell adhesion by electrochemically generated and functionalized polymer films. *J. Neurosci. Methods* **2001,** *112*, 65-73.

18. Xiong, Y.; Zeng, Y. S.; Zeng, C. G.; Du, B. L.; He, L. M.; Quan, D. P.; Zhang, W.; Wang, J. M.; Wu, J. L.; Li, Y.; Li, J. Synaptic transmission of neural stem cells seeded in 3-dimensional PLGA scaffolds. *J. Biomater.* **2009,** *30*, 3711-3722.

19. Lucido, A. L., Sanchez, F. S., Thostrup, P., Kwiatkowski, A. V., Leal-Ortiz, S., Gopalakrishnan, G.; Liazoghli, D.; Belkaid, W.; Lennox, R. B.; Grutter, P.; Garner, C. C.; Colman, D. R. Rapid assembly of functional presynaptic boutons triggered by adhesive contacts. *J. Neurosci.* **2009,** *29*, 12449-12466.

20. Gopalakrishnan, G.; Thostrup, P.; Lucido, A. L.; Belkaid, W.; Rouiller, I.; Colman, D. R.; Lennox, R. B. Lipid bilayer membrane-triggered presynaptic vesicle assembly. *ACS Chem. Neurosci.* **2010,** *1*, 86-94.

21. Dubochet, J.; Adrian, M.; Chang, J. -J.; Homo, J.-C.; Lepault, J.; McDowall, A. W.; Schultz, P. Cryo-electron microscopy of vitrified specimens. *Q. Rev. Biophys.* **1988,** *21*, 129-228.

22. Kaech, S.; Banker, G. Culturing hippocampal neurons. *Nat. Protoc.* **2006,** *1*, 2406-2415.

23. Zhao, J.; Liu, T.; Jin, S.; Wang, X.; Qu, M.; Uhlén, P.; Tomilin, N.; Shupliakov, O.; Lendahl, U.; Nistér, M. Human MIEF1 recruits Drp1 to mitochondrial outer membranes and promotes mitochondrial fusion rather than fission. *EMBO J.* **2011,** *30*, 2762-2778.

24. Song, W.; Chen, J.; Petrilli, A.; Liot, G.; Klinglmayr, E.; Zhou, Y.; Poquiz, P.; Tjong, J.; Pouladi, M.; Hayden, M.; Masliah, E.; Ellisman, M.; Rouiller, I.; Schwarzenbacher, R.; Bossy, B.; Perkins, G.; Bossy-Wetzel, E. Mutant huntingtin binds the mitochondrial fission GTPase dynamin-related protein-1 and increase its enzymatic activity. *Nat. Med.* **2011,** *17*, 377-382.

25. Mossman, K.; Groves, J. *Chem. Soc. Rev.* **2007,** *36,* 46-54.

26. Pautot, S., Lee, H., Isacoff, E. Y., and Groves, J. T. *Nat. Chem. Biol.* **2005,** *1*, 283-289.

27. Baksh, M. M.; Dean, C.; Pautot, S.; DeMaria, S.; Isacoff, E.; Groves, J. T. *Langmuir* **2005,** *21*, 10693-10698.

28. Lucido, A. L.; Gopalakrishnan, G.; Yam, P. T.; Colman, D. R.; Lennox, R. B. Isolation of functional presynaptic complexes from CNS neurons: a cell-free preparation for the study of presynaptic compartments in vitro. *ACS Chem. Neurosci.* **2010,** *1*, 535-541.

29. Gopalakrishnan, G.; Rouiller, I.; Colman, D. R.; Lennox, R. B. Supported bilayers formed from different phospholipids on spherical silica substrates. **2009** *Langmuir 25*, 5455-5458.

Linking Statement to Appendix II

Appendix II demonstrates the use of SS-BLMs as a suitable platform for incorporating molecular scaffolds (specifically 3D-DNA cages) and investigates their interactions with lipid membranes. This study aims to address the assembly and dynamics of DNA scaffolds in a biomimetic membrane model. SS-BLMs are therefore used as a robust simplified membrane environment where DNA/membrane interactions can be reproducibly investigated. The ease of SS-BLM characterization using fluorescence imaging is applied to examine the incorporation of 3D-DNA-cholesterol cages into a bilayer membrane. In addition, FRAP is used to assess their dynamics in a membrane environment. This proved to be useful for tuning the design of these DNA scaffolds for specific application. Functional DNA scaffolds developed for biological applications can benefit from the ability of the SS-BLM platform to serve as physically stable and experimentally accessible cell interfaces.

Appendix II

Dynamic Behavior of DNA Cages Anchored on Spherically Supported Lipid Bilayers

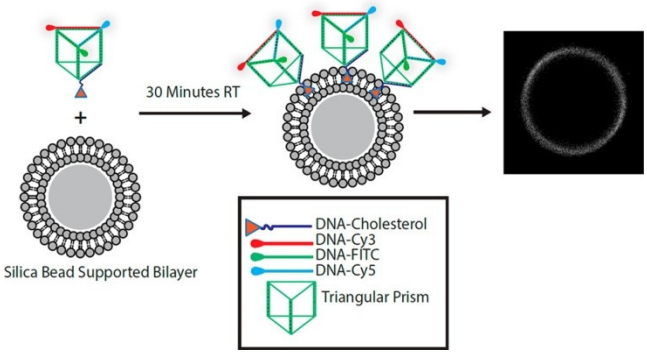

The following Appendix is reprinted with permission from "Dynamic Behavior of DNA Cages Anchored on Spherically Supported Lipid Bilayers", J. W. Conway, C. Madwar, T. G. Edwardson, C. K. McLaughlin, J. Fahkoury, R. B. Lennox, and H. F. Sleiman, J. Am. Chem. Soc., 2014, 136 (37), 12987-12997. The text below is a verbatim copy of the manuscript.

AII.1 Abstract

We report the anchoring of 3D-DNA-cholesterol labeled cages on spherically supported lipid bilayer membranes (SS-BLM) formed on silica beads, and their addressability through strand displacement reactions, controlled membrane orientation and templated dimerization. The bilayer-anchored cages can load three different DNA-fluorophores by hybridization to their "top" face (furthest from bilayer) and unload each of them selectively upon addition of a specific input displacement strand. We introduce a method to control strand displacement from their less accessible "bottom" face (closest to the bilayer), by adding cholesterol-substituted displacing strands that insert into the bilayer themselves in order to access the toehold region. The orientation of DNA cages within the bilayer is tunable by positioning multiple cholesterol anchoring units on the opposing two faces of the cage, thereby controlling their accessibility to proteins and enzymes. A population of two distinct DNA cages anchored to the SS-BLMs exhibited significant membrane fluidity and have been directed into dimer assemblies on bilayer *via* input of a complementary linking strand. Displacement experiments performed on these anchored dimers indicate that removal of only one prism's anchoring cholesterol strand was not sufficient to release the dimers from the bilayer; however, removal of both cholesterol anchors from the dimerized prisms *via* two displacement strands cleanly released the dimers from the bilayer. This methodology allows for the anchoring of DNA cages on supported lipid bilayers, the control of their orientation and accessibility within the bilayer, and the programmable dimerization and selective removal of any of their components. The facile coupling of DNA to other functional materials makes this an attractive method for developing stimuli-responsive protein or nanoparticle arrays, drug releasing biomedical device surfaces and self-healing materials for light harvesting applications, using a highly modular, DNA-economic scaffold.

AII.2 Introduction

DNA nanostructures have shown tremendous promise for the precise organization of functional materials.[1, 2, 3, 4] In order to integrate them into devices for diagnostic assays,[5, 6, 7, 8] optoelectronic,[9] plasmonic circuitry[10, 11, 12] or biomedical applications,[13, 14, 15, 16, 17, 18] it will be important to transition these structures from solution to solid surfaces. DNA structures have been typically immobilized on hard surfaces (such as gold or silicon),[2, 19] but these rigid surfaces diminish or completely shut down the 2D-diffusion of tethered DNA and serve as a significant

steric and diffusion barrier. On the other hand, lipid bilayers present a soft, fluid two-dimensional substrate that can effectively interface with numerous solid substrates.[4, 20, 21, 22] Anchoring DNA nanostructures to these bilayers may preserve their dynamic character, and depending on the lipid composition and experimental conditions, would allow 2D-motion of these structures with tunable kinetics.

DNA strands positioned on lipid membranes have been used in a variety of contexts. They can act as tethers of lipid vesicles to planar bilayers,[22] as mediators of vesicle fusion in analogy to SNARE proteins,[23, 24] as guides for the formation of "designer" microtissues from DNA tagged cells,[11] and as templates for the formation of supramolecular vesicle networks.[23, 24] DNA nanostructures anchored in lipid membranes have been shown to mimic the behavior of nanopore forming proteins[26, 27] and the properties of photosynthetic systems.[1, 28] Peptide nucleic acid-DNA hybrid structures can cluster in specific lipid domains, and this clustering can be changed to other domains with the addition of nucleases that degrade the DNA component.[29] Two studies have recently examined dynamic behavior of 2D-DNA origami structures on lipid bilayers, by photochemically switching the association of hexagonal origami tiles, or by hybridization of origami "barges" that are held at a distance from the lipid bilayer membrane.[30, 31] Another study using cholesterol functionalized DNA origami helical bundles examined the dynamics of these structures on free-standing bilayers while varying the buffer salt concentrations, and the consequent domain partitioning.[33]

We here report the association, dynamic behavior, hybridization and lift-off of cholesterol-labeled three-dimensional DNA cages on spherically supported lipid bilayer membranes (SS-BLMs) formed on silica beads. The anchored cages present two faces: a "top" accessible face furthest from the bilayer, and a "bottom" face closest to the bilayer. They can readily load different DNA-fluorophores on their top face and selectively unload each of them upon addition of a specific displacing strand. On the other hand, the bilayer membrane provides a steric barrier for the bottom face of the DNA cages nearest the lipid environment. We introduce a method to control the less sterically accessible bottom face, by using displacing DNA strands that can partially insert into the bilayer themselves *via* cholesterol modification. We show the ability to control the orientation of the cages within the bilayer by varying the position and number of cholesterol substituents, thereby tuning enzyme accessibility to the cages. In chemical terms, the spherical bilayer can serve as a versatile and tunable "protecting group" for DNA nanostructures.

Finally, we show the efficient on-bilayer diffusion of DNA cages, as well as their ability to dimerize by hybridization on the lipid bilayer. The resulting dimer prism is doubly anchored to the bilayer. Lifting off one of its two component prisms is not sufficient to release the dimer from the bilayer; however, removing both anchored prisms with two displacement strands cleanly released the dimer from the bilayer. The 3D-structures used here are DNA-minimal, fully dynamic and appear to be intimately coupled to the lipid bilayer, rather than floating on its surface. Because of the ease of coupling DNA to other functional materials, this approach has the potential to produce stimuli-responsive protein arrays, molecule-responsive drug releasing biomedical device surfaces, and self-healing materials for optoelectronic or light harvesting applications.

AII.3 Design of the DNA Cage and Assembly Strategy

The DNA cages used in these experiments consist of three 96-base DNA strands or "clips". Each clip is designed so that its two 10 base ends are complementary to the back of the next clip, and the third clip is complementary to the back of the first clip. The result is that hybridization of the three strands leads to a closed triangular prism (TP),[33] Fig. AII.1 (see the Experimental Section AII.13.3). This cage possesses 6 single stranded (ss) 20-base binding regions (green) with different sequences. The top ss regions are used to hybridize to DNA strands carrying fluorescent labels (Cy3, Cy5, and Alexa488), while the bottom face hybridizes to a DNA strand that carries a cholesterol anchor. The result is an amphiphilic 3D architecture (Fig. AII.2).

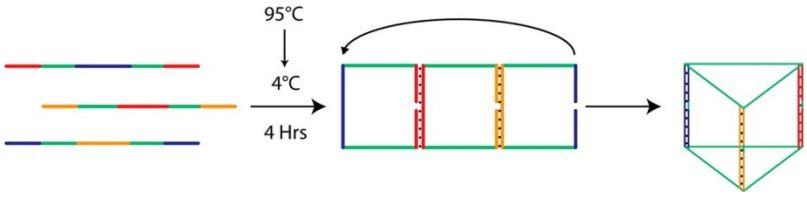

Figure AII.1 Clip-by-clip assembly of TP scaffold.

All short oligonucleotides designed to hybridize to the ss regions of the cage consist of the complementary 20 base region followed by a 6-base extension and chemical modification at either the 5′/3′ end (Fig. AII.2). The 6-base extension serves as a toehold initiation point for strand displacement of the 26mer DNA-conjugates from the scaffold. In this way, each of the

modified DNA strands can be selectively displaced from the prism by the addition of a strand that is fully complementary to the 26-base stretch (Fig. AII.2A).[33] Using this writing and erasing capability, we will compare the binding and removal of functional DNA-conjugates from a prismatic scaffold in solution and within a lipid bilayer environment.

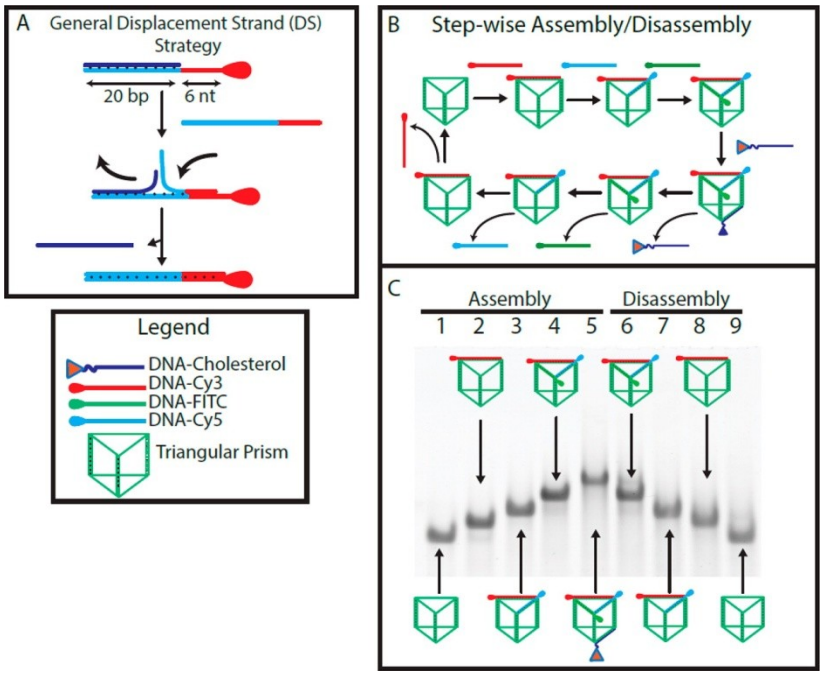

Figure AII.2 (A) Schematic representation of the displacement strategy. (B) Representation of the stepwise assembly/disassembly on a DNA triangular prism scaffold. (C) Nondenaturing polyacrylamide gel electrophoresis showing the stepwise addressability of the triangular DNA scaffold and its disassembly *via* strand displacement. Lane 1: TP scaffold, lane 2: previous + Cy3, lane 3: previous + Cy5, lane 4: previous + Alexa488 (A488), lane 5: previous + cholesterol anchor, lane 6: previous, displace cholesterol anchor, lane 7: previous, displace A488, lane 8: previous, displace Cy5, lane 9: previous, displace Cy3.

AII.4 In Solution Hybridization and Displacement of Fluorescent Labels and Cholesterol Anchors on the DNA Cage

To form the DNA cages, all strands were combined in one pot and annealed from 95 to 10 ˚C, over 4 h (see Experimental Section AII.13.3). Assembled structures were characterized by native polyacrylamide gel electrophoresis (Fig. AII.2C). Lane 1 shows a single band corresponding to the assembled DNA cage formed using three 96mer strands, indicating that the prism structure is the single major product formed in near quantitative yield. Lanes 2–5 show the sequential hybridization of the ss regions to three fluorescently labeled DNA strands on the top face and a

single cholesterol anchor-substituted strand on the bottom face. The band pattern indicates that the addition of each DNA-conjugate is accompanied by a corresponding decrease in gel mobility. This confirms the formation of the 3D triangular scaffold and successful loading of three different fluorescent tags and the cholesterol anchor unit.

Lanes 6–8 represent the sequential displacement of three bound fluorophore-DNA strands and the cholesterol-DNA in solution using four different displacement strands (DS). In each of these experiments, the fully loaded prism scaffold (lane 5) was used, and the required DSs were added in 3-fold excess relative to the target strand. The mixtures were incubated for 30 minutes at room temperature. The increase in gel mobility seen in lanes 6–9 corresponds to the stepwise formation of the initial ss DNA cage. In this way the fully functional DNA cage can be assembled and then disassembled using the correct series of chemical inputs.[35]

AII.5 Anchoring the DNA Cages on the Lipid Bilayer

In this study, we used SS-BLMs composed of the synthetic phospholipid 1,2-dioleoyl-*sn*-glycero-3-phosphatidylcholine (DOPC) on 5 μm silica beads, as a model lipid bilayer membrane.[3] Similar lipid bilayer systems have been used as nanovectors,[37] for protein screening,[38, 39] and as artificial supports for inducing functional neural synapse formation.[40] SS-BLMs offer many desirable features as biomembrane model systems in comparison to their vesicle counterparts. They have increased mechanical stability and control of particle size and reproducibility. They can also be readily concentrated into a pellet by centrifugation and washed without compromising the membrane integrity. Such manipulations are highly problematic with the related giant unilamellar vesicles (GUVs).[42] In comparison to planner supported bilayer membranes, SS-BLMs are considerably easier to manipulate and examine using a variety of microscopy and spectroscopy techniques that are not available for substrates with a planar geometry.[42, 43] Silica beads are also ideal for interfacing with biological systems due to their chemical inertness and biocompatibility.[37, 40] Finally, mesoporous silica particles have been used for finely controlled drug release and have been coupled to lipid bilayer membranes.[39]

Solutions of annealed DNA cages with cholesterol anchors (cholesterol anchor has 20 nt prism binding region and 6 nt toehold (26 nt version)) were combined with the bilayer coated bead solution in buffer. In general, the sample preparation using a large excess of DNA cages ensures that the beads are completely covered in a homogeneous layer of DNA cages as seen in Fig.

AII.5. After 15 minutes of incubation, the beads/DNA were centrifugated to remove any unbound DNA cage or DNA-conjugate (see Experimental Section AII.13.4 for preparation details). The amount of functionalized DNA prism bound to the SS-BLMs can be determined through fluorescence intensity quantification of the supernatant solution after prism release from the bilayer (see below, and Experimental Section AII.13.5). It was determined that 5.9×10^{-13} ($\pm 0.2 \times 10^{-13}$) mol of labeled TP were lifted off and collected from the surface of the beads. This represents 4% of the initial amount of DNA cage that was incubated with the SS-BLMs; therefore, there is approximately 6.6×10^5 labeled TP/bead or 8.4×10^3 TP/μm^2, based on the size of the SS-BLMs. On the basis of the approximate area of each prism, we predicted 4.7×10^4 TP/μm^2. This data implies partial but homogeneous coverage (see Fig. AII.5) of the spherically supported bilayer lipid membranes (SS-BLMs) with the DNA cages.

AII.6 Confocal Fluorescence Imaging of 3D DNA Constructs and Membrane Mobility

Figure AII.3 shows a typical confocal fluorescence image of a DNA prism functionalized with a single fluorophore and cholesterol anchor loaded on the DOPC SS-BLM. The image shows a homogeneous distribution of fluorescence intensity within the SS-BLM. A series of control samples served to investigate possible off-target membrane interactions from partially assembled functionalized DNA cages as well as the single-stranded fluorophore-labeled oligonucleotides. In all cases, a measurable and reproducible fluorescence signal is only observed for the fully assembled DNA cage containing both a hybridized fluorophore and cholesterol anchor.

It has been shown that DNA is able to bind to zwitterionic lipid mono/bilayers in the presence of divalent cations.[31] This work has compared the absorption of the DNA structures to a supported lipid bilayer with and without the cholesterol anchors and has determined that although there are some nonspecific interactions between the DNA and the lipids, the addition of the cholesterol anchors significantly increases the amount of landed DNA structure. Nonspecific binding may also be occurring in our system, but the washing steps during sample preparation minimize this binding. Furthermore, imaging conditions for all beads were kept constant for all samples to allow consistent comparison of fluorescent intensities. It should be noted that at higher laser power some residual fluorescence was observed in the bilayer, and that even after our lift-off experiments (Fig. AII.5) there remains some residual fluorescence on the vesicles. Both of these observations may be attributed to some nonspecific binding of DNA to the lipid bilayer.

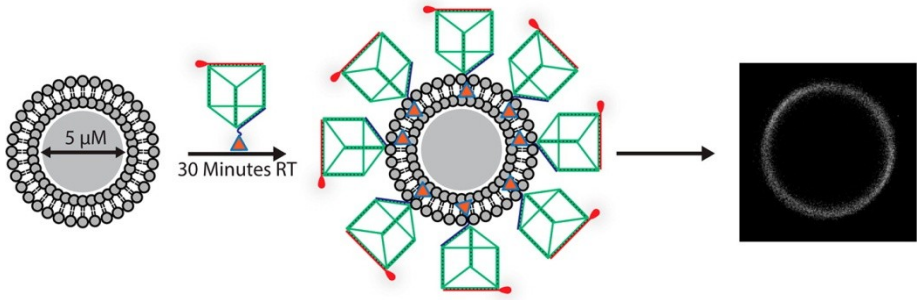

Figure AII.3 Representation of labeled system (left, not shown to scale) and a confocal fluorescent image of an SS-BLM (right).

The mobility of our prismatic scaffold within the bilayer environment was confirmed using fluorescence recovery after photobleaching (FRAP). Comparative FRAP measurements allow quantification of 2D-diffusion of the DNA cages that are anchored (26 nt version) within the supported lipid bilayers. This involves determining the mobility of a fluorescently labeled DNA cage anchored *via* cholesterol into a fluid SS-BLM lipid membrane formed from DOPC phospholipids (melting point of −20 ˚C) and comparing it to the mobility of a fluorescent lipid analogue (Bodipy-PC) in DOPC SS-BLM (see Experimental Section AII.13.6).

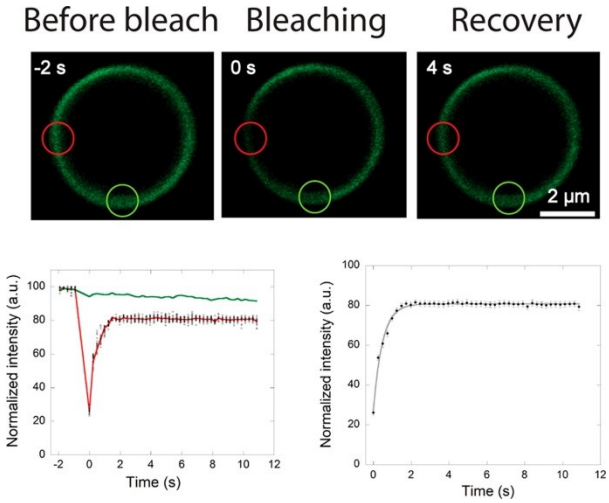

Figure AII.4 FRAP data. (Top) Images of DOPC SS-BLMs containing Alexa488 functionalized DNA cages before and after photobleaching a 1.3 µm spot, indicated by the red circle. A reference spot of the same size indicated by the green circle is used to correct for bleaching caused by imaging. (Bottom left) Individual FRAP data from 20 separate experiments, the averaged FRAP curve of the complete data set of 50 separate experiments (red) and the mean reference curve (green). All FRAP data are normalized to the prebleaching fluorescence. (Bottom right) The averaged FRAP data (and standard error values) fit to a one diffusing component model (*R* value of 0.994).

Figure AII.4 shows a FRAP study for DOPC SS-BLM containing Alexa488-functionalized DNA cages. Recovery of fluorescence intensity was evident, indicating that the DNA cages are mobile and able to diffuse in and out of the bleached spot on a timescale comparable to the control fluorescent lipid molecules (0.472 s for fluorescent DNA conjugates *vs* 0.377 s for fluorescent lipid analogues). Furthermore, this timescale for fluorescence recovery is in good agreement with previous measurements on labeled SSBLMs.[4, 43] The values of diffusion coefficients (*D*), half-life of fluorescence recovery (τ), as well as a ratio of mobile to immobile species are summarized in Table AII.1

Table AII.1. Summary of SS-BLM/DNA diffusion parameters.

Lipid System	Diffusion Half-time τ (s)	Diffusion constant *D* ($\mu m^2/s$)[a]	Mobile fraction (%)
Alexa488-DNA-CHOL	0.472	0.802	80.8±0.2
Bodipy-PC	0.377	1.00	95.9±0.3

[a] For details on fit model equations and calculations of diffusion coefficient, refer to the Experimental Section AII.13.7.

For the bleached DNA fluorescent conjugate, an average recovery maximum of 80% of the initial fluorescence intensity was observed (taking into account the bleaching caused by imaging). This could be explained by aggregated cholesterol-anchored DNA cages within the supported bilayers contributing to a population of immobile species. Although slightly lower than the values previously reported,[4, 43, 44, 45] which range from 0.6 to 3 $\mu m^2/s$ depending on the sample, our measurements of 0.8 and 1 $\mu m^2/s$ for the prism and lipids are very similar. The difference is likely related to the supported bilayer system itself and was not the focus of this study. FRAP analysis was performed using the equation for a 2D diffusion model, which is an approximation for a spherical system. This is usually done for giant unilamellar vesicles as they are large enough that the surface is assumed to be close to planar. This assumption may not be the same for our system (5 μm diameter beads). However, these values are only used for a comparison rather than to report an absolute value. In addition, it is adequate to compare the half-life of recovery for lipids to that for DNA structures, because this value is measured directly

and not extrapolated from experiment using diffusion equations. Overall, the similar diffusion characteristics of the fluorescent DNA conjugate to those of the fluorescent lipid analogue in SS-BLMs suggest that they undergo similar diffusion kinetics within the SS-BLM system.[4, 43, 44, 45]

AII.7 Stepwise On-Bilayer Hybridization and Strand Displacement from the Top Face of DNA Cages

Many of the existing examples of DNA rearrangements on supported bilayers rely on temperature or enzymatically induced disassembly to initiate domain formation or component partitioning.[29, 3] Strand displacement events on the supported bilayer provide a method to control DNA-mediated membrane interactions using a large number of strand stimuli of different sequences. We thus investigated whether the bilayer anchored DNA cages (26 nucleotide version) would be able to undergo toehold-mediated displacement with added DNA strands. First, we examined lift-off of the strands hybridized to the prism face furthest from the bilayer.

To do this, we prepared SS-BLMs and anchored the cholesterol substituted DNA prism as above. We added the three DNA-fluorophore strands (Cy3, Cy5, and Alexa488) sequentially to the bound prisms, each time incubating for 15 minutes, washing the beads and then collecting them by centrifugation. Figure AII.5 summarizes the confocal fluorescence images collected after each addition. Rows A–F in Fig. AII.5 show that the DNA cage can be readily hybridized on the supported bilayer membrane to all three of the fluorescent DNA-labels in a stepwise fashion. Confocal images following each incubation step show a homogeneous fluorescent distribution on the bilayer. Overlay images for the sequential labeling additions show colocalization at each step for all fluorophores. This confirms that each prism is able to readily bind several components while associated with a lipid bilayer environment.

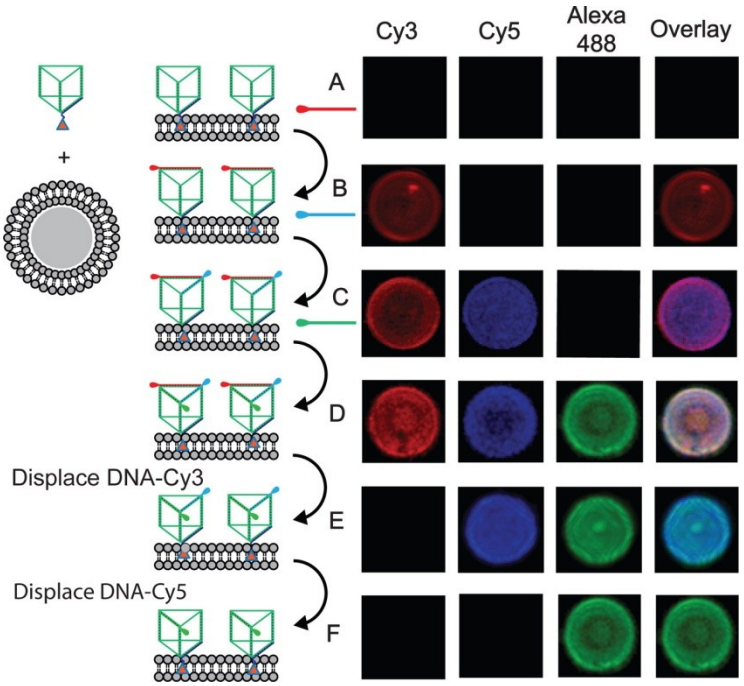

Figure AII.5 Confocal monitoring of the bilayer during the stepwise assembly and disassembly of the embedded triangular scaffold. Images are Z-stacked 2D images showing the 3D homogeneous morphology of the SS-BLMs. Row (A), addition of prism, row (B) Cy3 addition to anchored prisms, row (C) addition of Cy5, row (D) addition of Alexa488, row (E) addition Cy3 displacing strand, row (F) addition of Cy5 displacing strand. Steps A–D represent the assembly; steps E and F represent the disassembly.

We then added the displacement strands to remove the fluorophore labeled oligonucleotides sequentially from the embedded scaffold, as described above. Row E corresponds to the addition of the displacement strand for the DNA-Cy3 component, to the Cy3/Cy5/Alexa488 labeled prisms on the bilayers, followed by washing and centrifugation cycles. Row F corresponds to the same experiment with the displacement strand for the DNA-Cy5 component. Addition of the displacement strand results in the removal of the fluorophore from the anchored DNA cage and complete loss of the fluorescence signal for each corresponding targeted DNA-label. Following removal of the two fluorophores Cy3 and Cy5, only the single Alexa488 fluorophore is observed on the SS-BLM surface. This demonstrates that the top face of the DNA cage remains reversibly addressable while incorporated within a SS-BLM. Thus, functional components can be organized and selectively lifted off DNA cages anchored on bilayer membrane surfaces.

AII.8 Strand Displacement from the Bottom Face of DNA Cages

Displacement of the cholesterol anchor and subsequent release of the entire DNA cage from the SS-BLM surface was examined using a 6 bp toehold region on the DNA-cholesterol strand. This strand displacement would need to occur from the bottom face of the prism which is closest to bilayer, as shown in Figure AII.6. A triangular prism with a single DNA-Cy5 and a single DNA-cholesterol anchor was incorporated into the SS-BLM as described above.

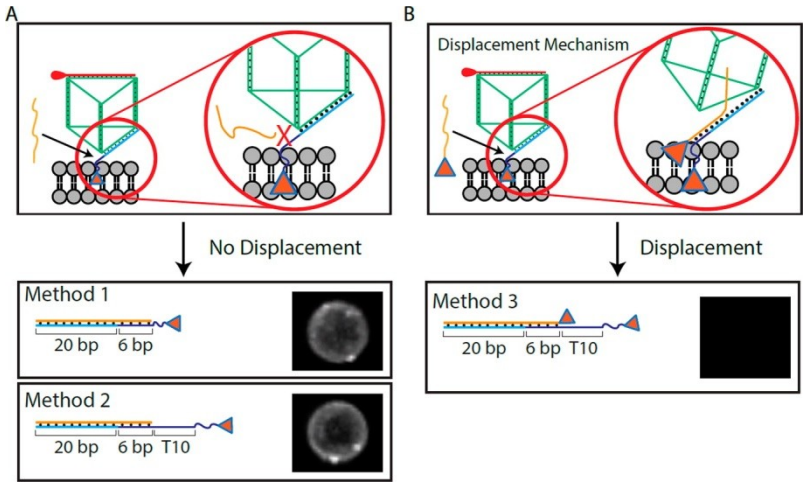

Figure AII.6 (A) Top, toehold displacement strategies for bottom face strand. (triangle represents cholesterol molecule) Bottom, design of toeholds: Method 1, the cholesterol labeled strand has a 6 base toehold closest to the cholesterol molecule. Method 2, the cholesterol labeled strand has an additional polythymidine (T10 spacer version) between the toehold and cholesterol units. The erasing strand (orange) is unsubstituted. (B) Top, in-bilayer toehold displacement strategy for bottom face strand. The erasing strand (orange) has a cholesterol unit (triangle), allowing it to anchor itself in the bilayer and gain access to the bottom face. Bottom, composition of toehold and erasing strand.

Our initial strategy (method 1, Fig. AII.6A) involved addition of an erasing strand fully complementary to the cholesterol-DNA (26 nt version) strand for 30 minutes, followed by washing. However, confocal images of the beads following this step displayed unchanged fluorescence intensity. This suggests that the six-base toehold is inaccessible to the displacing strand as it is located directly on the cholesterol anchor, which is embedded within the lipid bilayer. The displacement strand itself can effectively remove the DNA-cholesterol from the prism in solution, as confirmed by native polyacrylamide gel electrophoresis (PAGE) in Fig. AII.2 lane 6.

In a second attempt, we used a DNA-cholesterol anchor containing a polythymidine (T10 version) spacer between the cholesterol unit, and the toehold/binding region (Fig. AII.6A, method 2), in order to distance the toehold from the membrane cholesterol anchor. This modification however yielded similar results and the SS-BLMs retained their original fluorescence intensity, indicating that the T10 extension is insufficient to increase the toehold accessibility.

A third strategy (Fig. AII.6B, method 3) proved to be successful. This involves the use of a displacing strand that is itself functionalized with cholesterol, such that it is able to bind to the bilayer, and possibly achieve closer access to the bottom face of the prism. After addition of this cholesterol-DNA strand and washing, SS-BLMs with functionalized DNA prism exhibit near complete loss of fluorescence. This confirms that the erasing strand is now able to diffuse into the bilayer, find its complementary binding region and release the entire DNA assembly from the lipid bilayer surface (see below for analysis of the supernatant). Although displacement strategies have previously been used for removal of target strands in a DNA assembly, to our knowledge, this is the first example of a displacement strategy used within a lipid bilayer system to successfully release a 3D DNA cage. This strategy could not only be used for positioning and control of specific membrane components but could be extended to dynamically and selectively release any DNA macroassemblies that are anchored on a lipid bilayer.

AII.9 Enzyme Accessibility of DNA Cages on Bilayers

Biological applications using DNA cages assembled on supported bilayers are most likely to involve membrane protein interactions. In order to determine if the DNA scaffolds embedded within the SS-BLMs are accessible to enzymatic processing, DNase I, a nonspecific nuclease was added to prisms anchored (T10 spacer version) on this bilayer (30 minutes followed by washing).

Figure AII.7 summarizes the results for this assay. Column 1 represents confocal microscopy images of a standard DNA-bead solution before the addition of the nuclease, to confirm homogeneous fluorescent labeling. Column 2 is an image of the same DNA-bead solution containing prisms anchored *via* the T10 extended cholesterol anchor (see Fig. AII.6), incubated with DNase I. This image shows complete loss of the fluorescence signal, indicating that DNase

I is able to interact and digest the membrane bound DNA cages. This is in good agreement with similar studies involving fluorescently labeled duplex DNA constructs.[29]

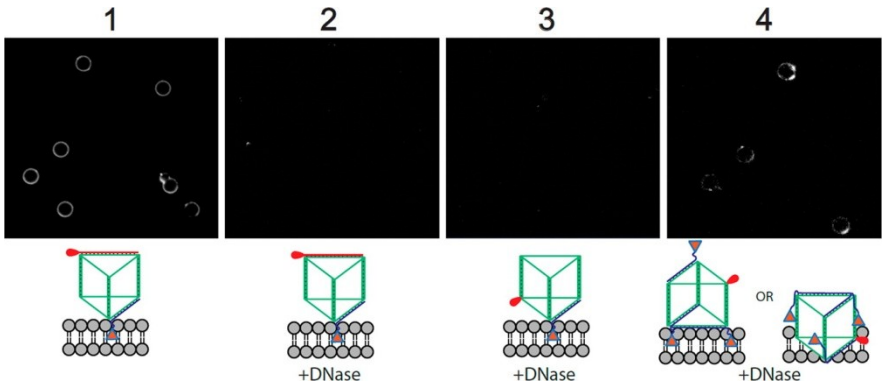

Figure AII.7 Confocal fluorescent images of the bilayer anchored triangular prism scaffold following DNase I incubation. (1) Hybridized Cy3 label on top face of prism (no DNase I). (2) Hybridized Cy3 label on top face of prism + DNase I. (3) Cy3 label as an internal modification on bottom face of prism + DNase I. (4) Cy3 label as an internal modification +3-Cholesterol anchors on the top and bottom faces of prism + DNase I.

To determine if only the topmost label binding region of the DNA scaffold is accessible for enzymatic degradation, we assembled a DNA prism containing an internalized Cy3 label, which is oriented on the bottom face of the prism and on the same side as the cholesterol-DNA anchor (T10 spacer version) (see Experimental Section AII.13.2). Following the enzyme treatment, loss of fluorescence is also observed (Fig. AII.7 column 3), which confirms that indeed the lower portion of scaffold (that is inaccessible to displacement strands, see Fig. AII.6) is being digested and not just the hybridized top label.

Lastly (Fig. AII.7, column 4), the labeled scaffold was again used. However, it was functionalized with 3 cholesterol anchoring units (T10 spacer version), two positioned on the bottom and one positioned on the top face (see Experimental Section AII.13.2 for DNA sequences). This arrangement of cholesterol units can potentially generate orientations that increasingly bury the DNA scaffold within the membrane, rendering it less accessible to nuclease degradation. There remains a significant amount of fluorescence intensity associated with the bilayer following enzyme incubation (Fig. AII.7, column 4), although it is slightly reduced when compared to the control sample. This indicates that the DNA construct is now only partially

accessible to nuclease degradation. Future work will examine the orientation and penetration depth of the DNA cage within the bilayer.

The modular nature of the DNA cage construction demonstrated here allows for orientational control of the cholesterol units on this scaffold. In turn, this control can be used to tune the position of the DNA cage either on the bilayer surface or deeper within the bilayer. Thus, cages can be more or less accessible to proteins based on their substitution patterns. This may also affect their ability for cellular internalization, when used as drug or oligonucleotide delivery vehicles.

AII.10 In Solution Dimerization of Prism Scaffolds

To expand the DNA/SS-BLM technology for biological and materials applications that require patterning or clustering of these cages on the bilayer, we investigated the reversible dimerization of the DNA cages associated with the bilayer environment. In this regard, we created two prisms (TP-A and TP-B), one functionalized with Cy3 and the second with Cy5 (Fig. AII.8A). Each prism is designed to hybridize a strand containing a 15 base overhang sticky-end, such that an added linking strand can dimerize the two prisms through the overhang components. The linking strand used hybridizes each 15 base overhang, and contains a 5 nt toehold allowing for its dynamic removal from the assembly and consequent dimer dissociation. Each prism is labeled with a unique DNA-cholesterol anchor (T10 spacer version) on the opposite face, and these anchors also contain overhang sequences. Thus, the prisms can individually be removed from the bilayer by using specific displacement strand inputs.

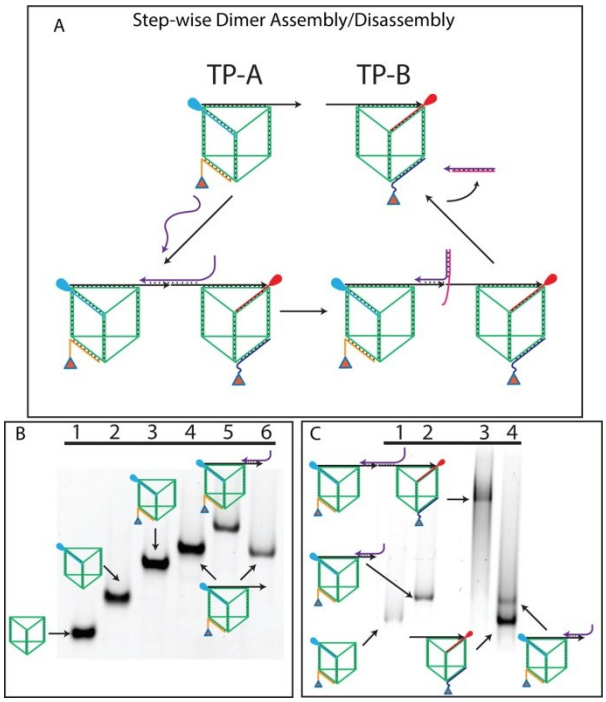

Figure AII.8 (A) Representation of the stepwise dimer assembly/disassembly. (B) Native PAGE results showing the stepwise loading of the scaffold. Lane 1: TP, lane 2: previous + Cy5 (blue), lane 3: previous + cholesterol anchor (yellow), lane 4: previous + overhang sticky-end (black), lane 5: previous + linking strand (purple), lane 6: previous displace the linking strand. (C) Native PAGE showing stepwise dimer assembly/disassembly. Lane 1: TP-A + Cy5 + cholesterol anchor + overhang, lane 2: TP-B + Cy5 + cholesterol anchor + overhang + linking strand, lane 3: samples in lane 1 and 2 are combined to form the dimer (12 h RT), lane 4: previous + linker displacement to recover monomers.

Figure AII.8B shows the stepwise assembly of all components on the DNA scaffold. Lanes 2, 3, and 4 show the corresponding decrease in gel mobility as the fluorescent tag, cholesterol anchor, and the overhang strand providing the sticky-end are assembled on one of the prisms (TP-A). Lanes 5 and 6 show the addition and consequent displacement of the final linking strand in solution on TP-A (TP-B assembles with the same efficiency, data not shown). In solution, dimerization of TP-A and TP-B is demonstrated in Fig. AII.8C, in which TP-A, prefunctionalized with all components including the linking strand (lane 1), is combined with TP-B, which is also preassembled with all necessary strands except the linking strand (lane 2). Lane 3 represents the dimerization of these two structures following 12 h of incubation at room temperature and shows a band with a corresponding decrease in gel mobility. The linker displacement strand was then added to the assemblies in 2.5 equiv leading to recovery of the initial starting components, as seen in lane 4 by the two bands with comparable mobility to lanes

1 and 2. The diffuse bands in this gel likely arise from lower dimerization efficiency of the two prisms in solution and/or partial dissociation of the TP dimer as it moves down the gel.

AII.11 Dimerization and Lift-off of the Prisms on the Bilayer

SS-BLMs in these experiments were prepared by combining a 1:1 mixture of TP-A (Cy5-labeled) and TP-B (Cy3-labeled) and anchoring them together on the beads. Figure AII.9B, row 1 shows representative confocal microscopy images of the beads in the two Cy3/Cy5 fluorescent channels.

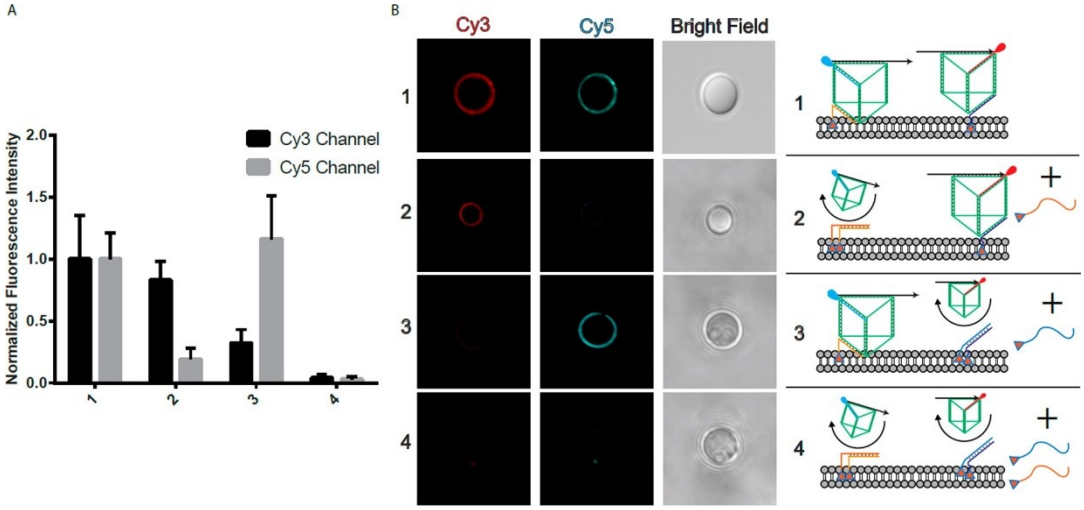

Figure AII.9 (A) Normalized fluorescence intensity measurements for rows 1 to 4 from (B). (B) Confocal fluorescent images of individual prism bilayer lift-off in a mixed prism population: Row 1: Control sample TP-A(Cy5) + TP-B(Cy3) no linker. Row 2: Displace TP-A (Cy5). Row 3: Displace TP-B (Cy3). Row 4: Displace both prisms.

Initial experiments confirmed that each individual prism population can be addressed within this mixed prism bilayer. In Fig. AII9B row 2, the cholesterol-labeled displacement strand for prism TP-A is added, and the images show bead fluorescence only in the Cy3 channel, consistent with TP-A removal. Row 3 shows the selective lift-off of prism TP-B and disappearance of the Cy3 fluorescence. Finally in row 4 both of the displacement strands are added, and we observe complete loss of fluorescence as both of the prism groups are released from the bilayer surface. Analysis of the fluorescence intensity of the beads, as monitored during the displacement and prism removal events, are shown in Fig. AII.9A and correlate with the captured images.

We then added an equimolecular amount of linking strand to these SS-BLMs in order to induce prism dimerization (Fig. AII.10, row 1). Successfully dimerized prisms should contain 2 cholesterol anchor points to the bilayer. If only a single DNA-cholesterol anchor is displaced, the remaining anchor may continue to hold the assembly on the bilayer. Figure AII.10 rows 2 and 3 show the results of performing a single anchor displacement on the dimerized DNA cages. When either TP-A or TP-B is addressed with its specific anchor displacement strand, we see that the beads remain fluorescent in both label channels. Quantitative analysis, Fig. AII.11, carried out for sample populations of at least 50 beads shows that the ratio of Cy3:Cy5 fluorescence is maintained, in agreement with the continued presence of the prism dimer that is now singly anchored.

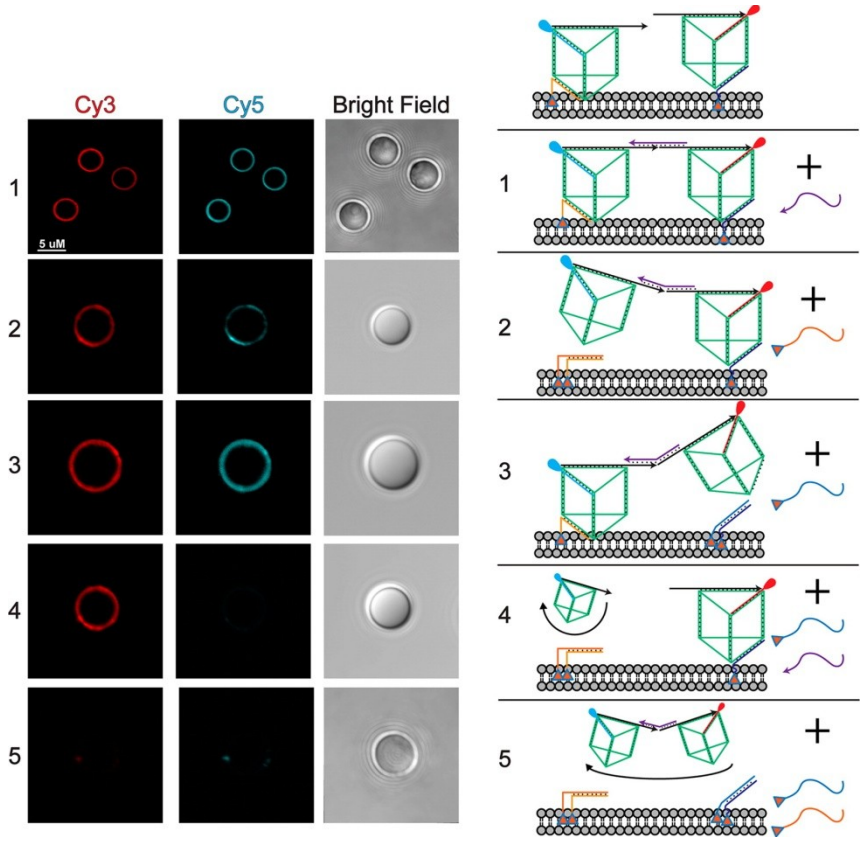

Figure AII.10 Confocal fluorescent images of dimerization and lift-off of the prisms on the bilayer: (1) control sample TP-A(Cy5) + TP-B(Cy3) with linker. (2) Displace TP-A (Cy5). (3) Displace TP-B (Cy3). (4) Displace TP-B (Cy3) and add the linker displacement strand to break the dimer. (5) Displace dimer prisms by adding both cholesterol erasing strands.

If the resulting prism dimer is singly anchored, then addition of the linker displacement strand should dissociate it into the two prism monomers, thus liberating the nonanchored prism component, which can be removed upon washing. Figure AII.10 row 4 shows the reaction

sequence in which the anchor of TP-A is first displaced, followed by linker displacement. Indeed, only the Cy3 fluorescence for TP-B remains on the beads, consistent with dissociation of the prism dimer into monomers and removal of TB-P after washing.

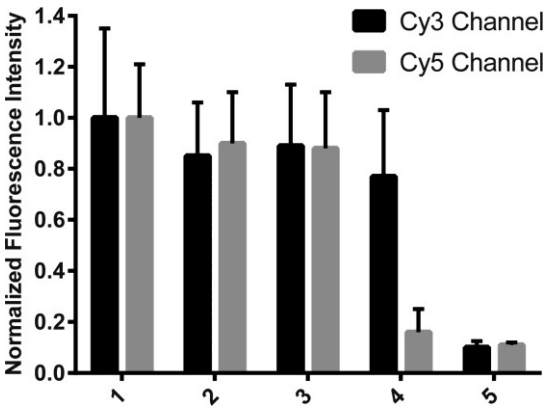

Figure AII.11 Normalized fluorescence intensity measurements for rows 1 - 6 from Fig. AII.10.

The dimerized prism can only be lifted off into the supernatant when DNA-cholesterol anchor displacement strands for both component prisms are added (Fig. AII.10 row 5). Quantitative analysis shows only a residual (10%) fluorescence remaining on the beads in either Cy3 or Cy5 channels (Fig. AII.11). The supernatant was collected after bead centrifugation. PAGE analysis indeed reveals the formation of a prism dimer, which can be separated into the two prism monomers upon displacement of the linking strand.

Following the removal of our dimerized product (Fig. AII.10, row 5) the supernatant was collected and analyzed using fluorescence scanning of PAGE (Fig. AII.12, lane 9). Lanes 1-3 and 4-6 in Fig. AII.12 corresponds to the fluorescently labeled respective prism populations, TP-A (Cy5 blue) and TP-B (Cy3 red). Dimerized prism assemblies, lanes 7-10, therefore appear as pink bands indicative of prism co-localization. This analysis is complicated by the fact that after multiple washing-centrifugation cycles, the supernatant contains some non-gel penetrating components (possibly some cholesterol-DNA anchors that have formed micellar aggregates), which may also affect the gel mobility of the other DNA components. Nevertheless, a diffuse band in the region associated with the prism dimer is apparent (lane 9), and this dimer band disappears after displacement of the linking strand, with concomitant appearance of the monomeric prism, lane 10. We carried out a control experiment, in which we generated a similar prism dimer in solution under the same conditions as the bilayer dimerization (1 hour at room

temperature). A parallel dimer band which reverts to monomers upon displacement of the linking strand is observed, Fig. AII.12 lanes 7, 8 with solution dimerization. Thus, gel analysis of the supernatant provides additional evidence for on-bilayer dimerization of the prisms and removal when two anchor displacement strands are added.

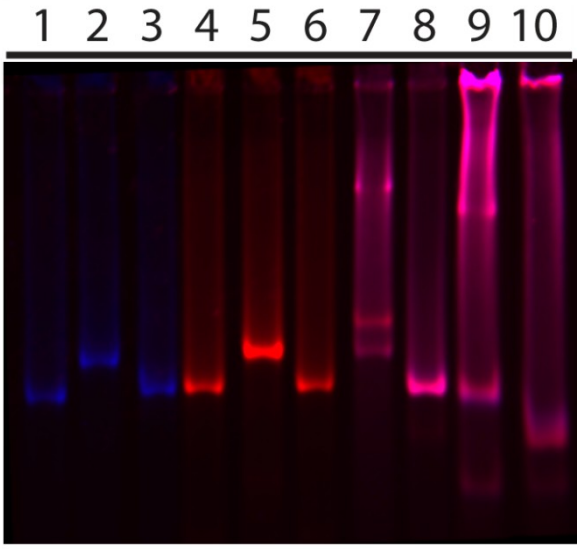

Figure AII.12. Lane 1: represents fully loaded TP-A (Cholesterol anchor, Cy5 tag, and sticky-end overhang), lane 2: addition of the linker, lane 3: displacement of the dimerizing linker strand on a TP-A, lane 4: TP-B (Cholesterol anchor, Cy3 tag, and sticky-end overhang), lane 5: addition of the linker to TP-B, lane 6: displacement of the dimerizing linker strand on TP-B. Lane 7: in solution dimerization of TP-A and TP-B following addition of the linker strand, lane 8: dimer disassembly following displacement of the linking strand. Lane 9: on bilayer dimerization of TP-A and TP-B following addition of the linker strand, lane 10: dimer disassembly on bilayer following displacement of the linking strand.

AII.12 Conclusions

These experiments have clearly shown that amphiphilic DNA cages can retain their dynamic behavior when associated with a supported bilayer membrane environment. The anchored DNA cage can load and selectively unload three different DNA-fluorophores on its top face *via* strand displacement. On the other hand, displacement of the cage from the bottom prism face required functionalization of the erasing strand with a cholesterol group. This addition renders the erasing strand more soluble within the bilayer. It is thus be able to adopt a favorable orientation with which to access the toehold region for displacement.

The DNA scaffolds were also tunable in terms of their orientation within a bilayer environment. This parameter was controlled by positioning multiple cholesterol anchors on the two faces of

the DNA cage, thus changing its orientation within the SS-BLMs. The resulting embedded cages were less susceptible to DNase I degradation, suggesting that access of anchored cages to proteins is tunable through site-specific modification of the cages themselves. This finding introduces new strategies to protect DNA cages from protein binding and nuclease degradation, when used in drug delivery applications.

Finally, we demonstrated the successful association of two different prisms by hybridization on-bilayer. The resulting dimer prism can only be released from the bilayer when both of its anchored prisms components are displaced, but stays associated with the bilayer if only one of its components is displaced.

The DNA cage used here is the simplest 3D object that we can form *via* our clip-by-clip assembly. We have shown that this 3D-assembly method is highly modular, allowing us to combine up to eight clipping strands into octameric prisms, which contain 16 asymmetric ss regions available for hybridization with various DNA conjugates (unpublished material). Unlike DNA origami constructs, the DNA cages appear to be intimately coupled to the lipid bilayer, which sterically blocks access to one or more of their sites. This will have interesting consequences on their ability for tunable cellular penetration and protein binding.

Overall, this approach allows stable association of DNA cages with lipid bilayers, controlling their orientation and accessibility within the membrane, bringing them together by hybridization and selectively lifting off any of their components. These events will potentially allow programmable dynamic control of protein binding, cell signaling, drug delivery, nanoelectronic and optical properties on lipid bilayers using a modular, easy to construct and DNA-economic scaffold.

AII.13 Experimental Section

AII.13.1 General

Gel Red™ was purchased from VWR. Acetic acid, tris(hydroxymethyl)-aminomethane (Tris), and urea were used as purchased from Aldrich. Acetic acid and boric acid were purchased from Fisher Scientific and used without further purification. Nucleosides (dA, dC, dG and T) and universal 1000Å LCAA-CPG supports with loading densities between 25-40 μmol/g and reagents used for automated DNA synthesis were purchased through Bioautomation Corporated.

Sizeexclusion columns (sephadex G-25, DNA grade) were purchased from Glen Research. 1×TAMg buffer is composed of 45 mM Tris and 12.6 mM $Mg(OAc)_2 \cdot 6H_2O$. The pH of the 1×TAMg buffer was adjusted to 8 using glacial acetic acid.

AII.13.2 Synthesis of Oligonucleotides and Modified DNA Conjugates

Standard automated oligonucleotide phosphoramidite solid-phase synthesis was performed on a Mermade MM6 synthesizer from Bioautomation. Gel electrophoresis experiments were carried out on an acrylamide 20 × 20 cm vertical Hoefer 600 electrophoresis unit. Annealing of all structures was conducted using an Eppendorf Mastercycler Pro. DNA quantification was performed using a BioTek Synergy HT microplate reader. All fluorescent labels, terminal amines and cholesterol modifications are purchased from Glen Research (with the exception of Alexa488) and used directly in manual off-column phosphoramidite coupling reactions or as ready to use prefunctionalized controlled pore glass (CPG) columns from which the oligonucleotide can be directly grown. The three fluorophores used to label oligonucleotides are the cyanine derivatives Cy3 and Cy5, and Alexa488. These dyes were chosen for their well separated excitation and emission spectra. Cy3 and Cy5 are manually inserted at the 5' position of the 26mer DNA strands. Alexa488 is purchased from Life Technologies as a succinimidyl ester (NHS ester), and coupling to DNA proceeds *via* an amine handle which is inserted at the 3' end of the DNA strand. The 3' cholesterol modification is available as a pre-functionalized CPG column while the 5' cholesterol is manually added as a phophoramidite through off-column coupling procedures. All samples were purified and characterized using denaturing polyacrylamide gel electrophoresis (PAGE). Quantification of DNA and DNA-conjugates is performed using UV absorbance measurements at 260 nm. DNA synthesis was performed on a 1 μmole scale, starting from a universal 1000 Å LCAA-CPG solid-supports. Coupling efficiency was monitored after removal of the S 3 dimethoxytrityl (DMT) 5′-OH protecting groups. The two cyanine derivatives Cy3™ and Cy5™, the cholesterol (CHOL), and amine (NH) phosphoramidites, as well as the cholesterol modified CPG, were purchased from Glen Research. Cy3, Cy5, and NH phosphoramidites were initially diluted with acetonitrile (ACN) to a concentration of 0.1 M in a glove box. For DNA couplings, approximately 10-fold excess of each phosphoramidite was used in comparison to DNA. For off-column couplings, an equal volume of ethylthiotetrazole (0.1M in acetonitrile, Glen Research) was combined with each

phosphoramidite and manually coupled on the DNA solid support with an extended reaction time of 15 minutes. After coupling, supports were removed from the glove box and returned to the DNA synthesizer for oxidation, capping and deblock steps. The cholesterol phosphoramidite was coupled in a similar fashion, however this compound was initially dissolved in dichloromethane (DCM). All sequences, modified and unmodified, were fully deprotected in concentrated ammonium hydroxide (60 ˚C/12 hours). The Alexa488™ modification was used as a succinimidyl ester (NHS ester), and coupling to the amine modified oligonucleotide was performed post synthesis and purification as per supplier protocols.

Number	Name	Sequence (5′ → 3′)
1	**DP1**	TCGCTGAGTATTTTGCCTGGCCTTGGTCCATTTGTTTTGCAAGTGTGGGCA CGCACACTTTT CGCACCGCGACTGCGAGGACTTTTCACAAATCTG
2	**Pol7-DP3**	CACTGGTCAGTTTTCCACCAGCTAGATGTTGAAGTTTTTACTCAGCGACAG ATTTGTGTTTT CGCTCTTCTATACTGGCGGATTTTGGTTTGCTGA
3	**HA4**	CCACACTTGCTTTTGTCGACACAGTAGCAGTGTGTTTTCTGACCAGTGTCA GCAAACCTTTTCCATGACGATGCACTACATGTTTTGTGTGCGTGC
4	**Pol1-DP3Top-DP1Bot**	TCGCTGAGTATTTTCCACCAGCTAGATGTTGAAGTTTTGCAAGTGTGGGCA CGCACACTTTTCGCACCGCGACTGCGAGGACTTTTCACAAATCTG
5	**Pol4-Int.Cy3-DP3**	CCACACTTGCTTTTCCACCAGCTAGATGTTGAAGT-**Cy3**-TTCTGACCAGT GTCAGCAAACCTTTTCGCTCTTCTATACTGGCGGATTTTGTGTGCGTGC
6	**Pol1-(TOP-(DP1BOT)-BOT-(DP3BOT)**	TCGCTGAGTATTTTCGCACCGCGACTGCGAGGACTTTTGCAAGTGTGGGC ACGCACACTTTTCGCTCTTCTATACTGGCGGATTTTCACAAATCTG
7	**Pol7-(TOP-(DP1TOP)-BOT-(DP3BOT)**	CACTGGTCAGTTTTGCCTGGCCTTGGTCCATTTGTTTTTACTCAGCGACAG ATTTGTGTTTTCGCTCTTCTATACTGGCGGATTTTGGTTTGCTGA
8	**DP1-Top-Alexa488**	CAAATGGACCAAGGCCAGGC-**NH- Alexa488**
9	**DP3-Top-Cy5**	**Cy5**-CTTCAACATCTAGCTGGTGGTCTTGA

10	**HA4-Top-Cy3**	**Cy3**- CTCTAGCACACTGCTACTGTGTCGAC
11	**DP1-Bot-CHOL**	GTCCTCGCAGTCGCGGTGCGAGTTGA-**CHOL**
12	**DP1-Bot-CHOL-T10**	GTCCTCGCAGTCGCGGTGCGAGTTGATTTTTTTTTT-**CHOL**
13	**DP3-Bot-CHOL-T10**	CTTCAACATCTAGCTGGTGGTCTTGATTTTTTTTTT-**CHOL**
14	**DS- DP1-Top-Alexa488**	TCTAGTGCCTGGCCTTGGTCCATTTG
15	**DS- DP3-Top-Cy5**	TCAAGACCACCAGCTAGATGTTGAAG
16	**DS- HA4-Top-Cy3**	GTCGACACAGTAGCAGTGTGCTAGAG
17	**DS- DP1-Bot-CHOL**	TCAACTCGCACCGCGACTGCGAGGAC
18	**DS- DP1-Bot-CHOL**	**CHOL**-TCAACTCGCACCGCGACTGCGAGGAC
19	**DS-DP3-Bot-CHOL**	**CHOL**-CGGATTCGCTCTTCTATACTGGCGGA
20	**DP1-3'over**	CAAATGGACCAAGGCCAGGC CTGATAGCAGCTCGT
21	**DP1-5'over**	ACCAGTCGATGTACGCAAATGGACCAAGGCCAGGC
22	**DP1-Linker**	TGACCACGTACATCGACTGGTTTTACGAGCTGCTATCAG
23	**DP1-Linker Comp**	CTGATAGCAGCTCGTAAAACCAGTCGATGTACGTGGTCA

Table AII.2 Oligonucleotides prepared *via* solid-phase synthesis. The TTTT represents a short non-base pairing spacer that is inserted within each strand and serves as the vertices of the assembled 3D structures. Non-nucleoside phosphoramidites Cy3™, Cy5™, CHOL, and NH/Alexa488™ have been inserted selectively into individual sequences as indicated.

All 96mer crude products were purified on an 8% polyacrylamide/8M urea polyacrylamide gel (PAGE; up to 20 OD260 of crude DNA per gel) at constant current of 30 mA for 2 hours (30 minutes at 250V followed by 1.5 hr at 500V), using the 1x TBE buffer. Following electrophoresis, the gels were placed on a fluorescent TLC plate wrapped in plastic wrap and illuminated with a UV lamp (254nm). The bands were excised, and the gel pieces were crushed and incubated in 12 mL of sterile water at 60 ºC for 12-16 hours. Samples were then dried to 1 mL, desalted using size exclusion chromatography (Sephadex G-25 columns, Glen Research), and quantified (OD260) using UV-Vis spectroscopy. Smaller strands (<50 base pairs) were purified using a 15% PAGE mixture and running conditions of 30 minutes at 250V followed by 45 minutes at 500V, followed by the same work up.

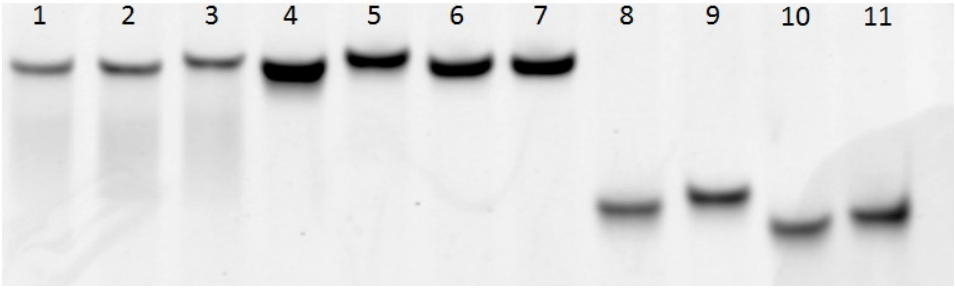

Figure AII.13 Denaturing PAGE analysis of synthesized oligonucleotides. Denaturing PAGE (8%, 1xTBE) gel ran for 30 minutes at 250V and then 1 hr at 500 V; Lane 1-1, Lane 2- 2, Lane 3- 3, Lane 4- 4, Lane 5- 5, Lane 6- 6, Lane 7- 7, Lane 8 – 20, Lane 9- 21, Lane 10- 22, Lane 11- 23.

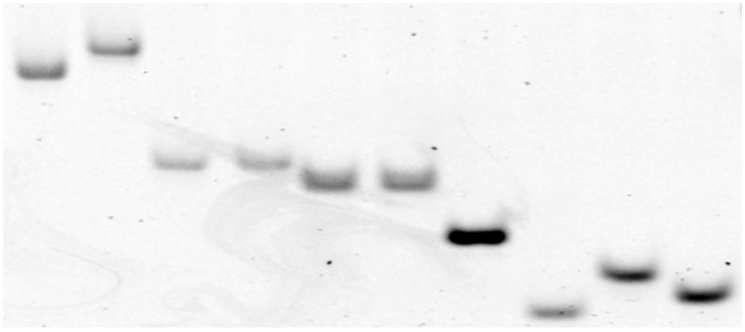

Figure AII.14 Denaturing PAGE analysis of synthesized oligonucleotides. Denaturing PAGE (12%, 1xTBE) gel ran for 30 minutes at 250V and then 1 hr at 500 V; Lane 1- 12, Lane 2-13, Lane 3-18, Lane 4-19, Lane 5-10, Lane 6-9, Lane 7-8, Lane 8-15, Lane 9-15, Lane 10-16, Lane 11-17

AII.13.3 Assembly and characterization of 3D DNA Cages

In general, equimolar amounts of each of the three scaffold clip strands (1 – 3) were combined in 1×TAMg buffer at a final 3D concentration of 0.250 μM. Functional strands (fluorescent tags and cholesterol anchors) are added in slight excess of 1:1.2 equivalents to ensure full loading of the cage structure. Samples were then subjected to an annealing protocol whereby strands were brought to 95 ˚C for 5 minutes and cooled back to 4 ºC over 4 hours. Regions of symmetry were introduced for binding of multiple DNA-cholesterol conjugates for the enzyme accessibility experiments using the clipping strands numbered 4, 6, and 7 (Table AII.2). These modified clipping strands were added as necessary for organization of up to 3 cholesterol functionalized strands. Clipping strand 5 contains an internalized Cy3 positioned within a vertex region for the enzyme accessibility experiments.

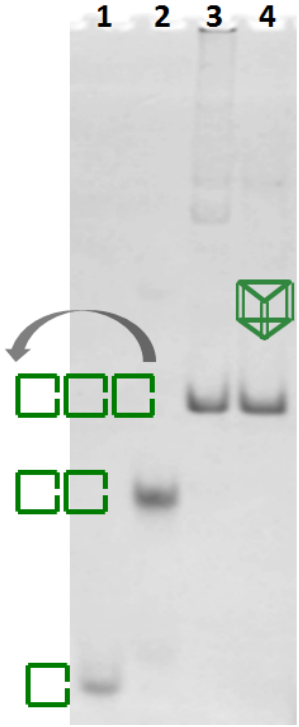

Figure AII.15 Native PAGE analysis of TP assembly. Native PAGE (6%, all samples are assembled in 1×TAMg) gel ran for 3 hours at 250V. Lanes 1 to 3 are RT additions of component strands and lane 4 is the thermocycled final product; Lane 1: Strand 1, Lane 2: Strand 1 + 2, Lane 3: Strands 1 + 2 + 3, Lane 4: Strands 1 + 2 + 3 (Thermocycled).

AII.13.4 Preparation of Bilayer Coated Beads

Spherically supported bilayers (SS-BLMs) are generated by mixing a solution of 5 μm silica beads (Bangs Laboratories) at a concentration of 9×10^6 particles/mL in PBS buffer, with an equal volume of small unilamella lipid vesicles (SUVs) solution in the same buffer for 30 minutes. The bead-vesicle solution is then washed by centrifugation (3× at 7000 rpm for 10 minutes) and the resulting pellet is re-suspended in 1× TAMg buffer. For the formation of DOPC SUVs, a chloroform solution of DOPC (1 mg/mL) is dried overnight under vacuum, and the resulting lipid film is then hydrated using PBS through vortex mixing, followed by sonication in a bath sonicator for 5-10 minutes. In general, 60 μL of a 250 nM solution of annealed DNA cages are combined with 60 μL of the bilayer coated bead solution and 380 μL of 1×TAMg buffer for a total volume of 500 μL. The bead/DNA solution is shaken gently and incubated for 15 minutes at RT and is then washed by centrifugation (1× at 7000 rpm for 10 minutes) and the resulting pellet is re-suspended in 1× TAMg. The washing steps allow for the removal of any unbound DNA cage or DNA-conjugate. The 60 μL of 250 nM DNA prisms we are adding to the incubation represents approximately 15×10^{-12} mols which is an excess of about 5× the number of prisms which could theoretically be accommodated at the surface. The higher value ensures complete coverage of the bilayer surface with the DNA scaffold (see Experimental Section AII.13.4). Working with concentrations in the nM range ensures unwanted aggregations from cholesterol mediated self-assembly. The amount of fully assembled DNA cage incubated with the SS-BLMs is determined based on the available molecular area of the total number of bilayer coated beads present in an incubation mixture. Each bead is 5 μm in diameter and the bilayer itself is approximately 5 nm in thickness. To simplify the calculation, the approximate surface area is determined using the 5 μm bead diameter only. The formula for the area of a sphere is $A = 4\pi r^2$, which gives a calculated value of 78.5 μm^2/bead. Therefore by using 60 μL of a 9×10^6 beads/mL stock solution we generate 4.24×10^7 μm^2 total available area. Each edge of our prism is 20 bp in length which is approximately equal to 7 nm in length. The triangular prism face of a DNA cage will thus occupy an area of 2.12×10^{-5} μm^2 assuming a rigid construct. Dividing the total available surface area by the area of a single prism face we calculate that approximately 2.00×10^{12} triangular prisms (or 3.32×10^{-12} mols of prisms) can theoretically be accommodated at the surface of the beads available.

AII.13.5 Bilayer Loading Quantification

Bilayer loading efficiency was determined using Cy5 fluorescence intensity signal. In these experiments the SSLBs were prepared and then coated with a DNA prism assembled with a cholesterol anchor and a Cy5 label. Samples were allowed to incubate and were then washed twice to ensure removal of any unbound prism scaffold. The cholesterol anchor displacing strand was then added to the washed mixture and incubated at RT for 1 hr. The supernatants were then collected and spin concentrated to a volume of approximately 20μL. These samples were then loaded on native PAGE next to a series of wells containing increasing amounts of a known concentration of Cy5-labeled DNA scaffold as a calibration curve (Fig. AII.15, Lanes 1 to 5). Once the gel run is complete, we scan for Cy5 fluorecence intensity using a ChemiDoc fluorescent imager (Bio-Rad). The Image Lab (Bio-Rad) software is then used for quantification of the band associated with the collected DNA material (Fig. AII.15, Lanes 7, 9, 11) using the band intensity for the calibration samples. After a second wash of the DNA/beads solution, the supernatants did not show any measurable fluorescence intensity, indicating that the incorporated DNA assemblies are stable within the SS-BLMs. Based on these results, it was determined that 5.91×10^{-13} ($\pm$ 0.173×10^{-13}) mols of labeled TP were lifted off and collected from the surface of the beads. This represents 4% of the initial amount of DNA cage that was incubated with the SS-BLMs. Based on the size of the SS-BLMs, the landed TPs occupy approximately 1.2×10^{-4} μm^2/TP. This value indicates that the TP structures occupy about 6× more area than our initial prediction. Our calculation assumed a perfect fit of all TPs packed onto the surface; on the bilayer surface the TPs likely behave as rigid constructs with a random packing which may account for the observed difference.

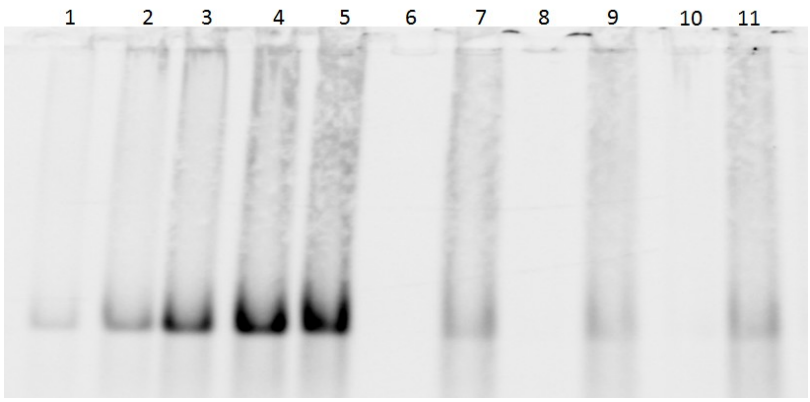

Figure AII.16 Native PAGE analysis of bilayer released DNA prisms. Native PAGE (6%, 1xTAM) gel ran for 2.5 hrs at 250V; Lanes 1 – 5 represent the calibration curve using a 0.25 μM solution with volumes of 2, 4, 6, 8, and 10 μL respectively. Lanes 7, 9, and 11 represent the spin concentrated supernatant following the addition of the cholesterol anchor displacing strand.

AII.13.6 Description of Confocal Microscopy Imaging

Images are obtained using either one or a combination of the following optical settings (*i*) λex 488 nm/ λem LP > 505 nm (single channel imaging) or λem BP 505−550 nm (multi-channel imaging), (*ii*) λex 543 nm/ λem LP > 565 nm (single channel imaging) or λem BP 550−615 nm (multi-channel imaging), and (*iii*) λex 633 nm/ λem LP > 685 nm, depending on the fluorescent tag(s) selection. The acquired intensity images were checked to avoid detector saturation and loss of offsets by carefully adjusting the laser power and detector gain. The obtained confocal images and 3D stacks are not subject to any post-acquisition image processing. For each sample, a minimum of 50 beads are imaged.

AII.13.7 Description of FRAP Experiments Details

The experiment proceeds by imaging DOPC SS-BLMs containing either Bodipy-PC or Alexa488 functionalized DNA cages. The fluorescent lipid analog Bodipy-PC (4,4-difluoro-5,7-dimethyl-4-bora-3a,4a,diaza-*s*-indacene-3-pentanoic acid) was purchased from Molecular Targeting Technologies (Pennsylvania, USA). A Zeiss LSM710 confocal laser scanning microscope is used with a 63x/1.4 oil-immersion objective and a 488 nm argon ion laser (25 mW). As seen in Fig. AII.16, a FRAP circular bleach spot, a reference spot and a third background spot (not shown here) were used for data collection and subsequent analysis. The

circular spots have a radius of 1.3 µm and the image size was 4.89 µm x 3.60 µm. Laser intensity of 100% were used for bleaching and a maximum of 10% for imaging. Five images were captured prior to FRAP bleaching in order to measure the initial average intensity, followed by 10 consecutive bleach iterations. In order to minimize the total scan time only the circular FRAP, reference and background spots were imaged. This allowed a reduction of the total experiment time, and calculation of a more reliable fluorescence recovery time and diffusion coefficient. At least 50 post-bleaching images were collected, each acquired with a scan time of 247 ms. FRAP data for each experiment were normalized to their respective initial prebleaching fluorescence intensity. After accounting for background fluorescence and bleaching caused by imaging, a FRAP average curve was constructed from the whole data set (50 separate experiments). The FRAP curve was then fitted, assuming the presence of one diffusive species, to a one component fit model with the equation $f(t) = A(1-e^{-\tau t})$ where A is the ratio of mobile to immobile species and τ is the "characteristic" diffusion time required to recover 50% of original fluorescence intensity. A lower limit of the diffusion coefficient D can be calculated from the equation $D \geq 0.224w^2/\tau$ where w is the radius of the photobleached area.[46] The observed recovery half time corresponds to the fastest recovery time that can be measured with the experimental parameters accessible to the confocal set up used for these measurements. Therefore the calculated diffusion coefficient value must be considered as a lower limit for the prism diffusion coefficient rather than an absolute value. All data processing and fitting were performed using Kaleidagraph (Synergy software).

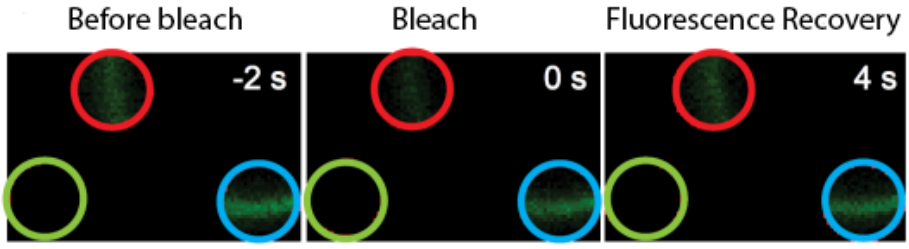

Figure AII.17 Experimental set up for FRAP data collection. Images of Bodipy-PC labeled DOPC bilayer coated SS-BLM before and after bleaching a 1.3 µm diameter circular spot (shown in red). The same size circular spot was applied for collecting reference and background fluorescence signals during the FRAP experiments (indicated in blue and green, respectively). Each image involved collecting fluorescence data from the three highlighted circular spots only.

AII.13.8 In solution hybridization and displacement of fluorescent labels and cholesterol anchors on the DNA cage

In general, equimolar amounts of each of the three scaffold clip strands (**1** – **3**) were combined in 1xTAMg buffer at a final 3D concentration of 0.250 μM. Functional strands (fluorescent tags and cholesterol anchors) are added in slight excess of 1:1.2 equivalents to ensure full loading of the cage structure. Samples were then subjected to an annealing protocol whereby strands were brought to 95 ºC for 5 minutes and cooled back to 4 ºC over 4 hours. Regions of symmetry were introduced for binding of multiple DNA-cholesterol conjugates for the enzyme accessibility experiments using the clipping strands numbered 4, 6, and 7 (SI-Table 1). These modified clipping strands were added as necessary for organization of up to 3 cholesterol functionalized strands. Clipping strand 5 contains an internalized Cy3 positioned within a vertex region for the enzyme accessibility experiments.

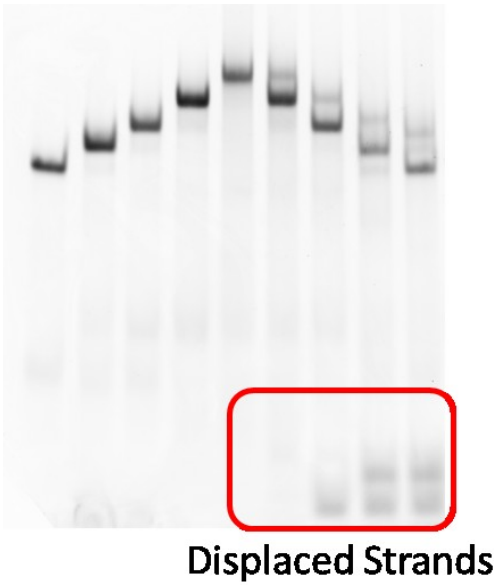

Figure AII.18 Native PAGE analysis of TP assembly. Native PAGE (6%, all samples are assembled in 1xTAMg) gel ran for 3 hours at 250V. Lanes 1 to 3 are RT additions of component strands and lane 4 is the thermocycled final product; Lane 1: Strand 1, Lane 2: Strand 1 + 2, Lane 3: Strands 1 + 2 + 3, Lane 4: Strands 1 + 2 + 3 (Thermocycled).

AII.13.9 Membrane Integrity Control

This figure shows the fluorescence microscopy for SS-BLMs prepared using the fluorescent DOPC analog (Bodipy-PC) and then further labeled using a Cy3 functionalized prism scaffold. The image shows homogeneous coverage of the bead with the labeled bilayer, as well as with the Cy3 labeled prism. This indicates the beads are completely covered in both a lipid bilayer and an outer shell of DNA cages.

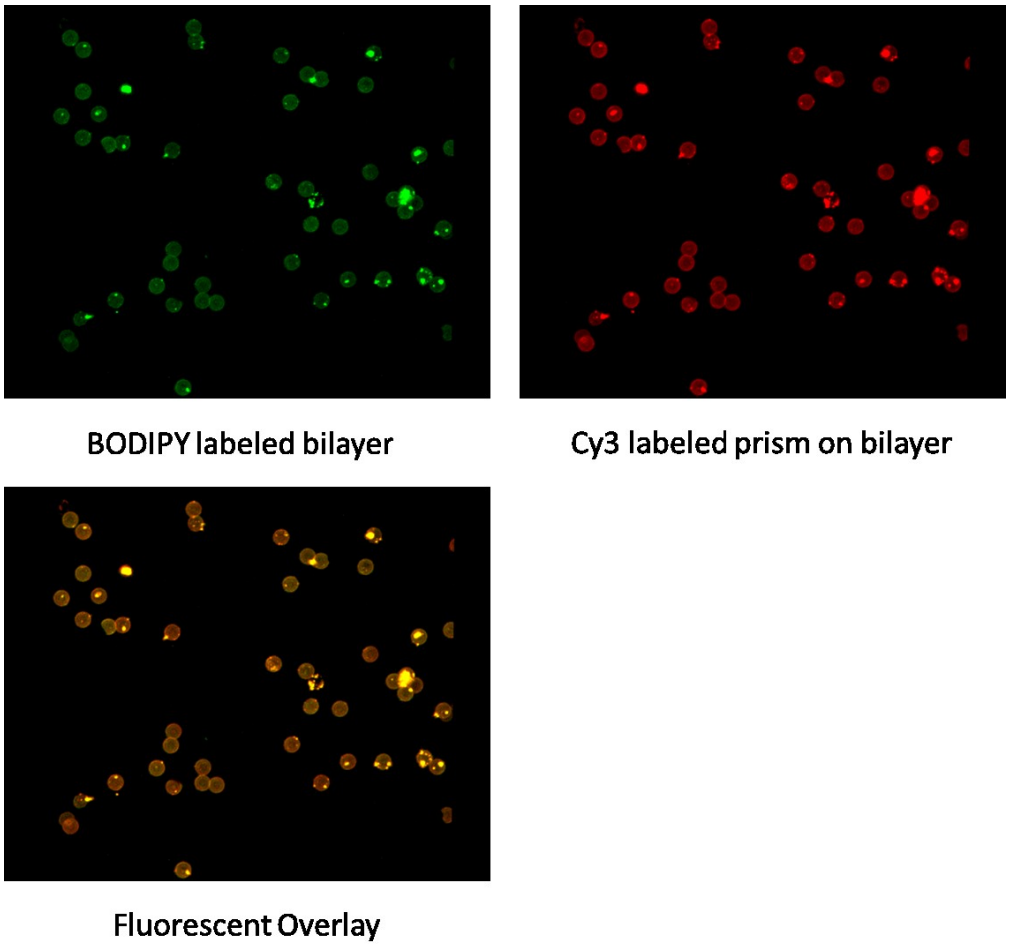

Figure AII.19 Membrane integrity and coverage. Top right, shows the fluorescence channel for the Bodipy-PC labeled bilayer. Top left, shows the same beads through the Cy3 channel. Bottom, shows the overlay of the two channels and confirms co-localization of the bilayer and the labeled prisms.

AII.14 References

1. Borjesson, K.; Wiberg, J.; El-Sagheer, A. H.; Ljungdahl, T.; Martensson, J.; Brown, T.; Norden, B.; Albinsson, B.; Functionalized nanostructures: redox-active porphyrin anchors for supramolecular DNA assemblies. *ACS Nano* **2010**, *4*, 5037-5046.

2. Howorka, S.; DNA nanoarchitectonics: assembled DNA at interfaces. *Langmuir* **2013**, *29*, 7344-7353.

3. Kwak, M.; Herrmann, A.; Nucleic acid amphiphiles: synthesis and self-assembled nanostructures. *Chem. Soc. Rev.* **2011**, *40*, 5745-5755.

4. van der Meulen, S. A. J.; Leunissen, M. E.; Solid colloids with surface-mobile DNA linkers. *J. Am. Chem. Soc.* **2013**, *135*, 15129-15134.

5. He, H. Z.; Chan, D. S. H.; Leung, C. H.; Ma, D. L.; G-quadruplexes for luminescent sensing and logic gates. *Nucleic Acids Res.* **2013**, *41*, 4345-4359.

6. Leung, C. H.; Chan, D. S. H.; He, H. Z.; Cheng, Z.; Yang, H.; Ma, D. L.; Luminescent Detection of DNA-binding Proteins. *Nucleic Acids Res.* **2012**, *40*, 941-955.

7. Ma, D. L.; He, H. Z.; Chan, D. S. H.; Leung, C. H.; Simple DNA-based logic gates responding to biomolecules and metal ions. *Chem. Sci.* **2013**, *4*, 3366-3380.

8. Ma, D. L.; He, H. Z.; Leung, K. H.; Zhong, H. J.; Chan, D. S. H.; Leung, C. H.; Drug repositioning by structure-based virtual screening. *Chem. Soc. Rev.* **2013**, *42*, 3427-3440.

9. Hung, Y. C.; Lin, T. Y.; Hsu, W. T.; Chiu, Y. W.; Wang, Y. S.; Fruk, L.; Functional DNA biopolymers and nanocomposite for optoelectronic applications. *Opt. Mater.* **2012**, *34*, 1208-1213.

10. Jones, M. R.; Osberg, K. D.; Macfarlane, R. J.; Langille, M. R.; Mirkin, C. A.; Templated techniques for the synthesis and assembly of plasmonic nanostructures. *Chem. Rev.* **2011**, *111*, 3736-3827.

11. Pal, S.; Dutta, P.; Wang, H. N.; Deng, Z. T.; Zou, S. L.; Yan, H.; Liu, Y.; Quantum efficiency modification of organic fluorophores using gold nanoparticles on DNA origami scaffolds. *J. Phys. Chem. C* **2013**, *117*, 12735-12744.

12. Young, K. L.; Ross, M. B.; Blaber, M. G.; Rycenga, M.; Jones, M. R.; Zhang, C.; Senesi, A. J.; Lee, B.; Schatz, G. C.; Mirkin, C. A.; Using DNA to design plasmonic metamaterials with tunable optical properties. *Adv. Mater.* **2014**, *26*, 653-659.

13. Keum, J. W.; Ahn, J. H.; Bermudez, H.; DNA-based delivery vehicles: pH-controlled disassembly and cargo release. *Small* **2011**, *7*, 3529-3535.

14. Li, J.; Pei, H.; Zhu, B.; Liang, L.; Wei, M.; He, Y.; Chen, N.; Li, D.; Huang, Q.; Fan, C. H.; Self-assembled multivalent DNA nanostructures for noninvasive intracellular delivery of immunostimulatory CpG oligonucleotides. *ACS Nano* **2011**, *5*, 8783-8789.

15. Schuller, V. J.; Heidegger, S.; Sandholzer, N.; Nickels, P. C.; Suhartha, N. A.; Endres, S.; Bourquin, C.; Liedl, T.; Cellular immunostimulation by CpG-sequence-coated DNA origami structures. *ACS Nano* **2011**, *5*, 9696-9702.

16. Walsh, A. S.; Yin, H. F.; Erben, C. M.; Wood, M. J. A.; Turberfield, A. J.; DNA cage delivery to mammalian cells. *ACS Nano* **2011**, *5*, 5427-5432.

17. Hamblin, G.D.; Carneiro, K.M.; Fakhoury, J.; Bujold, K.E.; Sleiman, H.F.; Rolling circle amplification-templated DNA nanotubes show increased stability and cell penetration ability. *JACS* **2012**, *134*, 2888-2891.

18. Fakhoury, J.; McLaughlin, C.; Edwardson, T.; Conway, J.; Sleiman, H.F.; Development and characterization of gene silencing DNA cages. *Biomacromol.* **2014**, *15*, 276-282.

19. Park, S. Y.; Lytton-Jean, A. K. R.; Lee, B.; Weigand, S.; Schatz, G. C.; Mirkin, C. A.; DNA-programmable nanoparticle crystallization. *Nature* **2008**, *451*, 553-556.

20. Banchelli, M.; Betti, F.; Berti, D.; Caminati, G.; Bombelli, F. B.; Brown, T.; Wilhelmsson, L. M.; Norden, B.; Baglioni, P.; Liposomes with double-stranded DNA anchoring the bilayer to a hydrogel core *J. Phys. Chem. B* **2008**, *112*, 10942-10952.

21. Beales, P. A.; Vanderlick, T. K.; Partitioning of membrane-anchored DNA between coexisting lipid phases. *J. Phys. Chem. B* **2009**, *113*, 13678-13686.

22. Chung, M.; Boxer, S. G.; Stability of DNA-tethered lipid membranes with mobile tethers. *Langmuir* **2011**, *27*, 5492-5497.

23. Chan, Y. H. M.; van Lengerich, B.; Boxer, S. G.; Lipid-anchored DNA mediates vesicle fusion as observed by lipid and content mixing. *Biointerphases* **2008**, *3*, FA17.

24. Stengel, G.; Zahn, R.; Hook, F.; DNA-induced programmable fusion of phospholipid vesicles. *JACS* **2007**, *129*, 9584-9585.

25. Li, C. Y.; Wood, D. K.; Hsu, C. M.; Bhatia, S. N.; DNA-templated assembly of droplet-derived PEG microtissues. *Lab Chip* **2011**, *11*, 2967-2975.

26. Burns, J. R.; Stulz, E.; Howorka, S.; Self-assembled DNA nanopores that span lipid bilayers. *Nano Lett.* **2013**, *13*, 2351-2356.

27. Langecker, M.; Arnaut, V.; Martin, T. G.; List, J.; Renner, S.; Mayer, M.; Dietz, H.; Simmel, F. C.; Synthetic lipid membrane channels formed by designed DNA nanostructures. *Science* **2012**, *338*, 932-936.

28. Woller, J. G.; Hannestad, J. K.; Albinsson, B.; Self-assembled nanoscale DNA-porphyrin complex for artificial light harvesting. *JACS* **2013**, *135*, 2759-2768.

29. Schade, M.; Knoll, A.; Vogel, A.; Seitz, O.; Liebscher, J.; Huster, D.; Herrmann, A.; Arbuzova, A. Remote control of lipophilic nucleic acids domain partitioning by DNA hybridization and enzymatic cleavage. *JACS* **2012**, *134*, 20490-20497.

30. Suzuki, Y.; Endo, M.; Yang, Y. Y.; Sugiyama, H.; Dynamic assembly/disassembly processes of photoresponsive DNA origami nanostructures directly visualized on a lipid membrane surface. *JACS* **2014**, *136*, 1714-1717. 31.

31. Johnson-Buck, A.; Jiang, S.; Yan, H.; Walter, N. G.; DNA-cholesterol barges as programmable membrane-exploring agents. *ACS Nano*, **2014**, *8*, 5641-5649.

32. Langecker, M; Arnaut, V.; List, J.; Simmel, F. C.; DNA nanostructures interacting with lipid bilayer membranes. *Accts. Chem. Res.* **2014**, *47*, 1807-1815.

33. Czogalla, A.; Petrov, E. P.; Uzunova, V.; Zhang, Y.; Seidel, R.; Schwille, P.; Switchable domain partitioning and diffusion of DNA origami rods on membranes. *Faraday Discuss* **2013**, *161*, 31-43.

34. Conway, J. W.; McLaughlin, C. K.; Castor, K. J.; Sleiman, H.; DNA nanostructure serum stability: greater than the sum of its parts. *Chem. Comm.* **2013**, *49*, 1172-1174.

35. Lo, P. K.; Karam, P.; Aldaye, F. A.; McLaughlin, C. K.; Hamblin, G. D.; Cosa, G.; Sleiman, H. F. Loading and selective release of cargo in DNA nanotubes with longitudinal variation. *Nat. Chem.* **2010**, *2*, 319-328.

36. Bayerl, T. M.; Bloom, M.; Physical properties of single phospholipid bilayers adsorbed to micro glass beads. A new vesicular model system studied by 2H-nuclear magnetic resonance. *Biophys. J.* **1990**, *58*, 357-362.

37. Mornet, S.; Lambert, O.; Duguet, E.; Brisson, A.; The formation of supported lipid bilayers on silica nanoparticles revealed by cryoelectron microscopy. *Nano Letters* **2005**, *5*, 281-285.

38. Tanaka, M.; Sackmann, E.; Polymer-supported membranes as models of the cell surface. *Nature* **2005**, *437*, 656-663.

39. Argyo, C.; Weiss, V.; Bräuchle, C.; Bein, T.; Multifunctional mesoporous silica nanoparticles as a universal platform for drug delivery. *Chem. Mater.* **2014,** *26*, 435-451.

40. Gopalakrishnan, G.; Thostrup, P.; Rouiller, I.; Lucido, A. L.; Belkaid, W.; Colman, D. R.; Lennox, R. B.; Lipid bilayer membrane-triggered presynaptic vesicle assembly. *ACS Chem. Neurosci.* **2010**, *1*, 86-94.

41. Schwille, P.; Diez, S.; Synthetic biology of minimal systems. *Crit. Rev. Biochem. Mol.* **2009**, *44*, 223-242.

42. Troutier, A. L.; Ladaviere, C.; An overview of lipid membrane supported by colloidal particles. *Adv. Colloid Interface Sci.* **2007**, *133*, 1-21.

43. Gopalakrishnan, G.; Rouiller, I.; Colman, D. R.; Lennox, R. B.; Lipid bilayer membrane-triggered presynaptic vesicle assembly. *Langmuir* **2009**, *25*, 5455-5458.

44. Borjesson, K.; Lundberg, E. P.; Woller, J. G.; Norden, B.; Albinsson, B.; Soft-surface DNA nanotechnology: DNA constructs anchored and aligned to lipid membrane. *Angew Chem Int Ed.* **2011**, *50*, 8312-8315.

45. Woller, J. G.; Borjesson, K.; Svedhem, S.; Albinsson, B. Reversible hybridization of DNA anchored to a lipid membrane *via* porphyrin. *Langmuir* **2012**, *28*, 1944-1953.

46. Soumpasis, D. M. Theoretical analysis of fluorescence photobleaching recovery experiments. *Biophys. J.* **1983**, *41*, 95-97.